UNIVERSITY OF SOUTHAMPTON

The Long-Term Modelling of Space Debris Clouds in High Earth Orbits

by Neil Williams (M.Eng)

- Thesis submitted for the degree of Doctor of Philosophy -

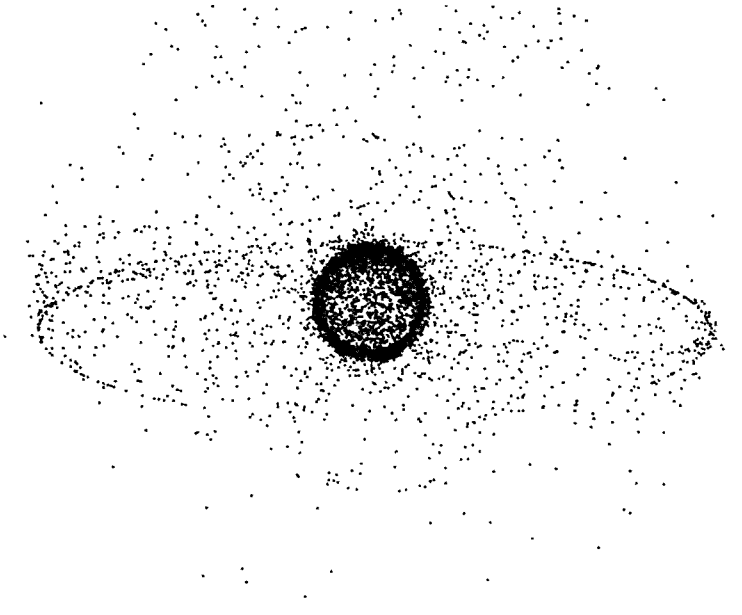

Astronautics Research Group
School of Engineering Sciences
Aeronautics and Astronautics

September 2003

UNIVERSITY OF SOUTHAMPTON

ABSTRACT

ASTRONAUTICS RESEARCH GROUP

SCHOOL OF ENGINEERING SCIENCES

AERONAUTICS AND ASTRONAUTICS

Doctor of Philosophy

THE LONG-TERM MODELLING OF SPACE DEBRIS CLOUDS IN HIGH EARTH ORBITS

by Neil Williams (M. Eng)

An increasing number of spacecraft and launch vehicle third stage rocket motors are being launched into geostationary orbit (GEO). This orbit is an important and unique resource and, unlike the low-Earth orbit (LEO) regime, the de-orbiting effects of drag on objects in the GEO regime are negligible – thus any object launched into GEO will not be removed by natural forces. The GEO regime thus represents a growing debris environment that poses a significant long-term collision hazard to future launched spacecraft. To date, relatively little work has been done in modelling space debris in GEO, although this is a trend that is just beginning to be reversed as more and more emphasis is placed on GEO debris modelling.

Space debris models can have very long run times and, depending on the input parameters, can take several days to generate a prediction of the future debris environment, even on the fastest of machines. The orbital propagator is one of the most time-consuming components in any debris model and thus, in an effort to reduce run-times, many debris models utilise various techniques to attempt to improve on the speeds of their orbital propagators. All of these techniques involve some forfeit in the accuracy of the results produced and most depend on assumptions which are only really valid in the LEO regime. To date, little work has been done in the development of a fast method of propagating debris clouds in the GEO regime. This PhD attempts to address this problem by developing an accurate and novel Fast Cloud Propagator (FCP) for use in high-Earth orbits, including GEO and the GEO regime.

The FCP has undergone rigorous testing and has proved itself capable of accurately modelling the debris clouds produced by a number of breakup events, as modelled by a number of leading breakup models, over various time periods (up to the maximum design threshold of 100 years), in a variety of test orbits. A comprehensive risk analysis exercise has shown that the FCP results are accurate enough to be used in future collision risk analyses and hence in future debris environment prediction studies. The speed increases attained by the FCP depend on the size of the debris cloud, where the efficiency of the FCP increases as the number of fragments in the cloud increases. If a large number of Monte Carlo simulations are required, as is desirable in debris environment prediction studies, then the FCP has demonstrated speed increases which can be thousands of times faster than conventional methods of space debris propagation.

Acknowledgements

First and foremost, I would like to thank my supervisor, Dr. Graham Swinerd, for his constant guidance and encouragement during our regular fortnightly meetings and for his swift and thorough proof reading of this thesis. I would also like to thank Dr. Hugh Lewis, not least for his orbital propagator, which is at the heart of the model described herein, but also for all his help with any programming problems I encountered and for proof reading Chapter 5 of this thesis.

Many thanks to Dr. Clare Martin and Dr. Roger Walker of QinetiQ, Farnborough, UK, who gave up so much of their precious time to attend so many meetings and for their continued interest in this work. I would also like to thank QinetiQ for contributing towards my project costs, which have allowed me to attend international conferences in Germany, France, Brazil and the USA.

I would like to extend my thanks to Dr. Paula Krisko of the Johnson Space Centre, NASA, USA, Mr. Peter Wegener of the Technical University of Braunschweig, Germany, Dr. Alessandro Rossi of ISTI, Italy, and again to Dr. Roger Walker of QinetiQ who were very quick to answer my queries regarding the implementation of their breakup models and who subsequently helped me validate and test those models.

Many thanks to Gavin Gittins for helping me conduct the risk analysis section of this work. My thanks also to Simon Richards for allowing me to bounce several useless ideas off him, before he finally came up with a good one, which I could then pretend was mine all along! Thanks also to Ismat for making sure that I never had too much stationery on my desk!

A big thank you goes to my parents for their unwavering support over the last four years – at last it looks like I'm going to get a "proper job"!

Last but not least, I'd like to thank Simon, Gav, Duncan, Paolo, Mark, Scott, Tom, Heather, Colleen and all my regular drinking-buddies for helping me occasionally escape office life, even if it was usually under the promise of that elusive "one pint". Cheers guys!

Neil Williams
September 2003

List of Acronyms

ASAT	Anti-SATellite (weapon)
CIRA	Cooperative Institute for Research in the Atmosphere
CNUCE	Centro Nazionale Universitario di Calcolo Elettrico
DAMAGE	Debris Analysis and Monitoring Architecture for the Geostationary Environment
DCP	Debris Cloud Propagator
DERA	Defence Evaluation and Research Agency
DoD	Department of Defence (US)
ESA	European Space Agency
ESOC	European Space Operations Centre
ETS	Experimental Test Site
EURECA	EUropean REtrievable CArrier
FCP	Fast Cloud Propagator
FOCUS	Fast Orbit Computation Utility Software
GEO	Geostationary Earth Orbit
GTO	Geostationary Transfer Orbit
HEO	Highly Elliptical Orbit
HIX	High Intensity Explosion
HST	Hubble Space Telescope
IDES	Integrated Debris Evolution Suite
ISTI	Institute of Information Science and Technologies
LDEF	Long Duration Exposure Facility

LEO	Low Earth Orbit
LIX	Low Intensity Explosion
LRIR	Long Range Imaging Radar
LSI	Low-Speed Impact
MASTER	Meteoroid and Space Debris Terrestrial Environment Reference Model
MEO	Medium Earth Orbit
MIT	Massachusetts Institute of Technology
MLI	Multi-Layer Insulation
NASA	National Aeronautics and Space Administration
NORAD	North American Aerospace Defence Command
PCD	Probabilistic Continuum Dynamics
PETRA	Propagator for Low Earth TRAjectories
POM	Population Orbit Matrix
PROOF	Program for Radar and Optical Observation Forecasting
RAAN	Right Ascension of the Ascending Node
SDM	Semi Deterministic Model
SDS	Space Debris Simulation (Software)
SOCIT	Satellite Orbital Debris Characterisation Impact Test
SRM	Solid Rocket Motor
SRP	Solar Radiation Pressure
SSN	Space Surveillance Network
STAT	STochastic Analogue Tool
STS	Space Transportation System
TSF	Time Scaling Factor
UoS	University of Southampton
USSPACECOM	United States SPACE COMmand
UV	Ultra-Violet

Glossary

Number distribution histograms

The histograms showing the number of fragments binned according to a particular orbital element, e.g. the number of fragments binned by semi-major axis. These are sometimes called *number distributions* for short.

Element-relationship scatter plot

A 2-dimensional scatter plot showing the values of one element plotted against another, sometimes referred to as *scatter plot* for short, e.g. the a vs. e scatter plot.

Pseudo-fragments

Imaginary fragments created purely for the purposes of increasing propagation speeds. Generally, pseudo-fragments are fragments that represent a larger set of fragments with similar characteristics. These are sometimes referred to as weighted particles. In the context of the FCP, developed herein, pseudo-fragments will contain the elements that represent the modes and 3-sigma limits of the *number distributions* in each element as well as other important parameters to describe the shape of the debris cloud.

Skeletal scatter plots

The *element–relationship scatter plots* showing only the orbital elements assigned to the *pseudo-fragments*.

Primary scatter plots

Five scatter plots used to re-construct the element-relationships at the desired epoch. For obits where $e \neq 0$, the primary scatter plots are the a vs. e, a vs. i, a vs. Ω, a vs. ω, and a

vs. M scatter plots. For orbits where $e \approx 0$ the primary scatter plots are the a vs. e, a vs. i, e vs. Ω, e vs. ω, and a vs. M scatter plots

Secondary scatter plots

The remaining 10 scatter plots that are re-created indirectly by the FCP as a result of re-creating the 5 primary scatter plots.

Actual

In the context of the FCP, developed herein, the word "Actual" shall refer to all things pertaining to the debris cloud that has been propagated using a conventional orbital propagator, e.g. actual debris cloud, actual scatter plot.

Simulated

In the context of the FCP developed herein, the word "Simulated" shall refer to all things pertaining to the debris cloud that has been propagated using the FCP, e.g. simulated debris cloud, simulated scatter plot.

Core distribution

The distribution of fragments that contribute to the underlying trend when viewed in any 2-dimensional *element-relationship scatter plot*.

Rogue fragments

Fragments with orbital elements that lie outside the *core distribution* when plotted in any *element-relationship scatter plot*, i.e. fragments with orbital elements that detract from the underlying trend of the plot.

Isotropic distribution

A distribution of orbital element-pairs in any *element-relationship scatter plot* where there is no correlation between the two sets of orbital element values. An isotropic distribution between two elements can be modelled by randomly assigning the values of one orbital element to another.

Element-Space

Six dimensional hyperspace, where each dimension is represented by one of the orbital elements. A distribution in six-dimensional hyperspace can clearly only be represented on paper by a number of two-dimensional subspace sets of the six-dimensional distribution. 15 subspace sets are required to describe the relationship of each orbital element with each of the other orbital elements (5+4+3+2+1 = 15). These subspace sets are in the form of *element-relationship scatter plots*.

Modified Elements

Orbital elements that have been 'mapped' to different values. In the FCP, developed herein, mapping occurs before and after cloud propagation. The mapping process is described fully in Chapter 5.

Modified Element-Space

Like *element-space*, except that the six-dimensional hyperspace is now occupied by the *modified elements* rather than the original orbital elements.

Contents

List of Figures

List of Tables

Chapter 1

Introduction

1.1 Overview

Since the space age began with the launch of Sputnik 1 in 1957, man has been polluting the near-Earth space environment with his orbital space debris. Mainly comprising left over rocket parts, spent spacecraft, launch fairings and jettisoned rocket motors, this orbital debris has grown over the years as mankind's utilisation of space has grown, and as mankind's space activities have increased almost exponentially over the years, so has our production of space debris. The orbital debris population in Earth orbit has now increased to a level where operational satellites are being placed at a significant risk of collision, which could cause them considerable damage. The effect on operations of orbital debris are being realised by spacecraft manufacturers, who have to contemplate the inclusion of heavy and expensive shielding into their designs to protect their spacecraft from debris damage.

As the space debris population continues to increase, there is a growing need to develop models that can quickly and reliably characterise the future debris population, so that future debris-related risks to orbiting systems may be assessed. These debris models can not only be used to assess the risks to existing orbiting objects but can also be used to predict launch trends and assess the risks to spacecraft launched in the future. Various debris mitigation strategies can be incorporated into these models, which will help

governments and space agencies determine the most effective measures for reducing the growth of space debris. Another useful role for the space debris model is to determine the impact that new space activities will have on the debris environment. This is becoming an important issue, as multiple-satellite constellation systems are about to be launched in the next decade to facilitate global mobile phone coverage and high-speed internet/multimedia services.

1.2 Technical Objectives

There is a constant trade-off in debris modelling between the accuracy of a debris model's results and the computational time expended in attaining those results. Consequently, many debris modellers have sought to increase the speed of their models by utilising various sophisticated techniques to improve on the speed of the slowest component in the model – that of the orbital propagator.

A faster debris model will be capable of generating more Monte Carlo iterations than a slower model. Monte Carlo iterations are desirable in debris modelling in order to smooth out the peaks and troughs in the predicted future spatial density distribution of fragments in near-Earth space caused by the prediction of unlikely events such as explosions or collisions. A number of iterations of the modelling of the debris environment are conducted, the results of which are averaged in order to produce a 'smoothed' predicted future spatial density distribution of fragments. It is hoped that this smoothed distribution will then more closely resemble the underlying trend in the actual future spatial density distribution of fragments in near-Earth space. The greater the number of Monte Carlo iterations that can be produced, the greater this smoothing effect will be. However, due to time constraints, most debris modellers tend to model very few iterations. A faster debris model would allow debris modellers to perform a greater number of Monte Carlo runs and will thus have the effect of producing a more accurate model with a greater level of confidence in the results thus produced.

A number of fast debris propagators exist, which claim to be able to reproduce the future environment to a high degree of accuracy. However, these propagators have limitations that only allow them to be used for certain debris size ranges or within certain altitude ranges, i.e. mostly low-Earth orbit (LEO) regions. To date, little work has been done in developing a fast debris propagator that is dedicated to propagating debris clouds in the geostationary (GEO) regime. The ability to develop a model capable of quickly and accurately modelling the long-term evolution of debris in the GEO regime is becoming ever more important as the GEO debris population continues to increase. The primary aim of this PhD is to develop such a model.

The objectives of this PhD can be broken down as follows:

- to review the current state-of-the-art research in fast debris propagators;
- to develop a Windows-based, semi-deterministic computer simulation model capable of quickly propagating large debris clouds through the GEO regime over long time periods (up to 100 years) whilst maintaining a high degree of accuracy in the results produced;
- to ensure that the model produced is portable, and can be used with a number of leading breakup models; and
- to assess the accuracy of the model by comparing the results produced with those from a conventional propagator for a number of breakup data sets.

1.3 Software Development

A Windows-based, semi-deterministic, suite of programs was developed and written in C/C++ in order to generate a breakup event and propagate the fragments emanating from this breakup. This suite of programs mainly comprises four breakup models and two orbital propagators – one conventional propagator, and the novel Fast Cloud Propagator

(FCP), which uses the conventional propagator to evolve the debris cloud as a series of fragment distributions.

The conventional propagator is capable of propagating debris fragments under the influence of the J_2, J_3, J_{22}, J_{31} and J_{33} Earth-gravity harmonics as well as luni-solar gravitational perturbation effects, SRP (Solar Radiation Pressure) perturbations and perturbations due to drag. This conventional propagator is the propagator used in the DAMAGE program. DAMAGE (Debris Analysis and Monitoring Architecture for the Geostationary Environment) is a debris environment model dedicated to modelling debris in high Earth orbits over the long term. It has been developed at the University of Southampton under EPSRC contract by Dr. Hugh Lewis. The fast cloud propagator evolves the debris cloud as a whole, by propagating the fragment distributions that describe the debris cloud. The FCP thus gains a considerable speed increase over a conventional propagator, which typically evolves the debris cloud by individually propagating the large numbers of fragments found in the cloud. The FCP is a novel method of propagating space debris and is described in detail in Chapter 5.

The model comprises four of the leading breakup codes, namely those used in the IDES, SDM, MASTER and EVOLVE 4.0 debris models. The principal advantage of incorporating four breakup models into the code is that the FCP can now be designed to work for all four models, thus making it portable across a number of leading debris models. The FCP propagates distributions of fragments and attempts to re-create the debris cloud at any required epoch using those distributions. However these distributions are a function of the breakup model used. Thus testing the FCP with different breakup models was imperative to assess its robustness and hence usefulness to the debris community. The breakup models are described in more detail in Chapter 4.

These breakup models were implemented primarily to test the robustness of the FCP. However, the work also stands alone as a comparative analysis between the various breakup models and their effect on the evolution of breakup clouds. This was presented as a conference paper to the international community at the 52nd International

Astronautical Congress in Toulouse, France in October 2001 [1]. An introduction to the FCP was presented at the World Space Congress in Houston, Texas, USA in October 2002 and was later revised for inclusion in the journal, Advances in Space Research, in February 2003 [2].

1.4 Thesis Structure

This thesis is structured in such a way as to guide the reader through a logical progression of steps from the statement of the problem and the objectives of this PhD, described in this chapter, to the fulfilment of those objectives and the validation and testing of the model.

Chapter 2 sets the scene by reviewing the literature to give an impression of the current orbital debris environment at various altitudes and at various size ranges. This chapter provides the results of a very general literature review on space debris and is particularly useful for the non-specialist reader. It describes how a debris cloud evolves following an on-orbit breakup event and gives a brief description of the measurement techniques used to measure the current population at various altitudes and at various particle size ranges. The differences between debris in the LEO regime and the GEO regime are also discussed. The chapter gives a brief overview of some of the shielding currently employed by spacecraft to shield against space debris impacts and describes the mitigation policies currently being considered and implemented in an attempt to reduce the proliferation of space debris in the future. Finally, Chapter 2 discusses the different types of debris models available in an effort to give a general overview of debris modelling in its current state. This Chapter will explain why debris in GEO is such a problem and will show that it is a problem that will become increasingly important with time.

Chapter 3 provides the results of a detailed literature review into fast orbital propagators and orbital propagation theory. The first half of this chapter focuses on the perturbative

effects experienced by an object in and around the GEO regime and discusses geopotential orbital perturbation theory as well as luni-solar gravitational perturbations and the perturbative effects due to SRP. The second half of this chapter provides the rationale for fast orbital propagators in general and describes the state-of-the-art in fast orbital propagation models. A review of these propagators highlights their strengths as well as their weaknesses, and thus provides the rationale for a new fast cloud propagator for use in the GEO regime.

Chapter 4 discusses the development and validation of the breakup models used in the IDES, SDM, MASTER and EVOLVE 4.0 debris environment models. This chapter provides a detailed comparison of their results and assesses the effects of using different breakup models on the long term evolution of a debris cloud in GEO. The variations between the results of different breakup models is a source of some concern to the debris community and is believed to be one of the principal reasons for the diversity of results produced by the different debris environment models.

Chapter 5 presents a comprehensive description of the novel FCP method. It begins with a description of the fragment number distributions for each element and the relationships between the orbital elements that make the development of the FCP possible. The general methodology of propagating distributions instead of individual fragments is described and the advantages are discussed. Although simple in premise, a number of sophisticated techniques had to be employed in order to quickly propagate the fragment distributions and accurately re-position the fragments at the desired epoch. These techniques are described fully in this chapter.

The results of the FCP are presented in Chapter 6. The results of two case studies are presented: one GEO and one non-GEO. The graphical comparison provided allows for a qualitative assessment of the FCP's accuracy. An analysis is then performed to quantify the errors in these case studies, as well as in 18 other case studies that were conducted. In order to determine whether these errors are acceptable, the risk posed to a target spacecraft by the conventionally propagated cloud is then compared to the risk posed by

the FCP propagated cloud for each of the 20 case studies. Finally, the speed increase of the FCP over the conventional propagator is presented as a function of the number of fragments in the debris cloud.

Chapter 7 provides a summary of the work contained herein, which is broken down chapter-by-chapter for the main chapters of this thesis. Chapter 7 summarises the orbital debris environment, fast debris propagation methods, breakup modelling and the novel fast cloud propagator, and highlights the advantages that the new FCP will bring to the debris research community.

The work presented in Chapter 5 of this thesis represents but a fraction of the possible development of this novel method. Chapter 8 describes the future work that could be undertaken to explore the full potential of the FCP methodology, as an invitation to researchers elsewhere to adopt and fully exploit the ideas presented.

Chapter 2

The Orbital Debris Problem

2.1 Introduction

This chapter is intended to describe the debris problem in broad terms. The main focus of the chapter is the proliferation of man-made artificial debris in near-Earth orbit, although the natural meteoroid environment is also described briefly. The chapter begins by summarising the sources of orbital debris and outlining historical trends in the debris population and the subsequent risks to spacecraft thus caused. The chapter describes the current debris environment in near-Earth orbit and highlights the differences in characteristics between LEO and GEO debris. It also discusses the limitations of measurement techniques, which is one of the primary reasons for undertaking the computational modelling of orbital debris. The chapter outlines some of the proposed solutions to the debris problem in terms of shielding and collision avoidance manoeuvres, and also in terms of strategies designed to curb the proliferation of artificial debris. The chapter ends with a broad discussion of the various types of computational debris models available. The objective of this chapter is to 'set the scene' by outlining the debris problem and the consequent need for fast computational modelling of orbital debris evolution.

2.2 Background

2.2.1 Natural Debris

Small fragments of cometary ice and rock traverse the near-Earth space environment at an average speed of 20 km/s. An average 40,000 metric tons of micrometeoroids and small dust particles enter the Earth's atmosphere each year [3]. In LEO, the man-made debris environment has now increased to such an extent that it now supersedes the natural meteoroid flux in certain size ranges. In geosynchronous orbits, however, the natural meteoroid hazard still predominates over the man-made debris hazard, although with the large increases in GEO man-made debris, this is a trend that is likely to be reversed in the medium to long-term future. Natural meteoroids represent the only hazard in interplanetary space, however, where their speeds can reach 70 km/s [3] .

One of the main differences between man-made, or artificial debris, and natural meteoroids is that artificial debris is permanently in Earth orbit, whereas micro-meteoroids are in orbit about the Sun and so have only a transient presence in near-Earth space. Cometary fragments of ice and rock are scattered around the orbit once occupied by the comet. As the Earth passes through such an orbit, it encounters a greater flux of the natural debris that lies in the comet remnant's wake. This accounts for the annual meteor showers that are sometimes visible in the night sky, the intensity of which is far greater when the comet has only passed by recently. This period of high particle concentration in near-Earth space causes significant problems for spacecraft as the natural debris flux increases.

2.2.2 Man-Made Debris: Sources and Sinks

Space debris sources are numerous and varied and include

- **intact, inactive payloads**, allowed to drift uncontrolled in their orbits,

- **fragments emanating from spacecraft and rocket body explosions**. Explosions can result in the creation of typically tens of thousands of fragments. The reasons for the explosions are varied and include
  - intentional detonation, for various political reasons,
  - ASAT (Anti-Satellite) weapons testing,
  - catastrophic failure of batteries, and
  - fuel tank explosion due to the inadvertent mixing of hypergolic fuels.
- **fragments emanating from hypervelocity collisions** between spacecraft or spent upper stages and debris fragments. This high energy fragmentation results in typically millions of smaller fragments being created, which tend to have much higher speeds than those generated in explosion-induced fragmentations.
- **operational debris,** or mission related debris, which are released as part of a spacecraft's deployment, activation or operation. These include fragments of pyrotechnic straps and bolts, spring release mechanisms, and spacecraft spin-up devices, which may be ejected during the staging and spacecraft separation process. Shortly after entering orbit, the spacecraft may release cords securing solar panels, as well as other appendages, or eject protective coverings from payload and attitude control sensors. On manned missions requiring EVA's (Extra-Vehicular Activities), there is yet further potential for the generation of operational debris, e.g. astronaut tools 'dropped' accidentally during space walks, etc. The amount of operational debris released can be quite large; a detailed study of a Russian launch mission revealed that 76 separate objects were released into space either by the spacecraft or the launch vehicle [3].
- **rocket bodies** released into operational and transfer orbits during spacecraft launch. These are a form of operational debris but are large enough in number and mass to require their own category. They include launch vehicle third stages (which may contain residual propellant), payload adaptors, and payload fairings. They are of particular concern for GEO-type missions, as the launch vehicles require a larger number of stages and the jettisoned parts may be released into transfer orbits that intersect operational orbits, e.g. GTO (Geostationary Transfer Orbit).

- **degradation debris**, which are very small particles caused as a result of spacecraft exposure to the space environment. Mechanisms causing this include paint flaking, MLI (Multi-Layer Insulation) embrittlement, atomic oxygen erosion, the effect of UV exposure, thermal cycling, etc.,
- **solid rocket motor ejecta**, which are very small particles of aluminium oxide (Al_2O_3) dust, typically less that 0.1 mm in diameter, but which collectively account for thousands of kilograms of debris. These particles are ejected at speeds of up to 4 km/s and can in turn help degrade spacecraft surfaces, including sensors and solar panels [3].
- **solid rocket motor 'slag'**, which is ejected from the motor, principally at the end of the motor firing. These can be several centimetres in size.
- **sodium potassium (NaK) coolant droplets**, found to be emanating from spent nuclear reactor systems in orbit, such as the Russian Ocean Reconnaissance Satellites (RORSATs).

There is, however, effectively only one space debris sink – that of atmospheric drag, although other perturbations may assist drag in its task. Atmospheric drag reduces the apogee altitude of the debris fragment's orbit and eventually causes the fragment to de-orbit and burn up in the atmosphere. Atmospheric drag only has an effect on LEO debris and debris near the perigee points of HEO (Highly Elliptical Orbits) such as GTO. Its effect decreases quickly with increasing altitude – any debris fragments above ~800 km are unlikely to be affected substantially by drag [4]. The effect of drag is amplified during periods of high solar activity, when the Sun heats the atmosphere and causes it to expand. The atmosphere thus becomes denser at higher altitudes and its effect on debris is more pronounced. The effects of lunar and solar gravitational perturbations may also play a prominent role in the removal of debris objects by lowering the perigees of the orbits, thus increasing the effects of drag and accelerating the objects' orbital decay. For example, a GTO rocket body could re-enter the Earth's atmosphere within a few months or remain in orbit for more than a century, depending on the position of the Sun and Moon at the time of its injection into GTO [3]. There is no natural sink whatsoever for debris in GEO orbits.

2.2.3 The Current Situation

The largest concentration of debris at present is in LEO with another concentration in the geostationary ring. This scenario is illustrated in Figure 2.1, which shows a snapshot of the debris environment (objects > 10cm) viewed from above the North pole.

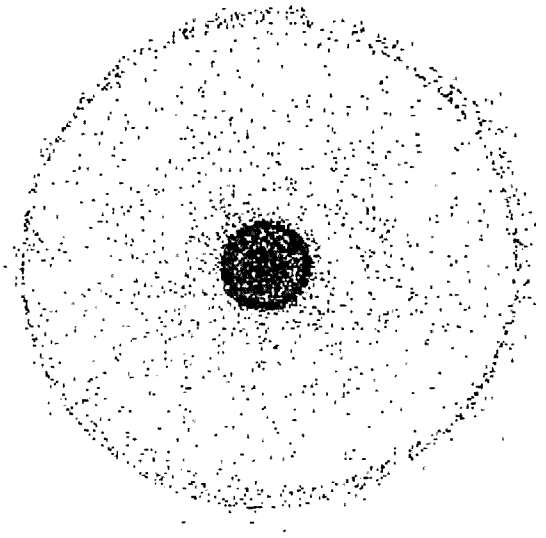

Figure 2.1 A snapshot of the debris environment viewed from above the North pole showing the high concentrations in LEO and in the GEO ring [3]

By far the majority of fragments in LEO are in the extremely small size range (< 1 mm). These are too small to be detected by ground based sensors and pose relatively little threat, as they rarely have the energy to cause any significant damage. They do however contribute to surface degradation effects on spacecraft. The larger fragments (greater than 10 cm in diameter), although fewer in number, contain far more potentially destructive energy due to their large mass. They can be easily tracked from the ground due to their large cross-sections however, and so collision avoidance manoeuvres can be executed if necessary, providing the spacecraft is capable of executing such a manoeuvre (as is the case for the space shuttle, for instance) and has the propellant to do so. The biggest problem lies with the intermediate debris fragments (between 1 mm and 10 cm in size), of which there are many thousands. Some of these fragments have the momentum and energy to cause catastrophic damage to spacecraft, yet are too small to be effectively tracked.

Although the vast majority of fragments (of the order of 10^{12}) are sub-millimetre in size, they only represent a fraction of a percent of the total orbital debris mass, which in 1995 was estimated to be over two thousand metric tons [5, 6]. It is estimated that less than 5% of the population of debris fragments account for over 99.9% of the mass of all the debris in near-Earth orbit, where these fragments are typically greater than 10 cm in size [3] .

Figure 2.2 shows the approximate USSPACECOM (United States Space Command, formerly NORAD, North American Aerospace Defence Command) catalogue composition as of 5 September 2001. The USSPACECOM catalogue contains all objects large enough to be tracked by the SSN (Space Surveillance Network, a network of radar tracking stations distributed around the globe) in Earth orbit, typically comprising objects greater than about 10 cm in LEO and greater than 1 m in GEO. As of October 2001, a total of 4643 launches had been recorded, producing 27,061 catalogued objects, of which approximately a third remained in orbit, the remaining two-thirds having been removed by natural decay or by de-orbiting in a controlled manner. The history of the on-orbit catalogued population is illustrated in Figure 2.3. It is estimated that only approximately 6% of the catalogue population is comprised of operational spacecraft [7].

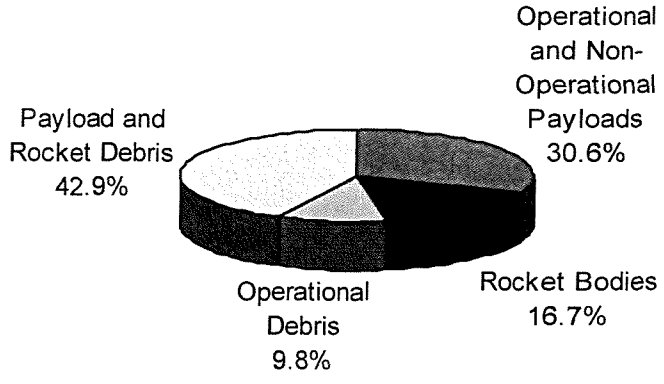

Figure 2.2: Approximate USSPACECOM catalogue composition on 5 September 2001 [7]

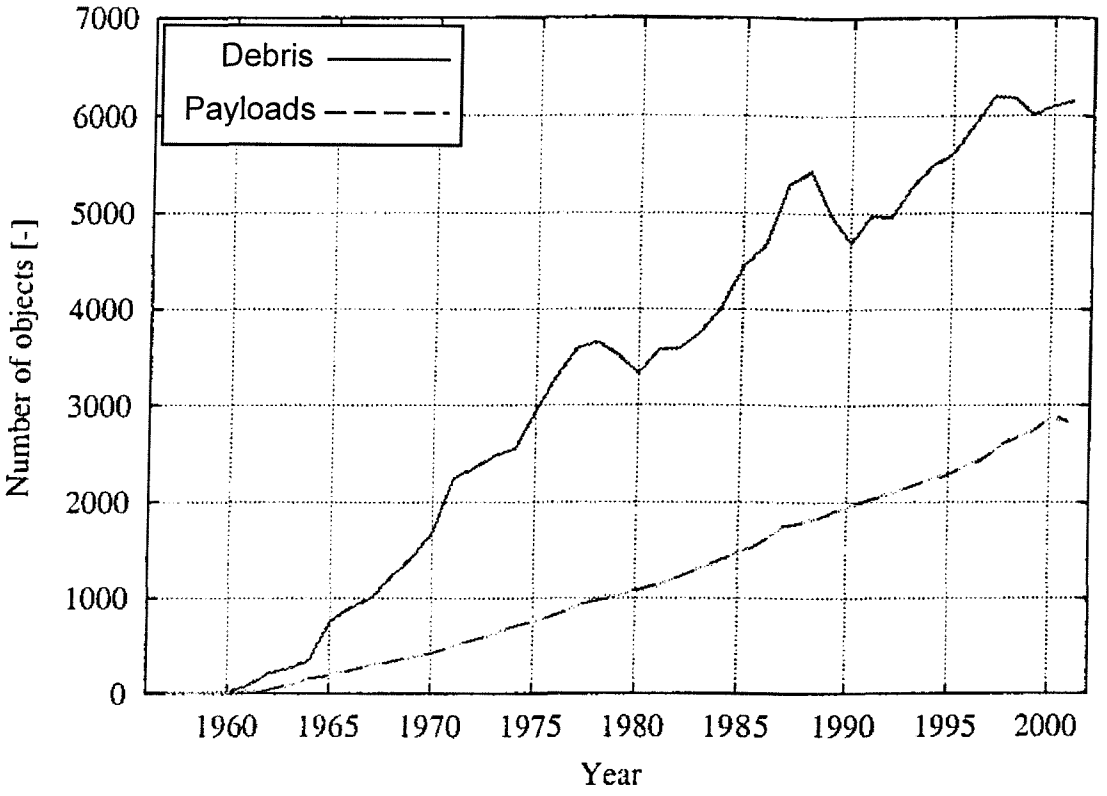

Figure 2.3 History of the on-orbit catalogue population as a function of time [7]

Figure 2.3 shows an almost linear increase of approximately 100 payload objects every year, which has caused an average increase of approximately 200 catalogued debris objects per year. Fluctuations in the debris curve are due to satellite break-ups and varying solar activity causing some large debris objects in LEO to de-orbit due to increased drag in the upper atmosphere.

Fragmentation events are a major cause of the debris growth depicted in Figure 2.3. The major causes of known breakups between 1961 and May 2001 are summarised in Table 2.2. In total, 170 breakups were recorded, a large portion of which were due to deliberate explosions and propulsion related events. However, the cause for approximately one third of the breakup events remains unknown.

Cause	Events
Unknown	56
Aerodynamic	9
Deliberate Explosion	48
Propulsion Related	49
Electrical	7
Collision	1
Total	**170**

Table 2.1 Causes of historical breakups as of 30 May 2001 (note that one event flagged as 'deliberate' was related to a collision) [7]

Propulsion related breakups are the most frequent. These tend to happen during the LEOP (Launch and Early Operations) phase of the mission, as depicted in Figure 2.4.

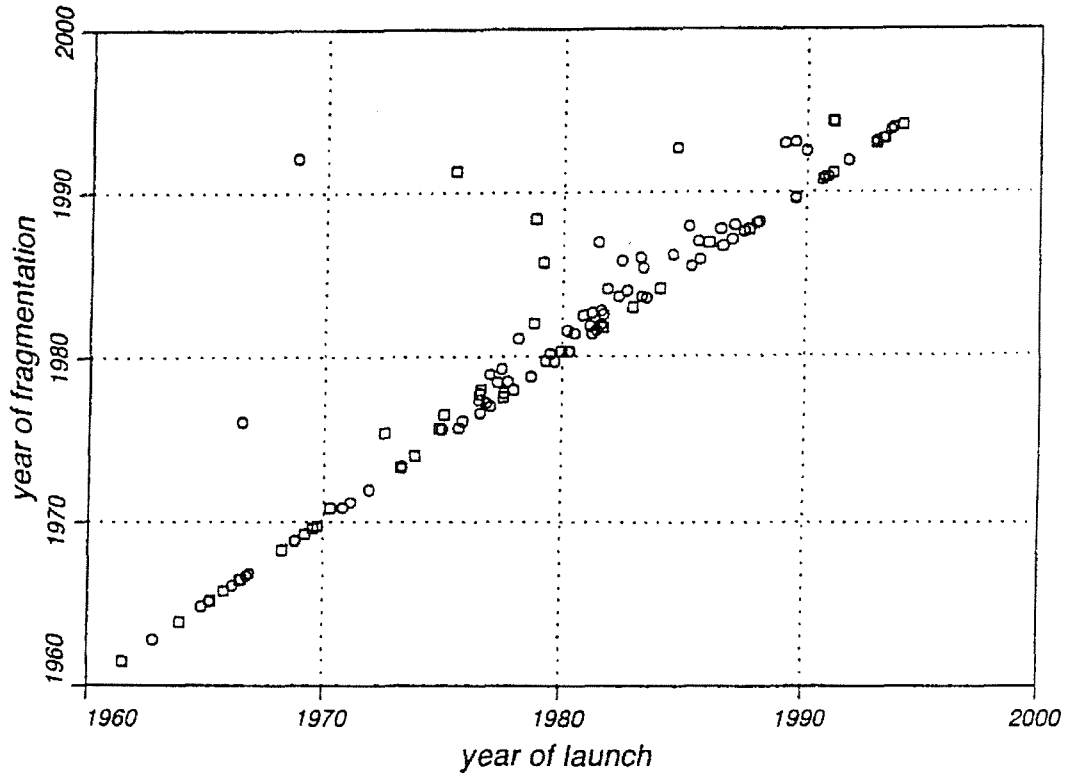

Figure 2.4 The date of fragmentation versus the launch date for objects launched from 1961 to 31 December 1997 [8]

Figure 2.4 clearly shows that the majority of on-orbit fragmentations occur close to their launch date (usually in LEOP). On average 3.7% of all launches resulted in an on-orbit

breakup [7]. Generally, the rate of fragmentations remained fairly constant during the 1990's at around 5 per year. It is this type of historical data that is used, in part, to predict the rate of explosions in future population projections.

The objects stored in the USSPACECOM catalogue can be broken down by object type and country of origin, as shown in Table 2.2. The table clearly shows that the USA and the CIS* are by far the major contributors to the orbital debris problem in near-Earth space. Interestingly, whilst the CIS have launched more payloads into orbit, the USA have produced the most debris objects large enough to be catalogued.

Country / Organisation	Payloads	Rocket Bodies	Debris	**Total**
China	32	20	285	**337**
CIS	1336	820	1687	**3843**
ESA	32	100	185	**317**
India	22	6	226	**254**
Japan	71	30	16	**117**
USA	966	570	2226	**3762**
Total	**2459**	**1546**	**4625**	**8630**

Table 2.2 Orbiting space objects by origin and type (stored in the USSPACECOM catalogue mid-2002) [9]

As of mid-2002, nearly 9000 fragments had been catalogued by USSPACECOM, of which 762 permanently resided in the GEO region – 585 of these were intact spacecraft [10]. However, the actual number of fragments is estimated to be significantly higher.

Table 2.3 compares the number of fragments in Earth-orbit categorised by orbit type and size (as predicted by the ESA MASTER model 1999, using a lower size threshold of 0.1 mm). The orbit types are LEO (defined by objects passing through altitudes lower than 2,000 km), MEO (Medium Earth Orbit, defined by objects passing through altitudes higher than 2,000 km and lower than 34,786 km, i.e. 1,000 km below the geosynchronous region), and GEO (defined by objects passing through altitudes between 34,786 km and

* CIS (the Commonwealth of Independent States) is an alliance of 12 of the 15 former Republics of the Soviet Union (Armenia, Azerbaijan, Belarus, Georgia, Kazakhstan, Kyrgyzstan, Moldava, Russia, Tajikistan, Turkmenistan, Ukraine, and Uzbekistan)

36,786 km, i.e. ±1,000 km around the geosynchronous orbit region, and ±15° of the equator, which equates to the latitude band swept out by a non-maintained GEO object within a 54 year cycle due to luni-solar and J_2 (Earth oblateness) perturbations [11]).

Table 2.3 displays the *mean* numbers in each orbit category, i.e. the numbers are weighted by the relevant resident times in each orbit class, thus, objects in highly elliptical orbits contribute only with a certain fraction.

Debris Size	Objects in LEO	Objects in MEO	Objects in GEO
> 0.1 mm	1.03×10^{10}	2.5×10^{11}	2.5×10^{10}
> 1 mm	3.8×10^{7}	2.1×10^{8}	2.1×10^{7}
> 1 cm	121,289	173,244	20,703
> 10 cm	13,207	2,191	564

Table 2.3 Debris population breakdown with size in each orbit class according to the ESA MASTER model 1999 [7]

It should be noted that, although the numbers of fragments are highest in the MEO regime, this regime occupies a far greater volume of space than the LEO and GEO regions. Thus, even though the fragment numbers in MEO are higher, the spatial density of fragments is lower.

The graphs in Figures 2.5 – 2.10 compare the numbers of objects in each size category as a function of semi-major axis, eccentricity and inclination for objects in the LEO and GEO regimes, as modelled by the MASTER 1996 model. The *no. of objects per class* axis is measured on a log scale, ranging from 10^0 to 10^{10} on each graph depicting the debris population in the LEO regime (Figures 2.5, 2.7 and 2.9), ranging from 10^{-1} to 10^8 on the debris population as a function of semi-major axis in GEO (Figure 2.6) and ranging from 10^0 to 10^8 on the graphs depicting the debris population as a function of eccentricity and inclination in the GEO regime (Figures 2.8 and 2.10).

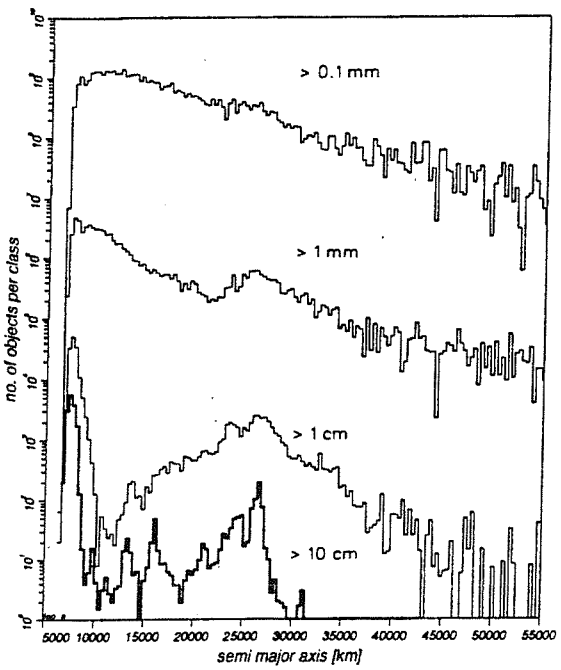

Figure 2.5 The number of debris objects in the LEO environment as a function of semi-major axis according to the ESA MASTER model 1996 [8]

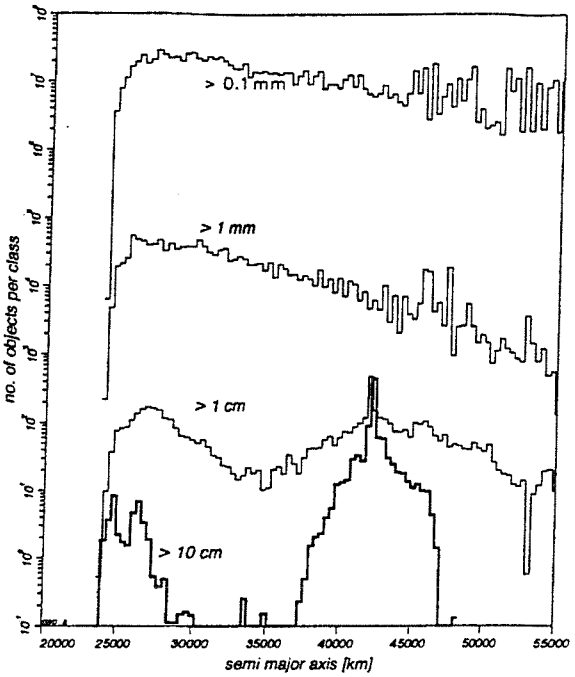

Figure 2.6 The number of debris objects in the GEO environment as a function of semi-major axis according to the ESA MASTER model 1996 [8]

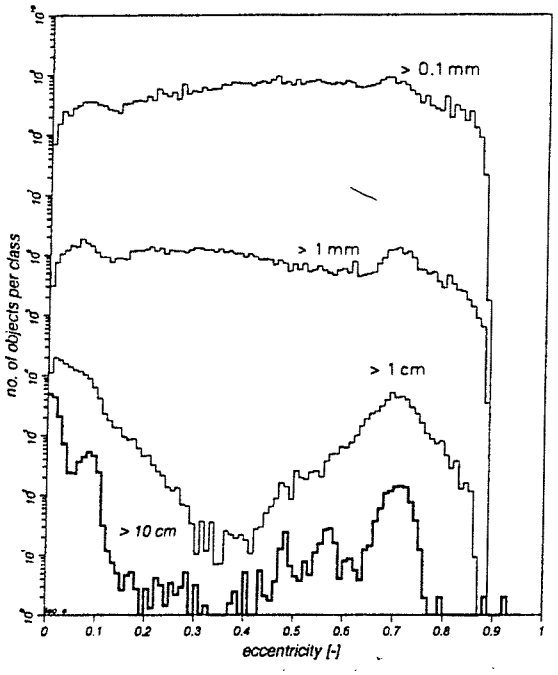

Figure 2.7 The number of debris objects in the LEO environment as a function of eccentricity according to the ESA MASTER model 1996 [8]

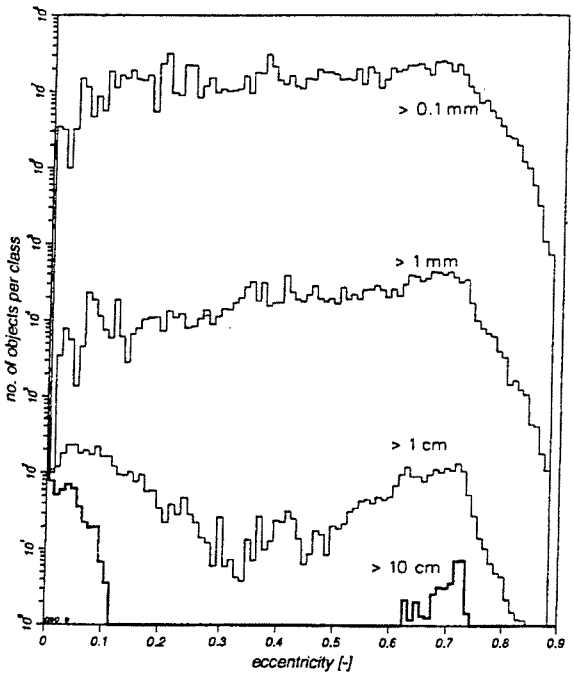

Figure 2.8 The number of debris objects in the GEO environment as a function of eccentricity according to the ESA MASTER model 1996 [8]

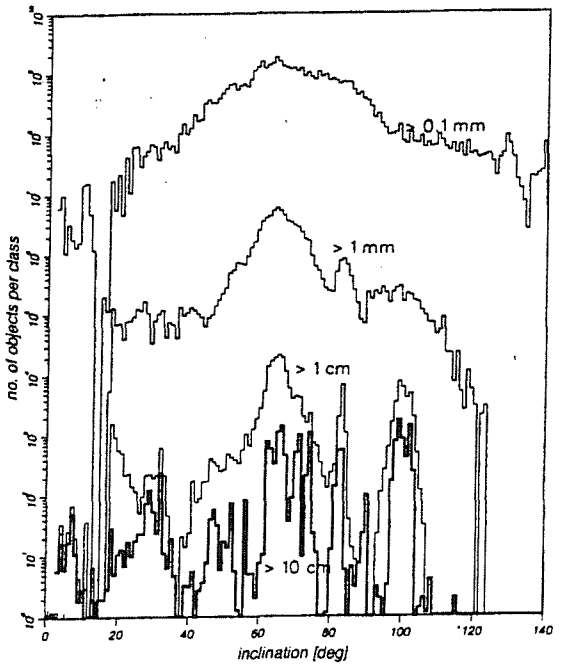

Figure 2.9 The number of debris objects in the LEO environment as a function of inclination according to the ESA MASTER model 1996 [8]

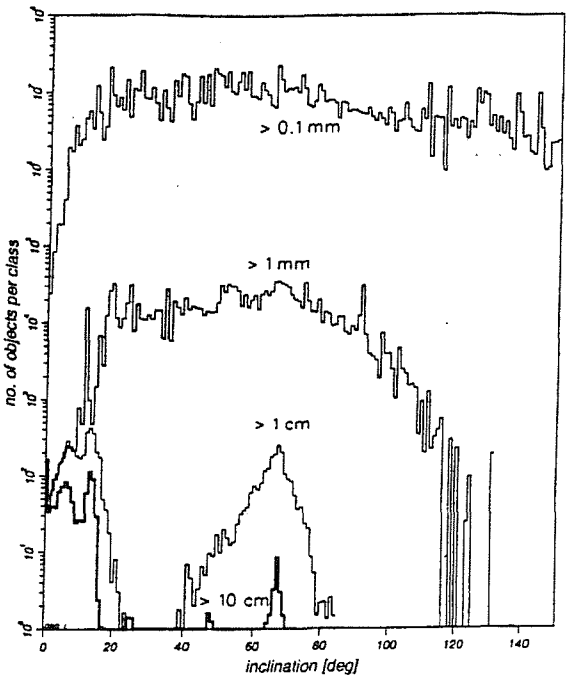

Figure 2.10 The number of debris objects in the GEO environment as a function of inclination according to the ESA MASTER model 1996 [8]

In Figure 2.5 the LEO environment includes orbits with semi-major axes of up to 55,000 km because it includes HEO (Highly Elliptical Orbits), with large semi-major axes and low perigee altitudes that traverse the LEO regime. Similarly, Figure 2.6 includes orbits with semi-major axes down to 20,000 km because this also includes HEO orbits that traverse the GEO regime.

The peaks in the LEO population distribution around a = 7,300 km and $e < 0.1$ (Figures 2.5 and 2.7) correspond mainly to near-circular orbits in the densely populated altitude region around 1,000 km. The objects in GTO-type 10.5-hour orbits creates a second large peak around a = 24,400 km and around e = 0.73. The presence of objects in highly eccentric Molniya-type 12-hour orbits creates a third maximum around a = 27,000 km and increases the peak in eccentricity around e = 0.73. The peaks in inclination (Figure 2.9) correspond to the latitudes of the major launch sites (KSC (Kennedy Space Centre) at i = 28.5°, Baikonur at i = 45.6°, Plesetsk at i = 62.8°), and with certain mission objectives, e.g. polar orbits at i = 90° and sun-synchronous orbits around i = 100°.

The peaks in the GEO population distribution around a = 25,000 km and a = 27,000 km (Figures 2.6 and 2.8) relate to 10.5-hour GTO transfer trajectories and Molniya-type 12-hour orbits. These also give rise to a peak in eccentricity at around e = 0.73. The largest peaks are caused by the near-circular 24-hour GEO and near-GEO objects, which cause peaks at around a = 42,000 km, $e < 0.1$ and $i < 15°$ (as these objects are kept within a 15° inclination deadband by station-keeping manoeuvres or due to a 54 year cyclic perturbation effect – see Figure 2.10). The dominance of near circular orbits is evident for catalogued objects (> 10 cm), as these comprise operational spacecraft and large pieces of debris that were released with relatively small delta-v's, and have thus not drifted far from the parent object. A sub-maximum is noted at i = 63° for the 12-hour orbits of the Molniya type.

It should be noted that the distributions become more uniformly spread in semi-major axis, eccentricity and inclination with decreasing object sizes. This is particularly true of the GEO distributions.

Breakups generate thousands of fragments that contribute to the current debris density, and there are indications [12] that the orbital region between 900 and 1000 km altitude may have already become unstable. In other words, the debris density may already have exceeded a critical density level where random collisions will start to occur and produce even more fragments. This process is called *collisional cascading*, and essentially describes the situation where the rate at which fragments are being produced by random collisions is increasing and is greater than the rate at which they are being removed naturally by aerodynamic drag. In this situation generally the debris population can grow exponentially as collision fragments produce more and more collisions.

2.2.4 The Evolution of a Debris Cloud

When a spacecraft fragmentation event occurs, the spacecraft initially breaks up into a dense debris cloud. As a result of their varying velocities, the fragments will spread out

into a toroidal cloud that will continue to expand until it reaches the limits of the maximum inclinations and altitudes of the debris fragments' orbits, and from there the cloud will continue to expand until it forms a wide band around the Earth, as illustrated in Figure 2.11.

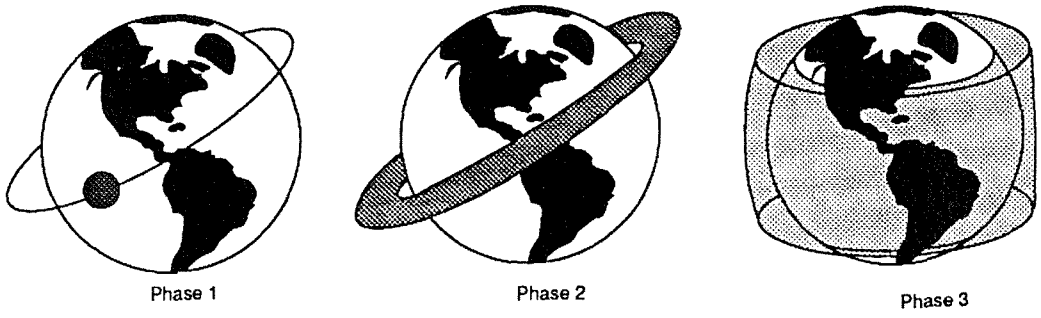

Figure 2.11: Diagram showing the debris cloud evolution from phase 1 to phase 3 [3, 13, 14]

The nature of the debris cloud can be split into three distinct phases. Phases 1, 2 and 3 represent the change in the debris cloud over time, and the associated debris impact hazards for a spacecraft exposed to the cloud can be thought of as short-term, intermediate and long-term, respectively [15].

Phase 1 cloud. This represents a short-term hazard, which exists immediately after the break-up event when the debris cloud is at its most localised. A spacecraft passing through this localised debris cloud has the highest probability of a collision because of the high spatial density of the cloud. This high risk of collision lasts only a short while, however, as the spacecraft quickly passes through the relatively small cloud.

Phase 2 cloud. This represents an intermediate hazard, which exists when the cloud has spread into a torus around the Earth. This will happen within only a few orbits due to the varying velocities of the different fragments. The cloud now encompasses the entire Earth and so occupies a much greater volume of space. Consequently the probability of a spacecraft entering the cloud is now much greater, but due to the fact that the spatial density within the cloud is now greatly reduced, the collision probability for a spacecraft is much smaller than for the short-term hazard. During this phase, a pinch point will exist

at the location of the fragmentation event, whilst a pinch line will exist 180° away from the pinch point in the orbital plane of the original target object. These are regions of high spatial density, especially the pinch point, which, during this phase of the cloud evolution, will be occupied by all the fragments of the debris cloud, albeit not all at the same time. The pinch point and pinch line occupy a small amount of space however. Thus, whilst the risks to a target object entering these regions of space are higher, the chances of a target object entering these regions in the first place are remote [16].

Phase 3 cloud. This represents a long-term hazard, which exists when the debris cloud has completely dispersed around the Earth and has become part of the background debris environment in Earth orbit. The probability of a spacecraft collision within this cloud is consequently very low. It will typically take months to years for the debris cloud to evolve from the second to the third phase. Orbital perturbations, such as the aspherical components in the shape of the Earth causing geopotential asymmetries in the gravitational field, atmospheric drag, solar radiation pressure (SRP) and luni-solar gravitational attractions, provide the mechanism for the transfer between these two phases.

2.2.5 The Differences in LEO and GEO Debris Characteristics

The nature of low Earth orbiting debris differs greatly from that of high Earth orbiting debris in terms of the number of fragments, typical speeds, fragment mass and size, as well as the way in which the debris orbits evolve due to orbital perturbations [17]. The differences in the number and distribution of debris in the LEO and GEO regimes has, to some extent, already been discussed in section 2.2.3. This section will thus concentrate on the other differences in the debris characteristics in these two regions.

Presently, and for the foreseeable future, the main driving force behind the creation of debris in the GEO region is explosions. However, it is likely that the collision risk will begin to out way the explosion risk in the long-term future. This will largely be due to the

implementation of explosion mitigating policies (which will be discussed later in this chapter) and the increasing number of objects in the GEO region, and particularly in GEO graveyard orbits, with additional interaction of objects between orbits.

The risk of a collision in GEO is currently calculated at approximately 1 in every 10,000 years [18], although other sources [11] have put the estimated risk closer to 1 in every 250,000 years (for a 1 cm fragment impacting a target object with a cross-sectional area of 10 m^2). In reality, the collision risk in GEO is highly uncertain. Additional space debris measurements in GEO are needed before more accurate risk assessments can be performed. In comparison, the risk of collision in LEO can be better ascertained due to the accumulation of more accurate on-orbit observational data. The risks in LEO are generally much greater than in GEO, although they are highly variable, depending on orbital altitude and fragment size range. The estimated mean times between impacts in LEO by orbit type and fragment size are presented in Table 2.4.

Height of circular orbit	Objects 0.1 – 1 cm	Objects 1 – 10 cm	Objects >10 cm
500 km	10 – 100 years	3,500 – 7,000 years	150,000 years
1,000 km	3 – 30 years	700 – 1,400 years	20,000 years
1,500 km	7 – 70 years	1,000 – 2,000 years	30,000 years

Table 2.4 Mean time between impacts on a satellite with a cross-sectional area of 10 square metres [18]

Of the 170 fragmentation events recorded in Earth orbit (Table 2.1), only two have been recorded in GEO, both of which were explosions: a catastrophic battery malfunction on the Ekran-2 spacecraft on 23 June 1978 and the fragmentation of a Titan Transtage on 21 February 1992 [11]. However, there remains a great deal of debris in GEO that is unaccounted for in the USSPACECOM catalogue (as observed by the ESA Space Debris Telescope in its 2001 campaign [19]). The ESA MASTER model predicts that there have been a total of 13 fragmentations in GEO, which is more consistent with the number of observed debris fragments. In truth, nobody is really sure of the number of fragmentation events that have occurred in the GEO region. Nor is anyone sure of the number or total mass of debris fragments that reside there. Even the total number of launch or mission

related objects in GEO is in dispute, as there also exist an unknown number of military satellites in the GEO vicinity, the orbital parameters of which are not available.

The effect of orbital perturbations differ considerably for objects in LEO and GEO. In LEO the predominant perturbations are due to the Earth oblateness and atmospheric drag, the latter of which reduces the altitude of a fragment's orbit and eventually causes it to de-orbit and burn up in the upper atmosphere. As explained, this represents the only sink for orbital debris and is the reason why the lifetimes for LEO debris is short in comparison with GEO debris – lifetimes for LEO debris are typically months to hundreds of years. Drag is clearly very altitude-dependent and so there is a large variation in the lifetimes of LEO debris, the shorter lifetimes corresponding to the low altitude debris and the longer lifetimes corresponding to the high altitude debris. In the absence of drag, the lifetime for GEO debris is potentially of the order of millions of years. GEO is an orbit of unique importance. This, combined with the fact that there is no effective debris sink there, makes it imperative that the international community takes care not to pollute this important resource. This also makes the accurate modelling of GEO debris important.

The effects of specific Earth-gravity perturbations are also different for LEO compared to GEO. In GEO the majority of spacecraft, and thus debris, are equatorial. Thus the effects of latitude dependent oblate Earth components, e.g. J_2, are not so important as these will have little or no effect on an equatorial orbit. Longitude dependent aspheric Earth components become relatively more important however – the effect of the J_{22} component has a resonant effect and causes longitude drift in GEO, so making it one of the major perturbative effects. Similarly, luni-solar gravitational attraction becomes relatively more important in high Earth orbits compared to LEO, as do SRP perturbations, albeit only for very small fragments, which tend to have low mass-to-area ratios (see Chapter 4).

LEO debris is relatively evenly distributed in terms of longitude and so many debris models take no account of the anomalies (i.e. true anomaly, mean anomaly or eccentric anomaly) of the debris fragments, and the RAAN (Right Ascension of the Ascending Node) and argument of perigee are often randomly distributed in order to save on

computational time. In GEO, however, the majority of the spacecraft, and thus large debris fragments, are clustered around particular longitudes [4, 20-22]. For example, the spatial density of debris will be particularly high above Europe and the East and West coasts of the United States, as compared with many other regions, since these are associated with highly populated areas. Consequently the angular anomalies of debris fragments need to be taken into account when considering GEO debris. This is only true of spacecraft and large debris fragments (typically > 1 cm), as these will have been ejected with relatively low delta-v's and will thus not have strayed far from the orbit of the parent object. Smaller fragments, typically with higher delta-v's, are likely to be more evenly spread in longitude.

The speed of orbiting objects varies with altitude. Consequently, the typical relative speeds for LEO objects would be around 8 – 15 km/sec [3], whereas objects in GEO have much lower encounter speeds of up to around 3 km/sec [3]. Indeed, a collision in GEO can have an impact speed so low that it may be best described as a rendezvous, rather than a collision. This difference has a significant effect on the collision-induced breakup characteristics of objects in LEO as compared to GEO. The higher impact speeds in LEO imply that if a collision occurs it will be a very high-energy collision, causing damage and the resulting debris fragments to be expelled at very high velocities. The lower speeds in GEO imply that generally the impact damage is less, and that if a breakup did occur the amount of energy involved would be small, resulting in fewer fragments travelling at lower speeds.

The significance of these differences between LEO and GEO debris is that it is not sufficient to merely extend any LEO-dedicated model (e.g. a fast propagator) up to GEO altitudes, since the problems faced in GEO are fundamentally different. Thus a dedicated GEO fast propagator must be developed which incorporates all the important aforementioned differences. Novel solutions must be found to overcome the unique problems posed by modelling debris in the GEO regime if a fast propagator capable of modelling the evolution of debris clouds in this region is to be developed. It is this requirement that provides the rationale for the work contained in this thesis.

2.2.6 Measurement Techniques

The differences between the number of catalogued fragments and the estimated number of actual fragments is due to the accuracy and sensitivity of the measuring equipment available. Orbital debris is predominantly tracked using radar but can also be tracked via optical methods. Radar typically has a high enough resolution to track 10 cm diameter fragments in LEO and 1 m diameter fragments in GEO [7, 8, 18, 23]. It is this resolution that predominantly drives the accuracy of the USSPACECOM catalogue. The resolution of optical equipment in tracking debris fragments is highly variable however, and depends on many external factors, such as the reflectivity of the fragment, the position of the Sun relative to the fragment at the time of observation, the clarity of the sky, the fragment orbit and orientation, etc. Radar is used predominantly because of its relatively constant tracking resolution. However, the threshold size that can be detected by radar decreases with altitude, and so optical methods can sometimes provide a more proficient means of detection at higher altitudes, as shown in Figure 2.12.

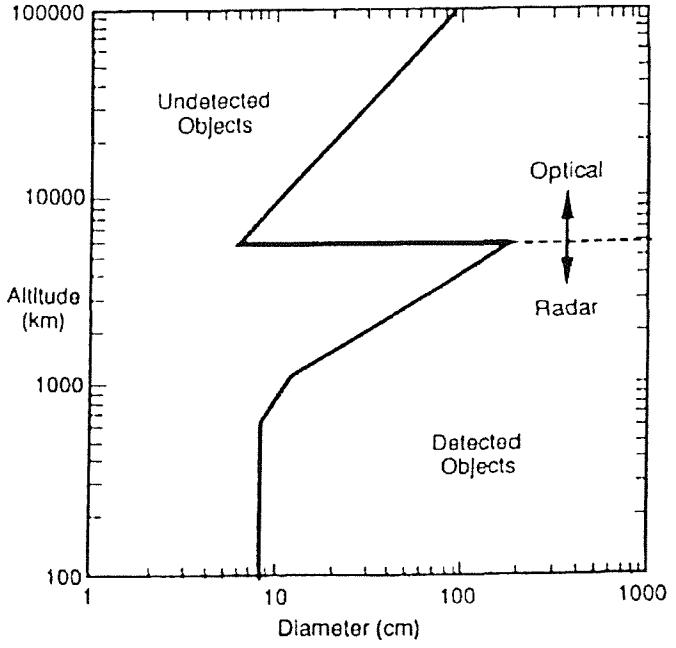

Figure 2.12: Graph illustrating the typical resolution of optical and radar measuring equipment at different altitudes [14, 24]

Figure 2.13 shows the number of fragments plotted against fragment size in LEO and clearly shows that the majority of debris fragments are extremely small and are below the resolution of the tracking equipment. Figure 2.13 also lists a number of sources for the measurement of debris, e.g. LDEF (Long Duration Exposure Facility), Haystack radar, etc. These sources, with the exception of LDEF, are all part of USSPACECOM's Space Surveillance Network (SSN), which is responsible for the tracking and cataloguing of debris.

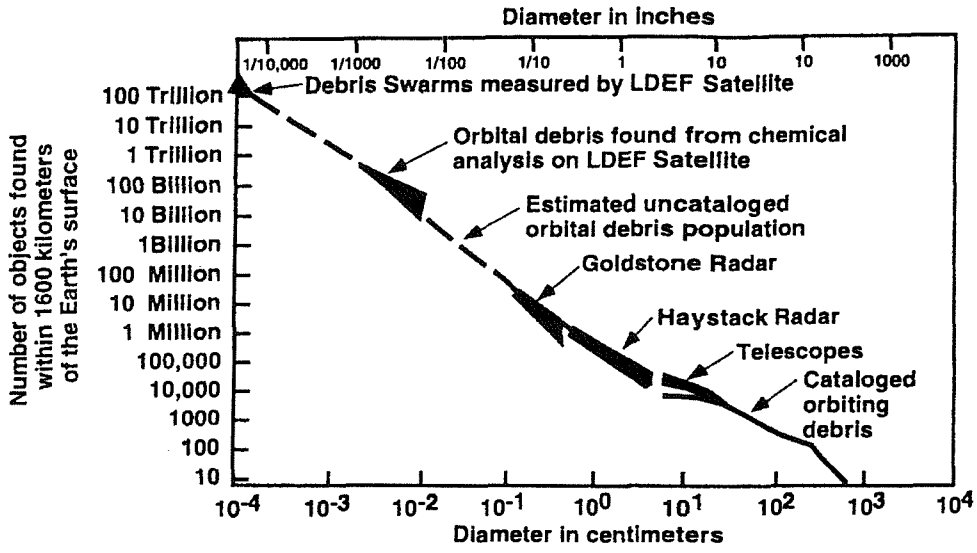

Figure 2.13: A graph comparing the number of debris fragments with their size in LEO [3]

LDEF is a spacecraft that was launched by NASA in 1984 to provide long-term data on the space environment and its effects on space materials, systems and operations. It was cylindrical in shape and carried 57 experiments mounted in 86 trays about its periphery. The experiments were largely trays of different materials, so that the effects of the space environment (and notably that of the debris environment) could be ascertained. LDEF remained in LEO for around 5 years 8 months, during which time it experienced one half of a solar cycle, as it was deployed at a solar minimum and retrieved at a solar maximum. LDEF has thus provided space debris investigators with a valuable source of debris data on the size, flux and speed of debris in its particular orbit. Data on the small debris population has also been acquired by the retrieval of other surfaces from orbit – for example, the EURECA (EUropean REtrievable CArrier) spacecraft, the HST (Hubble

Space Telescope) solar array, space shuttle orbiter surfaces (notably the window on STS-7, which was badly damaged by an impact in June 1983), the Solar Maximum Mission and MIR, to name but a few [18].

2.3 Proposed Solutions to the Debris Problem

2.3.1 Spacecraft Shielding and Collision Avoidance

Increasing amounts of space debris in the LEO and GEO environments influence the design of future space missions. The need to protect spacecraft from debris collisions has prompted a look at necessary design considerations to enhance spacecraft survivability, which can be categorised into passive and active collision protection measures. The current passive collision protection methods tend to utilise stand-off aluminium shielding as in the case of the International Space Station (ISS). The shielding on the ISS is 0.16 cm thick. The space station structural wall is also covered with 30 layers of Mylar thermal insulation. This has been shown to protect against collision of debris particles up to around 0.5 cm in diameter [4] at fragment speeds typically encountered in its orbit (which at 3am on 5th September 2003 was a = 6,766.5 km, e = 0.0006034, i = 51.6°, Ω = 337.7°, ω = 208.4°, M = 151.7° [25]).

An example of an active collision protection method, and perhaps the most effective way to avoid a damaging collision with a debris fragment, would be to avoid the fragment altogether. The requirements for collision avoidance would involve,

1. the detection of debris particles,
2. the determination of the particle's orbit,
3. preparation of the spacecraft for acceleration,
4. manoeuvre execution, and
5. the return of the spacecraft to the original orbit and normal operation.

A great deal of propellant would need to be stored on board the spacecraft in order to prepare for this contingency (approximately 50 kg of fuel per avoidance manoeuvre based on a generic 10 tonne spacecraft [4]). This would obviously increase mission costs significantly. Furthermore, the manoeuvring of the spacecraft into another orbit might move it out of the path of one debris fragment only to move it into the path of another. Removing the spacecraft from the path of the entire debris cloud would take substantially more fuel. Additionally, any acceleration of the spacecraft could require increased structural integrity in order to cope with the increased dynamic loads. This may especially be true for lightweight structures such as solar arrays and antennas.

Since the amount of propellant required to perform an avoidance manoeuvre increases with the inverse square of the detection range [4], it is clearly highly desirable to detect the fragment and determine its orbit as quickly as possible. The most effective method for doing this, if not the most efficient, would be to use on-board radar equipment. However, this is likely to be heavy as well as having a high power demand. The primary choice is likely to be a passive method using optical or infrared sensors. However these methods may not be as reliable and their effectiveness may be compromised by other factors, such as the reflectivity of the debris fragment. An ideal solution may be to use a separate space-based radar for tracking the debris fragments, and then relay the fragment positions to the 'target' spacecraft. This would provide an early warning system that the spacecraft could use whilst minimising the impact on its design.

The shielding and collision avoidance methods mentioned above remain far from ideal, however. Both require substantially greater mass, and sometimes power, and thus increase the overall cost, as well as causing significant impact on the spacecraft operations. The best option, by far, would be to curb the amount of debris created in the first place.

2.3.2 Debris Mitigation Policies

NASA, the U.S. DoD (Department of Defence), and space agencies in Russia, Japan and Europe are participating jointly in minimising debris creation resulting from space operations. Debris control methods fall into three main categories [12]:-

- those requiring minimal impact on operations;
- those requiring changes in hardware or operations; and
- those requiring technology development.

Options in the first category, which are recommended for immediate implementation, include venting residual fuel from fuel tanks of non-operational spacecraft and upper stages in order to make these inert. This will limit the number of explosions caused by the inadvertent ignition of residual propellants. Other passivation measures include the discharging of batteries, the release of pressurised fluids and the unloading (despinning) of momentum wheels and similar attitude control devices. These types of mitigation procedures are becoming commonplace amongst space fairing nations, as they have little impact on the principal operations of the space vehicle.

Policies restricting the testing of anti-satellite weapons have already been implemented by most space-faring nations in order to limit the debris thus caused. The intentional detonation of satellites has also been curbed since the threat posed by the debris problem first came to light.

Operational debris can be restricted to some extent by tethering items to the spacecraft, e.g. lens caps, etc., and thus not allowing them to drift freely into space. Other forms of operational debris however, such as interface rings and payload fairings, etc., which are jettisoned during spacecraft separation, are harder to restrict as they are, at present at least, an unavoidable bi-product of mission operations.

Options in the first category which are GEO-specific include the injection of GEO spacecraft and spent parts into super-synchronous graveyard orbits (also known as

disposal or storage orbits) at the end of their useful lives. The de-orbiting of spacecraft from GEO altitudes is not a feasible solution due to the large amount of fuel that would be required – hence the need for graveyard orbits. This removes the spacecraft from the path of operational spacecraft in GEO, but only serves as a short term measure. Eventually the graveyard orbits themselves will become crowded, increasing the risk of collisions between the non-operational spacecraft in this region and further contributing to the debris problem.

There is some debate currently about the altitude required for graveyard orbits to be truly effective. There is a trade-off to be made here between making the graveyard orbit high enough such that any breakup-induced debris clouds in the graveyard orbit will not affect operational GEO spacecraft, and keeping the fuel, and hence cost, required to place a spacecraft into its graveyard orbit to a minimum. Current, internationally agreed mitigation policies recommend transfer to a super-synchronous, graveyard orbit about 300 km above the GEO ring at the end-of-life of the spacecraft to prevent collisions between spent and operational spacecraft in GEO [7, 26]. At present, only approximately one third of retiring spacecraft are actually brought to a sufficiently high orbit. A further 30% of spacecraft perform re-orbiting manoeuvres but are placed into orbits which are either far too close to GEO or which cross the path of GEO spacecraft [11]. This may be due to insufficient fuel gauging or due to a last-minute requirement for several more months of spacecraft operation. The number of objects launched into the GEO region has grown at a nearly constant rate of about 30 objects per year since the early eighties. The increasing number of spacecraft in GEO combined with an increasing design lifetime for GEO spacecraft (which is now approaching 12 – 15 years) means that debris in the GEO regime is expected to continue to grow linearly in the future [11, 27]. Interestingly, due to the continued re-orbiting of spacecraft into the GEO disposal orbit at the end-of-life, the number of objects greater than 10 cm in the GEO disposal orbit is predicted to far exceed that which resides in the GEO ring within the next hundred years. However, breakups (due largely to explosions) and orbital perturbations mean that contamination from GEO debris fragments will begin to affect objects in the GEO disposal regime (and vice versa) within this period [27, 28].

Options in the second category include removing dead spacecraft and upper stages from orbit using de-orbiting manoeuvres to ensure atmospheric re-entry over the oceans. This is clearly only a feasible option for LEO spacecraft. This can either be done using the space shuttle (if the spacecraft is required to be de-orbited in its intact state for whatever reason, e.g. LDEF) or by keeping enough residual fuel on-board to perform a retrograde burn to de-orbit the spacecraft at end-of-life. This latter option is far less expensive and is safer than using the space shuttle and so it is the preferred solution. De-orbiting manoeuvres in LEO generally consist of a retrograde burn, designed to lower the perigee of the spacecraft's orbit to such an extent as to enable drag effects to de-orbit the spacecraft within a certain time-period. Several studies have been conducted, examining the trade-offs between de-orbit times and the propellant requirement for a de-orbiting burn. These studies have concluded that the optimum de-orbit lifetime is approximately 25 years [7, 8, 29, 30]. This de-orbiting scenario will maintain a low population level in LEO (in light of future increasing launch traffic rates) without incurring disproportionately large penalties in terms of additional fuel requirements.

Options in the third category require new developments (where technical feasibility and cost effectiveness must be shown). Examples in this category include drag enhancement devices to increase the drag on LEO spacecraft at the end-of-life to promote a rapid decay in the orbit; the use of lasers, either to eliminate orbital debris or to produce additional radiation pressure on the debris fragments, thus producing retrograde delta-v's that will assist drag effects in de-orbiting the fragments; and space tethers, which could be deployed by spacecraft at their end-of-life to help de-orbit the spacecraft.

There are two general categories of tethers: momentum-exchange tethers, which allow momentum and energy to be transferred between objects in space; and electrodynamic tethers, which interact with the Earth's magnetosphere to generate power or propulsion. Momentum-exchange tethers could be used to de-orbit spacecraft by deploying a weight from the spacecraft into a lower orbit (a vertical orientation of the system will occur due to gravity gradient stabilisation). Angular momentum will then be drained from the

spacecraft in the higher orbit to the object in the lower orbit by virtue of the different speeds of the two objects, causing the orbit of the spacecraft to decay [31]. Electrodynamic tethers are deployed such that they extend through the Earth's magnetic field. The spacecraft passes a current through the conductive tether, which interacts with the Earth's magnetic field, inducing a drag force (called the Lorenz force) on the tether. The direction of the Lorenz force depends on the direction of current flow. Thus, by manipulating the current direction and magnitude, an electrodynamic drag force of a specified strength can be used to retard the spacecraft and help decay its orbit [32, 33].

2.4 Debris Modelling

2.4.1 Artificial Debris Modelling

Principally, orbital debris environment models can be divided into two distinct groups: engineering models and evolutionary models [12].

Engineering models comprise largely of empirical expressions that have been derived from the generalisation of a number of measurement data sets. These models can also extrapolate from the available data to make inferences about the regions of the environment for which there is little data. These regions normally comprise the small particle size range, where the fragment sizes fall below the resolution of the measuring and tracking equipment (typically 10 cm in LEO and around 1 m in GEO, as previously described) although the sparse measurement data in this region may be supplemented to an extent by measurements from retrieved surfaces, e.g. LDEF and EURECA. The assumptions used in these models mainly concern the distribution of the population and the spatial densities at these untrackable sizes. It is normally assumed that the catalogued population for sizes above this threshold are complete (as stored in the USSPACECOM catalogue, for instance). Generally, these models allow a quick and simple definition of

the current debris environment and will also allow estimates to be made of the changes to the debris distribution in the future.

One example of this type of model is the NASA Engineering Model [34], first developed in 1985 and updated in 1989. It was the recommended design standard for estimating the flux levels for different sized particles in LEO, which it did by using the measurements from the USSPACECOM catalogue (1976 – 1988), the MIT ETS (Massachusetts Institute of Technology Experimental Test Site) optical telescope (1984) and impact analyses of the Space Shuttle and Solar Maximum Mission retrieved surfaces (1984). Assumptions adopted in the development of the model included that the data in the USSPACECOM catalogue was complete above 10 cm in size and below 1000 km in altitude, and that all the debris fragments occupy circular orbits. At any given fragment size range, the model was capable of estimating the flux on spacecraft in LEO, both directly from the aforementioned data sets and by interpolating between any gaps in the data.

Another, more advanced example of an engineering model is the NASA ORDEM96 model (developed in 1996) [35]. The main difference between ORDEM96 and its predecessor is that the debris environment is split into six different distributions, according to the type of debris source (comprising intact objects, large fragments, small fragments, sodium-potassium coolant droplets, paint flakes and aluminium oxide particles). Another major difference is that the orbits occupied by these fragments are no longer all assumed to be circular – they are divided into circular and elliptical orbits and into six different inclination bands. Each inclination band comprises two families of objects – one in a circular orbit and one in an elliptical orbit (with an assumed fixed apogee of 20,000 km altitude). The fragment types according to debris source each cover particular parts of the size range (from 1 micron to >10 cm). The populations within ORDEM96 were derived from the USSPACECOM catalogue, the Haystack radar, LDEF returned surfaces and data from NASA's EVOLVE model (an evolutionary deterministic model of a type that will be described below).

Evolutionary models utilise a number of support models to predict the generation of debris fragments from a number of different sources and evolve the debris population to some desired epoch. The support models comprise launch traffic models, breakup models, sodium-potassium coolant leakage models, solid rocket particle ejection models, orbital propagation models, and flux determination and collision prediction models. Evolutionary models can, themselves, be split into two distinct categories: the statistical Particle-In-a-Box models, and the complex deterministic models.

Particle-In-a-Box (PIB) models are statistical in approach and thus provide a quick and simple projection of the future debris population. They represent the populations of orbital debris residing in altitude and mass bins. The model computes interactive collision risks between objects in each of the bins and employs Monte Carlo techniques to predict the number of collisions that will occur in each bin. The PIB models gain their speed and simplicity by using pre-determined analytical expressions that have been derived from several runs of the more complicated deterministic models in order to predict changes in the future environment. Thus, essentially, a particular PIB model quickly recreates the trends modelled by whichever deterministic model that was used to calibrate it. For example, pre-determined formulae are used to calculate the changing numbers of fragments in the mass and altitude bins due to explosions, collision-induced breakups, launch-related debris and the decay of objects due to drag. Examples of PIB models include the CHAIN model developed by Eichler [36] and the Russian SDPA (Space Debris Prediction and Analysis) model developed by Nazarenko [37].

Due to their high computational speed, PIB models are ideal for conducting a large number of Monte Carlo runs and analysing the effects of a wide range of mitigation measures on the future orbital debris environment. Since PIB models do not store individual objects (just object numbers per bin) their speed does not tend to decrease as the debris population increases. However, PIB models do not possess the complexity and resolution required to predict the future debris population in detail and assess the collision risks to individual spacecraft or specific orbiting systems.

Deterministic models are the most detailed and complex of all the debris models, and as such they are also the most widely used, as they have the greatest potential for improving our characterisation of the current and future debris environments. The debris environment is represented by each individual fragment (or in some cases by pseudo-fragments that represent a number of individual fragments with similar characteristics). The individual fragments are described completely by their orbital elements and their physical characteristics, comprising their mass, size and mass-to-area ratios (and sometimes their ballistic coefficients). Each fragmentation event is modelled separately, with the resulting fragments being allocated orbital elements and physical characteristics according to complex equations that have been empirically derived from data gathered from ground-based tests and observed on-orbit fragmentations. The debris fragments are propagated over time by complex orbital propagators that calculate the perturbative effect to the orbit of each fragment (or pseudo-fragment). This is done at each time-step by the superposition of the effects of each disturbing force (e.g. drag, individual aspherical components of the geopotential, lunar and solar gravitational attractions) to each orbital element. This yields a snapshot of the debris environment at any required epoch. The evolved population can then be used to determine the flux encountered by target objects that traverse the near-Earth environment with the aim of assessing collision risks and triggering collision-induced fragmentations in the model. Explosion rates are commonly generated for individual groups of objects of a particular type and orbit. This is based on historical data for the target object type (some objects/spacecraft are historically more prone to explode than others), the age of the target object, whether it has on-board residual fuel, and many other factors. A weighted random number generator is then used to determine whether or not an object will explode, where the weighting factor takes into account the aforementioned considerations. Future launch traffic is calculated by a launch traffic model, which extrapolates from historical launch data, based on spacecraft type, country of origin, injection orbit, etc.

Deterministic models offer higher precision, higher resolution and greater flexibility than PIB models, but they do so at the expense of computational speed and computer memory requirements, especially as the simulated population grows with time. Consequently,

these models tend to perform only a limited, and often inadequate, number of Monte Carlo iterations in predicting the future debris environment. This can sometimes yield results which are adversely affected by unlikely events that can have a profound impact on the future debris environment, such as catastrophic collision events. The limited number of Monte Carlo runs means that the effect of these events is sometimes not adequately 'smoothed out' in the resulting averaged population, leading to anomalously high or low peaks and troughs in the future predicted spatial density distribution of fragments. Examples of evolutionary deterministic models include NASA's EVOLVE model [38-42] (developed at the Johnson Space Centre), the Italian SDM model [43-47] (developed by ISTI, the Institute of Information Science and Technologies, formerly CNUCE, the Centro Nazionale Universitario di Calcolo Elettrico), ESA's MASTER model [48-52] (developed by ESOC, the European Space Operations Centre, in conjunction with the University of Braunschweig), the British IDES model [12, 53] (developed by Walker at QinetiQ, formerly the Defence Evaluation and Research Agency), and most recently, the British DAMAGE model [54, 55] (developed by Lewis and Swinerd at the University of Southampton). These models are all very similar in their approach, with the exception that the MASTER model is only used to make predictions of the current debris environment, whereas the others can be used to predict the current and future debris populations. The differences between the breakup models inherent to these four debris environment models will be discussed in detail in Chapter 4.

2.4.2 Meteoroid Modelling

There also exist a large number of models dedicated to predicting the characterisation of the natural debris environment at different times of the year. Some model the background meteoroid environment, whereas others concentrate more on meteor streams. An example of a meteoroid model is the Divine-Staubach model [56, 57], which is used in the ESA MASTER model to take into account the background meteoroid flux. The Divine-Staubach model essentially calculates the background meteoroid flux upon a target at any cell within a Sun-centred control volume based on a static model of the meteoroid

population. This provides a fast method of flux generation but due to its static nature would not be appropriate for use in modelling the dynamic artificial debris environment. The new release of the ESA MASTER model also uses other meteoroid models (Cour-Palais, Cook and Jenniskens) to model meteor streams and their contribution to the flux encountered by a target [58, 59].

Chapter 3

Debris Propagation

3.1 Introduction

The orbits of space debris fragments are greatly influenced by a host of orbital perturbations, as discussed in Chapter 2. It is important that these are modelled correctly, as they can cause large changes in the orbit over prolonged periods of time. Thus the accurate modelling of orbital perturbations is an important part of any debris modelling software. The principal aim of this section of work is to investigate the perturbations that affect orbits in the geostationary regime and to summarise the equations that will be used to propagate debris fragments in and around this regime. These equations will be used to propagate the debris clouds modelled by the FCP – see Chapter 5. The secondary aim of this chapter is to review some of the methods used in various propagators to speed up the lengthy process of debris propagation.

3.2 Orbital Perturbation Theory

Lagrange's planetary equations, which describe the variations of the elements in terms of an arbitrary disturbing function, R, have been derived by Roy [60]. These are robust in the sense that they describe the variations in the elements caused by any disturbance, be it due to any of the aspherical components of the Earth's gravitational field, drag, SRP or

otherwise, depending on the disturbing function used. Lagrange's planetary equations are given by

$$\frac{da}{dt} = \frac{2}{na}\frac{\partial R}{\partial M}, \tag{3.1}$$

$$\frac{de}{dt} = \frac{1}{na^2 e}\left\{\left(1-e^2\right)\frac{\partial R}{\partial M} - \sqrt{1-e^2}\,\frac{\partial R}{\partial \omega}\right\}, \tag{3.2}$$

$$\frac{dM}{dt} = \frac{\left(1-e^2\right)}{na^2 e}\frac{\partial R}{\partial e} - \frac{2}{na}\left(\frac{\partial R}{\partial a}\right), \tag{3.3}$$

$$\frac{d\Omega}{dt} = \frac{1}{na^2\sqrt{1-e^2}\sin i}\frac{\partial R}{\partial i}, \tag{3.4}$$

$$\frac{d\omega}{dt} = \frac{\sqrt{1-e^2}}{na^2 e}\frac{\partial R}{\partial e} - \frac{\cot i}{na^2\sqrt{1-e^2}}\frac{\partial R}{\partial i}, \tag{3.5}$$

and

$$\frac{di}{dt} = \frac{1}{na^2\sqrt{1-e^2}}\left\{\cot i\frac{\partial R}{\partial \omega} - \operatorname{cosec} i\frac{\partial R}{\partial \Omega}\right\}, \tag{3.6}$$

where a is the orbit's semi-major axis, e is the eccentricity, i is the inclination, Ω is the right ascension of the ascending node (RAAN), ω is the argument of perigee, M is the mean anomaly of the orbiting object, R is the disturbing function used and n is the orbital mean motion, which is given by,

$$n = \frac{\sqrt{\mu}}{\sqrt{a^3}} \tag{3.7}$$

This section will summarise the perturbation effects experienced by objects in GEO, the region of interest in this thesis. As such, only the gravitational perturbations of the aspherical components of the geoid and the gravitational attractions of the Moon and Sun will be considered. Drag effects will be ignored, as they are only prominent in LEO, below around 800 km. SRP effects will also be ignored here, as their effect is small compared to the effect of the gravitationally induced perturbations, and SRP effects are not modelled by the FCP, as will be discussed in Chapter 5.

The aspherical components of the Earth's shape, causing asphericity in the Earth's gravitational potential, is illustrated in Figure 3.1, which shows a contour map of the height of the geoid in metres relative to a spheroid of flattening 1/298.257 (calculated as the equatorial diameter (12756.28 km) minus the polar diameter (12713.51 km) divided by the equatorial diameter – thus taking into account the oblateness of the Earth).

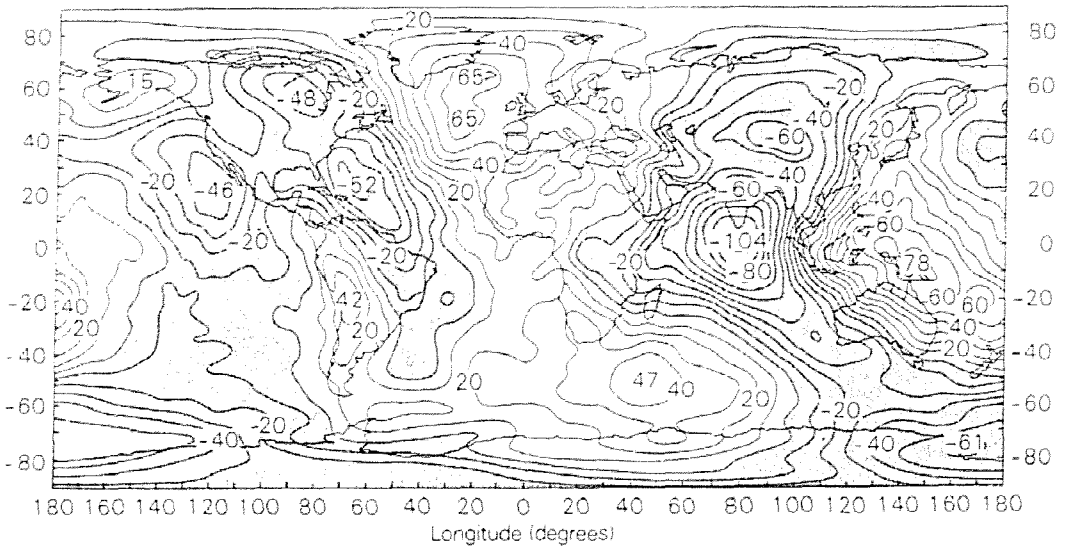

Figure 3.1 Contour map showing the height of the geoid in metres relative to a spheroid of flattening 1/298.257. The depressed areas are shaded and the elevated areas are white. The contour lines are at 10 m intervals. [61]

The Earth can be described as a sphere modified by a whole series of complex shapes, called harmonics. Zonal harmonics are latitude-dependent additions to the spheroid that account for deviations from the sphere along its lines of longitude (i.e. varying with

different values of latitude). The most significant of these is the effect of the second order zonal harmonic, J_2, which accounts for Earth oblateness effects. The second largest and another prominent zonal harmonic is the third order zonal harmonic, J_3, which accounts for the bottom-heavy pear-shaped component of the Earth's asphericity. Sectoral harmonics are longitudinally dependent additions to the spheroid that account for deviations from the sphere along its lines of latitude (i.e. varying with different values of longitude). The most significant of these is the second order sectoral harmonic, J_{22}, which represents an elliptically-shaped equatorial cross-section, and induces long-periodic resonant effects on spacecraft in GEO. Other, more complex harmonics can neither be described as purely latitude dependent or longitudinally dependent – instead they are dependent on both latitude and longitude and are known as tesseral harmonics, after the tessera in Roman pavements, as they describe the shape of the geopotential as a sum of spherical harmonics, each of which resembles a mosaic in longitude and latitude.

The zonal harmonic (latitude-dependent) potential at a point, an arbitrary distance, r, away from the centre of the Earth has been derived and expressed as a set of spherical harmonics of the form,

$$U = \frac{GM_E}{r}\left[1 - \sum_{n=2}^{\infty} J_n \left(\frac{R_E}{r}\right)^n P_n(\sin\phi)\right], \tag{3.8}$$

where G is the Universal Gravitational Constant, M_E is the mass of the Earth and J_n are the zonal harmonic coefficients, where the subscript n is an integer value that can theoretically take values from 2 to ∞ (n=1 being the spherical component). R_E is the Earth's mean equatorial radius, φ is the latitude of the point at which U is calculated and $P_n(\sin\varphi)$ are the Legendre polynomials, the first three of which are given by,

$$P_0(\sin\varphi) = 1, \tag{3.9}$$

$$P_1(\sin\varphi) = \sin\varphi, \tag{3.10}$$

and

$$P_2(\sin\varphi) = \tfrac{1}{2}(3\sin^2\varphi - 1). \tag{3.11}$$

By subtracting the potential due to the spherical component, GM_E/r, from this equation, we are left with the sum due to the non-spherical (zonal) components of the geopotential, essentially the disturbing function. This can be expressed in the form,

$$R = GM\left[\begin{array}{l}\dfrac{A_2}{a^3}\left(\dfrac{a}{r}\right)^3\left\{\dfrac{1}{3}-\dfrac{1}{2}\sin^2 i+\dfrac{1}{2}\sin^2 i\cos 2(\theta+\omega)\right\}\\ +\dfrac{A_3}{a^4}\left(\dfrac{a}{r}\right)^4\left\{\left(\dfrac{15}{8}\sin^2 i-\dfrac{3}{2}\right)\sin(\theta+\omega)-\dfrac{5}{8}\sin^2 i\sin 3(\theta+\omega)\right\}\sin i\\ +\dfrac{A_4}{a^5}\left(\dfrac{a}{r}\right)^5\left\{\dfrac{3}{35}-\dfrac{3}{7}\sin^2 i+\dfrac{3}{8}\sin^4 i+\sin^2 i\left(\dfrac{3}{7}-\dfrac{1}{2}\sin^2 i\right)\cos 2(\theta+\omega)+\dfrac{1}{8}\sin^4 i\cos 4(\theta+\omega)\right\}\end{array}\right] \tag{3.12}$$

which can be further broken down as follows,

$$R_1 = GM\frac{A_2}{a^3}\left(\frac{1}{3}-\frac{1}{2}\sin^2 i\right)\left(1-e^2\right)^{-3/2}, \tag{3.13}$$

$$R_2 = GM\frac{A_4}{a^5}\left(\frac{3}{35}-\frac{3}{7}\sin^2 i+\frac{3}{8}\sin^4 i\right)\left(1-e^2\right)^{-7/2}\left(1+\frac{3}{2}e^2\right), \tag{3.14}$$

$$R_3 = GM\left\{\frac{3}{2}\frac{A_3}{a^4}\sin i\left(\frac{5}{4}\sin^2 i-1\right)e\left(1-e^2\right)^{-5/2}\sin\omega+\frac{A_4}{a^5}\sin^2 i\left(\frac{9}{28}-\frac{3}{8}\sin^2 i\right)e^2\left(1-e^2\right)^{-7/2}\cos 2\omega\right\}, \tag{3.15}$$

$$R_4 = GM\frac{A_2}{a^3}\left(\frac{a}{r}\right)^3\left[\left(\frac{1}{3}-\frac{1}{2}\sin^2 i\right)\left\{1-\left(\frac{r}{a}\right)^3\left(1-e^2\right)^{-3/2}\right\}+\frac{1}{2}\sin^2 i\cos 2(\theta+\omega)\right], \tag{3.16}$$

where all the symbols have their usual meanings. $R = R_1 + R_2 + R_3 + R_4$, where R_1, R_2, R_3 and R_4 are the first-order secular, second-order secular, long-periodic and short-periodic parts of the disturbing function respectively [62]. The relationship between the constants A_n ($n = 2$, 3 or 4) and the zonal harmonic coefficients have been derived to be,

$$A_2 = \frac{3}{2} J_2 R_E{}^2, \tag{3.17}$$

$$A_3 = -J_3 R_E{}^3, \tag{3.18}$$

$$A_4 = -\frac{35}{8} J_4 R_E{}^4. \tag{3.19}$$

By substituting these equations into any of Lagrange's planetary equations, we can evaluate the changes in any of the elements due to the asphericity of the Earth. For instance, substituting equation (3.13) into equation (3.4) yields the secular change in Ω due to J_2 as follows,

$$\frac{d\Omega}{dt} = \frac{-A_2 n \cos i}{p^2}, \tag{3.20}$$

where p is the semi-latus rectum, given by

$$p = a\left(1 - e^2\right), \tag{3.21}$$

The elements exhibit either short-term periodic, long-term periodic or secular variations, or a combination thereof in many cases. Short-term periodic variations are obviously less important than long-term periodic or secular variations since they do not contribute significantly to the change in the element over the long term. It is for this reason that short-term periodic variations are normally left out of debris models in order to save on computational time expended in running the model. The remainder of this sub-section will describe the equations that are modelled by Lewis's DAMAGE propagator (which will be used in the FCP) in order to propagate the debris fragments in GEO.

The J_2 perturbation equations presented in Merson [63] are summarised as,

$$\left(\frac{di}{dt}\right)_{J2} = -\frac{3}{2} \mu \frac{J_2 R_E{}^2}{hr^3} \sin 2i \sin(\theta + \omega) \cos(\theta + \omega), \tag{3.22}$$

$$\left(\frac{d\omega}{dt}\right)_{J2} = \frac{3}{4} n J_2 \left(\frac{R_E}{p}\right)^2 \left(5\cos^2 i - 1\right), \tag{3.23}$$

$$\left(\frac{d\Omega}{dt}\right)_{J2} = -\frac{3}{2} \frac{J_2 R_E^{\,2}}{\left[a\left(1-e^2\right)\right]^2} n(\cos i), \tag{3.24}$$

$$\left(\frac{dn}{dt}\right)_{J2} = \frac{3}{2} \frac{J_2 R_E^{\,2}}{p^2} n_0 \left(1 - \frac{3}{2}\sin^2 i\right)\sqrt{1-e^2}, \tag{3.25}$$

and

$$\left(\frac{da}{dt}\right)_{J2} = -\frac{3}{2} \frac{J_2 R_E^{\,2}}{p^2} a_0 \left(1 - \frac{3}{2}\sin^2 i\right)\sqrt{1-e^2}, \tag{3.26}$$

where all the symbols have their usual meanings and h is the magnitude of the orbital angular momentum vector and J_2 is the second order zonal harmonic coefficient (J_2 = 0.001082626 [64]). Lewis decided to model only the perturbations affecting Ω and ω because the literature [12, 63] suggests that these have the most noticeable effect on the orbit, and that a reasonable approximation to the change in the orbit's characteristics could be attained by applying these equations and omitting the others. Omitting the less significant effects would then have the advantage of saving on the computational time expended in running the program. There is a constant trade-off in debris modelling between the accuracy of the results obtained and the computational speed in attaining those results, as discussed in Chapter 1. Thus it is sensible to model only the major changes to the elements in accounting for the J_2 and J_3 aspherical components of the geopotential (i.e. the changes in Ω and ω according to J_2 and the changes in a and e according to J_3 – these are the changes to the elements modelled by Walker's LEO-dedicated IDES model to account for the aspherical components of the geopotential). However, the effects of the sectoral harmonics have resonant effects in geosynchronous orbits. Therefore, even though their influence is several orders of magnitude lower than that of the J_2 and J_3 zonal harmonics, their effect accumulates over time. Thus the effect on all the orbital elements must be modelled for the sectoral harmonics in order to avoid large errors in the evolution of geosynchronous orbits over the long term.

The equations implemented for the J_3 perturbations are given below.

$$\left(\frac{de}{dt}\right)_{J3} = -\frac{3}{2}\frac{nJ_3R_E^{\ 3}}{a^3\left(1-e^2\right)^2}\sin i\left[1-\frac{5}{4}\sin^2 i\right]\cos\omega, \tag{3.27}$$

and

$$\left(\frac{di}{dt}\right)_{J3} = \frac{3}{2}\frac{nJ_3R_E^{\ 3}}{a^3}\frac{e}{\left(1-e^2\right)^3}\cos i\left[1-\frac{5}{4}\sin^2 i\right]\cos\omega, \tag{3.28}$$

again, where all the symbols have their usual meanings and J_3 (= -2.536×10^{-6} [64]) is the third order zonal harmonic coefficient.

The equations implemented for the J_{22} perturbations are given by,

$$\left(\frac{da}{dt}\right)_{J22} = -3naJ_{22}\left(\frac{R_E}{a}\right)^2(1+\cos i)^2\left(1-\frac{5}{2}e^2+\frac{13}{16}e^4\right)\sin 2(\omega+M+\Omega-\lambda_{22}-\theta), \tag{3.29}$$

$$\left(\frac{de}{dt}\right)_{J22} = \frac{3}{4}neJ_{22}\left(\frac{R_E}{a}\right)^2(1+\cos i)^2\left(1-\frac{11}{4}e^2+\frac{21}{16}e^4\right)\sin 2(\omega+M+\Omega-\lambda_{22}-\theta), \tag{3.30}$$

$$\left(\frac{di}{dt}\right)_{J22} = \frac{3}{2}J_{22}\left(\frac{R_E}{a}\right)^2\sin i(1+\cos i)\left(1-2e^2-\frac{e^4}{16}\right)\sin 2(\omega+M+\Omega-\lambda_{22}-\theta), \tag{3.31}$$

$$\left(\frac{d\Omega}{dt}\right)_{J22} = -\frac{3}{2}nJ_{22}\left(\frac{R_E}{a}\right)^2(1+\cos i)\left(1-2e^2-\frac{e^4}{16}\right)\cos 2(\omega+M+\Omega-\lambda_{22}-\theta), \tag{3.32}$$

and

$$\left(\frac{d\omega}{dt}\right)_{J22} = \frac{3}{4}nJ_{22}\left(\frac{R_E}{a}\right)^2(1+\cos i)\left\{\cos i\left(\frac{7}{4}e^2-\frac{9}{8}e^4-3\right)+\frac{23}{4}e^2-e^4-5\right\} \cos 2(\omega+M+\Omega-\lambda_{22}-\theta), \tag{3.33}$$

where J_{22} (= 1.7208 × 10^{-6} [54]) is the Earth's second order sectoral harmonic coefficient and λ_{22} is the longitude of the reference stable point with respect to the J_{22} harmonic (which is 105°W relative to the prime meridian).

The equations implemented for the J_{33} perturbations are summarised below.

$$\left(\frac{da}{dt}\right)_{J33} = -\frac{45}{4} naJ_{33}\left(\frac{R_E}{a}\right)^3 (1+\cos i)^3\left(1-6e^2+\frac{423}{64}e^4\right) \sin 3(\omega + M + \Omega - \lambda_{33} - \theta), \tag{3.34}$$

$$\left(\frac{de}{dt}\right)_{J33} = \frac{45}{16} neJ_{33}\left(\frac{R_E}{a}\right)^3\left(1-\frac{25}{4}e^2+\frac{511}{64}e^4\right)(1+\cos i)^3 \sin 3(\omega + M + \Omega - \lambda_{33} - \theta), \tag{3.35}$$

$$\left(\frac{di}{dt}\right)_{J33} = \frac{45}{8} nJ_{33}\left(\frac{R_E}{a}\right)^3 \sin i(1+\cos i)^2\left(1-\frac{11}{2}e^2+\frac{255}{64}e^4\right) \sin 3(\omega + M + \Omega - \lambda_{33} - \theta), \tag{3.36}$$

$$\left(\frac{d\Omega}{dt}\right)_{J33} = -\frac{45}{8} nJ_{33}\left(\frac{R_E}{a}\right)^3 (1+\cos i)^2\left(1-\frac{11}{2}e^2+\frac{255}{64}e^4\right) \cos 3(\omega + M + \Omega - \lambda_{33} - \theta), \tag{3.37}$$

and

$$\left(\frac{d\omega}{dt}\right)_{J33} = nJ_{33}\left(\frac{R_E}{a}\right)^3\left\{(1+\cos i)^2\cos i\left(-\frac{135}{8}+\frac{3825}{128}e^2\frac{225}{512}e^4\right)-\frac{45}{2}+\frac{7785}{128}e^2-\frac{5625}{256}e^4\right\} \cos 3(\omega + M + \Omega - \lambda_{33} - \theta), \tag{3.38}$$

where J_{33} (= 0.16456 × 10^{-6} [54]) is the Earth's third order sectoral harmonic coefficient and λ_{33} is the longitude of the reference stable point with respect to the J_{33} harmonic (which is 18.662°E relative to the prime meridian).

The equations implemented for the J_{31} perturbations can be summarised as,

$$\left(\frac{da}{dt}\right)_{J31} = -2naJ_{31}\left(\frac{R_E}{a}\right)^3\left\{\frac{15}{16}\sin^2 i(1+3\cos i)-\frac{3}{4}(1+\cos i)\right\}\left(1+2e^2+\frac{239}{64}e^4\right) \sin(\omega+M+\Omega-\lambda_{31}-\theta), \tag{3.39}$$

$$\left(\frac{de}{dt}\right)_{J31} = \frac{3}{4}neJ_{31}\left(\frac{R_E}{a}\right)^3\left\{\frac{5}{4}\sin^2 i(1+3\cos i)-(1+\cos i)\right\}\left(\frac{1}{2}+\frac{7}{8}e^2+\frac{199}{128}e^4\right) \sin(\omega+M+\Omega-\lambda_{31}-\theta), \tag{3.40}$$

$$\left(\frac{di}{dt}\right)_{J31} = \frac{3}{16}nJ_{31}\left(\frac{R_E}{a}\right)^3\sin i(1+10\cos i+15\cos^2 i)\left(1+\frac{5}{2}e^2+\frac{327}{64}e^4\right) \sin(\omega+M+\Omega-\lambda_{31}-\theta), \tag{3.41}$$

$$\left(\frac{d\Omega}{dt}\right)_{J31} = \frac{3}{4}nJ_{31}\left(\frac{R_E}{a}\right)^3\left\{\frac{5}{2}\cos i(1+3\cos i)-\frac{15}{4}\sin^2 i+1\right\}\left(1+\frac{5}{2}e^2+\frac{327}{64}e^4\right) \cos(\omega+M+\Omega-\lambda_{31}-\theta), \tag{3.42}$$

and

$$\left(\frac{d\omega}{dt}\right)_{J31} = nJ_{31}\left(\frac{R_E}{a}\right)^3\left\{\begin{array}{l}\frac{3}{4}+\cos i\left(\frac{165}{16}+\frac{8151}{256}e^2+\frac{25509}{1024}e^4\right)+\\ \cos^2 i\left(-\frac{45}{8}-\frac{4305}{256}e^2-\frac{4125}{256}e^4\right)+\\ \cos^3 i\left(-\frac{315}{16}-\frac{14715}{256}e^2-\frac{64215}{1024}e^4\right)\end{array}\right\}\cos(\omega+M+\Omega-\lambda_{31}-\theta), \tag{3.43}$$

where J_{31} (= 2.005 × 10^{-6} [54]) is one of the Earth's tesseral harmonic coefficients and λ_{31} is the longitude of the reference stable point with respect to the J_{31} harmonic (which is 6.614°W relative to the prime meridian).

Other bodies in the solar system impose additional gravitational forces on objects orbiting the Earth, most notably the Sun and the Moon, which generate effects that are of a similar

order of magnitude. Since the Sun and the Moon will rarely lie in the same plane as the orbiting object, their main effect will be to change the inclination of the object's orbit.

The effects of solar gravitational attractions on an orbit can be understood by imagining the satellite's orbit and the ecliptic plane (the Sun's relative orbit around the Earth) mapped out onto the celestial sphere, as illustrated in Figure 3.2, where i is the inclination of the satellite orbit with respect to the ecliptic and $\boldsymbol{h}$ is the angular momentum vector of the satellite's orbit. The mutual gravitational attraction of the two orbits creates a torque about the line of nodes, which tends to turn the satellite orbit into the ecliptic. The gyroscopic effect of the torque on the satellite orbit induces a gyroscopic precession of the orbit about the pole of the ecliptic, thus causing a regression of nodes along the ecliptic.

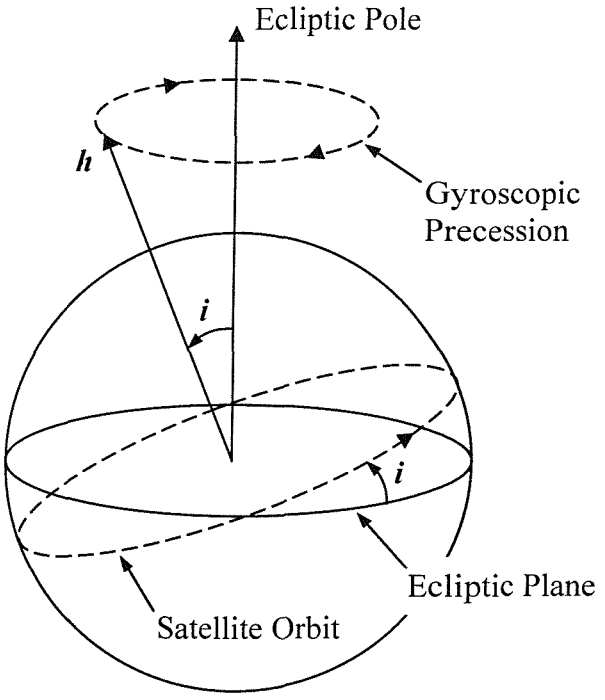

Figure 3.2 The gyroscopic precession of a satellite's orbit due to solar gravitational perturbations

The same treatment can be used to understand lunar gravitational perturbations, *i.e.*, by imagining the satellite's orbit and the Moon's relative orbit around the Earth mapped out onto the celestial sphere. The Moon will cause a regression of the orbit about an axis

normal to the Moon's orbital plane, which has a 5° inclination with respect to the ecliptic. Luni-solar gravitational perturbations also affect the eccentricity and inclination of a satellite orbit.

The equations implemented for lunar gravitational perturbations [65, 66] can be summarised as,

$$\left(\frac{de}{dt}\right)_{LUNAR} = \frac{-3kM}{4\sqrt{\mu a^3}} e\sqrt{1-e^2}\left[M_1 M_2 \cos(2\omega) - \frac{1}{2}\left(M_1^{\,2} - M_2^{\,2}\right)\sin(2\omega)\right], \tag{3.44}$$

$$\left(\frac{di}{dt}\right)_{LUNAR} = \frac{3kM}{4\sqrt{\mu a^3}} \frac{M_3}{\sqrt{1-e^2}}\left[M_1\left(2+3e^2+5e^2\cos(2\omega)\right)+5M_2 e^2 \sin(2\omega)\right], \tag{3.45}$$

$$\left(\frac{d\Omega}{dt}\right)_{LUNAR} = \frac{3kM}{4\sqrt{\mu a^3}} \frac{M_3}{\sin i\sqrt{1-e^2}}\left[5M_1 e^2 \sin(2\omega)+M_2\left(2+3e^2-5e^2\cos(2\omega)\right)\right], \tag{3.46}$$

and

$$\left(\frac{d\omega}{dt}\right)_{LUNAR} = \frac{3kM}{2\sqrt{\mu a^3}}\sqrt{1-e^2}\left[\begin{array}{l} 5\left(M_1 M_2 \sin(2\omega)+\frac{1}{2}\left(M_1^{\,2}-M_2^{\,2}\right)\cos(2\omega)\right) \\ -1+\frac{3}{2}\left(M_1^{\,2}+M_2^{\,2}\right)+ \\ \frac{5a}{2ea_M}\left(1-\frac{5}{4}\left(M_1^{\,2}-M_2^{\,2}\right)\left(M_1\cos\omega+M_2\cos\omega\right)\right) \\ -d\Omega_{LUNAR}\cos i \end{array}\right], \tag{3.47}$$

where kM is the Moon's gravitational constant, which is 8.6999×10^{-14} Nm^{2}kg^{-2} and a_M is the semi-major axis of the Moon's orbit, which is 384400.0 km. M_1, M_2 and M_3 are lunar direction cosines, defined as

$$M_1 = \cos\alpha_M \cos\phi_M + I_{CM} \sin\phi_M \sin\alpha_M, \tag{3.48}$$

$$M_2 = \cos i\left[-\sin\alpha_M \cos\phi_M + I_{CM} \sin\phi_M \cos\alpha_M\right] + \sin i I_{SM} \sin\phi_M, \tag{3.49}$$

and

$$M_3 = \sin i[\cos\phi_M \sin\alpha_M - I_{CM} \sin\phi_M \cos\alpha_M] + \cos i I_{SM} \sin\alpha_M, \tag{3.50}$$

where I_{CM} and I_{SM} are the cosine and sine of the inclination of the lunar orbit respectively and ϕ_M is the mean anomaly + argument of perigee of the Moon. The relevant terms are defined as,

$$I_{CM} = \cos\xi \cos i_\xi - \sin\xi \sin i_\xi \cos\lambda_{\Omega M}, \tag{3.51}$$

$$I_{SM} = \sqrt{1 - I_{CM}^{\ 2}}, \tag{3.52}$$

$$\phi_M = \lambda_M - \lambda_{\Omega M} + \sin^{-1}\left(\frac{\sin\xi \sin\lambda_{\Omega M}}{I_{SM}}\right), \tag{3.53}$$

and

$$\alpha_M = \Omega - \tan^{-1}\left(\frac{\Omega_{SM}}{\Omega_{CM}}\right), \tag{3.54}$$

where λ_M is the mean lunar longitude, $\lambda_{\Omega M}$ is the mean longitude of the ascending node of the lunar orbit, ξ is the mean obliquity of the ecliptic (which is 23.44°), i_ξ is the inclination of the lunar orbit with respect to the ecliptic (which is 5.145°) and Ω_{SM} and Ω_{CM} are the sine and cosine of the right ascension of the ascending node of the Moon, given respectively by

$$\Omega_{SM} = \frac{\sin i_\xi \sin\lambda_{\Omega M}}{I_{SM}}, \tag{3.55}$$

and

$$\Omega_{CM} = \sqrt{1 - \Omega_{SM}^{\ 2}} \tag{3.56}$$

The equations implemented for the solar gravitational perturbations[65, 66] can be summarised as,

$$\left(\frac{de}{dt}\right)_{SOLAR} = \frac{-15kS}{2\sqrt{\mu a^3}} e\sqrt{1-e^2}\left[S_1 S_2 \cos(2\omega) - \frac{1}{2}\left(S_1^{\,2} - S_2^{\,2}\right)\sin(2\omega)\right], \tag{3.57}$$

$$\left(\frac{di}{dt}\right)_{SOLAR} = \frac{3kS}{4\sqrt{\mu a^3}} \frac{S_3}{\sqrt{1-e^2}}\left[S_1\left(2+3e^2+5e^2\cos(2\omega)+5S_2 e^2 \sin(2\omega)\right)\right], \tag{3.58}$$

$$\left(\frac{d\Omega}{dt}\right)_{SOLAR} = \frac{3kS}{4\sqrt{\mu a^3}} \frac{S_3}{\sin i\sqrt{1-e^2}}\left[5S_1 e^2 \sin(2\omega)+S_2\left(2+3e^2-5e^2\cos(2\omega)\right)\right], \tag{3.59}$$

and

$$\left(\frac{d\omega}{dt}\right)_{SOLAR} = \frac{3kS}{2\sqrt{\mu a^3}} e\left[\begin{array}{l} 5\left(S_1 S_2 \sin(2\omega)+\frac{1}{2}\left(S_1^{\,2}-S_2^{\,2}\right)\cos(2\omega)\right) \\ -1+\frac{3}{2}\left(S_1^{\,2}+S_2^{\,2}\right)+\frac{5a}{2ea_S}\left(1-\frac{5}{4}\left(S_1^{\,2}-S_2^{\,2}\right)\right) \\ \left(S_1\cos\omega+S_2\cos\omega\right) \end{array}\right] - d\Omega_{SOLAR}\cos i, \tag{3.60}$$

where kS is the Sun's gravitational constant, which is 3.96392×10^{-14} Nm^2kg^{-2} and a_S is the semi-major axis of the Earth's orbit around the Sun, which is 1.4968×10^8 km (1 AU). S_1, S_2 and S_3 are solar direction cosines, defined as

$$S_1 = \cos\Omega\cos\lambda_S + \cos\xi\sin\lambda_S\sin\Omega, \tag{3.61}$$

$$S_2 = \cos i\left[-\sin\Omega\cos\lambda_S + \cos\xi\sin\lambda_S\cos\Omega\right] + \sin i\sin\xi\sin\lambda_S, \tag{3.62}$$

and

$$S_3 = \sin i\left[\cos\lambda_S\sin\Omega - \cos\xi\sin\lambda_S\cos\Omega\right] + \cos i\sin\xi\sin\lambda_S, \tag{3.63}$$

where λ_S is the mean solar longitude.

These perturbation equations were all implemented into the DAMAGE propagator and were validated using ESA's FOCUS propagator [67]. Test cases were also run, which were compared to identical test cases in the literature [68].

3.3 Fast Orbital Propagators

3.3.1 Rationale

The rationale for using a fast orbital propagator is simple. The individual propagation of all fragments of a debris cloud is practically impossible with conventional numerical or semi-analytical integration methods because of excessive CPU times and excessive memory requirements. This is particularly true of high-energy breakups, which release a far greater number of fragments than their low-energy counterparts. This leads to the aforementioned trade-off between the accuracy of the results and the computational effort required to generate those results. Furthermore, there seems to be no valid case for using an extremely accurate orbital propagator to propagate the fragments ejected from a breakup event because of the significant uncertainties in modelling that breakup event in the first place – see Chapter 4.

Debris models are constantly attempting to strike a balance between accuracy and speed. Fragment propagation is one of the two most time consuming aspects of any debris model, the other being flux determination. Thus a fast orbital propagator that loses little accuracy compared to conventional propagation methods is highly desirable. This section describes some of the varied and imaginative ways in which debris modellers have sought to decrease debris propagation times.

3.3.2 Review of Fast Orbital Propagators

3.3.2.1 PETRA

PETRA (Propagator for low Earth TRAjectories) was proposed by Rüdiger Jehn of ESOC, Darmstadt, in his PhD thesis in 1996 [69]. The core of the orbital propagator is essentially three look-up tables – one for semi-major axis, one for eccentricity and one for the ascending node. In each look-up table, the evolution of 16 different reference

orbits are stored, each one with a different eccentricity, ranging from 1×10^{-8} to 0.215. The evolution of the 16 reference orbits is calculated under the influence of air drag (in terms of the effect it has on the orbits' semi-major axes and eccentricities) and in terms of Earth oblateness due to the J_2 Earth second order zonal harmonic (in terms of its effect on RAAN). The evolution of these reference orbits is computed under the assumption of constant solar activity, constant fragment scale height and constant fragment area-to-mass ratio. In propagating a debris cloud, the evolved position of each fragment is calculated by interpolating from the orbital elements in each look up table, using the two reference orbits closest to the orbit being evolved. This gives an immediate approximation for the position of the fragment at the required epoch, which can be further refined by utilising various techniques to account for changes in the solar activity, scale height and area-to-mass ratios of the fragments.

The effect of air drag on the orbits' semi-major axis and eccentricity are calculated from the drag equations of King-Hele [70], given by

$$\Delta a = -\int_0^{2\pi} a^2 \rho \frac{A_{eff} C_D}{m} \sqrt{\frac{(1+e\cos E)^3}{1-e\cos E}} dE \text{, and} \tag{3.64}$$

$$\Delta e = -\int_0^{2\pi} a\rho \frac{A_{eff} C_D}{m} (1-e^2)\cos E \sqrt{\frac{1+\cos E}{1-\cos E}} dE, \tag{3.65}$$

where Δa is the change in semi-major axis per revolution, Δe is the change in eccentricity per revolution, ρ is the air density, A_{eff} is the effective area of the orbiting object, C_D is the drag coefficient, m is the mass of the orbiting object and E is the eccentric anomaly.

In calculating the reference orbits, Jehn assumed that the area-to-mass ratio is fixed at 1 m^2/kg and the initial orbits all have an initial semi-major axis of 8378.15 km, yielding an initial mean height of 2000 km (8378.15 – Earth radius). Jehn also assumed that the air density, ρ, remains constant throughout each revolution of the spacecraft. An analysis conducted by Jehn showed that this latter assumption could lead to errors in the Δa calculated by equation (3.64) of up to 18% in orbits with high eccentricities. However

this assumption, together with the assumption of a constant area-to-mass ratio, can be compensated for at the end of the propagation phase, as will be described later.

The calculation of the change in semi-major axis per revolution, Δa, from equation (3.64), allows an estimate of the time it takes the semi-major axis to decrease by 1 km using the simple ratios from the equation

$$\Delta t = \frac{T}{\Delta a}, \tag{3.66}$$

where T represents the orbital period, Δt is the time it takes the semi-major axis to decrease by 1 km and Δa is the change in semi-major axis per revolution.

Hence the decay time can be calculated as a function of the mean height for the 16 orbits with varying eccentricities to generate the first look-up table, the results of which are plotted in Figure 3.3. Figure 3.4 shows a close-up of the results in Figure 3.3 for mean heights of 200 to 1000 km.

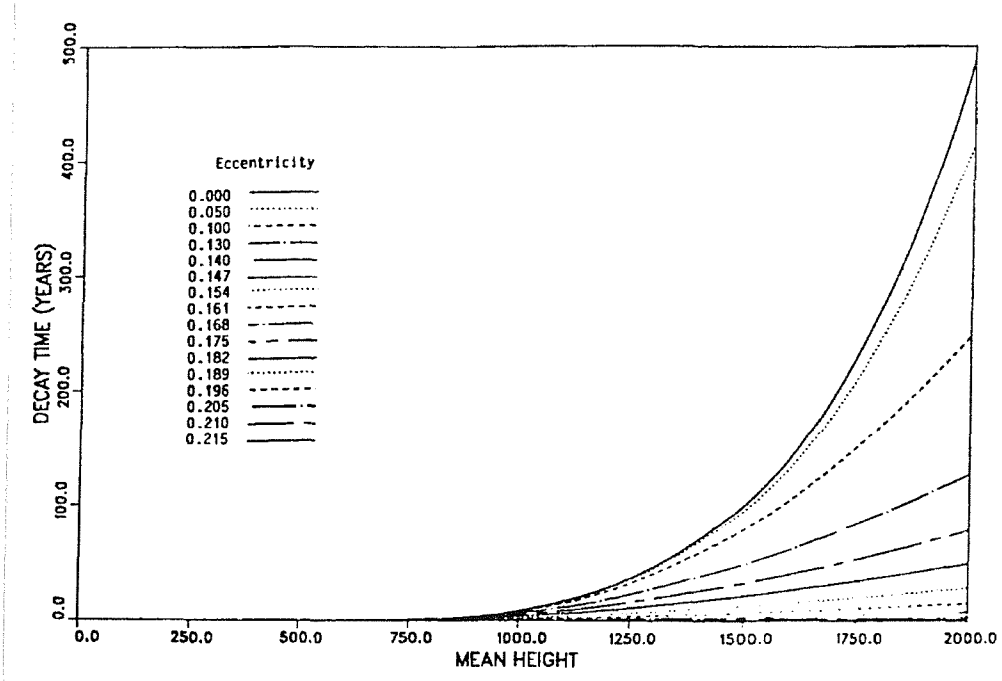

Figure 3.3: The mean height vs. decay time for each of the 16 reference orbits used in PETRA

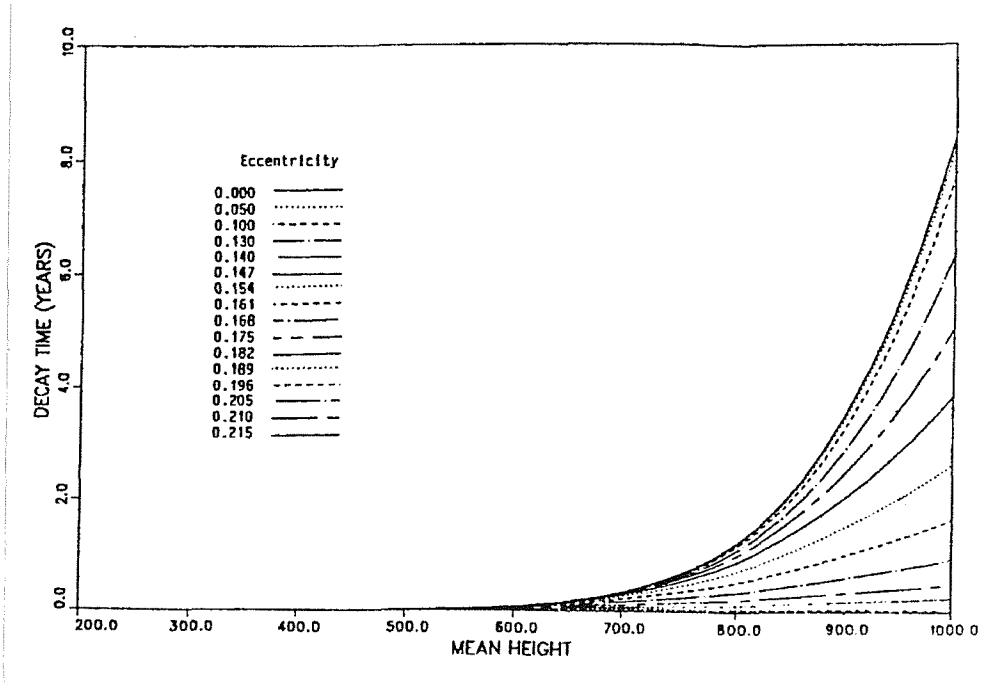

Figure 3.4 A close-up view of the mean height vs. decay time for each of the 16 reference orbits used in PETRA for mean heights between 200 and 1000 km.

The change in eccentricity for every 1 km change in semi-major axis can also be calculated using ratios from the equation

$$\Delta e_{1km} = \frac{\Delta e}{\Delta a}, \tag{3.67}$$

where Δe_{1km} is the change in eccentricity per 1 km change in semi-major axis and Δe is the change in eccentricity per revolution, as calculated by equation (3.65). Hence the eccentricity can be calculated as a function of the mean height for the 16 orbits with varying eccentricities to generate the second look-up table, the results of which are plotted in Figure 3.5.

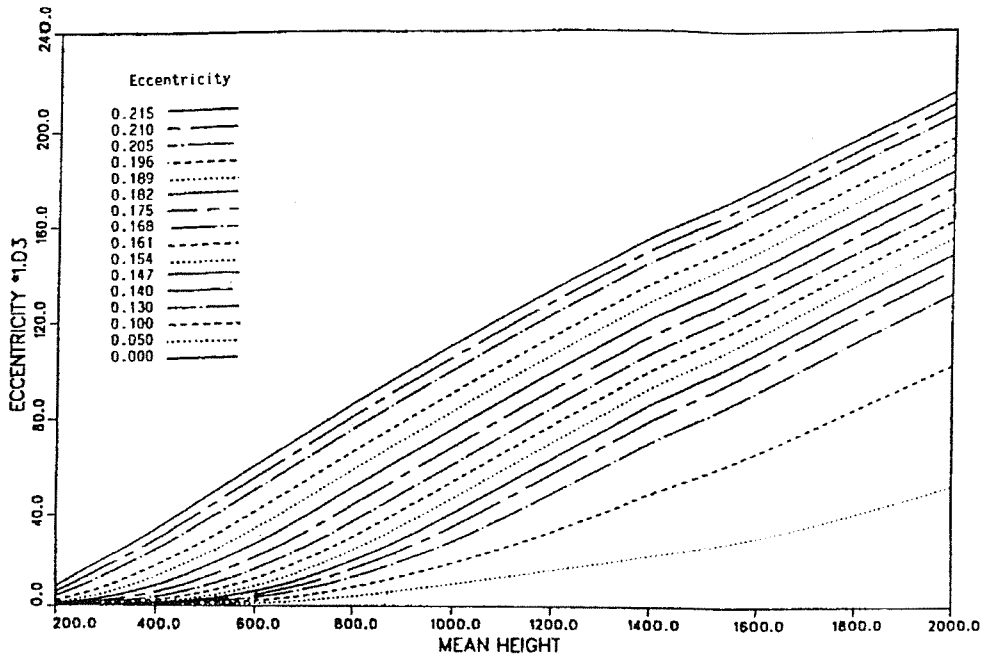

Figure 3.5 The mean height vs. eccentricity for each of the 16 reference orbits used in PETRA

Finally, the change in RAAN due to Earth oblateness can be calculated as a function of eccentricity for each of the 16 reference orbits from equation (3.24). These results are stored in the third look-up table and graphically illustrated against the mean height in Figure 3.6.

The curves in Figure 3.6 were generated by assuming an inclination of 0°, thus causing the cos*i* term in equation (3.24) to disappear. For inclinations other than 0°, the change in the RAAN over time (expressed in Figure 3.6 as the change in RAAN against the decay in the mean height) should be multiplied by cos*i* in order to attain the final true value for the RAAN.

This process is repeated from the mean starting height of 2000 km until it reaches 200 km, at which point the orbit is considered to have decayed completely. The values of semi-major axis, eccentricity, RAAN and decay time are recorded and stored into one of the look-up tables every time the orbital altitude has decayed by 20 km.

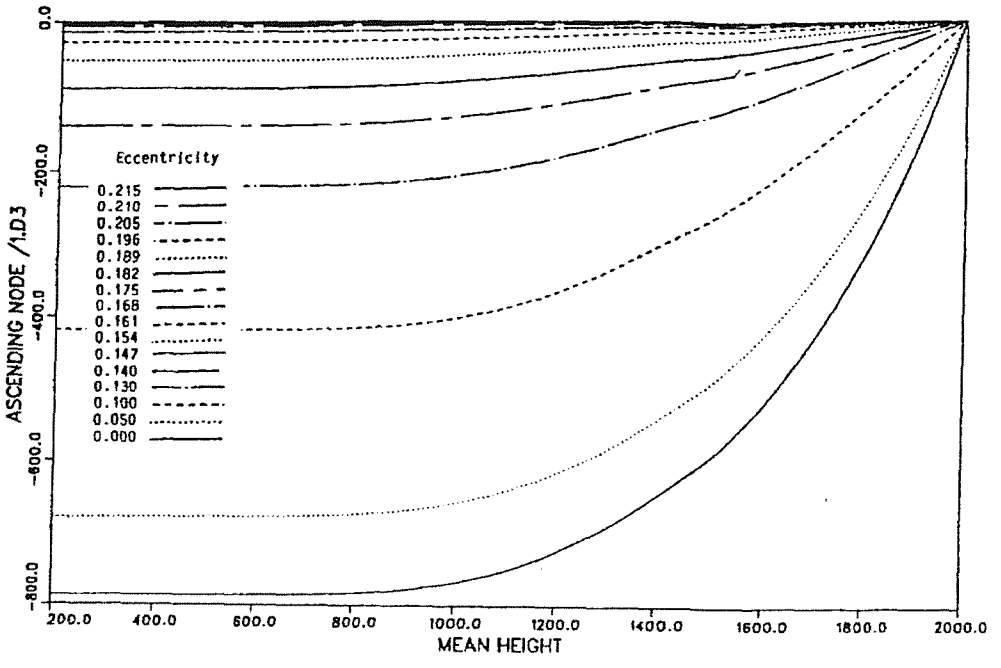

Figure 3.6 The mean height vs. RAAN for each of the 16 reference orbits used in PETRA

Having established the change in decay time, eccentricity and RAAN as a function of the mean height for the 16 reference orbits, the debris fragments can be propagated by interpolating from the data in Figures 3.3 – 3.6. Two reference orbits will be required for interpolation – one with an eccentricity just above the eccentricity of the debris fragment and one with an eccentricity just below the eccentricity of the debris fragment. In order to avoid the errors induced by linear interpolation between non-linear curves (such as those in Figures 3.3 and 3.4 below mean heights of around 1000 km), Jehn proposes a transformation from the mean height to a new transformed mean height, where the transformed mean height vs. decay time curves for the 16 reference orbits are linear. Thus standard linear interpolation can be performed using the mean height above 1000 km and using the transformed mean height below 1000 km, in order to recover the decay time for any low-Earth orbit (mean height < 2000 km), with eccentricities less than 0.215. Similarly, interpolation can be performed on Figures 3.5 and 3.6 to recover the new eccentricity and the new RAAN of the orbit.

The assumption of a constant area-to-mass ratio and constant scale height can be compensated for by varying the propagation times. Equation (3.64) shows that the change in semi-major axis Δa is directly proportional to the area-to-mass ratio, which is obvious if A_{eff}/m is moved outside the integral. Thus the varying area-to-mass ratio can be compensated for by multiplying the propagation time by the actual area-to-mass ratio so that.

$$DT = \frac{A_{eff}}{m}(t_{end} - t_{start}), \tag{3.68}$$

where DT is the adjusted propagation time, and t_{start} and t_{end} are the start and end epochs respectively (all of which are measured in years). This adjusted propagation time thus effectively passes more quickly for fragments with high area-to-mass ratios and passes more slowly for fragments with low area-to-mass ratios, thus compensating for the varying magnitudes of drag effects on different fragments.

Varying the propagation time to account for the activity of the Sun is more difficult, because the effect on air density is altitude dependent and varies with time as the Sun's activity changes. A dimensionless measure of time, t_d, is defined which is given by

$$t_d = \frac{\rho(F_{10.7}(t), h)}{\rho(150, h)}, \tag{3.69}$$

where h is the altitude and $F_{10.7}$ is the solar radio flux (the intensity of the microwave radiation emitted by the Sun at a wavelength of 10.7 cm or a frequency of 2800 MHz, which is a commonly used reference value at which to measure the Sun's activity). The air density, ρ, is calculated as a function of solar activity and altitude and is based on the CIRA 72 atmospheric model. In equation (3.69) the air density is normalised by the air density at a solar radio flux of 150×10^4 Jy*. The new time variable t_d increases quickly when the air density is high (causing the orbit to decay quickly) and increases slowly when the air density is low.

* The Jy unit (or Jansky) is a measure of flux, where 1 Jy = 10^{-26} $Wm^{-2}Hz^{-1}$

A Time Scaling Factor (TSF) is then calculated by the following equation:

$$TSF = \frac{1}{t - 1961} \int_{1961}^{t} t_d(t', h)\, dt', \tag{3.70}$$

where t is the required epoch (measured in years) and t_d is the modified time and 1961 is a reference epoch, corresponding to the first on-orbit fragmentation event. Figure 3.7 plots the trend given by equation (3.70) for a number of different altitude curves.

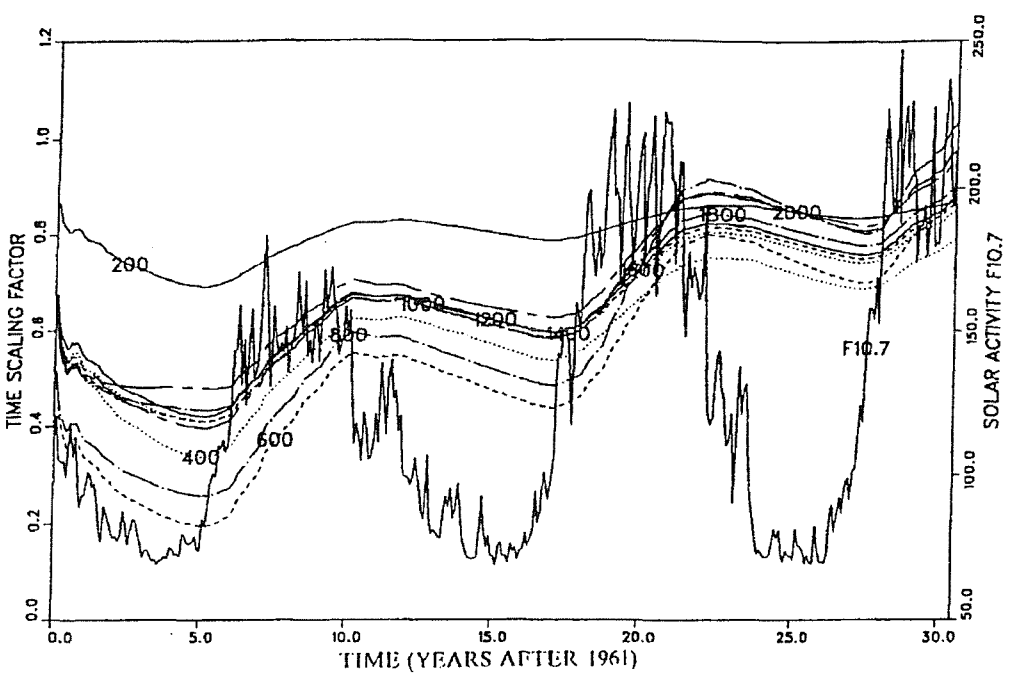

Figure 3.7 The TSF (Time Scaling Factor) as a function of years elapsed since 1961 for various altitudes (denoted by the annotation on the curves – measured in km). The curve marked F10.7 gives the solar radio flux at 10.7 cm wavelength and is to be read off the solar activity axis only.

The calculation of the time adjusted for solar activity, t_s, when the initial epoch differs from 1961 is easily done by calculating TSF at the required target epoch with respect to 1961, then subtracting TSF at the initial epoch with respect to 1961. This is given by

$$t_s(t_{start}, t_{end}, h) = TSF(t_{end}, h)t_{end} - TSF(t_{start}, h)t_{start}, \tag{3.71}$$

where t_{start} is the initial start epoch and t_{end} is the final target epoch.

The adjusted propagation time, after taking into account the area-to-mass ratio and solar activity is thus given by

$$DT = \frac{A_{eff}}{m} t_s \,, \tag{3.72}$$

where t_s is the time adjusted for solar activity, as given by equation (3.71).

3.3.2.2 SDM-DCP

The SDM model [44-46], developed by ISTI of Pisa, Italy, utilises a fast propagator called DCP (Debris Cloud Propagator) in order to propagate its debris fragments. This cloud propagator provides a fast method of propagating fragments but considerable speed is also achieved by the sampling method used to determine which of those fragments should be propagated in the first place. Both these elements of SDM's fast propagation technique will be explained in this sub-section.

The Earth environment is binned into 800 altitude shells of 50 km thickness that extend up to an altitude of 40,000 km. This defines the region of space of interest in SDM. The objects are also assigned to mass bins, which increase logarithmically from 10 mg upwards.

The population of objects considered in SDM is divided into two categories, namely the *historical population* and the *running population.* The historical population consists of objects greater than 1 mg that have been created previously by explosions, collisions or other objects that were released into space. The historical population is saved to file every year, in the form of a spatial density distribution as a function of altitude and mass. 200 of these files exist in SDM ranging from 1994 to 2194. Thus if the debris population in July 2003 were required, then SDM would load the historical population file for 2003. Everything that is then formed after the beginning of 2003, by explosions, collisions and launches, forms the second population category, the *running population.* All objects above a user-defined threshold mass are propagated individually by the DCP. All objects below this mass are represented by a sample object (representing a number of actual objects of the same mass), which is then propagated. The sample-factor (the number of

actual objects represented by the sample object) is also user defined. In the example, the running population would be propagated for 6 months, from the beginning of January 2003 to the start of July 2003, and then added to the background or historical population to give the population at the beginning of July.

For the first few days after the breakup event, the DCP propagates a debris cloud by propagating it along an "average orbit" and then randomising the fragments about this orbit to give their positions the required epoch. Several months after the breakup event, the RAAN and the argument of perigee (for inclinations away from the critical 63.4°) also start to be randomised. Long-term perturbations acting only (or mainly) on mean anomaly, RAAN or argument of perigee are not very important in LEO and these elements are randomised. This is because the fragments are relatively evenly spread in terms of mean anomaly, RAAN and argument of perigee in LEO. This however is not the case in GEO, where clusters of fragments exist around the Earth, as discussed in section 2.2.5.

Air drag is one of the most important perturbations in LEO, but is only important at low altitudes. SDM ignores the effects of air drag above 900 km. Luni-solar perturbations are, largely negligible for low altitude near-circular orbits, although they can cause slight reduction in perigee heights for highly eccentric orbits, such as GTO and Molniya orbits, which in turn can lead to dramatic increases in drag effects. However, the evolution and lifetime of such orbits crucially depends on the starting position of the ascending node and since this information is unavailable for debris objects, luni-solar perturbations have been ignored completely in the SDM propagator. Earth-gravity effects also become unimportant as these affect the values of the argument of perigee and RAAN, which are randomised by SDM in LEO. Consequently the only elements that are modified due to orbital perturbation effects are semi-major axis and eccentricity, and these are affected only by air drag in the model, and only below 900 km in height. Thus by ignoring most of the perturbative forces, DCP is an extremely fast propagator.

3.3.2.3 STAT

The STAT (Stochastic Analogue Tool) [45] is another debris model developed by ISTI. It differs from SDM in the sense that STAT is a stochastic model, whereas SDM is a semi-deterministic model (as the names suggest). STAT is particularly suited to the long-term analysis of the evolution of the debris environment due to its stochastic approach. The debris environment is binned according to a three-fold subdivision in semi-major axis (from 6378 to 46378 km), eccentricity (from 0 to 1) and mass (from 1 mg to 10,000 kg). An important feature of STAT is that it propagates the orbit of individual representative objects, one for each bin, and so the computing time is independent of the number of fragments in the population. The representative object is propagated as a weighted particle, with the weighting factor assigned according to the number of fragments that the weighted particle represents, i.e. the number of particles in the bin. These representative particles are propagated under the assumption that the neighbouring particles in the bin would have a similar evolution. A rigid displacement in the semi-major axis – eccentricity space of the rectangle to which the representative particle belongs is performed. This is represented in Figure 3.8, which shows the original bin, bin A, say, that has been propagated using the representative particle approach to a new position, illustrated by bin B. This approach disregards the fact that the rectangle is actually distorted by the orbital evolution.

The fragments in the propagated rectangle can then be re-binned by taking the ratio of the percentage of rectangle B covered by each bin and then multiplying these percentages by the total number of fragments in rectangle B and adding them to the appropriate bin.

In this method, only a and e are propagated. The values of i are used in the calculations but are not propagated and the values of ω and Ω are randomised.

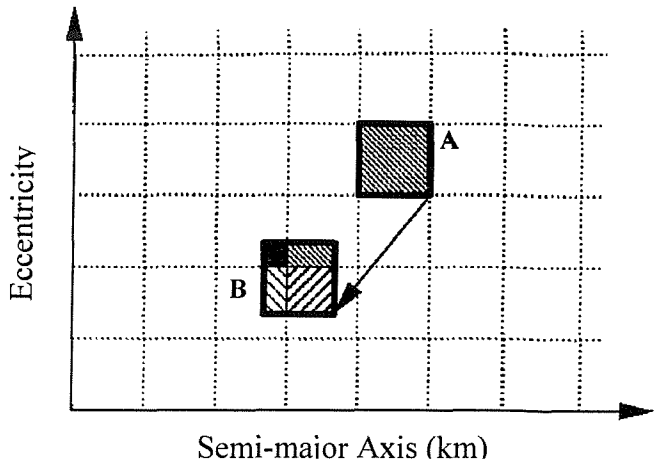

Figure 3.8: The rigid displacement of a bin in the *a-e* coordinates in STAT

3.3.2.4 IDES

The IDES propagator [12] individually propagates the orbits of large objects (greater than 10 cm in diameter) with respect to atmospheric drag, Earth-gravity, luni-solar gravity and SRP perturbations. The small objects are treated differently however.

The original method used in IDES to treat small objects was to bin the fragments into a POM (Population Orbit Matrix), where the particles were binned according to perigee radius, eccentricity, inclination, mass and object type. Ten particles from each bin were chosen randomly and were propagated. These ten fragments represented the total number of fragments in the bin and were thus given a weighting value equal to a tenth of the total number of objects in the bin. The ten fragments were propagated and were added, together with their weighting factors, to the five-dimensional bin to which they were propagated. Essentially, propagating ten fragments was a form of the Monte Carlo technique, which attempted to smooth out any results that were the consequence of random variation. Thus the average of the ten propagations was used in this method. The POM is illustrated in Figure 3.9, where all the symbols have their usual meanings and r_p signifies the perigee radius, N_t is the number of fragments per bin and n is the number of

representative weighted particles. Thus the weighting of each of the representative particles is given by N_t/n.

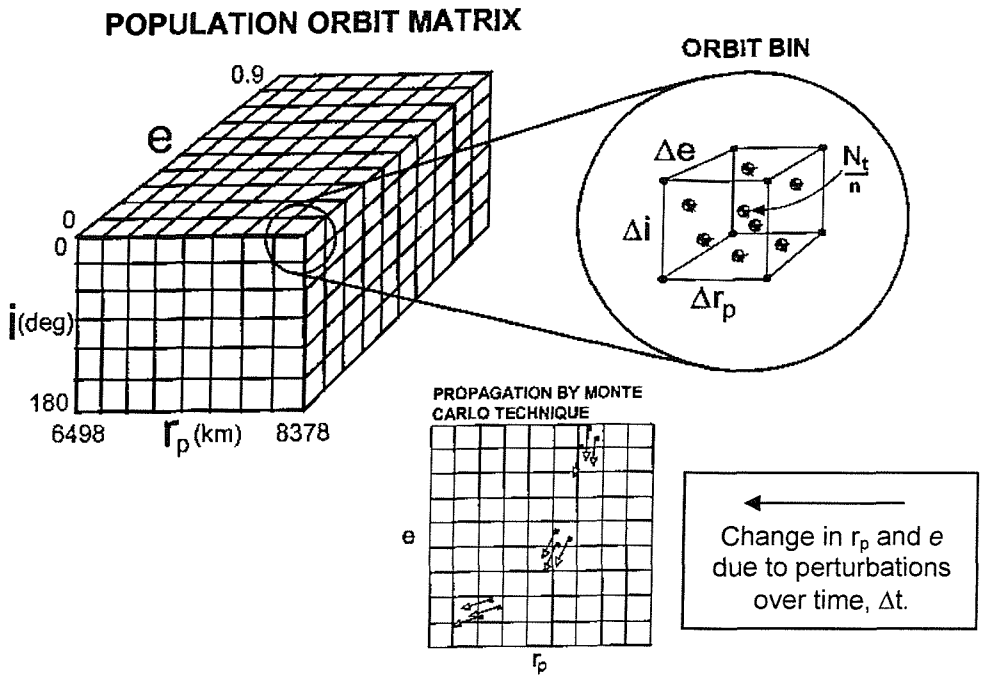

Figure 3.9: The POM that was used in IDES

The POM method has since been superseded by a slightly different method, which uses weighted particles to represent a large number of small fragments. The weighted particles are then propagated conventionally.

3.3.3 Summary

In summary, it can be said that fast orbital propagators can be subdivided into two categories – namely those that speed up the propagation of each fragment and those that improve propagation times by propagating fewer fragments. Those propagators that fall into the first category include PETRA, which uses sophisticated techniques and look up tables to propagate each individual fragment, thus negating the need for the slow iterative

process of perturbing each orbital element over each time-step. Those that fall into the second category include SDM-DCP, STAT and IDES, where the propagation speed of each individual fragment remains unchanged but a considerable speed increase is gained by propagating a smaller number of representative or weighted particles, instead of all the fragments in the debris cloud. The majority of fast propagators fall into the second category, as this method is easy to implement and requires only a small modification to the existing code.

These models all make assumptions about the nature of the orbital debris environment and the perturbing effects of orbital perturbations, e.g. PETRA assumes that only the effects of air drag on semi-major axis and eccentricity and the effects of Earth oblateness on the RAAN are significant. Many other models assume that the fragments are evenly spread in longitude and that the final values of RAAN, argument of perigee and mean anomaly can be randomly assigned, rather than being calculated. These assumptions are made in order to gain considerable speed improvements, but they do so at the expense of accuracy. However, the significant increase in speed is deemed to be worth the reduction in accuracy in most cases. The assumptions upon which these fast propagators are based are orbit-dependent and are mostly only valid in LEO. A fast debris propagator designed for use in the GEO regime must rely upon methods that are not dependent upon such assumptions.

Chapter 4

Breakup Modelling

Breakup modelling in its current state is an imprecise science. The physics of hypervelocity impacts between simple objects is very complicated, and that of impacts between complicated spacecraft structures even more so. During a hypervelocity impact, such as those that occur in LEO orbits, the shock wave propagates through the spacecraft structure faster than the speed of sound in the material and the spacecraft material in the immediate vicinity of the impact momentarily acts like a fluid [3, 24]. In order to accurately model this type of collision, specialist hydrodynamic codes are used and even their accuracy is questionable. In order for these programs to produce accurate results about the nature of the debris cloud created by such an impact, they need a great deal of accurate input information – information which is not available for collision events. The physics of the so-called low velocity impacts that occur in GEO are very different. Here, the most likely maximum impact speed is around 800 m/s [21, 71-73], although impact speeds of up to around 3 km/s are possible between GEO objects and objects in GTO intersecting the geostationary ring [73]. These speeds are far less than the speed of sound in the material (usually taken as the speed of sound in aluminium, which is approximately 5 km/s [12, 27, 69]). Nevertheless, the physics of the impact event is very complicated and requires too many inputs to be accurately modelled from a theoretical standpoint.

Explosion events are also difficult to model from a theoretical standpoint. Not enough is known about the source or nature of the explosion to be able to model it accurately.

Explosion sources can be due to battery malfunction or the ignition of residual hypergolic propellant in the propellant tanks. The characteristics and consequences of an explosion also depends upon the position of the explosion source within the spacecraft, the intensity of the explosion, as well as the spacecraft structure itself.

The explosion and collision breakup models used in debris models thus use simple, empirically-derived equations that require few inputs [74-76].

Four of the leading breakup models, IDES, SDM, MASTER and EVOLVE 4.0, were compared in terms of their distributions of the cumulative number of fragments, fragment delta-v's and mass-to-area ratios with respect to fragment mass. These comparisons were made for a number of fragmentation scenarios including high and low intensity explosions, catastrophic and non-catastrophic hypervelocity collisions and low-speed collisions. It has been found that the IDES, SDM and MASTER models are generally in fairly good agreement for all these distributions in all scenarios, although there are slight differences to be found in certain cases. The EVOLVE 4.0 model produces generally different results for all scenarios, most notably in its delta-v and mass-to-area distributions. The major differences between all the models, in terms of the equations that characterise them, are discussed in this section. An example scenario of a low-intensity explosion in GEO was chosen and the resulting debris cloud for all models was propagated using the same high-fidelity orbital propagator. The distributions defining the propagated clouds for each model were compared. Generally, the properties of the debris clouds produced by the IDES, SDM and MASTER models were in fairly good agreement for most scenarios, whilst the properties of the debris clouds produced by the EVOLVE 4.0 model were significantly different in all cases.

The primary objective of this work is to implement four of the leading breakup models in order to facilitate the development of a fast cloud propagator that will be robust and portable for use with all four models. In doing so, the properties of the debris clouds produced by each model will be investigated and compared with those produced by the other models. The main differences in these properties will be described and explained in

terms of the defining equations and parameters used in each breakup model. The work in this chapter represents an extension of the work presented at the 52nd International Astronautical Congress in Toulouse, France in October 2001 [1]. The main additional work undertaken here is the analysis of the differences between the models at producing low-speed impact induced fragmentations, the type of collision scenario likely to be experienced by objects in GEO.

There are over 120 equations that define the properties of the debris clouds produced by the aforementioned breakup models. In the interests of producing a concise thesis, these equations will not be reproduced here. However, the interested reader will find them readily available in the relevant literature for each breakup model (IDES [12], SDM [44-46], MASTER [51, 52], EVOLVE [39, 40]).

4.1 Introduction

The majority of space debris environment models use isotropic breakup models to generate fragments that are then propagated to determine the future debris population. These breakup models rely on empirically derived equations in order to generate fragments and to determine the fragments' initial conditions, including their mass, size, delta-v and mass-to-area ratios. However, ground based experiments have yielded a variety of data such that a range of best-fit curves have been generated, depending on the experiment that was undertaken. This in turn has led to the generation of a number of different sets of equations, with a corresponding diverse range of values assigned to their defining parameters. This problem has been exacerbated because the experimental data are limited in terms of relative impact speed, fragment mass, size, delta-v and mass-to-area ratios, and yet many models extrapolate the results beyond these limits, especially in terms of delta-v [77]. In what follows, the results from various debris environment models are routinely compared and it is likely that many of the differences may be directly related to the different defining parameters and equations used in the breakup

model [78]. Thus, it is essential to assess the effects the defining equations have on a debris cloud's properties and evolution.

The purpose of this section is not to determine those breakup equations and parameters that most closely resemble the actual empirical data set, but to assess the sensitivity of the debris cloud properties to the different models used to generate the cloud. The breakup models of IDES, SDM, MASTER and EVOLVE 4.0 were compared in terms of their distributions of the cumulative number of fragments, fragment delta-v's and mass-to-area ratios with respect to fragment mass. Various breakup scenarios were examined, including high-intensity explosions (HIX), low-intensity explosions (LIX), catastrophic and non-catastrophic hypervelocity collisions and low-speed collisions. An example scenario of a low intensity explosion was generated in a geostationary reference orbit, and the fragments generated by each of the four models were then propagated using the same high-fidelity orbital propagator each time. The cloud fragments generated by each model were propagated over a period of 100 years and the resulting debris clouds were compared. The comparison of snapshots of the debris clouds' spatial distribution, after a propagation time of 100 years, was not helpful, as in all cases the debris cloud dispersed into a toroid around the Earth and any differences in the clouds were not immediately obvious. Thus the debris clouds generated by each model were compared in this instance in terms of their Gabbard diagrams, *e*-plots (eccentricity vs. orbital period plots), and *i*-plots (inclination vs. orbital period plots).

4.2 Model Structure

Each of the four breakup models (IDES, SDM, MASTER and EVOLVE 4.0) is broken down into its constituent parts comprising the generation of the cumulative number of fragments, delta-v's and mass-to-area ratios per fragment mass bin (per fragment diameter bin in the case of EVOLVE 4.0). This provides three main functions for each breakup model, which are called from a main breakup calling function as and when required, thus providing a modular, hierarchical structure to the code. Fragment mass

allocation (diameter allocation in the case of EVOLVE 4.0) is then performed by the main program in order to maintain consistency across all four models. Thus the only difference between the various results generated was solely due to the equations inherent to the breakup model being run, and was in no way related to any portion of the breakup-calling function.

The main breakup model is capable of running in two modes. The first mode generates just enough data in order to accurately plot the breakup trends, such as the cumulative number of fragments vs. mass, delta-v vs. mass and area-to-mass ratios vs. mass for each of the four breakup models. The second mode generates each fragment and allocates mass, diameter, mass-to-area ratio, delta-v and delta-v directions in terms of azimuth and elevation to each individual fragment. This mode can prove to be extremely computationally intensive in terms of its memory requirements, and thus the time taken to complete the simulation, depending on the number of fragments generated, which is a function of the user-specified minimum fragment mass or diameter chosen.

When the program is run in its second mode and individual fragments have been generated, each fragment is propagated individually by the DAMAGE orbital propagator. The propagator used in DAMAGE includes the effects of the gravitational perturbations of the major Earth aspherical harmonics comprising J_2, J_3, J_{22}, J_{31}, J_{33} as well as luni-solar gravitational perturbations and SRP perturbations.

Different types of randomising spreading functions are applied to many of the distributions calculated by each model. These spreading functions are used to spread the data randomly about a given mode value according to some distribution, where the initial mode value is calculated from the relevant cumulative number of fragments, delta-v or mass-to-area ratio versus fragment mass curve (examples of which are depicted in Figures 4.3 – 4.17). The randomising spreading functions for each model are summarised in Table 4.1.

	CN	ΔV	M/A
IDES	None	Triangular	Log-normal
SDM	None	Triangular	Log-normal
MASTER	None	Triangular	Log-normal
EVOLVE	None	Normal	Normal

Table 4.1 Summary of the randomising functions applied to the distributions calculated by each breakup model.

'Triangular' refers to a commonly used triangular spreading function [45, 51, 52]. 'Normal' refers to a normal distribution and 'log-normal' refers to a log-normal distribution where the means and standard deviations vary for each and are calculated by the model. 'CN' refers to the cumulative number of fragments vs. mass distribution, 'ΔV' refers to the delta-v vs. mass distribution and 'M/A' refers to the mass-to-area ratio vs. mass distribution.

It should be noted that there are two other sources of randomisation in the model. Firstly, there is the allocation of azimuth and elevation to each fragment, which define the fragment's delta-v direction. These are randomly distributed such that on average the ejection directions are spread uniformly around a unit sphere in order to emulate an isotropic breakup. Secondly, there is the aforementioned fragment mass allocation (or fragment diameter allocation in the case of EVOLVE 4.0), which randomly allocates the masses (or diameters) to each fragment within each mass (or diameter) bin. These randomisations have no effect on the breakup plots presented in this paper however; they only affect the Gabbard diagrams.

4.3 Running the Model

For the first set of results, giving a comparison of the breakup plots of each model, the program was run in its first mode and the minimum fragment mass chosen was around 10^{-6} kg. For the second set of results, where the fragments were individually propagated,

the program was run in its second mode, but due to computational constraints the minimum fragment mass chosen for this run was 10^{-2} kg.

It was decided to turn the delta-v and mass-to-area ratio randomisations off for each model in the simulation in order to achieve an average or peak value for the distributions. This provides a more meaningful comparison.

Normally, IDES, SDM and MASTER calculate a mean or peak value for the delta-v vs. mass distribution and mass-to-area vs. mass distribution, which are then randomised according to the summary in Table 4.1. Turning off the randomisation simply means using these peak values. In EVOLVE 4.0, where normal distributions form an inherent part of the equations for delta-v and mass-to-area relationships, the randomisation was eliminated by replacing the normal distribution with the mean of the distribution in all appropriate equations.

The threshold between a catastrophic collision (where the entire target object is destroyed) and a non-catastrophic collision (where it is not) is based upon the specific energy delivered to the target by the projectile. Specific energy is defined as the ratio of impactor kinetic energy to target mass. This threshold value has been empirically derived to be 40 J/g [79] (or 45 J/g in the case of SDM [44, 80]).

EVOLVE 4.0 and IDES include Hanada's low velocity collision model [71, 72] in order to model collisions at speeds less than the speed of sound in the material. This model is primarily used to describe collision-induced breakups in geosynchronous orbits. IDES and EVOLVE use the Hanada low-speed impact equations for energy-to-mass ratios below 40 J/g and impact speeds of less than 5 km/sec (the speed of sound in aluminium, the material predominantly used in spacecraft construction). Hanada's equations were empirically derived from laboratory impact tests conducted at speeds of 150 m/s, however they are now used for all low-speed impact induced fragmentations, and are triggered for any collision-induced fragmentation in the GEO regime.

4.4 Model Validation

The in-house versions of each breakup model described herein were validated using the original versions of each model (from data provided by Walker, Wegener, Krisko and Rossi), using the breakup plots for each scenario as a basis for comparison.

4.5 Mass Conservation

The four models discussed herein purport to conserve mass through the coefficients of the mass distribution equations. In the in-house versions of these models, however, this cannot always be accurately achieved by the careful choice of coefficients alone, since the fragments are randomly allocated masses within each mass bin (the binning of the fragments into each mass bin is done according to the mass distribution equations). Thus a fixed coefficient cannot be relied upon to conserve the mass of fragments that have been randomly generated. The scatter plots in Figures 4.1 and 4.2 illustrate the total mass of the fragments generated compared to the required breakup mass for a number of runs of each of the four models for an example scenario of a low-speed collision (defined here by a 1 kg projectile impacting a 1500 kg target object with a speed of 800 m/s). The required breakup mass is defined as the total ejecta mass calculated by the breakup model being used.

The required breakup mass differs greatly for the MASTER/SDM breakup models (shown in Figure 4.1) and the IDES/EVOLVE breakup models (shown in Figure 4.2) because the IDES and EVOLVE breakup models use Hanada's low velocity collision equations to predict the required breakup mass, whereas the MASTER and SDM models use the normal non-catastrophic breakup equations.

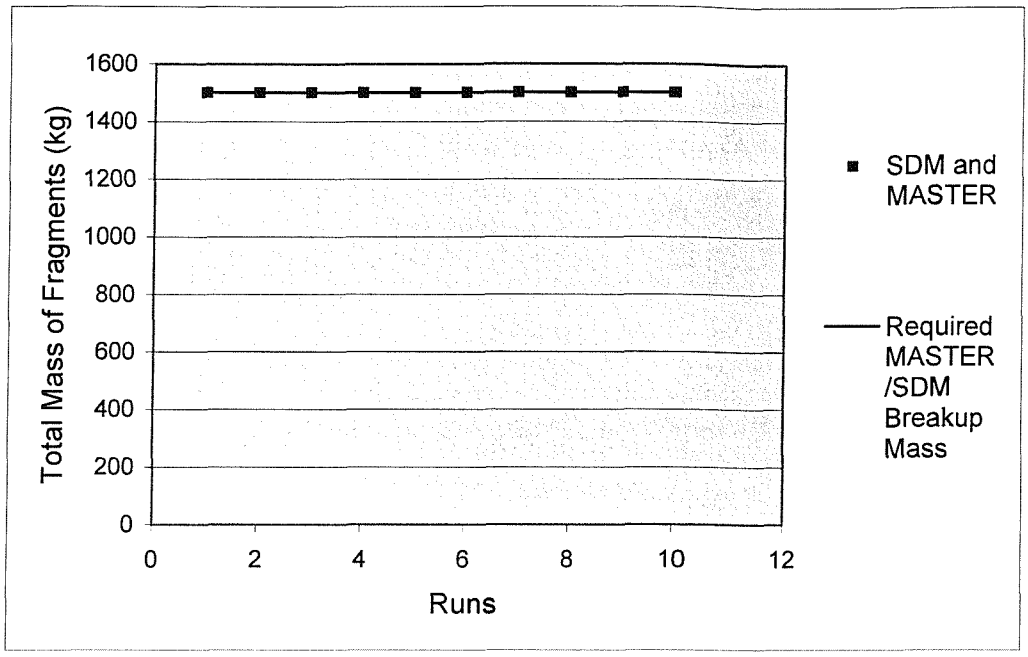

Figure 4.1 Scatter plots showing the MASTER and SDM cloud masses compared to the required breakup mass

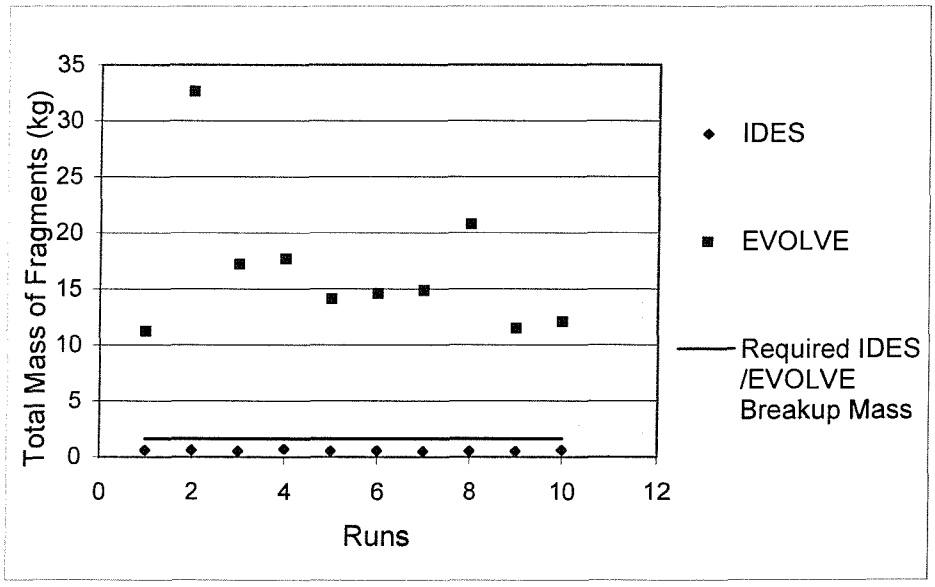

Figure 4.2: Scatter plots showing the IDES and EVOLVE cloud masses compared to the required breakup mass

As can be seen, there is a large variation in the total masses of all the fragments generated by the IDES and EVOLVE 4.0 models and mass is never actually conserved. The SDM and MASTER models perform rather well at conserving mass by contrast. Thus in order

to conserve mass, a dynamic mass conservation routine has been implemented which adds up the fragment masses and divides this by the required breakup mass to produce a scaling factor. The mass of each fragment is then divided by this scaling factor and consequently the total mass of the cloud after the breakup event becomes equal to the total ejecta mass. It should be noted that IDES and EVOLVE may only fail to conserve mass for the example illustrated. A detailed analysis of the mass conservation capability of each of the four models for each scenario has not been undertaken. However, the fact that mass is not conserved in this example scenario is enough to warrant the implementation of a dynamic mass conservation routine as a fail-safe precaution.

4.6 Results

It should be noted that all the following breakup plots (with the exception of the Gabbard diagrams, *e*-plots and *i*-plots) have $\log_{10}$ axes. For the sake of clarity only the indices are shown on the axes of these graphs.

4.6.1 Comparison of Breakup Plots

All the breakup plots presented in this section were for a target with a mass of 1500 kg.

4.6.1.1 Explosions

Figures 4.3, 4.5 and 4.7 show the models' results for the low-intensity explosion (LIX) event and Figures 4.4, 4.6 and 4.8 show the models' results for a high-intensity explosion (HIX) event.

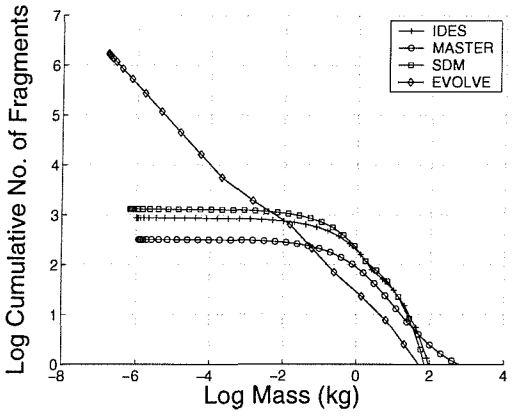

Figure 4.3 Comparison of the cumulative number of fragments vs. fragment mass for a LIX event

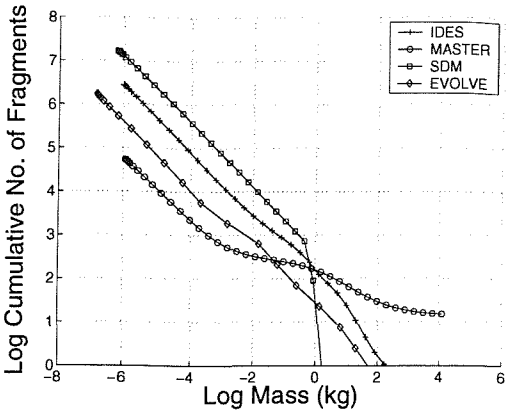

Figure 4.4 Comparison of cumulative number of fragments vs. fragment mass for a HIX event

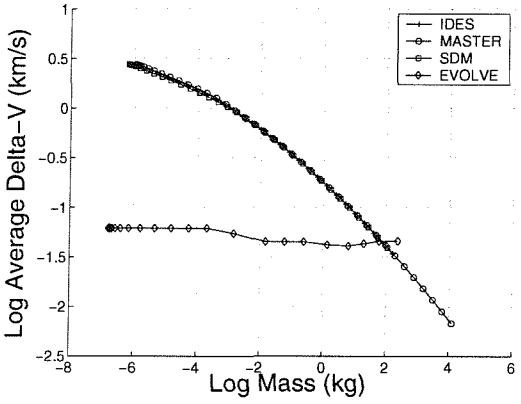

Figure 4.5 Comparison of fragment delta-v's vs. fragment mass for a LIX event

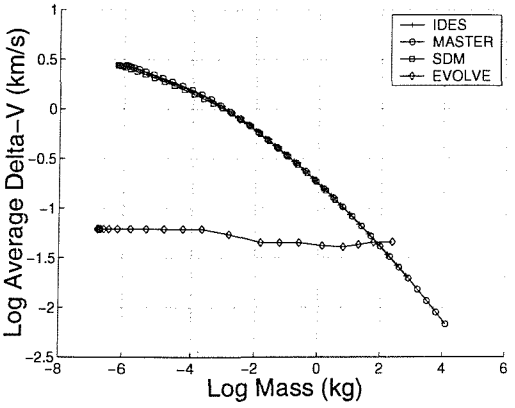

Figure 4.6 Comparison of fragment delta-v's vs. fragment mass for a HIX event

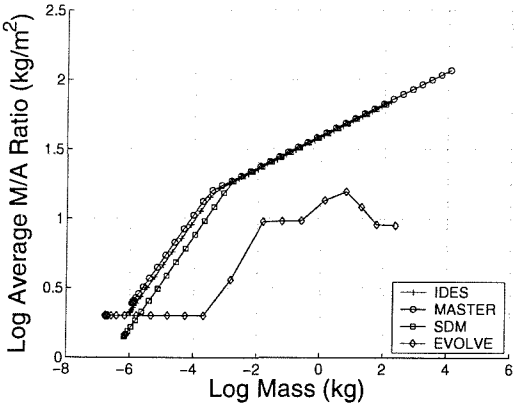

Figure 4.7 Comparison of mass-to-area ratios vs. fragment mass for a LIX event

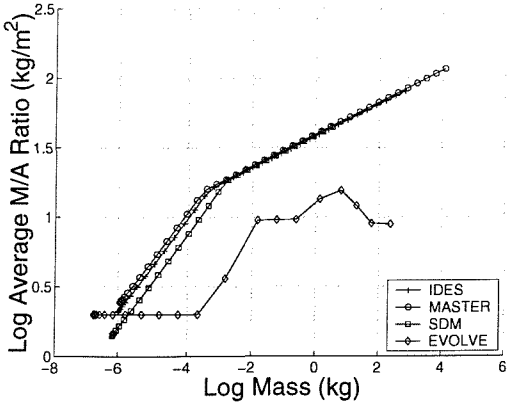

Figure 4.8 Comparison of fragment mass-to-area ratios vs. fragment mass for a HIX event

4.6.1.2 Collisions

Figures 4.9, 4.11 and 4.13 show the models' results for the catastrophic collision event induced by a projectile with a mass of 10 kg, whilst Figures 4.10, 4.12 and 4.14 show the models' results for a non-catastrophic collision event induced by a projectile with a mass of 1 kg. For both catastrophic and non-catastrophic collisions, the speed of the projectile was maintained at 10 km/sec.

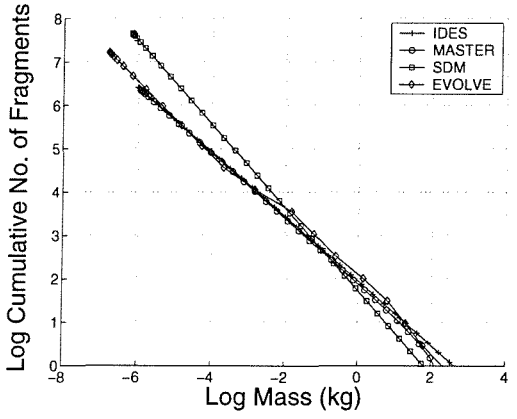

Figure 4.9 Comparison of the cumulative number of fragments vs. fragment mass for a catastrophic collision

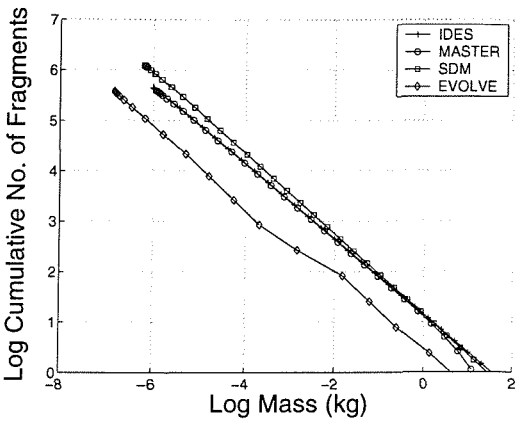

Figure 4.10 Comparison of cumulative number of fragments vs. fragment mass for a non-catastrophic collision

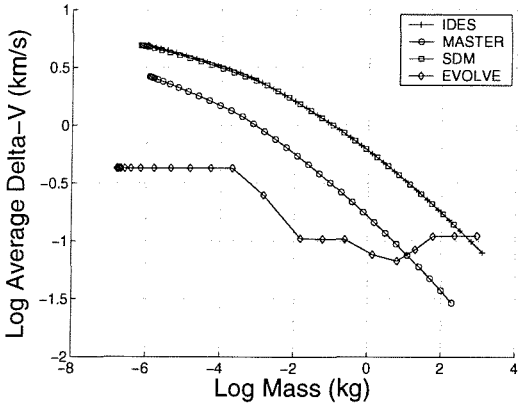

Figure 4.11 Comparison of fragment delta-v's vs. fragment mass for a catastrophic collision

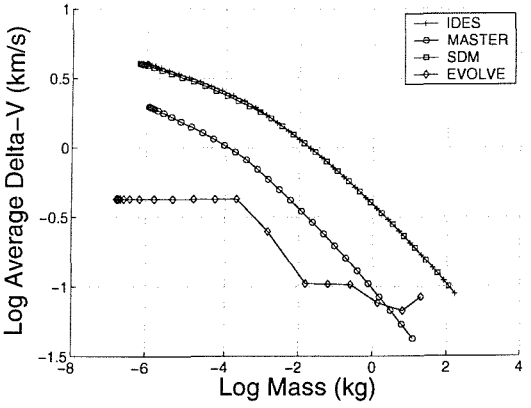

Figure 4.12 Comparison of fragment delta-v's vs. fragment mass for a non-catastrophic collision

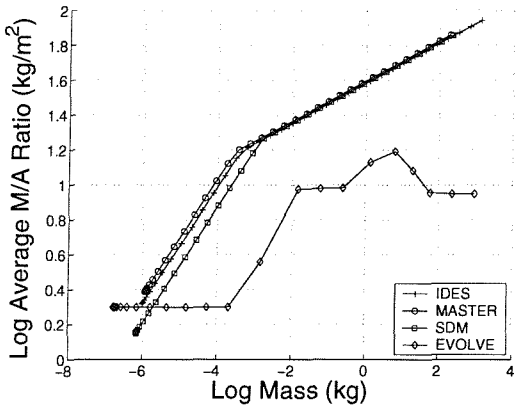

Figure 4.13 Comparison of fragment mass-to-area ratios vs. fragment mass for a catastrophic collision

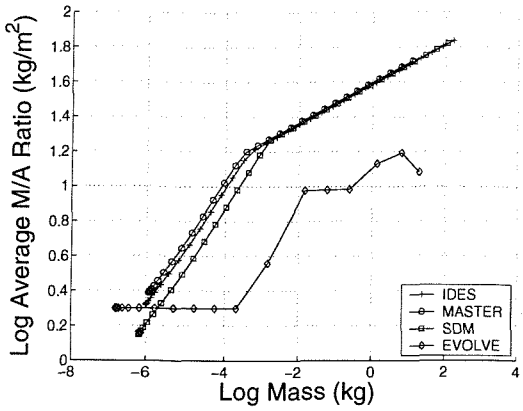

Figure 4.14 Comparison of fragment mass-to-area ratios vs. fragment mass for a non-catastrophic collision

Figures 4.15, 4.16 and 4.17 show the models' results for a low-speed collision event induced by a projectile with a mass of 1 kg and impact speed of 800 m/s.

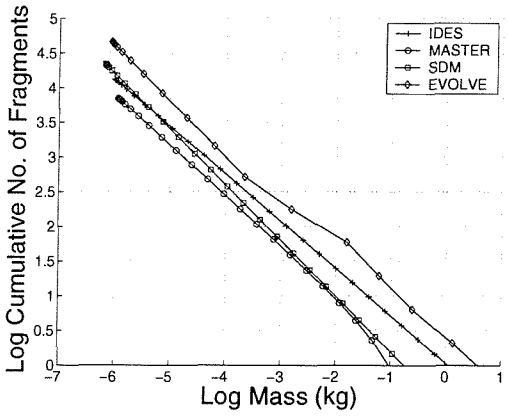

Figure 4.15 Comparison of the cumulative number of fragments vs. fragment mass for a low-speed collision

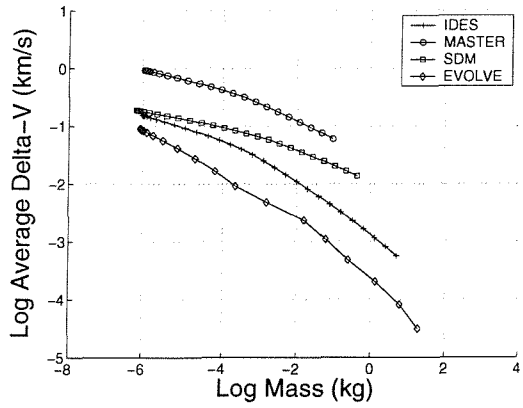

Figure 4.16 Comparison of fragment delta-v's vs. fragment mass for a low-speed collision

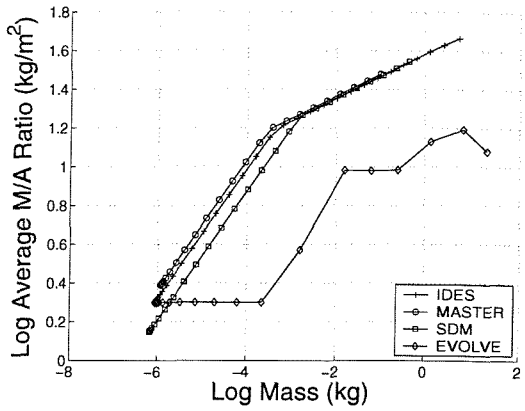

Figure 4.17 Comparison of fragment mass-to-area ratios vs. fragment mass for a low-speed collision

4.6.2 Comparison of Propagated Debris Clouds

The Gabbard diagrams, *e*-plots and *i*-plots for the LIX event are illustrated in Figures 4.18 through 4.25, Figures 4.26 through 4.33 and in Figures 4.34 through 4.41, respectively. The breakup orbit used in this analysis was a geostationary orbit and the fragments were propagated under the effects of all the geopotential and luni-solar gravitational perturbations listed in Chapter 3.

Breakup Epoch

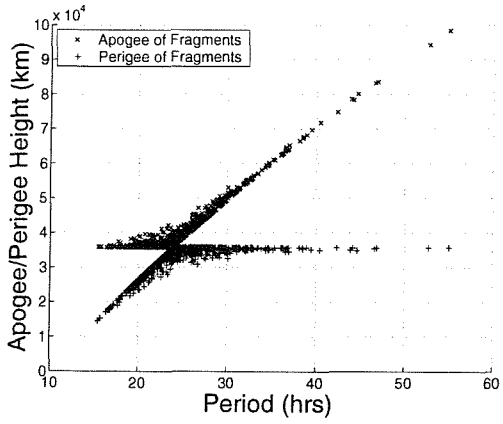

Figure 4.18 Gabbard diagram of the LIX breakup modelled by IDES

Breakup Epoch + 100 years

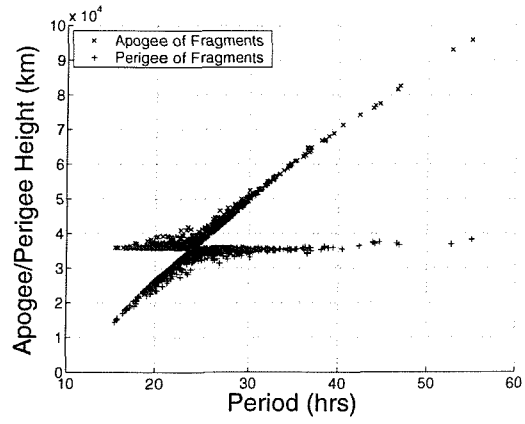

Figure 4.19 Gabbard diagram of the LIX breakup modelled by IDES after 100 years

Breakup Epoch ***Breakup Epoch + 100 years***

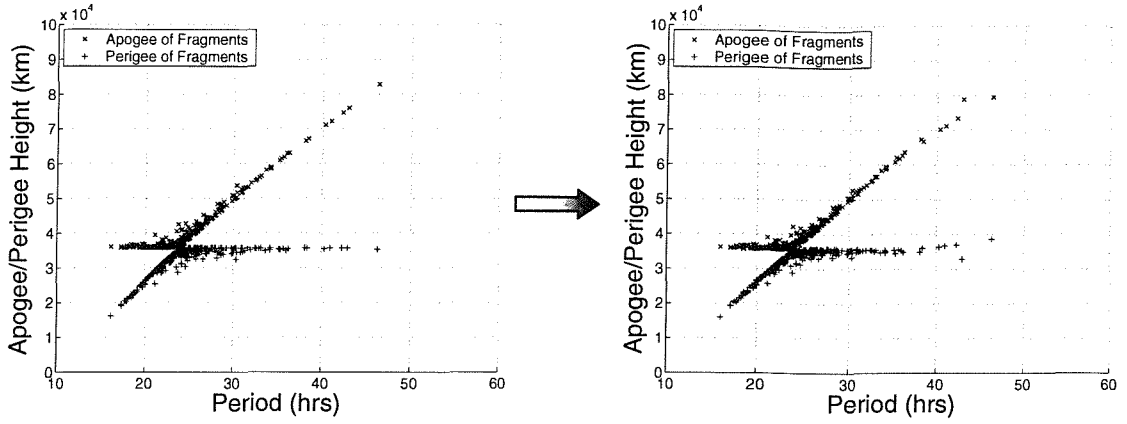

Figure 4.20 Gabbard diagram of the LIX breakup modelled by MASTER

Figure 4.21 Gabbard diagram of the LIX breakup modelled by MASTER after 100 years

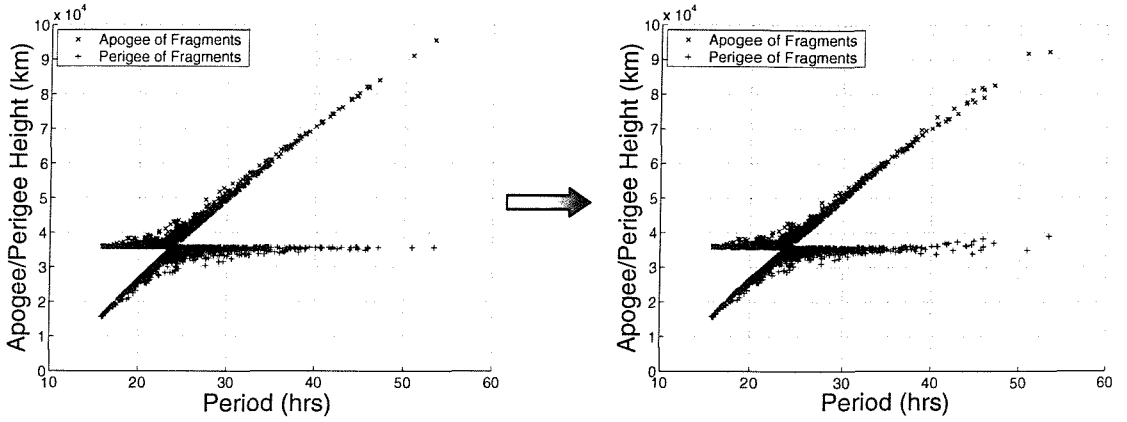

Figure 4.22 Gabbard diagram of the LIX breakup modelled by SDM

Figure 4.23 Gabbard diagram of the LIX breakup modelled by SDM after 100 years

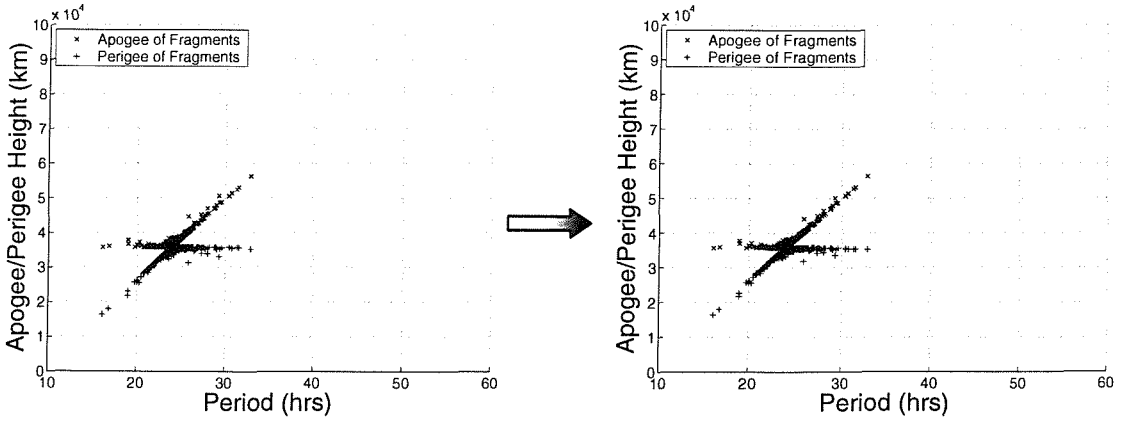

Figure 4.24 Gabbard diagram of the LIX breakup modelled by EVOLVE 4.0

Figure 4.25 Gabbard diagram of the LIX breakup modelled by EVOLVE 4.0 after 100 years

Breakup Epoch ***Breakup Epoch + 100 years***

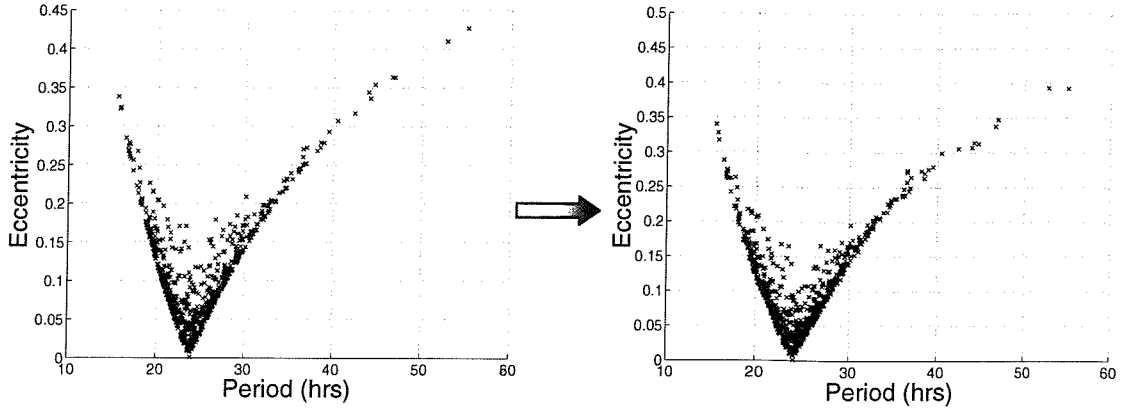

Figure 4.26 *e*-plot of the LIX breakup modelled by IDES

Figure 4.27 *e*-plot of the LIX breakup modelled by IDES after being propagated for 100 years

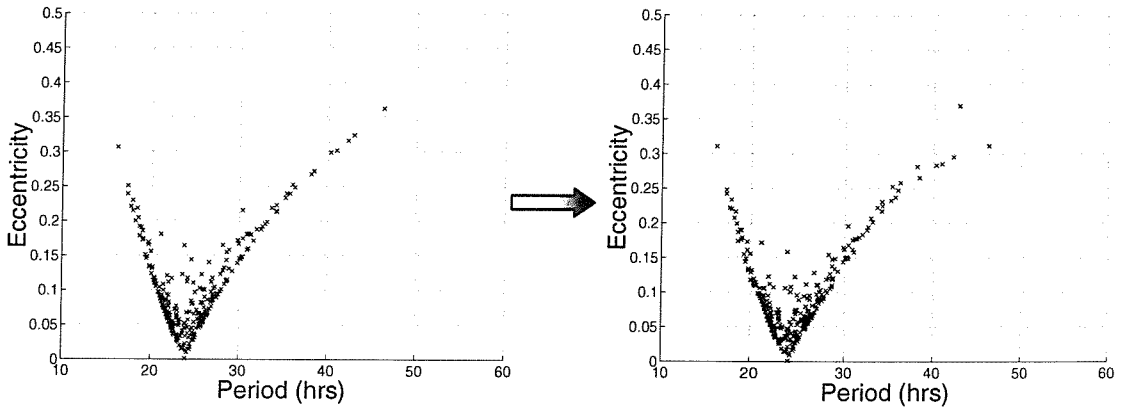

Figure 4.28 *e*-plot of the LIX breakup modelled by MASTER

Figure 4.29 *e*-plot of the LIX breakup modelled by MASTER after being propagated for 100 years

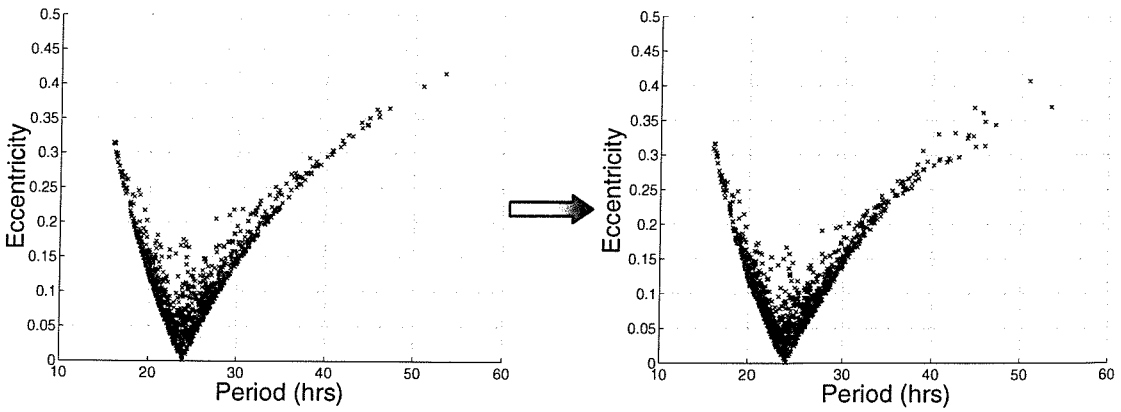

Figure 4.30 *e*-plot of the LIX breakup modelled by SDM

Figure 4.31 *e*-plot of the LIX breakup modelled by SDM after being propagated for 100 years

Breakup Epoch ***Breakup Epoch + 100 years***

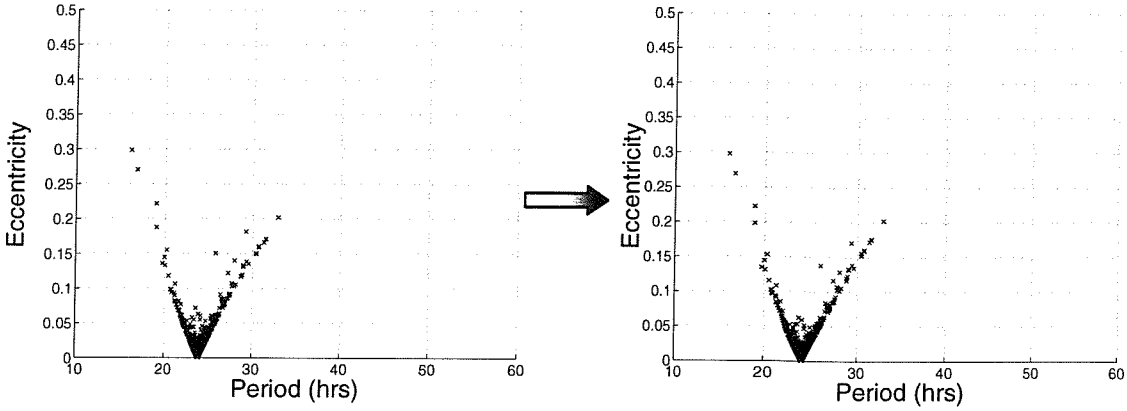

Figure 4.32 *e*-plot of the LIX breakup modelled by EVOLVE 4.0

Figure 4.33 *e*-plot of the LIX breakup modelled by EVOVE 4.0 after being propagated for 100 years

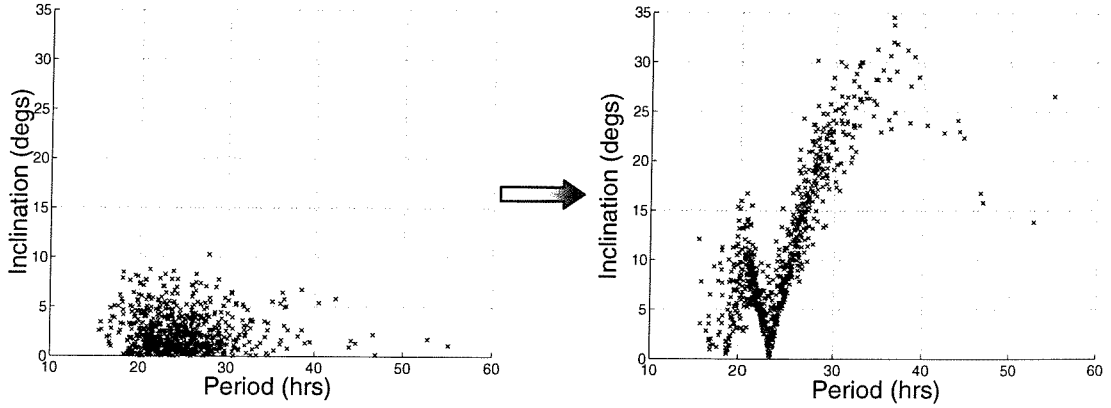

Figure 4.34 *i*-plot of the LIX breakup modelled by IDES

Figure 4.35 *i*-plot of the LIX breakup modelled by IDES after being propagated for 100 years

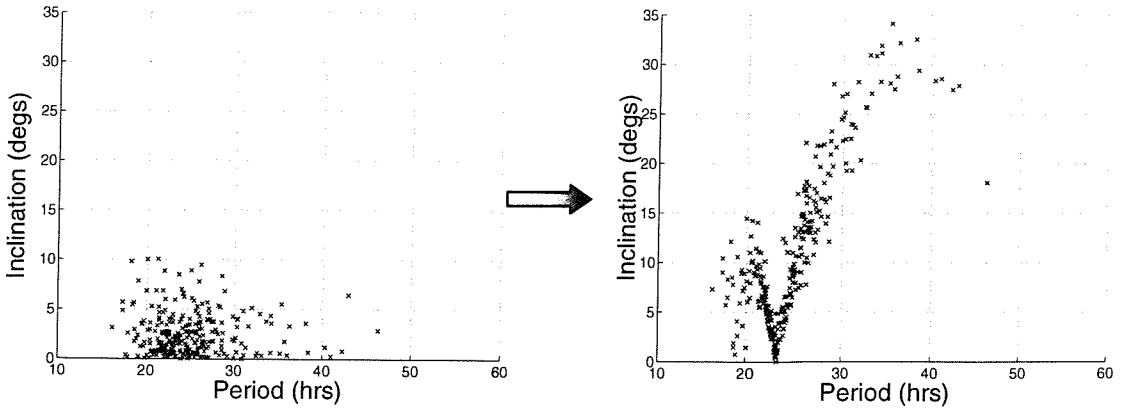

Figure 4.36 *i*-plot of the LIX breakup modelled by MASTER

Figure 4.37 *i*-plot of the LIX breakup modelled by MASTER after being propagated for 100 years

Breakup Epoch ***Breakup Epoch + 100 years***

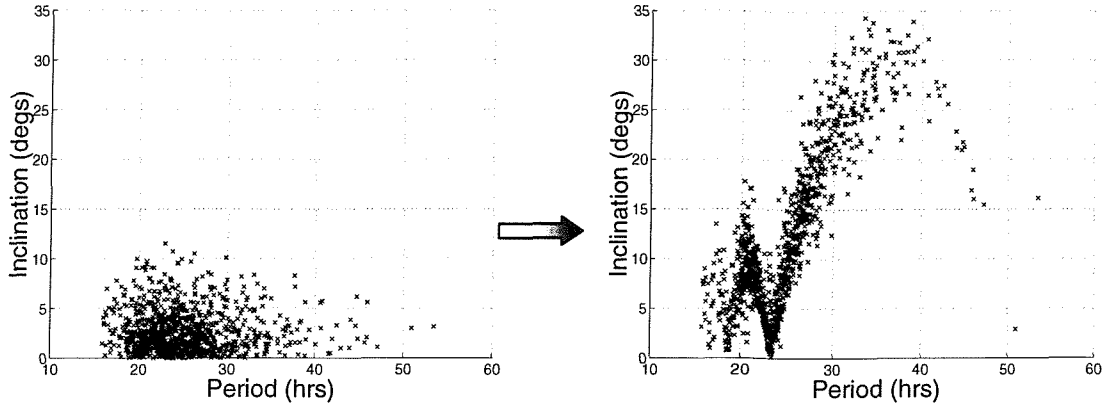

Figure 4.38 *i*-plot of the LIX breakup modelled by SDM

Figure 4.39 *i*-plot of the LIX breakup modelled by SDM after being propagated for 100 years

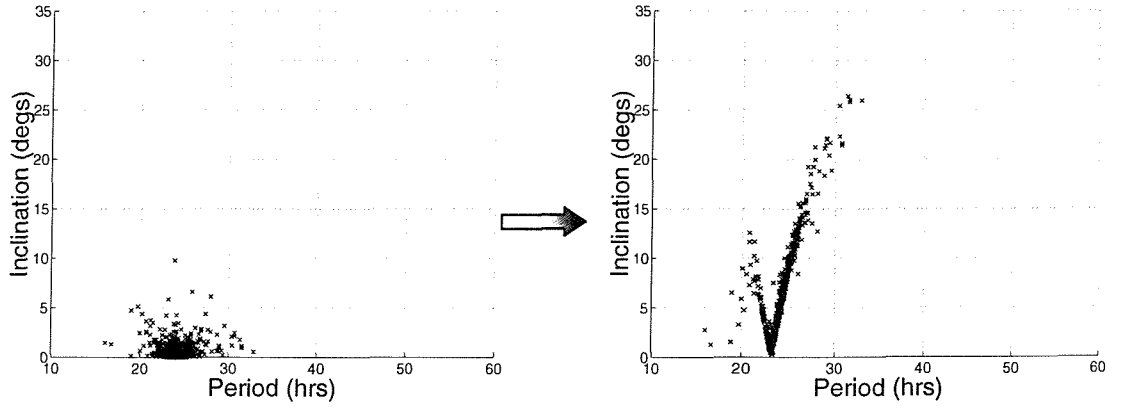

Figure 4.40 *i*-plot of the LIX breakup modelled by EVOLVE 4.0

Figure 4.41 *i*-plot of the LIX breakup modelled by EVOLVE 4.0 after being propagated for 100 years

4.6.3 Comparison of Breakup Plots

4.6.3.1 Comparison of Mass Distributions

IDES, SDM and MASTER exhibit different mass distributions (cumulative number of fragments vs. mass) for all five scenarios, whereas EVOLVE 4.0 exhibits the same cumulative number vs. mass curve for both high and low intensity explosions, but different curves for catastrophic, non-catastrophic and low-speed collisions. SDM predicts the highest number of total fragments in all cases with the exception of low-

speed collisions (Figure 4.15) and low-intensity explosions (Figure 4.3), where EVOLVE 4.0's power law curve ensures that it predicts a higher number of total fragments by around three orders of magnitude. This is because EVOLVE 4.0 assumes the same mass distribution for high and low intensity explosions and thus there is no levelling off of the cumulative number of fragments below around 1 kg in the case of low-intensity explosions, as there is with the IDES, SDM and MASTER breakup models. In all cases MASTER predicts the lowest number of total fragments, except for non-catastrophic hypervelocity collisions, where EVOLVE predicts the lowest number of fragments.

All models generally show the same trends, with the exception of EVOLVE 4.0, which uses a simple power law to predict the cumulative number of fragments for a low-intensity explosion across the whole mass range, and SDM, which predicts a sharp drop in the cumulative number of fragments at masses approaching 1 kg for a high-intensity explosion.

All models distinguish between catastrophic and non-catastrophic collisions by using different sets of equations to recreate the mass distribution of fragments with the exception of the MASTER model. The IDES, SDM and EVOLVE models use the catastrophic collision equations if the energy imparted to the target object is greater than 40 J/g and use non-catastrophic equations if the energy-to-mass ratio is below this threshold value. The SDM and MASTER models use the same set of equations to simulate the mass distribution for a low-speed collision induced scenario as they do for a non-catastrophic collision scenario, whereas the IDES and EVOLVE models further distinguish between these scenarios by using yet another set of equations for low-speed collision induced fragmentations. IDES and EVOLVE use the Hanada low-speed impact equations for energy-to-mass ratios below 40 J/g and impact speeds of less than 5 km/sec. For low-speed impacts EVOLVE predicts the largest number of fragments for a given mass value, whereas for non-catastrophic collisions it predicts the lowest.

It should be noted that the mass distribution curve for MASTER for a low-intensity explosion becomes asymptotic at high mass values and thus the curve never actually

reaches zero cumulative number of fragments. This trend can partly be seen in Figure 4.3 above 10^2 kg. This is due to the fact that the author had to make assumptions about two of the constants used in the MASTER LIX mass distribution model, namely the explosion intensity and the total number of objects. These constants are normally calculated as a function of the number of fragments actually observed following an on-orbit low-intensity explosion. This works well for MASTER, which simulates historical fragmentation events, but an assumption needs to be made when attempting to use this model for predicting future LIX events. The constants in this case were assumed to be equal to the constants calculated from a previous low-intensity explosion of a 1500 kg spacecraft. The MASTER LIX cumulative number of fragments vs. mass distribution curve above 10^2 kg should thus be treated with some caution. It is unlikely that this curve becomes asymptotic for actual historical LIX events modelled by MASTER.

4.6.3.2 Comparison of Delta-V Distributions

The delta-v vs. mass curves are identical for HIX and LIX scenarios for each of the four models. This is due to the fact that none of the models distinguish between these two types of explosions as far as the delta-v equations are concerned. For both LIX and HIX scenarios, the IDES, SDM and MASTER models are in almost perfect agreement across the entire mass range. EVOLVE 4.0 shows a significantly different relationship with only a slight reduction in delta-v with increasing mass.

The EVOLVE 4.0 delta-v curves for catastrophic and non-catastrophic collisions are identical. The delta-v curves for the other three models are very similar to each other for catastrophic and non-catastrophic collisions. None of the models distinguish between these two types of collisions as far as their delta-v equations are concerned. However, the IDES, SDM and MASTER models all predict a slightly lower delta-v across the entire mass range for non-catastrophic collisions compared to catastrophic collisions. This is because the delta-v values for these three models are calculated as a function of the projectile energy, which in turn is a function of the projectile mass, which has been set an

order of magnitude lower for the non-catastrophic collision scenario compared to the catastrophic collision scenario.

The IDES and SDM models for both these collision scenarios are in perfect agreement across most of the mass spectrum. MASTER shows a similar trend but predicts slightly lower delta-v's across the entire mass range. This is due to a difference in the constant used to calculate the debris threshold diameter, which in turn is used in the delta-v equations. The debris threshold diameter function used in IDES, SDM and MASTER is given by

$$d_m = \frac{\sqrt[3]{E_p}}{c}, \tag{4.1}$$

where d_m is the threshold debris diameter, E_p is the projectile energy and c is the constant, which varies according to the model being run.

IDES and SDM share the same value for c, which renders their curves identical above the threshold debris diameter, and very similar, albeit not identical, below this threshold value. MASTER, however, uses a significantly different value, which accounts for the differences between the results. If the IDES/SDM constant is used in place of the MASTER constant then the MASTER model also generates the same delta-v vs. mass curve as IDES across the entire mass spectrum for both collision scenarios. This is because IDES and MASTER share the same delta-v equations. SDM also shares the same equation but only above the threshold debris diameter. EVOLVE 4.0, again, predicts a shallower, more disjointed curve.

IDES and EVOLVE again use Hanada's equations for modelling the delta-v's imparted to fragments following a low-speed impact induced fragmentation, whereas SDM and MASTER use their non-catastrophic collision equations. This results in the SDM and MASTER models predicting noticeably higher delta-v values for a given fragment mass than the IDES and EVOLVE models. In this scenario, the MASTER model predicts the

highest delta-v's, followed by the SDM model, then the IDES model and the EVOLVE model predicts the lowest delta-v values.

If IDES and EVOLVE both employ the Hanada mass distribution (cumulative number of fragments vs. mass distribution) and velocity distribution equations then one might ask why the mass and velocity distribution curves for these two models are different? This is because the Hanada mass distribution equations for IDES are calculated as a function of fragment mass, whereas in EVOLVE they are modified, using SOCIT (Satellite Orbital Debris Characterisation Impact Test) data, to calculate the mass distribution as a function of fragment diameter. The different mass-to-area equations (and thus mass-to-diameter equations) used by IDES and EVOLVE (see Figure 4.17) thus ensures that they will give very different mass distribution curves. Similarly, the velocity distributions for both models are calculated as a function of fragment diameter. Thus, for a particular input mass the different mass-to-diameter equations employed by the two models cause different velocity profiles to be generated, even when the same delta-v distribution equations are used.

4.6.3.3 Comparison of Mass-to-Area Distributions

The mass-to-area ratios as a function of fragment mass are identical for LIX, HIX, catastrophic and non-catastrophic collision scenarios for each model as illustrated in Figures 4.7, 4.8, 4.13, 4.14 and 4.17. None of the models make any distinction between the different scenarios when calculating mass-to-area vs. mass relationships.

The IDES, SDM and MASTER curves are in perfect agreement above fragment masses of around 10^{-3} kg, although they differ slightly in their prediction of mass-to-area ratios below this mass value. EVOLVE 4.0 again gives a significantly different distribution with a generally shallower curve.

4.6.4 General Comparison of the Different Models

Many of the models distinguish between the different scenarios for the various distributions; for example, all the models distinguish between high and low intensity explosions as far as their mass distributions are concerned, with the exception of EVOLVE 4.0, which uses the same mass distribution for both. These distinctions for each of the four models are summarised in Table 4.2, where LIX and HIX refer to low-intensity and high-intensity explosion scenarios respectively and 'CN', 'ΔV' and 'M/A' refer to the cumulative number vs. mass, delta-v vs. mass and mass-to-area ratio vs. mass distributions respectively.

Note that Table 4.2 not only compares the different equations that each model uses for the different scenarios, but also compares the different equations that the models use with respect to one another. The same subscript after the distribution indicates that the same equations or sets of equations have been used. For instance, it can be seen from Table 4.2 that IDES and SDM share the same delta-v distribution for both explosion scenarios. This does not necessarily imply that the curves produced by the same equations will be the same however – although the equations may be identical, the inputs to the equations may be different. This is illustrated in the case of the delta-v distributions for IDES and MASTER for both catastrophic and non-catastrophic collision scenarios. The equations used are identical but due to the aforementioned difference in one of the constants used, the curves are different. The use of identical equations does give rise to identical trends however.

	LIX	HIX	Catastrophic Collision	Non-catastrophic Collision	Low-speed Collision
IDES	CN_1	CN_2	CN_3	CN_4	CN_5
	ΔV_1		ΔV_2		ΔV_3
	M/A_1				
SDM	CN_6	CN_7	CN_8	CN_9	
	ΔV_1		ΔV_4		
	M/A_2				
MASTER	CN_{10}	CN_{11}	CN_{12}		
	ΔV_5		ΔV_2		
	M/A_3				
EVOLVE	CN_{13}		CN_{14}	CN_{15}	CN_{16}
	ΔV_6		ΔV_7		ΔV_8
	M/A_4				

Table 4.2: A Summary of the distinction between the different sets of equations used by each model for the different scenarios. The subscripts distinguish between the different sets of equations used.

All the distributions for all the scenarios for the IDES, SDM and MASTER models are fairly smooth and only occasionally show sharp deviations at the transition point between two different sets of equations. The delta-v and mass-to-area ratio distributions for EVOLVE 4.0 however are all quite disjointed. This is due to the relatively complex set of equations used by EVOLVE 4.0 to calculate the delta-v and mass-to-area ratio distributions. The latter is split into six different regimes according to fragment diameter. The resulting six different distributions can be clearly seen in most of the mass-to-area ratio curves, as there is no smooth transition between them. The delta-v curves also clearly show six different distributions, especially in the catastrophic collision scenario. This is largely because the fragment delta-v's in EVOLVE 4.0 are calculated as a function of the fragment area-to-mass ratios.

4.6.5 Comparison of Propagated Debris Clouds

It is interesting to note how the variations in the mass, velocity and mass-to-area distributions between the different models manifest themselves into variations in the

orbital elements, not only at the breakup epoch, but also at some later date. These variations can be seen in the Gabbard diagrams, *e*-plots and *i*-plots in Figures 4.18 – 4.41.

The first thing to note is the difference in the numbers of fragments created by the 4 models. IDES, SDM and EVOLVE create roughly the same number of fragments above a threshold mass of 1 gram, but the data points in the plots produced by the MASTER model are a great deal more rarefied, due to the relatively low number of fragments produced by this model. The second difference which is immediately noticeable from all these plots is the difference in the energy levels involved. IDES, SDM and MASTER all show a fairly equal spread in the fragments' apogee and perigee heights as well as in their eccentricities and inclinations. EVOLVE, however, shows a remarkably smaller spread, with the Gabbard diagrams, *e*-plots and *i*-plots looking far smaller when reproduced on the same scale as the other models' results. This difference in the energy imparted to the fragments has already been noted from the delta-v vs. mass plots.

There has been little change to the Gabbard diagrams at the breakup epoch with respect to the diagrams 100 years later. The only noticeable change is that the maximum apogees, corresponding to the fragments' orbits with the longest periods and thus greatest semi-major axes, start to decrease over time. Similarly the orbital perigees of these same fragments start to increase due to the effects of orbital perturbations. It should also be noted that there has been little change in the periods of these fragments' orbits, which implies little change in their semi-major axes. It can thus be said that these relatively eccentric orbits are tending to become more circular as they are propagated under the influence of the aforementioned perturbations. This trend can clearly be seen in most of the Gabbard diagrams and is borne out by the decreasing eccentricities of the orbits with long periods in the *e*-plots. Apart from an increase in the scatter of the data points, this has been the only noticeable change in the Gabbard diagrams over the propagation period of 100 years. It is interesting to note that this effect is least obvious in the EVOLVE 4.0 Gabbard diagrams. The fragments generated by EVOLVE 4.0 were not ejected into orbits that were as eccentric as the orbits of the fragments generated by the other three models because EVOLVE 4.0 predicted lower delta-v's across the entire mass range. Thus the

circularising effect of orbital perturbations on the fragments' orbits with the longest periods is less noticeable. It is important to realise however that this circularising effect is an artefact of the orbit and propagation time period – a different orbit or propagation time period will yield different results.

There has also been little change in the *e*-plots over time, other than in the reduction in eccentricity for highly eccentric orbits, as mentioned above. The *i*-plots, however, have shown a considerable change over time, with distinct V-shaped plots being formed after 100 years of propagation. These relatively large changes in inclination are predominantly due to the accumulation of luni-solar gravitational effects on the orbit over this long time period. The V-plots are an artefact of the geostationary orbit – inclinations cannot take negative values and so as the inclination decreases to zero the RAAN changes by 180° and the inclination begins to increase again, forming a V-shaped plot.

Any additional differences between the models' results at the breakup epoch + 100 years (compared to the differences between the results at the breakup epoch) is thus best ascertained from the *i*-plots, since there has been little change to the Gabbard diagrams or *e*-plots over this period. The main additional differences here are due to the difference in the numbers of fragments generated and the velocity imparted to the fragments. The EVOLVE model produces a smaller distribution with a noticeably smaller spread in inclination and orbital period than the other models – it forms a distinct V-plot at the breakup epoch + 100 years. The other models form plots whose core distributions form V-plots but there are fragments trailing off either side with decreasing inclinations at high and low orbital periods. This is especially noticeable for IDES and SDM, as the additional fragments produced by these models add more weight to these trailing edges.

Finally, it should be noted that these diagrams are characteristic of the breakup scenario, the propagation time and the original breakup orbit, in this case a geostationary orbit. For instance, in a LEO orbit the Gabbard diagrams produced would look very different and the differences between the initial and propagated Gabbard diagrams would certainly be more apparent. This is because orbital perturbations, due largely to the presence of drag,

have far more of an effect in low Earth orbits than they do in higher orbits. Similarly, if the simulation had been run over a different propagation time period then it is possible that there would have been no visible circularising effect on the fragment orbits with high eccentricities – the diagrams presented here are merely a snapshot of the debris cloud after 100 years. The long periodic changes in eccentricity will manifest themselves differently in these diagrams at a different epoch. Similar results from low-speed impact induced fragmentations have trailing edges to the V-shaped *i*-plots which are far less noticeable after 100 year propagation of fragments generated by the IDES, SDM and MASTER models.

It is important to look at the effects of using different breakup models on the long-term properties of a debris cloud, as these effects will determine the nature of the predicted future debris environment. An analysis of the different outcomes of a breakup model, not only immediately after the event, but also after some considerable time, may help explain some of the major differences found in the various predictions made for the future debris environment by the different debris models.

4.7 Conclusions

The differences between the results of the breakup models in many cases are only slight, but in other cases they are quite significant. This is especially true of the NASA EVOLVE 4.0 model, which often stands apart as having noticeably different results. This is unsurprising however, as NASA have chosen to base most of their equations on fragment diameter, and in the case of the delta-v equations, on fragment area-to-mass ratios. Conversely, the other three models have based all their equations on fragment mass. This unique approach taken by NASA, as well as their relatively complicated delta-v and mass-to-area ratio calculations, is largely responsible for their different results. The new version of the EVOLVE model essentially presents a re-working of many of the more commonly accepted breakup equations, which are used by the other models and which were used in previous versions of EVOLVE. The new EVOLVE 4.0 distribution

functions are based upon additional, new breakup data, including SSN (Space Surveillance Network) data archived on the *Janus* database server, Long Range Imaging Radar (LRIR) data, or Haystack data, as it is commonly known, and ground based tests. Among these tests were the SOCIT hypervelocity impact tests, the Atlas 24D explosion test, tests conducted by NASA and Physical Sciences Incorporated for government sponsors, and ESA-sponsored explosive fragmentations of Ariane rocket body models [81].

Upon examination of the cumulative numbers of fragments, fragment delta-v and mass-to-area ratio vs. mass distributions for a range of scenarios for all four break-up models, it can generally be said that IDES, SDM and MASTER were in fairly good agreement for most scenarios, whilst the results of EVOLVE 4.0 were significantly different.

The break-up models that agree with one another for certain distributions only do so because they have used the same equations or sets of equations, which in turn are empirically derived from the same limited sets of data – thus they are not truly independent of one another. There remains a great deal of discrepancy between the models for certain distributions however, especially in the results of the EVOLVE 4.0 model. These break-up models form part of debris environment models that are used routinely to predict the nature of the future debris environment and to conduct various other studies – for example, assessing the effectiveness of various mitigation measures. The question must be asked – how much confidence can one have in the results of these studies when there is such a variation and large degree of uncertainty in the underlying break-up models used to generate the results upon which they are based? These uncertainties clearly demand immediate attention if any confidence is to be placed in the results of debris models.

It cannot easily be determined which model predicts the actual outcome of a breakup event with the highest degree of accuracy, and such analysis is beyond the scope of this PhD programme. Clearly, the only way to determine this and to eliminate many of the uncertainties in breakup models is to conduct a much larger number of ground-based

experiments and on-orbit observations of breakup events, thus increasing the pool of data upon which these empirically derived equations are based.

The main driving parameters for any breakup event include the breakup model chosen to simulate the event, the breakup scenario and the target mass. Additionally, the main driving parameters for a collision induced breakup include the projectile mass and the collision velocity. Generally, high energy fragmentations (i.e. high-intensity explosions or collisions with high collision velocities or large projectile masses) produce greater numbers of fragments than their low energy counterparts, particularly in the small mass range. These fragments also tend to have greater delta-v's. The target mass makes little difference to the nature of the fragmentation, unless of course the fragmentation energy is high enough to destroy the entire target object, in which case the ejecta mass is likely to be greater for a more massive object, which in turn will result in more fragments. The fragmentation properties (i.e. the number of fragments produced, the mass distribution, the delta-v distribution and the mass-to-area ratio distribution) are totally independent of the breakup orbit. However, the resulting orbital elements of the debris cloud fragments are of course inextricably linked to the delta-v magnitudes and directions allocated to the fragments by the breakup model.

The properties of debris clouds, as predicted by all four breakup models, can now be fully investigated with the intention of developing a fast cloud propagator that not only works for one breakup model, but is portable across all leading breakup models.

Chapter 5

A New Fast Cloud Propagator

5.1 Introduction

The orbital propagator is the most time consuming component in any space debris environment model, although the assessment of collision probabilities can also be a lengthy process. The propagator's speed is sensitive to a number of input parameters, including the propagation time, the time-step and the number of fragments. Depending on these input parameters, orbital propagators can take several hours or days to run, even on the fastest computers. As a result, debris modellers tend not to run many Monte Carlo simulations when attempting to model the future debris environment, as to do so would be very time consuming. (As a guide, QinetiQ usually perform around 10 Monte Carlo runs of the IDES model and NASA usually perform around 30 Monte Carlo runs of the EVOLVE model when predicting the future debris environment.) This in turn means that debris modellers only have a small pool of data from which to derive the average future debris environment. This can result in anomalous peaks or troughs in the predicted future spatial density of fragments in Earth orbit, caused by unlikely events predicted in certain Monte Carlo runs, the effects of which may not have been smoothed out greatly by the remaining Monte Carlo runs. Clearly, the greater the number of Monte Carlo data files that can be generated, the more closely the predicted future debris environment will match the actual future debris environment, bearing in mind the limitations of the models used. In order to facilitate a large number of Monte Carlo runs, however, a dramatic

increase is needed in the speed of debris models. The single most effective way to produce such a speed increase is to increase the speed of the slowest component – that of the orbital propagator.

The propagation models described in Chapter 3 are concerned with the fast propagation of individual fragments. The majority of these models use weighted particles to represent a large number of small fragments, which are then propagated to the required epoch. However, the original azimuth and elevations of the delta-v's assigned to the fragments at the breakup epoch by the breakup models are uniformly, randomly distributed about a unit sphere, and their magnitudes are randomised about the relevant delta-v distributions described in Chapter 4. Thus every time the breakup model is run, the initial orbital elements of the fragments will change. The original elements of the individual fragments are, therefore, arbitrary (within the confines of these distributions), and so it follows that the positions of the individual fragments at some later time are also arbitrary. Consequently, the important factors in propagating debris cloud fragments are the shape and position of the debris cloud and the distribution of fragments within that cloud at any particular time. Thus a debris cloud propagator that can re-create the shape and position of a debris cloud and the distribution of fragments within that cloud at any time, without propagating those fragments individually, should be extremely fast, whilst recovering all the important information required to define the cloud. This provides the rationale for devising a new fast debris cloud propagator that will propagate a debris cloud as a whole, rather than as the sum of individual fragments. This chapter describes the development of such a propagator.

This propagator, called the Fast Cloud Propagator, or FCP, is described in section 5.2. This section describes the original properties of a debris cloud and the distribution of fragments within the cloud. It then describes how these distributions can be represented by a limited number of parameters, which can be propagated through time and used to re-create the distributions, and hence the debris cloud, at any required epoch following the breakup event.

The effects of SRP are described in the final section of this chapter and are compared to the effects of the other perturbations affecting objects in high-Earth orbits. A sensitivity analysis is conducted to describe the importance of SRP effects with increasing fragment mass (and hence decreasing mass-to-area ratios).

5.2 Methodology

This section describes a new propagation method in which a debris cloud can be propagated as a series of distributions, instead of being propagated as a set of individual fragments or pseudo-fragments. This new propagation method aims to improve current propagation times, whilst maintaining a high degree of accuracy.

5.2.1 The Properties of a Debris Cloud

The only way to propagate a distribution of fragments through time is to propagate a set of distribution parameters. It is important to choose these parameters such that they fully characterise the distribution. They can then be used to re-create the distribution at any time. The selection of these distribution parameters at the breakup epoch forms a major part of the FCP methodology. However, before describing how these parameters are chosen, it is important to examine the properties of the debris cloud, since these properties govern the choice of the distribution parameters. The properties of a debris cloud can be described by distributions showing the number of fragments with particular orbital elements (these shall henceforth be referred to as *number distributions*) and by the relationships of these elements with one another, which can be illustrated using 15 scatter plots of the fragments plotted in two-dimensional element-space.

5.2.1.1 Number Distributions in Element-Space

An example of the number of fragments taking various orbital element values is given in the histograms in Figures 5.1 – 5.6. These are the histograms for a low-speed impact (LSI) scenario (produced by a 10 kg projectile impacting a 1500 kg target object with an impact velocity of 800 m/s) as predicted by the IDES breakup model in an arbitrary non-geostationary breakup orbit (a = 42164.8 km, e = 0.3, i = 30°, Ω = 170°, ω = 90°, M = 215°). It should be noted that the number distributions produced by this breakup event are typical of the number distributions produced by many breakup events in orbits where $e \neq 0$ and $i \neq 0°$. The peaks and troughs in the distributions are due to sampling variations – however the underlying distribution shapes are still quite clear and approximate to normal distributions in all cases in this example. In order to emphasise this point, a series of ten Monte Carlo runs was generated and the fragments in the resulting debris clouds were binned according to each element before the average number of fragments per bin was calculated. This had the effect of smoothing out the peaks and troughs introduced by sampling variations and resulted in the distributions presented in Figures 5.7 – 5.12. These figures have a normal distribution curve superimposed on top of them to allow the reader to assess the validity of the assumption that each of these distributions approximates to a normal distribution. The normal curve was fitted to the element values using the statistics software package SPSS [82].

Figures 5.7 – 5.12 show that the Monte Carlo averaged distributions approximate to normal distributions in all cases. The accuracy of the fit in each case can be assessed by a Q-Q plot (Quantile-Quantile plot). These plot the observed or actual values of the orbital elements against those expected of a normal distribution. A straight line through the graph denotes the optimum scatter for a perfect normal distribution. Thus the correlation of the data points to this straight line shows the validity of the assumption that the distributions are normal – any deviation from this straight line shows a deviation from a normal distribution. The Q-Q plots for the Monte Carlo averaged number distributions in Figures 5.7 – 5.12 are presented in Figures 5.13 – 5.18. The R^2 values give a measure of the fit of the data points to the straight line (R^2 = 1 represents a perfect fit). These were

generated by calculating the mean and standard deviation of the element distributions using SPSS [82]. Matlab [83] was then used to create and sample a normal distribution with these parameters and then the data analysis software in Microsoft Excel was used to produce correlations between these sampled values and those of the orbital elements. These correlations were then squared to give the R^2 values.

Confidence limits for a 95% confidence level were calculated for the each of the R^2 values [84]. These confidence limits are case dependent and are particularly dependent on the number of fragments generated (in this case totalling 2743) – the larger the number of fragments, the narrower the confidence interval. The confidence intervals for each of the R^2 values in Figures 5.13 - 5.18 is zero (to 3 decimal places).

The Q-Q plots show a good correlation between the recorded results and those expected of a perfect normal distribution. This is also reflected in the R^2 values, which are over 0.99 in each case. The results sometimes show a slight deviation from the normal towards the edges of the distribution. However, it must be noted that there are very few fragments at the edge of the distribution compared to the total number of fragments overall. Thus the number of fragments that actually deviate from the normal line is actually quite small. The assumption of normal distributions to approximate the shape of these number distributions is therefore deemed to be a good one.

Almost all breakups produce number distributions in element-space that can be represented by normal distributions. The only exceptions are for the number distributions in inclination when the debris cloud crosses the celestial equator and in eccentricity when the cloud has fragments in circular orbits. These situations occur when $i \approx 0°$ or $e \approx 0$, respectively (e.g. GEO). These situations can also occur for very high energy breakup events, such as high-intensity explosions.

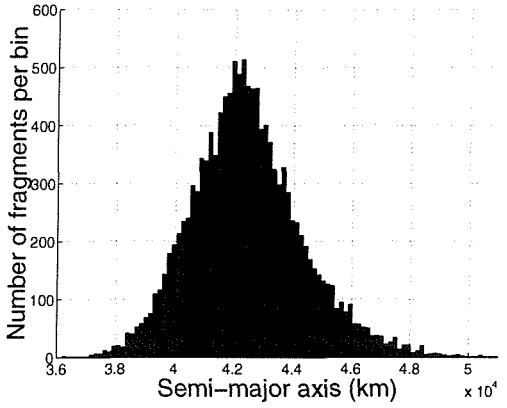

Figure 5.1 The number distribution in semi-major axis after a LSI-induced breakup in a non-geostationary orbit

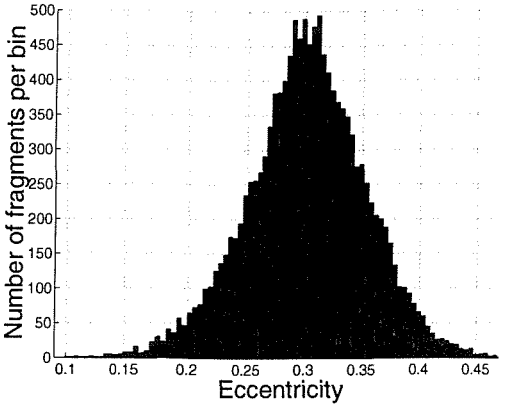

Figure 5.2 The number distribution in eccentricity after a LSI-induced breakup in a non-geostationary orbit

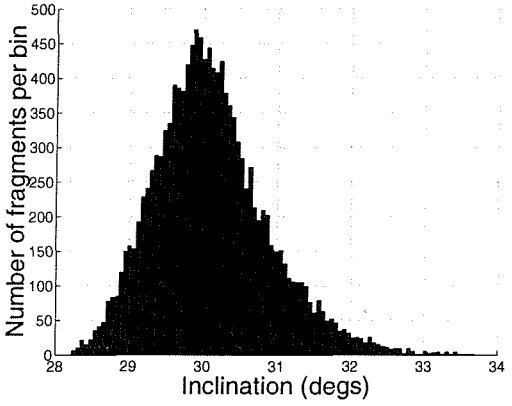

Figure 5.3 The number distribution in inclination after a LSI-induced breakup in a non-geostationary orbit

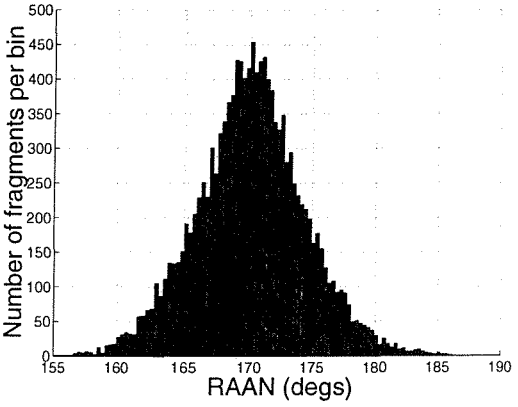

Figure 5.4 The number distribution in RAAN after a LSI-induced breakup in a non-geostationary orbit

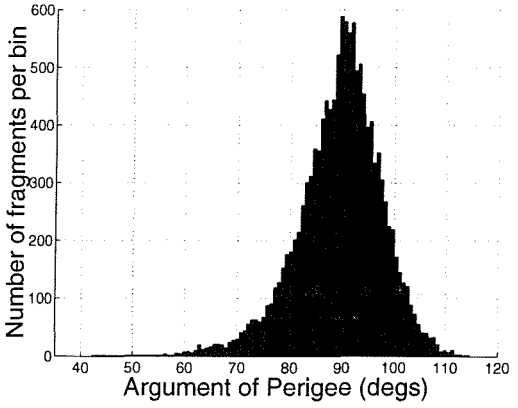

Figure 5.5 The number distribution in argument of perigee after a LSI-induced breakup in a non-geostationary orbit

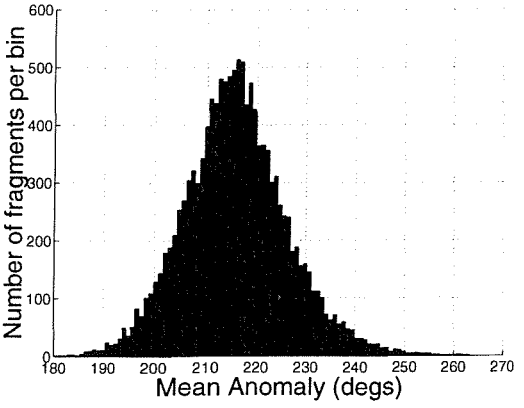

Figure 5.6 The number distribution in mean anomaly after a LSI-induced breakup in a non-geostationary orbit

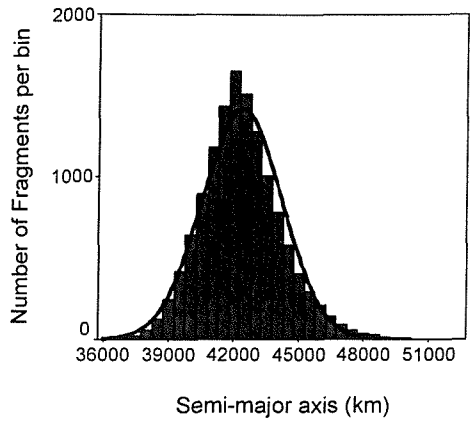

Figure 5.7 The Monte Carlo averaged number distribution in semi-major axis after a LSI-induced breakup in a non-geostationary orbit

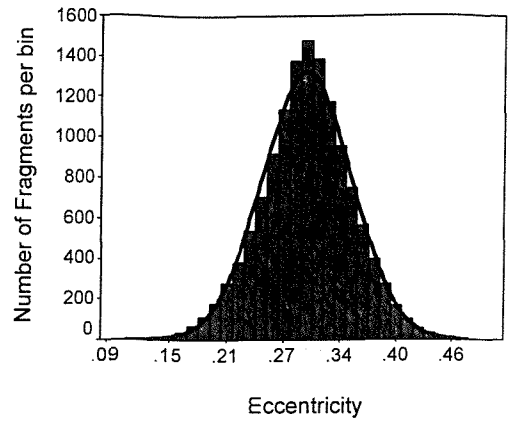

Figure 5.8 The Monte Carlo averaged number distribution in eccentricity after a LSI-induced breakup in a non-geostationary orbit

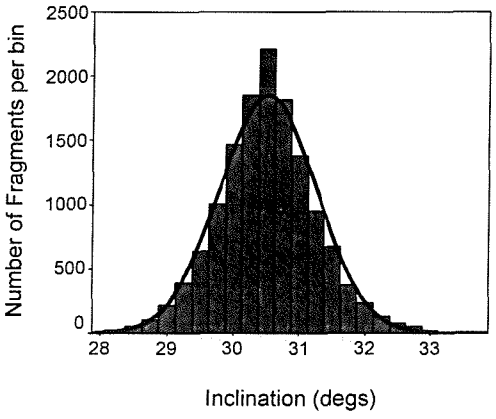

Figure 5.9 The Monte Carlo averaged number distribution in inclination after a LSI-induced breakup in a non-geostationary orbit

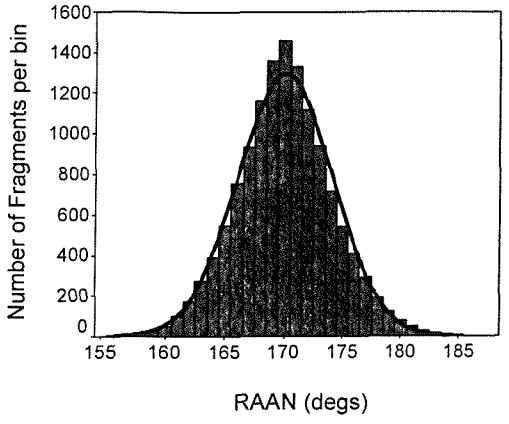

Figure 5.10 The Monte Carlo averaged number distribution in RAAN after a LSI-induced breakup in a non-geostationary orbit

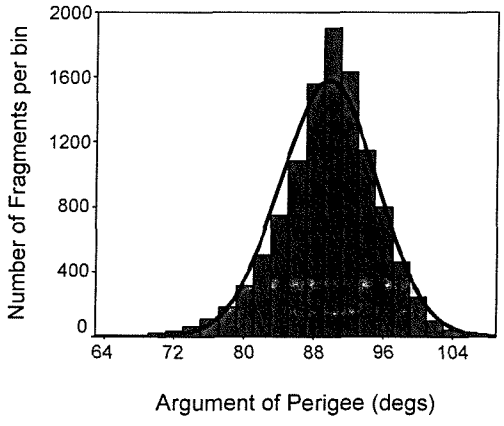

Figure 5.11 The Monte Carlo averaged number distribution in argument of perigee after a LSI-induced breakup in a non-geostationary orbit

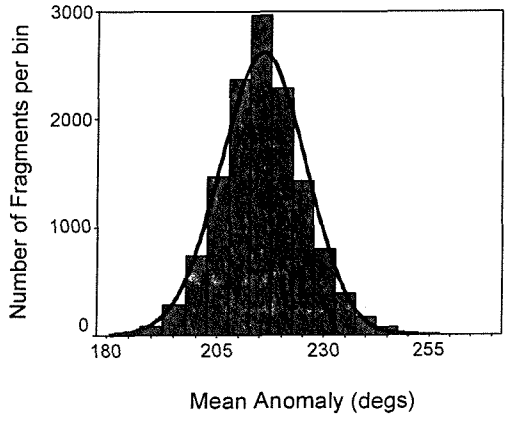

Figure 5.12 The Monte Carlo averaged number distribution in mean anomaly after a LSI-induced breakup in a non-geostationary orbit

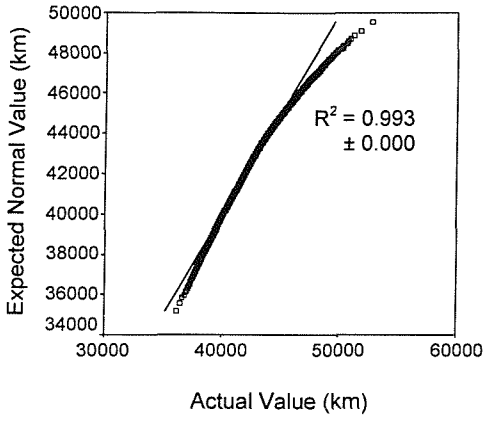

Figure 5.13 Normal Q-Q plot for the number distribution in semi-major axis after a LSI-induced breakup in a non-geostationary orbit

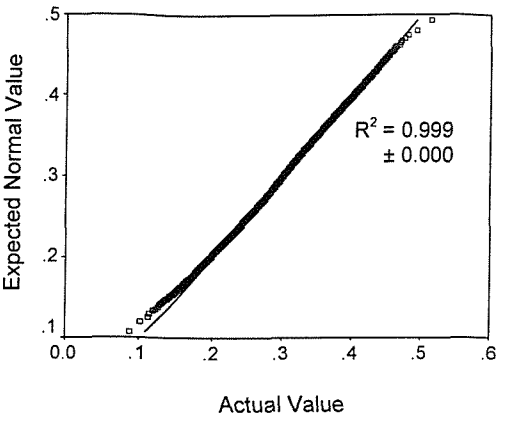

Figure 5.14 Normal Q-Q plot for the number distribution in eccentricity after a LSI-induced breakup in a non-geostationary orbit

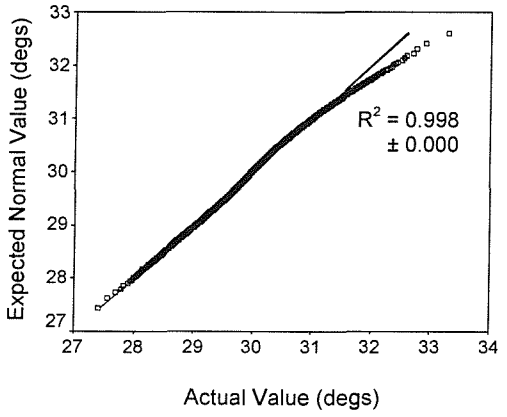

Figure 5.15 Normal Q-Q plot for the number distribution in inclination after a LSI-induced breakup in a non-geostationary orbit

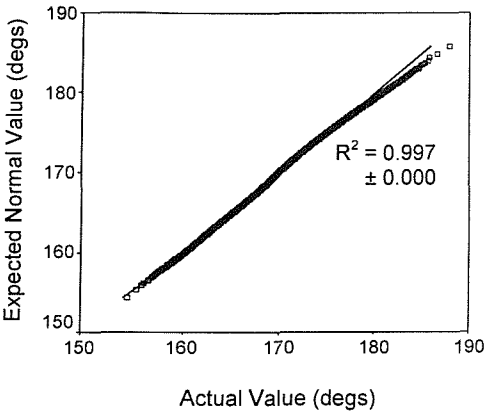

Figure 5.16 Normal Q-Q plot for the number distribution in RAAN after a LSI-induced breakup in a non-geostationary orbit

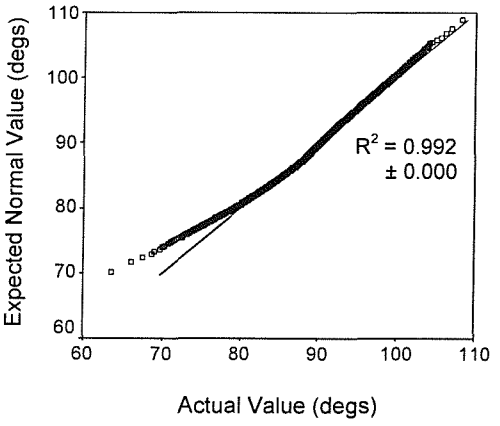

Figure 5.17 Normal Q-Q plot for the number distribution in argument of perigee after a LSI-induced breakup in a non-geostationary orbit

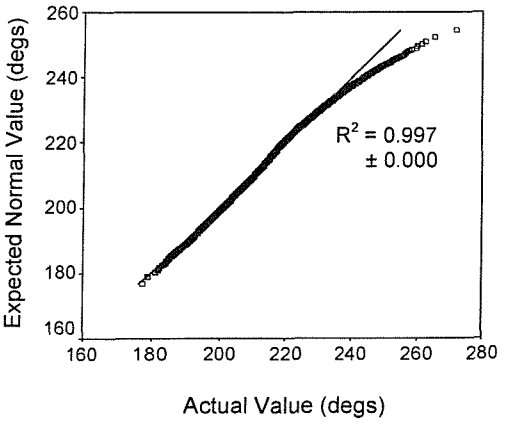

Figure 5.18 Normal Q-Q plot for the number distribution in mean anomaly after a LSI-induced breakup in a non-geostationary orbit

High energy-breakups or breakups with $i \approx 0°$ or $e \approx 0$ can produce skewed number distributions in eccentricity and inclination, which approximate to gamma distributions. A good example of such a distribution is given in Figure 5.19, which shows the number of fragments with various eccentricity values for the same breakup scenario used for Figures 5.1 – 5.18 but in a GEO orbit (e = 0.001). This plot is again typical of many of the plots produced by breakups of this type. The peaks and troughs in this histogram have again been eliminated using Monte Carlo averaging techniques (average of 10 runs). Figure 5.20 shows a gamma Q-Q plot for the histogram in Figure 5.19, in order to assess the validity of the assumption that it approximates to a gamma distribution. The straight line denotes the expected results for a perfect gamma distribution, again, with the R^2 value showing the accuracy of the fit. The actual eccentricity values have a high correlation with the gamma line (R^2 = 0.998 ± 0.000) with only a few high eccentricity values falling below the gamma line. Thus the assumption of a gamma distribution for plots of this type is also deemed to be a good one.

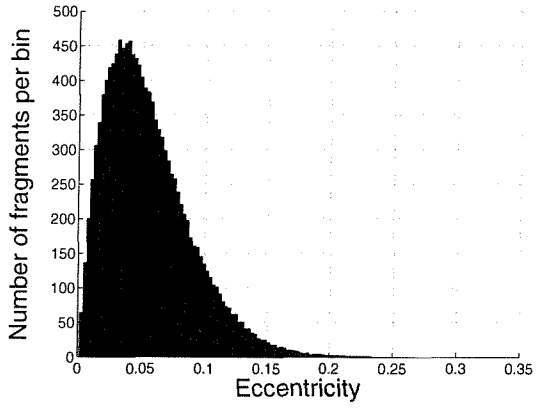

Figure 5.19 The number distribution in eccentricity after a LSI-induced breakup in GEO

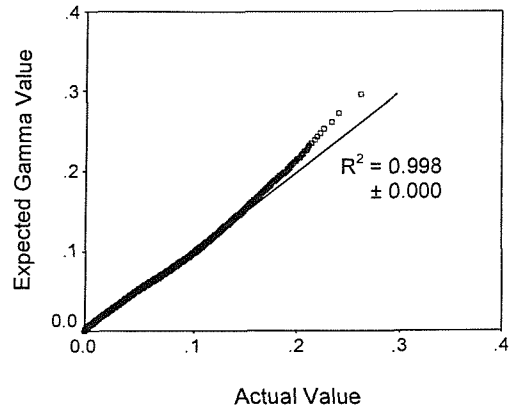

Figure 5.20 A Gamma Q-Q plot for the number distribution in eccentricity after a LSI-induced breakup in GEO

A normal distribution can be expressed by the probability density function described by

$$p(x) = \frac{1}{\sqrt{2\pi\sigma^2}} \exp\left(\frac{-(x-\mu)^2}{2\sigma^2}\right), \tag{5.1}$$

where x is the sampled value (i.e. the orbital element value), μ is the mean of the distribution and σ is the standard deviation. The coefficient of the exponent normalises the distribution so that the area under the normal curve becomes unity – this essentially converts the normal distribution into a probability density function.

A gamma distribution can be expressed by the gamma probability density function given by

$$p(x)=\frac{\left(\frac{x-\mu}{\beta}\right)^{\gamma-1}\exp\left(-\frac{x-\mu}{\beta}\right)}{\beta\,\Gamma(\gamma)}, \tag{5.2}$$

for $x \geq \mu$ and $\beta > 0$, where μ is the location parameter, β is the scale parameter, γ is the shape parameter and Γ is the gamma function, expressed as

$$\Gamma(a)=\int_0^\infty t^{a-1}e^{-t}dt. \tag{5.3}$$

In order for these equations to be used to construct a normal or gamma distribution, they must be integrated to give the area under the curve. A uniformly distributed random number is equated to the integral of the equation and the equation is then solved for x. This is the way in which a uniformly distributed random number, which can be generated easily using the built in 'rand()' function in C++, is converted to a normally distributed or gamma distributed random number, thus re-creating the normal or gamma probability density distribution (or number distribution). Unfortunately, neither the normal or gamma probability density functions can be integrated easily. Thus numerical methods using iterative techniques have to be used to convert the uniformly distributed random number into the normally distributed or gamma distributed random numbers. The method used to generate a normally distributed random number in the FCP is the commonly used 'Polar method' [85-88] (a variation of the Box and Muller method [89]) and the gamma distribution is re-created using the 'Gamdev function'[85].

5.2.1.2 The Element-Relationships

When characterising a debris cloud, it is also important to examine the relationships that the elements have with one another. These relationships, combined with the number distributions, can be used to fully characterise the debris cloud. 15 two-dimensional scatter plots (5 + 4 + 3 + 2 + 1 = 15) are needed in order to fully illustrate any distribution in 6-dimensional space. These 15 *element-relationship scatter plots* for the example scenario described in section 5.2.1.1 at the breakup epoch are illustrated in Figures 5.21 – 5.35. These scatter plots are typical of the scatter plots produced by many breakup events where $i \neq 0°$ and $e \neq 0$.

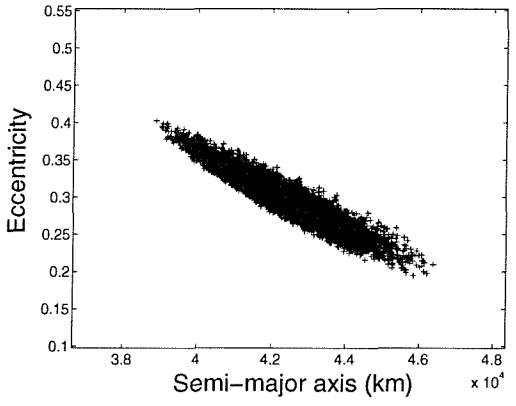

Figure 5.21 The semi-major axis vs. eccentricity scatter plot at the breakup epoch

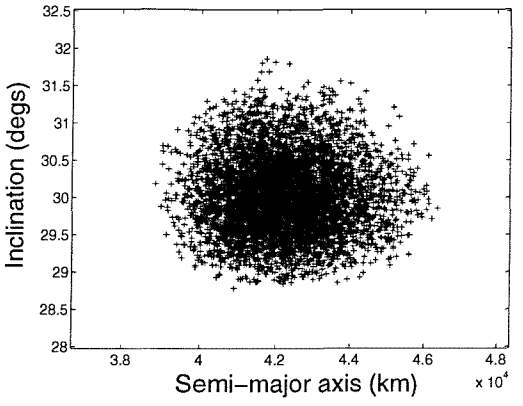

Figure 5.22 The semi-major axis vs. inclination scatter plot at the breakup epoch

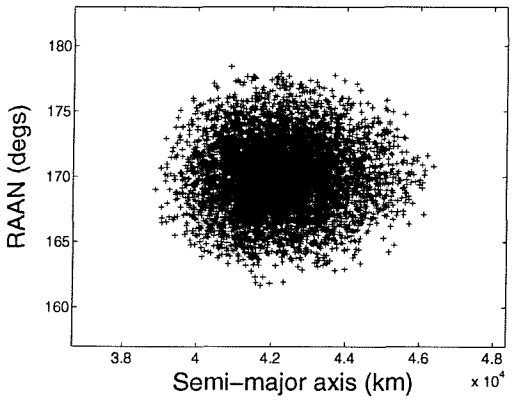

Figure 5.23 The semi-major axis vs. RAAN scatter plot at the breakup epoch

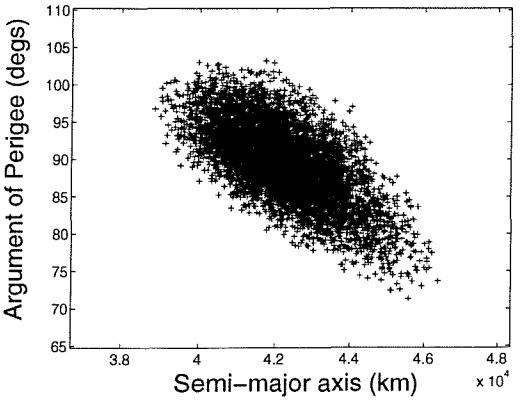

Figure 5.24 The semi-major axis vs. argument of perigee scatter plot at the breakup epoch

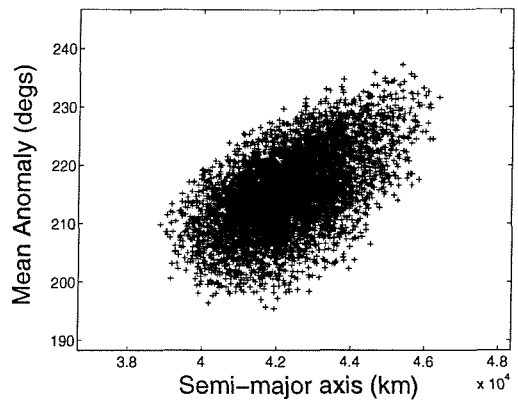

Figure 5.25 The semi-major axis vs. mean anomaly scatter plot at the breakup epoch

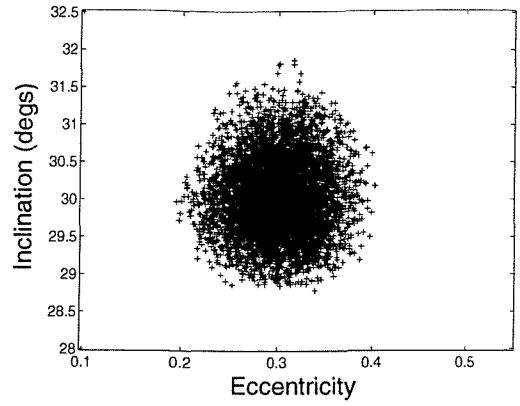

Figure 5.26 The eccentricity vs. inclination scatter plot at the breakup epoch

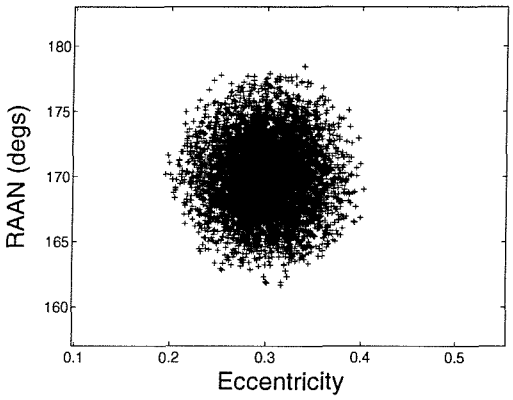

Figure 5.27 The eccentricity vs. RAAN scatter plot at the breakup epoch

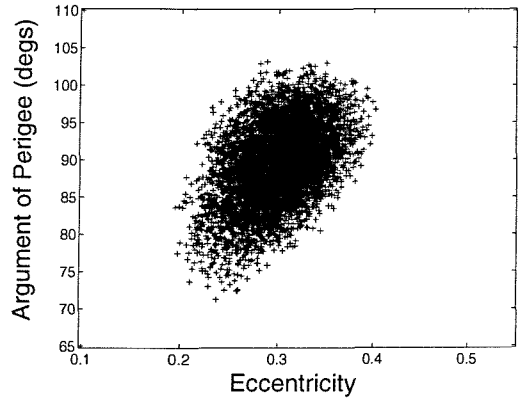

Figure 5.28 The eccentricity vs. argument of perigee scatter plot at the breakup epoch

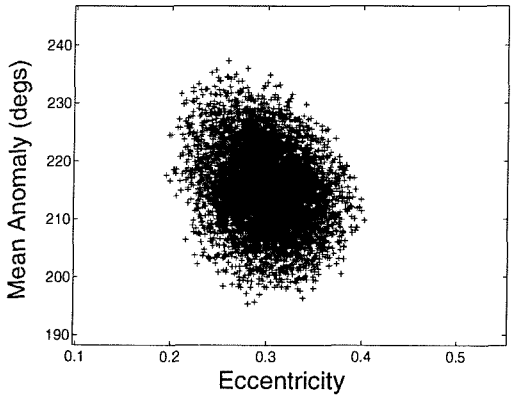

Figure 5.29 The eccentricity vs. mean anomaly scatter plot at the breakup epoch

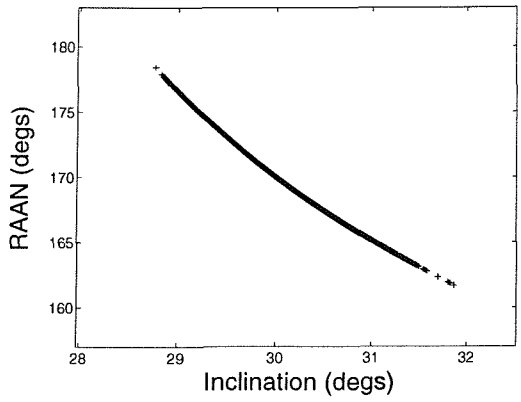

Figure 5.30 The inclination vs. RAAN scatter plot at the breakup epoch

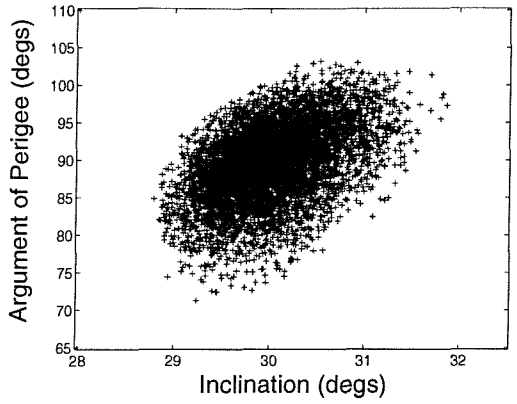

Figure 5.31 The inclination vs. argument of perigee scatter plot at the breakup epoch

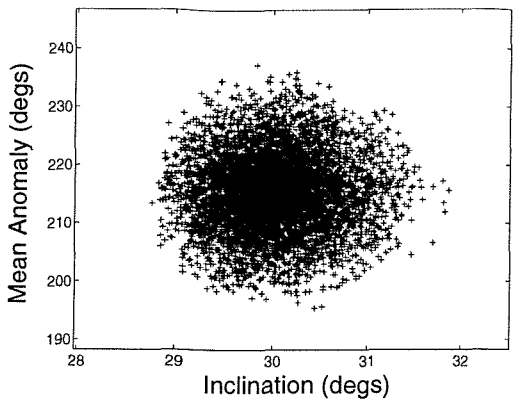

Figure 5.32 The inclination vs. mean anomaly scatter plot at the breakup epoch

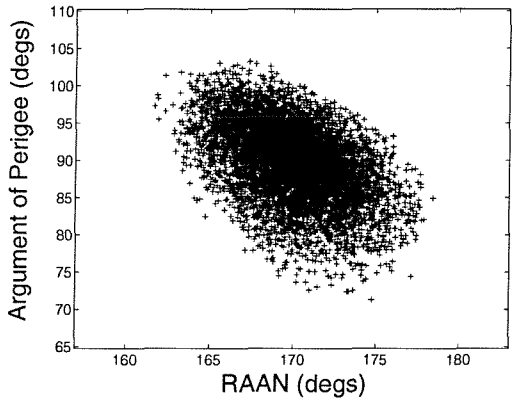

Figure 5.33 The RAAN vs. argument of perigee scatter plot at the breakup epoch

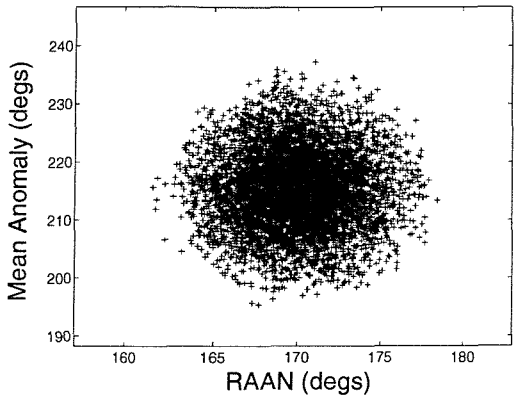

Figure 5.34 The RAAN vs. mean anomaly scatter plot at the breakup epoch

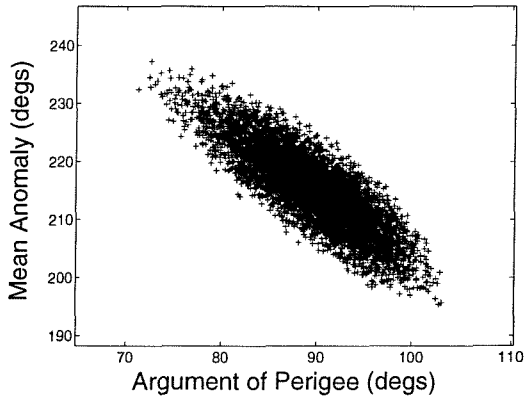

Figure 5.35 The argument of perigee vs. mean anomaly scatter plot at the breakup epoch

5.2.2 Model Structure

A schematic illustrating the FCP model structure and showing the integration of the FCP with the breakup models discussed in Chapter 4 is presented in Figure 5.36.

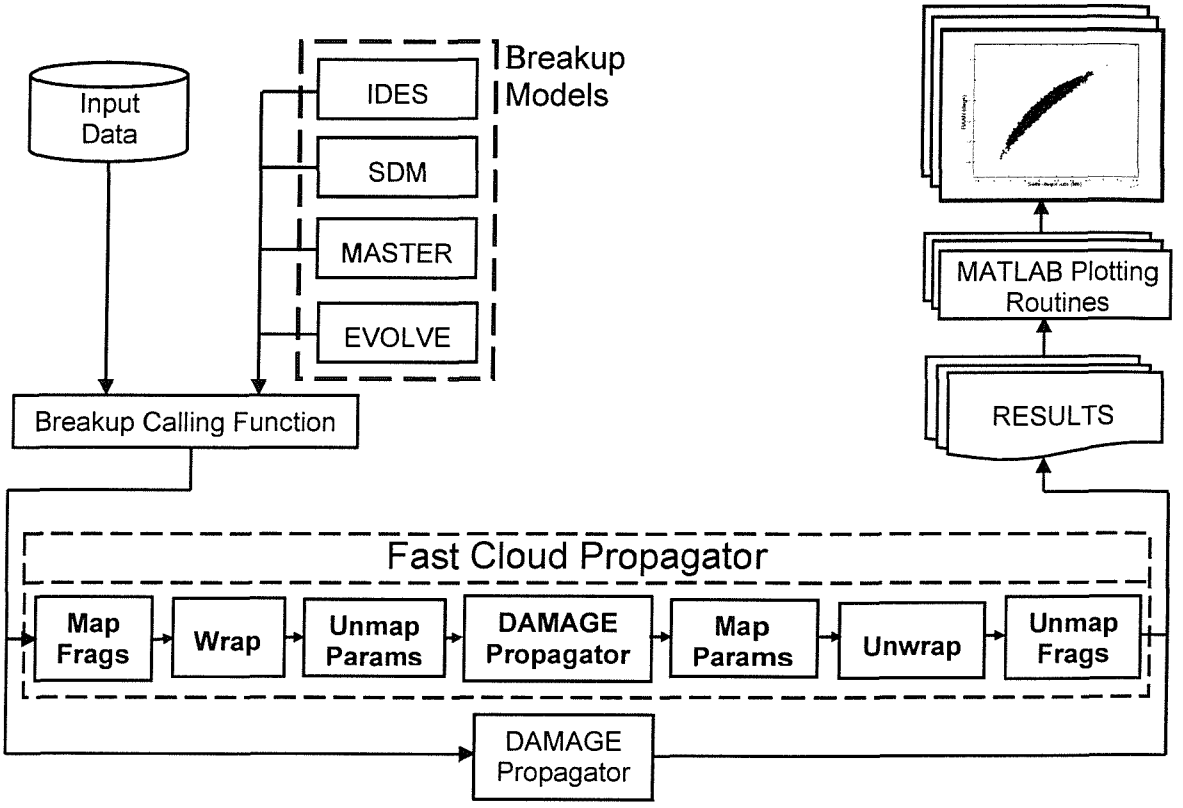

Figure 5.36 The FCP program flowchart

The Breakup Calling Function is used to call one of the four breakup models discussed in Chapter 4, namely those of the IDES, SDM, MASTER or EVOLVE debris models. The breakup calling function also reads all the input parameters required for the simulation from the input data file. The output from the breakup models are the fragments' properties at the breakup epoch, comprising the fragment identification numbers, fragment masses, fragment weighting factors (set to unity for all fragments by default), fragment diameters, fragment mass-to-area ratios and the fragment's orbital elements.

This data is then read by either the DAMAGE propagator, if conventional propagation is selected by the user, or by the FCP, if fast cloud propagation is selected.

The FCP comprises 7 modules – the 'Map Frags', 'Wrap' and 'Unmap Params' modules, which essentially perform the pre-processing of data ready for the propagation of the distribution parameters that characterise the orbital element distributions, the DAMAGE propagator (described in Chapter 3), which performs this propagation in the conventional manner, and the 'Map Params', 'Unwrap', and 'Unmap Frags' modules which perform the post-processing of the data and recovery of the debris cloud fragments.

The 'Wrap' module essentially 'wraps up' the fragments into a set of distributions, carefully selects the distribution parameters required to describe these distributions, and puts them in a form that is compatible with the DAMAGE propagator. The 'Unwrap' module re-creates the distributions from the propagated distribution parameters and 'unwraps' them to recover the orbital elements of all the fragments.

The fragments with orbital element values of $e \approx 0$ or $i \approx 0°$ need to have their orbital elements mapped to different values in order that the Wrap and Unwrap routines can be executed. This is because the 'Wrap' and 'Unwrap' routines require continuous number distributions if they are to function properly, and continuous distributions do not always exist following breakups in orbits with $e \approx 0$ or $i \approx 0°$. Similarly, the elements must be returned to their unmapped state for the DAMAGE propagator to propagate them. Hence the need for mapping and unmapping routines before and after both the Wrap and Unwrap functions. These mapping and unmapping routines, as well as the other routines that comprise the FCP, are discussed in detail in the next few sections.

After FCP propagation or conventional propagation, the results from either the FCP or the conventional propagator can be manipulated by a library of functions in MATLAB, designed to produce various graphs of the data. Examples of such graphs are shown in Figures 5.1 – 5.6 and in Figures 5.21 – 5.35.

5.2.3 Mapping the Fragments' Elements (The 'Map Frags' Routine)

The mapping of the fragments' orbital elements is conducted in the 'Map Frags' routine. Figure 5.37 re-creates the FCP flowchart from Figure 5.36 and highlights the position of the 'Map Frags' routine within the FCP.

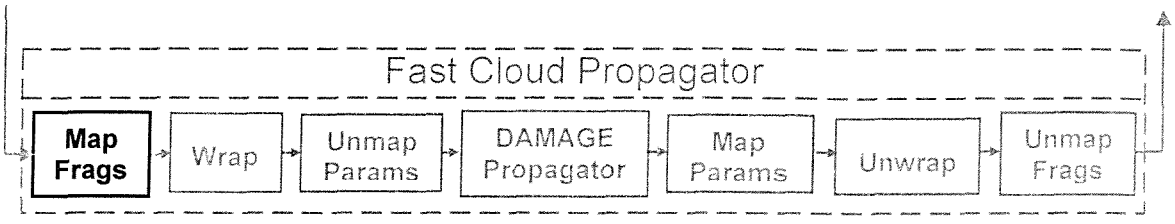

Figure 5.37 The position of the Map Frags module in the FCP

The number distributions for orbits with $i \approx 0°$ or $e \approx 0$ are often non-continuous. If $i \approx 0°$ in the breakup orbit then the number distributions in the resulting debris cloud will exhibit a half-normal distribution in inclination and a non-continuous distribution in RAAN and argument of perigee. If $e \approx 0$ in the breakup orbit then the number distributions in the resulting debris cloud will exhibit a gamma distribution in eccentricity and a non-continuous distribution in argument of perigee and mean anomaly. According to its design, however, the Wrap function requires continuous distributions that approximate to either normal or gamma distributions, if it is to propagate these distributions using the minimum amount of information possible to gain the maximum possible speed increase. Thus a mapping routine must be employed, to convert these distributions to normal or gamma distributions. The mapping routine maps the orbital elements of each fragment according to the following criteria:

$$\left.\begin{aligned} i_{NEW} &= -i_{OLD} \\ \Omega_{NEW} &= \Omega_{OLD} + 180° \\ \omega_{NEW} &= \omega_{OLD} + 180° \end{aligned}\right\} if\left(\Omega_{OLD} - \Omega_{TARG} > 90° \;\&\; \Omega_{OLD} - \Omega_{TARG} < 270°\right), \qquad (5.4)$$

$$\left.\begin{aligned} i_{NEW} &= -i_{OLD} \\ \Omega_{NEW} &= \Omega_{OLD} - 180^\circ \\ \omega_{NEW} &= \omega_{OLD} - 180^\circ \end{aligned}\right\} if\left(\Omega_{TARG} - \Omega_{OLD} > 90^\circ \;\&\; \Omega_{TARG} - \Omega_{OLD} < 270^\circ\right), \tag{5.5}$$

$$\left.\begin{aligned} \omega_{NEW} &= \omega_{OLD} - 180^\circ \\ M_{\mathrm{NEW}} &= M_{OLD} - 180^\circ \end{aligned}\right\} if\left(\omega_{OLD} - \omega_{TARG} > 90^\circ \;\&\; \omega_{OLD} - \omega_{TARG} < 270^\circ\right), \tag{5.6}$$

$$\left.\begin{aligned} \omega_{NEW} &= \omega_{OLD} + 180^\circ \\ M_{NEW} &= M_{OLD} + 180^\circ \end{aligned}\right\} if\left(\omega_{TARG} - \omega_{OLD} > 90^\circ \;\&\; \omega_{TARG} - \omega_{OLD} < 270^\circ\right), \tag{5.7}$$

where the subscript *NEW* refers to the new, mapped value of the fragment's orbital element, the subscript *OLD* refers to the old, original value of the fragment's orbital element and the subscript *TARG* refers to the orbital element of the target object immediately prior to the breakup event. In each equation, the expression after the *if* statement is a quadrant test to assess whether there has been a quadrant change in the orbital elements following the breakup. These are the tests used to trigger element mapping. Note that the eccentricity number distribution is not itself mapped for orbits with $e \approx 0$. This is because the number distribution in eccentricity already resembles a gamma distribution in such circumstances.

These new mapped elements shall henceforth be referred to as *modified elements*, and the space in which they exist shall be referred to as *modified element-space*. The effects of mapping on the number distributions in inclination, RAAN and argument of perigee, for the example when $i = 0°$ in the breakup orbit, is illustrated in Figures 5.38 – 5.40. It should be noted that in Figure 5.39 the fragments all take one of two values in RAAN in the unmapped distribution (where the two values are separated by 180°) and the fragments all take just one value in RAAN in the mapped distribution.

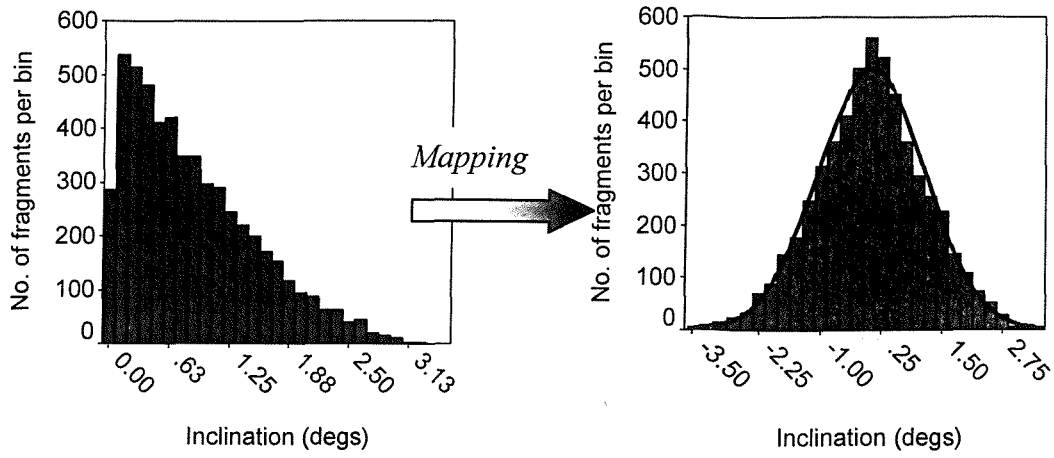

Figure 5.38 The effects of mapping on the number distribution in inclination. The unmapped distribution is illustrated on the left, whilst the mapped distribution with a superimposed normal curve is illustrated on the right

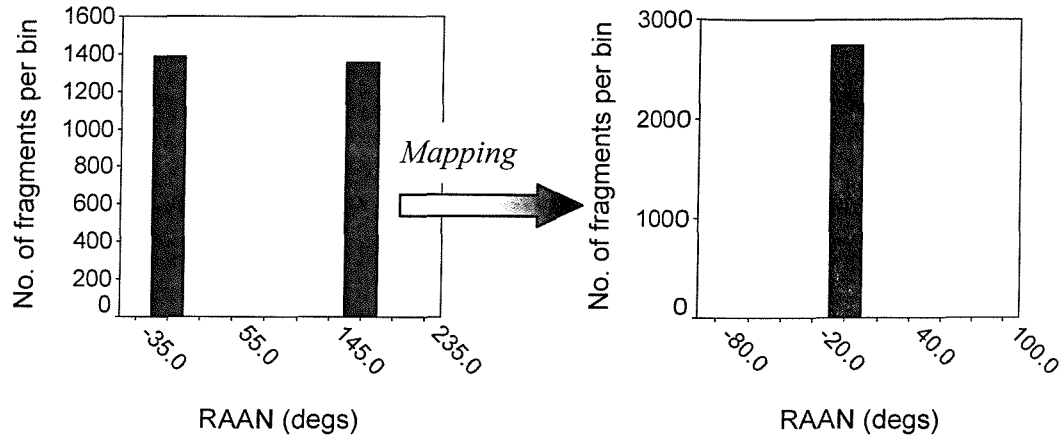

Figure 5.39 The effects of mapping on the number distribution in RAAN. The unmapped distribution is illustrated on the left, whilst the mapped distribution is illustrated on the right

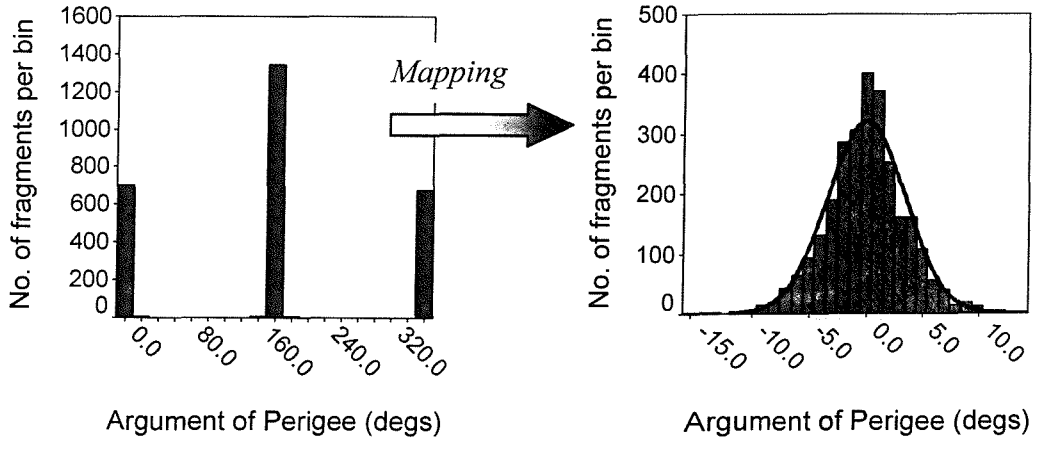

Figure 5.40 The effects of mapping on the number distribution in argument of perigee. The unmapped distribution is illustrated on the left, whilst the mapped distribution with a superimposed normal curve is illustrated on the right

5.2.4 Selecting the Distribution Parameters (The 'Wrap' Routine)

The selection of the distribution parameters is conducted in the 'Wrap' routine. Figure 5.41 re-creates the FCP flowchart from Figure 5.36 and highlights the position of the 'Wrap' routine within the FCP.

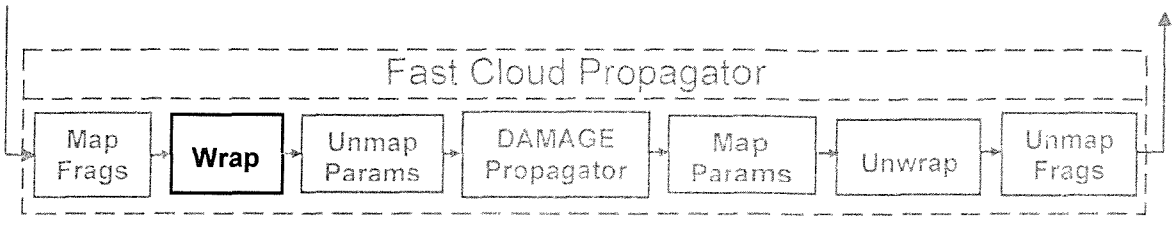

Figure 5.41 The position of the Wrap module in the FCP

Having described the distributions and relationships that must be re-created in order to re-create accurately the debris cloud at any epoch, the method used for choosing the distribution parameters can now be addressed. A normal distribution can be characterised entirely by just three parameters, namely its mean (μ), its standard deviation (σ) and its area, which corresponds to the total number of fragments. However, a normal distribution may not remain normal throughout the propagation period. Very often the distributions can change shape and become skewed to more closely resemble gamma distributions rather than normal distributions. These need four parameters to represent them, namely the mode and the upper and lower limits of the distribution, as well as the total number of fragments. Thus every distribution will be characterised by three parameters – the mode value (which is also the mean for a normal distribution) and the upper and lower limits (either one of which can be used to yield the standard deviation for a normal distribution). The total number of fragments can essentially be ignored here, as this remains constant throughout the propagation period. The limits of a distribution often tend to infinity, as is the case for a normal distribution and for one of the limits of a gamma distribution. Thus the limits of a distribution will henceforth be defined as the values that bound 99.7% of

the fragments, the equivalent of the 3σ limits in a normal distribution. This has the secondary effect of eliminating any fragments that are not part of the core distribution, i.e. the main distribution that describes the underlying trend in any element-relationship scatter plot. These fragments, which shall henceforth be referred to as *rogue fragments*, are undesirable and would otherwise greatly disrupt the functioning of the FCP, as will become clear in later sub-sections. There is no strict definition for these rogue fragments, other than the fact that they clearly do not contribute to the underlying trend in the element-relationship scatter plots. They usually lie outside the 3σ limits of the number distributions.

The distribution parameters for each element need to be allocated to fragments if they are to be propagated, and the combination of parameters allocated to each fragment is of the utmost importance if the FCP is to propagate the debris cloud accurately. The fragments to which the distribution parameters are assigned are thus not necessarily real fragments (i.e. fragments produced by the breakup model), as they exist only to propagate the distributions. These fragments shall thus be referred to as *pseudo-fragments*.

The distribution parameters allocated to the pseudo-fragments can be split into two categories: those that describe the size and position of the cloud at any time; and those that describe the shape of the cloud and its spread in the 15 element-relationship scatter plots at any time. Consequently these shall be known as the *size parameters* and *spread parameters*, respectively.

5.2.4.1 The Size Parameters

The modes of the number distributions at the breakup epoch are allocated to one pseudo-fragment, which is numbered zero. Where normal distributions exist, these mode values give the coordinates of the target object. In such cases, the target object, whether it is completely destroyed in the breakup event or not, is effectively propagated as pseudo-fragment zero. The pseudo-fragments numbered 1 to 12 contain the upper and lower

limits of each of the 6 orbital elements, where the remaining 5 orbital elements for each of these 12 pseudo-fragments are dictated by the element-relationship scatter plots. For instance, if x and y are arbitrary orbital elements and an x vs. y element relationship scatter plot was *non-isotropic*[*], then the pseudo-fragments representing the upper and lower limits of element x are assigned the values of element y that correspond to those x values in the original debris cloud and vice versa. If however the x vs. y element relationship scatter plot is isotropic then the pseudo-fragments representing the upper and lower limits of element x are assigned the mode value of element y and the pseudo-fragments representing the upper and lower limits of element y are assigned the mode value of element x. Figure 5.42 shows how these size parameters are chosen for a non-isotropic distribution using an example a vs. ω scatter plot. Figure 5.43 shows how they are selected for an isotropic distribution using an example a vs. i scatter plot. Table 5.1 also illustrates this by showing the size parameters allocated to pseudo-fragments 0 – 12 for the element-relationship scatter plots in Figures 5.21 – 5.35.

The mode values are assigned to the fragments in these cases since, in the absence of any pattern in the scatter plot, these represent the most likely value for a particular orbital element. Thus, when coupled with the upper and lower limits of a corresponding element, they would most accurately reflect the shape of an isotropic scatter plot. This method of assigning mode values for isotropic scatter plot distributions instead of using real cloud fragments eliminates the error that might occur if, for instance, there was an isotropic x-y scatter plot where the upper x value corresponded, not to the mode y value, as would be expected, but to an anomalously high or low y value. In such a circumstance the distribution parameters would not accurately reflect the shape of the scatter plot. If none of the scatter plots are isotropic then the pseudo-fragments are effectively real fragments sampled from the debris cloud.

[*] The term 'isotropic', as far as it refers to scatter-plot distributions, shall mean a distribution where the x-axis elements can be randomly assigned to the y-axis element, i.e. where there is no relationship between them. Examples of these can be seen in Figures 5.22, 5.23, 5.26, 5.27, 5.32 and 5.34. The isotropic scatter plot should not be confused with an isotropic breakup, which is a breakup cloud with approxiamtely uniform characteristics in all directions. An isotropic breakup will not necessarily generate isotropic distributions in each pair of element-relationship scatter plots.

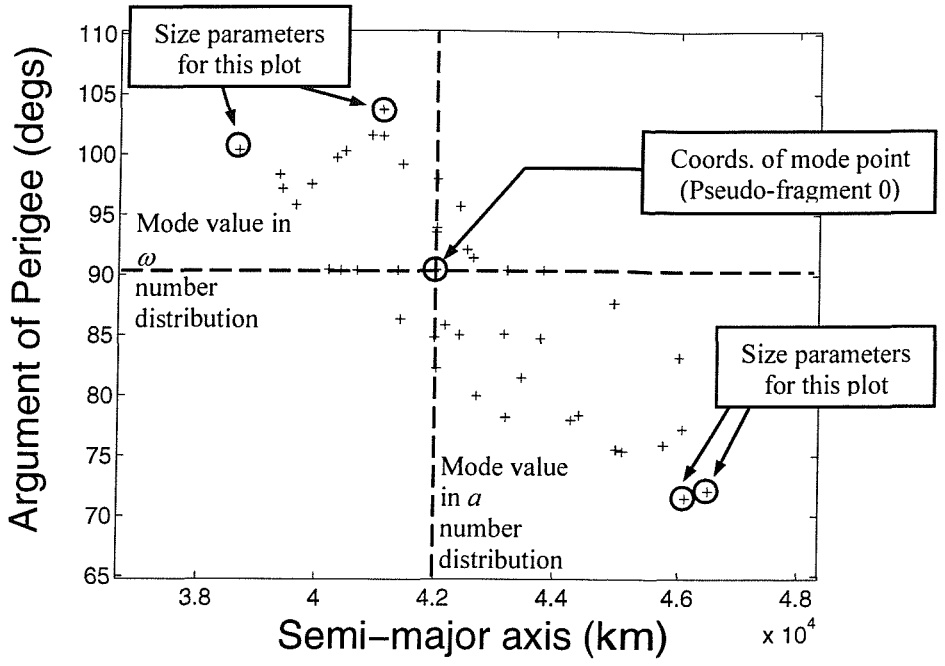

Figure 5.42 A scatter plot showing the semi-major axis and argument of perigee coordinates for all the pseudo-fragments at the breakup epoch. The circled coordinates illustrate the method by which the size parameters are assigned to a non-isotropic scatter plot.

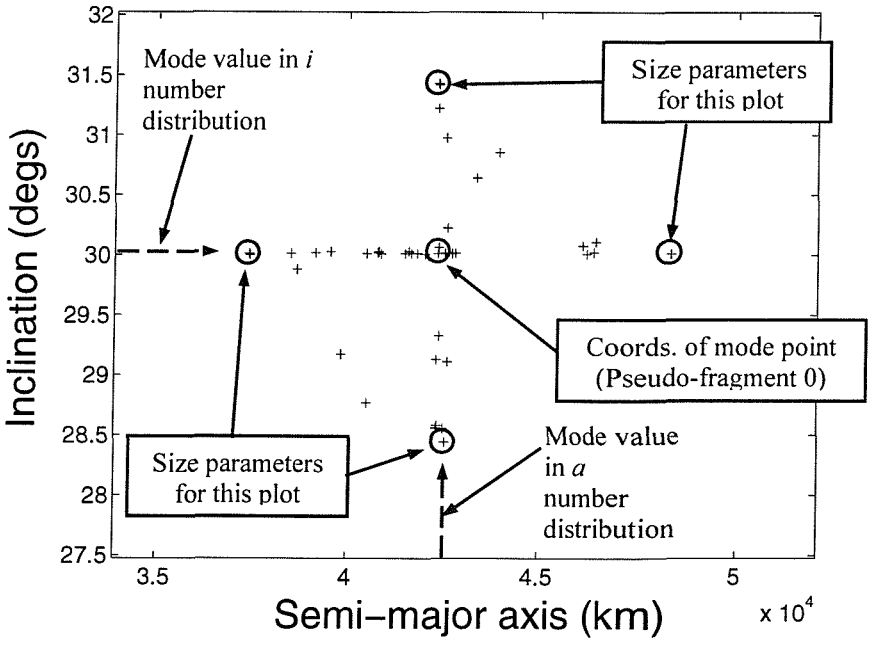

Figure 5.43 A scatter plot showing the semi-major axis and inclination coordinates for all the pseudo-fragments at the breakup epoch. The circled coordinates illustrate the method by which the size parameters are assigned to an isotropic scatter plot.

Pseudo-Fragment Number	a	e	i	Ω	ω	M
0	μ_a	μ_e	μ_i	μ_Ω	μ_ω	μ_M
1	$\mu_a + 3\sigma_a$	e_{REAL}	μ_i	μ_Ω	ω_{REAL}	M_{REAL}
2	$\mu_a - 3\sigma_a$	e_{REAL}	μ_i	μ_Ω	ω_{REAL}	M_{REAL}
3	a_{REAL}	$\mu_e + 3\sigma_e$	μ_i	μ_Ω	ω_{REAL}	M_{REAL}
4	a_{REAL}	$\mu_e - 3\sigma_e$	μ_i	μ_Ω	ω_{REAL}	M_{REAL}
5	μ_a	μ_e	$\mu_i + 3\sigma_i$	Ω_{REAL}	ω_{REAL}	μ_M
6	μ_a	μ_e	$\mu_i - 3\sigma_i$	Ω_{REAL}	ω_{REAL}	μ_M
7	μ_a	μ_e	i_{REAL}	$\mu_\Omega + 3\sigma_\Omega$	ω_{REAL}	μ_M
8	μ_a	μ_e	i_{REAL}	$\mu_\Omega - 3\sigma_\Omega$	ω_{REAL}	μ_M
9	a_{REAL}	e_{REAL}	i_{REAL}	Ω_{REAL}	$\mu_\omega + 3\sigma_\omega$	M_{REAL}
10	a_{REAL}	e_{REAL}	i_{REAL}	Ω_{REAL}	$\mu_\omega - 3\sigma_\omega$	M_{REAL}
11	a_{REAL}	e_{REAL}	μ_i	μ_Ω	ω_{REAL}	$\mu_M + 3\sigma_M$
12	a_{REAL}	e_{REAL}	μ_i	μ_Ω	ω_{REAL}	$\mu_M - 3\sigma_M$

Table 5.1 The size parameters allocated to each of the orbital elements of the first 13 pseudo-fragments by the 'Wrap' module after the LSI breakup described by Figures 5.21 – 5.35. Since the number distributions in Figures 5.21 – 5.35 are all normal, the modes of the distributions are equal to the means. Hence the mean parameter (μ) is used in place of the mode parameter (M) in this table to avoid confusion with the mean anomaly, M.

The pseudo-fragments in Table 5.1 are split into pairs and the values in bold show how the distribution parameters were chosen. For example, pseudo-fragments 1 and 2 were chosen on the basis of the size parameters $\mu_a + 3\sigma_a$ and $\mu_a - 3\sigma_a$, respectively, pseudo fragments 3 and 4 were chosen on the basis of the size parameters $\mu_e + 3\sigma_e$ and $\mu_e - 3\sigma_e$, respectively, etc. x_{REAL} is the actual value of element x (as modelled by the breakup model) for the fragment chosen according to the parameter in bold.

Every breakup data file the author has generated (including all those used in the error analysis in Chapter 6) has yielded scatter plots with the same pattern of isotropic and non-isotropic distributions – the a vs. i, a vs. Ω, e vs. i, e vs. Ω, i vs. M and Ω vs. M scatter plots are always isotropic and the remaining scatter plots are always non-isotropic. This is because these elements are independent of one another. The other elements have a relationship with one another immediately after a breakup event. For example, in an eccentric orbit, a prograde delta-v near the orbit's apogee will cause an increase in a fragment's semi-major axis and will cause a decrease in the fragment's eccentricity. A

negative correlation between semi-major axis and eccentricity will thus be visible in the a vs. e scatter plot (see Figure 5.21). Conversely, a prograde delta-v applied at the orbit's *perigee* will cause both semi-major axis and eccentricity to increase, resulting in a positive correlation in the a vs. e scatter plot. This pattern of isotropic/non-isotropic scatter plot distributions only exists at the breakup epoch however and does not exist for breakup orbits with $i \approx 0°$ or $e \approx 0$ (e.g. GEO), unless their orbital elements have been mapped to modified element-space. At any epoch other than the breakup epoch, an isotropic test must be used to determine whether a scatter plot distribution is isotropic or not. This test is executed as part of the 'Unwrap' function and is thus explained in section 5.2.9.

5.2.4.2 The Spread Parameters

The next set of pseudo-fragments to be propagated contain the spread parameters necessary to re-create the shape of the cloud. There are 60 of these, and they are numbered 13 – 72. Each scatter plot has 4 of these spread parameters, which denote the 3σ limits of y in a mapped x-y scatter plot at the mode value of x, and the 3σ limits of x at the mode value of y. This is illustrated in Figure 5.44, which uses the example of an a vs. ω scatter plot to show the positions of the distribution parameters. These spread parameters can be used at any given epoch to re-create the variance in the scatter plot distributions.

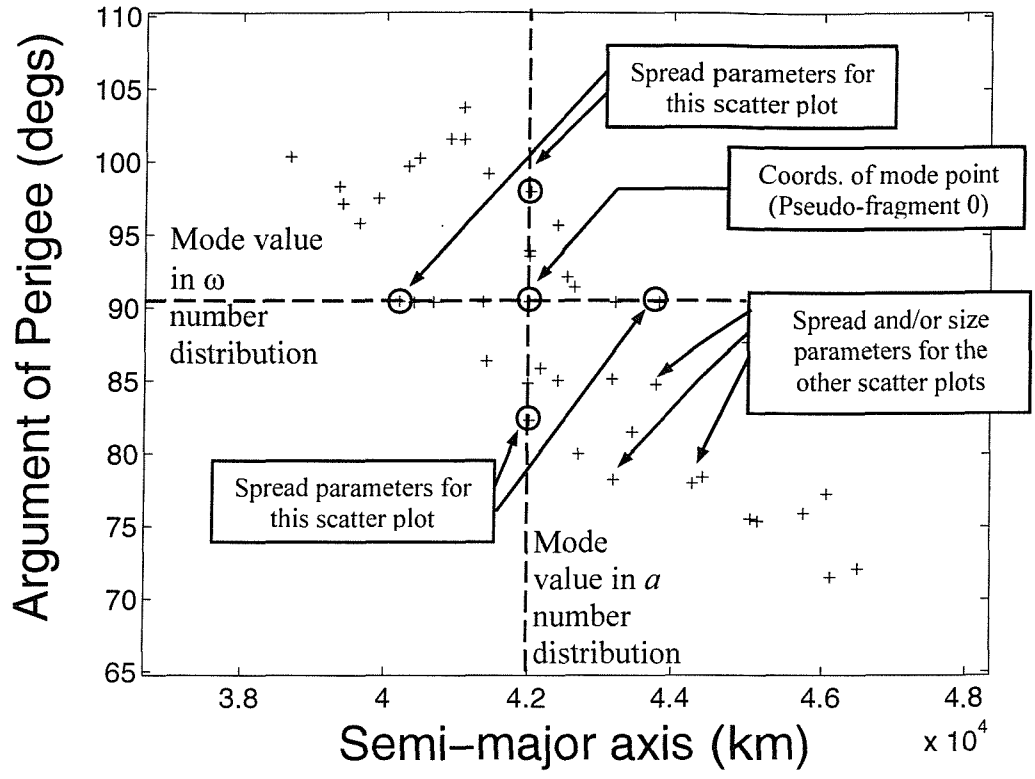

Figure 5.44 A scatter plot showing the semi-major axis and argument of perigee coordinates for all the pseudo-fragments at the breakup epoch. The circled coordinates illustrate the method by which the spread parameters are assigned.

The coordinates that have been circled in Figure 5.44 have been chosen using the original a vs. ω scatter plot (which contains all the fragments at the breakup epoch). These parameters represent the spread parameters that were derived using this scatter plot, as denoted by the annotations on the graph. The a-ω coordinates that are not circled were not derived from this particular plot, but instead were derived from other plots. For example, one of these semi-major axis coordinates may be the coordinate belonging to the fragment with the minimum inclination; another may belong to the fragment with the maximum mean anomaly, etc.

Table 5.2 gives the coordinates allocated to the orbital elements of pseudo-fragments 13 – 72 based on the scatter plots in Figures 5.21 – 5.35. Since the number distributions in Figures 5.21 – 5.35 are all normal, the modes of the distributions are equal to the means.

Hence the mean parameter (μ) is, again, used in place of the mode parameter (M) in this table to avoid confusion with the mean anomaly, M. The notation in the table is as follows: $(x_{MAX})_{\mu y}$ is the maximum x value at the mean value of y (this criteria is used to select the fragment), y_{REAL} and z_{REAL} are the real values of elements y and z for that particular fragment (as generated by the breakup model), and by definition, if the fragment was selected because it has the value $(x_{MAX})_{\mu y}$ then $y_{REAL} \approx \mu_y$. These approximations are also illustrated throughout the table.

Pseudo-Fragment Number	a	e	i	Ω	ω	M
13	$(a_{MAX})_{\mu e}$	$e_{REAL}(\approx\mu_e)$	i_{REAL}	Ω_{REAL}	ω_{REAL}	M_{REAL}
14	$(a_{MIN})_{\mu e}$	$e_{REAL}(\approx\mu_e)$	i_{REAL}	Ω_{REAL}	ω_{REAL}	M_{REAL}
15	$(a_{MAX})_{\mu i}$	e_{REAL}	$i_{REAL}(\approx\mu_i)$	Ω_{REAL}	ω_{REAL}	M_{REAL}
16	$(a_{MIN})_{\mu i}$	e_{REAL}	$i_{REAL}(\approx\mu_i)$	Ω_{REAL}	ω_{REAL}	M_{REAL}
17	$(a_{MAX})_{\mu\Omega}$	e_{REAL}	i_{REAL}	$\Omega_{REAL}(\approx\mu_\Omega)$	ω_{REAL}	M_{REAL}
18	$(a_{MIN})_{\mu\Omega}$	e_{REAL}	i_{REAL}	$\Omega_{REAL}(\approx\mu_\Omega)$	ω_{REAL}	M_{REAL}
19	$(a_{MAX})_{\mu\omega}$	e_{REAL}	i_{REAL}	Ω_{REAL}	$\omega_{REAL}(\approx\mu_\omega)$	M_{REAL}
20	$(a_{MIN})_{\mu\omega}$	e_{REAL}	i_{REAL}	Ω_{REAL}	$\omega_{REAL}(\approx\mu_\omega)$	M_{REAL}
21	$(a_{MAX})_{\mu M}$	e_{REAL}	i_{REAL}	Ω_{REAL}	ω_{REAL}	$M_{REAL}(\approx\mu_M)$
22	$(a_{MIN})_{\mu M}$	e_{REAL}	i_{REAL}	Ω_{REAL}	ω_{REAL}	$M_{REAL}(\approx\mu_M)$
23	$a_{REAL}(\approx\mu_a)$	$(e_{MAX})_{\mu a}$	i_{REAL}	Ω_{REAL}	ω_{REAL}	M_{REAL}
24	$a_{REAL}(\approx\mu_a)$	$(e_{MIN})_{\mu a}$	i_{REAL}	Ω_{REAL}	ω_{REAL}	M_{REAL}
25	a_{REAL}	$(e_{MAX})_{\mu i}$	$i_{REAL}(\approx\mu_i)$	Ω_{REAL}	ω_{REAL}	M_{REAL}
26	a_{REAL}	$(e_{MIN})_{\mu i}$	$i_{REAL}(\approx\mu_i)$	Ω_{REAL}	ω_{REAL}	M_{REAL}
27	a_{REAL}	$(e_{MAX})_{\mu\Omega}$	i_{REAL}	$\Omega_{REAL}(\approx\mu_\Omega)$	ω_{REAL}	M_{REAL}
28	a_{REAL}	$(e_{MIN})_{\mu\Omega}$	i_{REAL}	$\Omega_{REAL}(\approx\mu_\Omega)$	ω_{REAL}	M_{REAL}
29	a_{REAL}	$(e_{MAX})_{\mu\omega}$	i_{REAL}	Ω_{REAL}	$\omega_{REAL}(\approx\mu_\omega)$	M_{REAL}
30	a_{REAL}	$(e_{MIN})_{\mu\omega}$	i_{REAL}	Ω_{REAL}	$\omega_{REAL}(\approx\mu_\omega)$	M_{REAL}
31	a_{REAL}	$(e_{MAX})_{\mu M}$	i_{REAL}	Ω_{REAL}	ω_{REAL}	$M_{REAL}(\approx\mu_M)$
32	a_{REAL}	$(e_{MIN})_{\mu M}$	i_{REAL}	Ω_{REAL}	ω_{REAL}	$M_{REAL}(\approx\mu_M)$
33	a_{REAL}	$e_{REAL}(\approx\mu_e)$	$(i_{MAX})_{\mu e}$	Ω_{REAL}	ω_{REAL}	M_{REAL}
34	a_{REAL}	$e_{REAL}(\approx\mu_e)$	$(i_{MIN})_{\mu e}$	Ω_{REAL}	ω_{REAL}	M_{REAL}
35	$a_{REAL}(\approx\mu_a)$	e_{REAL}	$(i_{MAX})_{\mu a}$	Ω_{REAL}	ω_{REAL}	M_{REAL}
36	$a_{REAL}(\approx\mu_a)$	e_{REAL}	$(i_{MIN})_{\mu a}$	Ω_{REAL}	ω_{REAL}	M_{REAL}
37	a_{REAL}	e_{REAL}	$(i_{MAX})_{\mu\Omega}$	$\Omega_{REAL}(\approx\mu_\Omega)$	ω_{REAL}	M_{REAL}
38	a_{REAL}	e_{REAL}	$(i_{MIN})_{\mu\Omega}$	$\Omega_{REAL}(\approx\mu_\Omega)$	ω_{REAL}	M_{REAL}
39	a_{REAL}	e_{REAL}	$(i_{MAX})_{\mu\omega}$	Ω_{REAL}	$\omega_{REAL}(\approx\mu_\omega)$	M_{REAL}
40	a_{REAL}	e_{REAL}	$(i_{MIN})_{\mu\omega}$	Ω_{REAL}	$\omega_{REAL}(\approx\mu_\omega)$	M_{REAL}

Pseudo-Fragment Number	a	e	i	Ω	ω	M
41	a_{REAL}	e_{REAL}	$(i_{MAX})_{\mu M}$	Ω_{REAL}	ω_{REAL}	$M_{REAL}(\approx\mu_M)$
42	a_{REAL}	e_{REAL}	$(i_{MIN})_{\mu M}$	Ω_{REAL}	ω_{REAL}	$M_{REAL}(\approx\mu_M)$
43	a_{REAL}	$e_{REAL}(\approx\mu_e)$	i_{REAL}	$(\Omega_{MAX})_{\mu e}$	ω_{REAL}	M_{REAL}
44	a_{REAL}	$e_{REAL}(\approx\mu_e)$	i_{REAL}	$(\Omega_{MIN})_{\mu e}$	ω_{REAL}	M_{REAL}
45	a_{REAL}	e_{REAL}	$i_{REAL}(\approx\mu_i)$	$(\Omega_{MAX})_{\mu i}$	ω_{REAL}	M_{REAL}
46	a_{REAL}	e_{REAL}	$i_{REAL}(\approx\mu_i)$	$(\Omega_{MIN})_{\mu i}$	ω_{REAL}	M_{REAL}
47	$a_{REAL}(\approx\mu_a)$	e_{REAL}	i_{REAL}	$(\Omega_{MAX})_{\mu a}$	ω_{REAL}	M_{REAL}
48	$a_{REAL}(\approx\mu_a)$	e_{REAL}	i_{REAL}	$(\Omega_{MIN})_{\mu a}$	ω_{REAL}	M_{REAL}
49	a_{REAL}	e_{REAL}	i_{REAL}	$(\Omega_{MAX})_{\mu\omega}$	$\omega_{REAL}(\approx\mu_\omega)$	M_{REAL}
50	a_{REAL}	e_{REAL}	i_{REAL}	$(\Omega_{MIN})_{\mu\omega}$	$\omega_{REAL}(\approx\mu_\omega)$	M_{REAL}
51	a_{REAL}	e_{REAL}	i_{REAL}	$(\Omega_{MAX})_{\mu M}$	ω_{REAL}	$M_{REAL}(\approx\mu_M)$
52	a_{REAL}	e_{REAL}	i_{REAL}	$(\Omega_{MIN})_{\mu M}$	ω_{REAL}	$M_{REAL}(\approx\mu_M)$
53	a_{REAL}	$e_{REAL}(\approx\mu_e)$	i_{REAL}	Ω_{REAL}	$(\omega_{MAX})_{\mu e}$	M_{REAL}
54	a_{REAL}	$e_{REAL}(\approx\mu_e)$	i_{REAL}	Ω_{REAL}	$(\omega_{MIN})_{\mu e}$	M_{REAL}
55	a_{REAL}	e_{REAL}	$i_{REAL}(\approx\mu_i)$	Ω_{REAL}	$(\omega_{MAX})_{\mu i}$	M_{REAL}
56	a_{REAL}	e_{REAL}	$i_{REAL}(\approx\mu_i)$	Ω_{REAL}	$(\omega_{MIN})_{\mu i}$	M_{REAL}
57	a_{REAL}	e_{REAL}	i_{REAL}	$\Omega_{REAL}(\approx\mu_\Omega)$	$(\omega_{MAX})_{\mu\Omega}$	M_{REAL}
58	a_{REAL}	e_{REAL}	i_{REAL}	$\Omega_{REAL}(\approx\mu_\Omega)$	$(\omega_{MIN})_{\mu\Omega}$	M_{REAL}
59	$a_{REAL}(\approx\mu_a)$	e_{REAL}	i_{REAL}	Ω_{REAL}	$(\omega_{MAX})_{\mu a}$	M_{REAL}
60	$a_{REAL}(\approx\mu_a)$	e_{REAL}	i_{REAL}	Ω_{REAL}	$(\omega_{MIN})_{\mu a}$	M_{REAL}
61	a_{REAL}	e_{REAL}	i_{REAL}	Ω_{REAL}	$(\omega_{MAX})_{\mu M}$	$M_{REAL}(\approx\mu_M)$
62	a_{REAL}	e_{REAL}	i_{REAL}	Ω_{REAL}	$(\omega_{MIN})_{\mu M}$	$M_{REAL}(\approx\mu_M)$
63	a_{REAL}	$e_{REAL}(\approx\mu_e)$	i_{REAL}	Ω_{REAL}	ω_{REAL}	$(M_{MAX})_{\mu e}$
64	a_{REAL}	$e_{REAL}(\approx\mu_e)$	i_{REAL}	Ω_{REAL}	ω_{REAL}	$(M_{MIN})_{\mu e}$
65	a_{REAL}	e_{REAL}	$i_{REAL}(\approx\mu_i)$	Ω_{REAL}	ω_{REAL}	$(M_{MAX})_{\mu i}$
66	a_{REAL}	e_{REAL}	$i_{REAL}(\approx\mu_i)$	Ω_{REAL}	ω_{REAL}	$(M_{MIN})_{\mu i}$
67	a_{REAL}	e_{REAL}	i_{REAL}	$\Omega_{REAL}(\approx\mu_\Omega)$	ω_{REAL}	$(M_{MAX})_{\mu\Omega}$
68	a_{REAL}	e_{REAL}	i_{REAL}	$\Omega_{REAL}(\approx\mu_\Omega)$	ω_{REAL}	$(M_{MIN})_{\mu\Omega}$
69	a_{REAL}	e_{REAL}	i_{REAL}	Ω_{REAL}	$\omega_{REAL}(\approx\mu_\omega)$	$(M_{MAX})_{\mu\omega}$
70	a_{REAL}	e_{REAL}	i_{REAL}	Ω_{REAL}	$\omega_{REAL}(\approx\mu_\omega)$	$(M_{MIN})_{\mu\omega}$
71	$a_{REAL}(\approx\mu_a)$	e_{REAL}	i_{REAL}	Ω_{REAL}	ω_{REAL}	$(M_{MAX})_{\mu a}$
72	$a_{REAL}(\approx\mu_a)$	e_{REAL}	i_{REAL}	Ω_{REAL}	ω_{REAL}	$(M_{MIN})_{\mu a}$

Table 5.2 The spread parameters allocated to each of the orbital elements of pseudo-fragments 13 – 72 by the 'Wrap' module after the LSI breakup described by Figures 5.21 – 5.35.

5.2.5 Unmapping the Distribution Parameters (The 'Unmap Params' Routine)

The unmapping of the pseudo-fragments' orbital elements prior to propagation is conducted in the 'Unmap Params' routine. Figure 5.45 re-creates the FCP flowchart from Figure 5.36 and highlights the position of the 'Unmap Params' routine within the FCP.

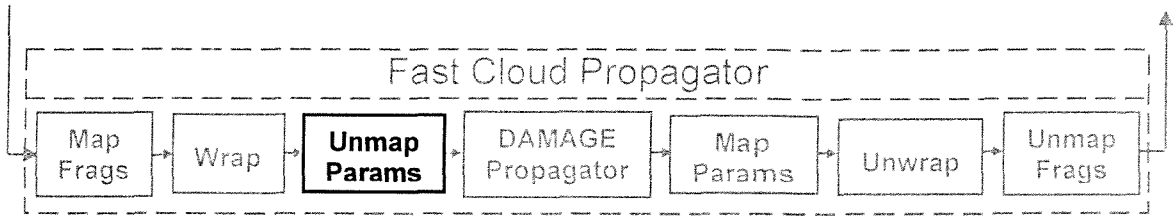

Figure 5.45 The position of the Unmap Params module in the FCP

Unmapping must be performed on the distribution parameters (i.e. the orbital elements assigned to the pseudo-fragments) prior to propagation because negative inclinations cause a miscalculation in the directions of the Sun and Moon, which are needed when computing the effects of luni-solar perturbations.

The unmapping routine performed on the distribution parameters following the Wrap function is essentially the exact reverse of the mapping routine performed before the 'Wrap' function. The defining equations in this routine are given by

$$\left.\begin{aligned} i_{NEW} &= -i_{OLD} \\ \Omega_{NEW} &= \Omega_{OLD} + 180^\circ \\ \omega_{NEW} &= \omega_{OLD} + 180^\circ \end{aligned}\right\} \text{if } i_{OLD} < 0^\circ, \tag{5.8}$$

$$\left.\begin{aligned} \omega_{NEW} &= \omega_{OLD} + 180^\circ \\ M_{NEW} &= M_{OLD} + 180^\circ \end{aligned}\right\} \text{if } a \le a_{eMIN}, \tag{5.9}$$

where the subscripts *NEW* and *OLD* refer to the new, unmapped and old, mapped values of the pseudo-fragments' orbital elements, respectively. The value a_{eMIN} refers to the value of a at the minimum value of e in the original breakup cloud. Essentially, the a vs. e scatter plot resembles a V-shape at the breakup epoch for breakup orbits with $e \approx 0$. The a_{eMIN} value is the semi-major axis value at the bottom of the V-plot for which $e \approx 0$. This test must be in place of the $e_{OLD} < 0$ test, since eccentricity was not mapped in the 'Map Params' routine. Therefore there are no pseudo-fragments with negative eccentricities in modified element space to allow this test to be used.

5.2.6 Propagating the Distributions through Element-Space

The distribution parameters assigned to the 73 pseudo-fragments are propagated conventionally by the DAMAGE propagator. Figure 5.46 re-creates the FCP flowchart from Figure 5.36 and highlights the position of the DAMAGE Propagator within the FCP.

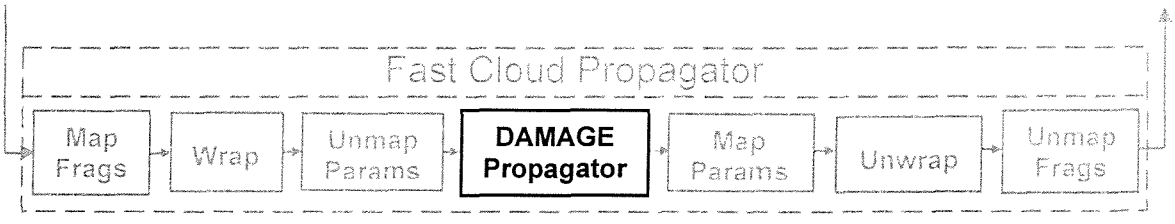

Figure 5.46 The position of the DAMAGE Propagator module in the FCP

This sub-section describes how the limits of the distributions at the breakup epoch can be propagated to yield the new limits of the distributions at any later epoch. It describes how the limits of the distributions will change in such a way as to always encompass roughly 99.7% of the fragments.

The only variables upon which the equations that govern the gravitational perturbations to each orbital element over any time-step are dependent are the values of the orbital

elements at the previous time-step. Unlike drag or SRP perturbations, they are not dependent upon the physical characteristics of the fragments. For example, the secular changes to the argument of perigee ω and the right ascension of the ascending node Ω due to the J_2 geopotential harmonic are given by equations 5.10 and 5.11 respectively as

$$\frac{d\omega}{dt} = \frac{3}{2}\frac{J_2 R_E^{\,2}}{\left[a\left(1-e^2\right)\right]^2} n\left[2 - \frac{5}{2}\sin^2 i\right], \tag{5.10}$$

and

$$\frac{d\Omega}{dt} = -\frac{3}{2}\frac{J_2 R_E^{\,2}}{\left[a\left(1-e^2\right)\right]^2} n\cos i, \tag{5.11}$$

where all the symbols have their usual meanings and n is given by

$$n = \sqrt{\frac{\mu}{a^3}}\,. \tag{5.12}$$

These equations have been repeated from Chapter 3. Clearly $\left(\frac{d\omega}{dt}\right)_{MAX}$ occurs at a_{MIN}, e_{MAX}, and $(\sin i)_{\mathrm{MIN}}$, i.e. i_{MIN}. Similarly, $\left(\frac{d\omega}{dt}\right)_{MIN}$ occurs at a_{MAX}, e_{MIN} and i_{MAX}.

A similar argument applied to $\frac{d\Omega}{dt}$ shows that the maximum and minimum values are also governed by extreme values of the relevant orbital elements.

The long-periodic changes to an orbit's eccentricity and inclination due to the J_3 zonal harmonic are given by

$$\frac{de}{dt} = -\frac{3}{2}\frac{nJ_3 R_E^{\,3}}{a^3\left(1-e^2\right)^2}\sin i\left[1 - \frac{5}{4}\sin^2 i\right]\cos\omega, \tag{5.13}$$

and

(5.14)

$$\frac{di}{dt} = \frac{3}{2} n \frac{J_3 R_E^{\ 3}}{a^3} \frac{e}{\left(1-e^2\right)^3} \cos i \left[1 - \frac{5}{4} \sin^2 i\right] \cos \omega .$$

$\left(\frac{de}{dt}\right)_{MAX}$ occurs at a_{MIN}, e_{MAX}, i_{MAX}, and at $(\cos \omega)_{MAX}$, i.e. ω_{MIN}. Similarly, $\left(\frac{de}{dt}\right)_{MIN}$ occurs at a_{MAX}, e_{MIN}, i_{MIN} and ω_{MAX}.

Again, a similar argument applied to $\frac{di}{dt}$ shows that the maximum and minimum values are governed by extreme values of the relevant orbital elements.

A similar argument applies to the changes in the elements due to the J_{22}, J_{33} and J_{31} Earth-gravity aspherical harmonics, as well as the changes in the elements due to luni-solar gravitational effects (see Chapter 3), in that the changes to the elements are greatest and least at the most extreme starting values of the elements.

Generally speaking, the minimum and maximum changes in the elements over any particular time-step occur in orbits that have the most extreme elements at the previous time-step. Thus the maximum possible change in eccentricity due to J_3, for instance, will occur for a fragment with an orbit that has the minimum a, the maximum e, the maximum i and the minimum ω, as previously stated. A fragment with such a combination of elements may not exist, however, and to assume that it does may result in the gross over-estimation or under-estimation of the size of the propagated debris cloud – the combination of elements describing a fragment's position is determined from the element relationship scatter plots, as previously illustrated in Figures 5.42 – 5.44.

Each of the number distributions in Figures 5.1 – 5.6 can be regarded as a one-dimensional sub-space set of the larger six-dimensional distribution in element-space, where each dimension is represented by one of the orbital elements. This six-dimensional distribution can be described completely by these number distributions and the element-relationship scatter plots in Figures 5.21 – 5.35, as previously described. Consider the

two-dimensional normal distribution illustrated in Figure 5.47 [90]. Each sub-space set of the distribution is represented by an orbital element, where two of these elements are represented by x and y. The probability of there being a fragment at any coordinate (x, y) is given by $P(x, y)$, and the probability of there being a fragment with a value x is given by $P(x)$ as shown in the one-dimensional cross-section on the right hand side.

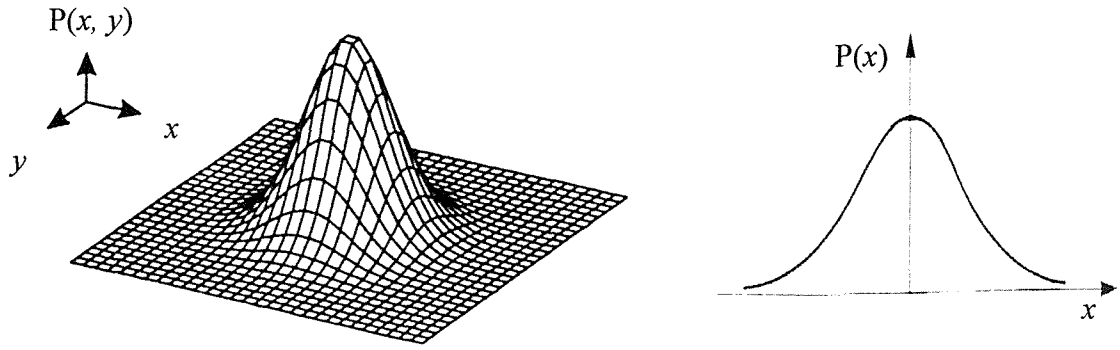

Figure 5.47 The two-dimensional normal distribution (left) and the one-dimensional normal distribution (right)

A six-dimensional shell can be defined around the six-dimensional number distribution in element-space. This six-dimensional distribution is a hyperellipsoid and the size-parameters lie on its surface. It has already been explained that the most likely largest and smallest changes to the elements of any fragment in the debris cloud over any particular time-step occur to the fragments with the largest or smallest elements at the previous time-step. Thus the greatest or smallest changes to the debris cloud can be ascertained by propagating the shell of the hypersphere, which is represented by the 73 pseudo-fragments. This process is depicted in two dimensions in Figure 5.48, which uses the semi-major axis and RAAN elements to illustrate the point.

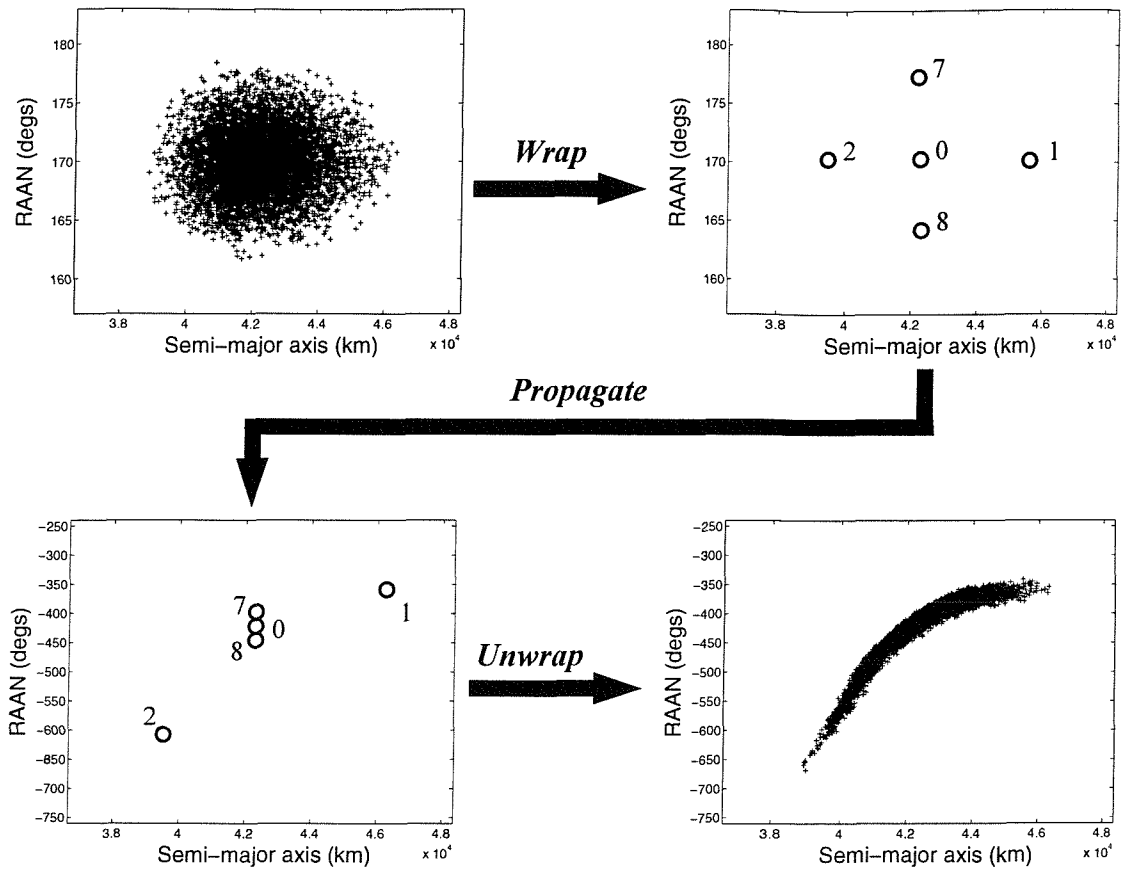

Figure 5.48 Sampling and propagating the hyperspace distribution. Pseudo-fragments 1, 2, 7 and 8 represent the shell of the hyperellipsoid in a-Ω sub-space and pseudo-fragment 0 represents the mode coordinates, i.e. the point of greatest fragment density in the hyperellipsoid. The starting coordinates for pseudo-fragments 0, 1, 2, 7 and 8 were given in Table 5.1.

In order to maintain these continuous distributions throughout the propagation period, the RAAN, argument of perigee and mean anomaly values are allowed to increase or decrease indefinitely, instead of being maintained in the range 0 – 360°. This has the effect of maintaining normal or gamma distributions in the long term. It will be shown in Chapter 6 that such distributions can be maintained up to (and possibly beyond) 100 years of propagation time, with no deterioration in the distributions.

5.2.7 Pre-mapping the Distribution Parameters (The 'Map Params' Routine)

The pre-mapping of the pseudo-fragments' orbital elements is conducted in the 'Map Params' routine following their propagation by the DAMAGE propagator. Figure 5.49 re-creates the FCP flowchart from Figure 5.36 and highlights the position of the 'Map Params' routine within the FCP.

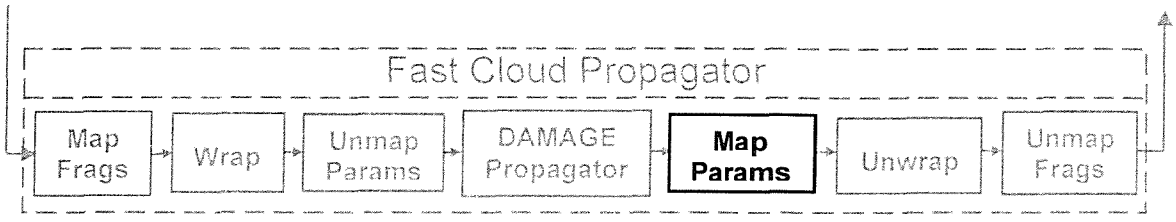

Figure 5.49 The position of the Map Params module in the FCP

In scatter plots containing RAAN or argument of perigee, the presence and spread of rogue fragments can be so great that any underlying trend within the plot is impossible to distinguish when plotted to scale on a graph, and even when these fragments are removed, there can exist several similar distributions on the same scatter plot, all separated by 360°. An example of such scatter plots are shown in Figures 5.50 and 5.52. The first step is to eradicate the rogue pseudo-fragments and reduce the distributions present in any one scatter plot to just one simplified trend. This is referred to as *pre-mapping*, as it precedes the mapping process, and eradicates the rogue pseudo-fragments by mapping the RAAN, argument of perigee and mean anomaly values by multiples of 360°. Thus it does not affect the resulting debris cloud in any way. Pre-mapping is undertaken for the pseudo-fragments propagated by the FCP as well as for the fragments propagated by the conventional propagator. This allows a meaningful comparison to be made between the two sets of scatter plots – see Chapter 6. Before pre-mapping is undertaken, the fragments/pseudo-fragments are sorted in ascending order according to

semi-major axis. This allows the pre-mapping routine to produce continuous distributions in a-Ω space, a-ω space and a-M space. The equations used in pre-mapping are given by

$$\begin{aligned}
&\textit{for } x = 1...N-1 \ \{ \\
&\quad \Omega_x = \Omega_x - 360^\circ \textit{ while } \Omega_x \geq \Omega_{x-1} + 180^\circ, && (5.15) \\
&\quad \Omega_x = \Omega_x + 360^\circ \textit{ while } \Omega_x < \Omega_{x-1} - 180^\circ, && (5.16) \\
&\quad \omega_x = \omega_x - 360^\circ \textit{ while } \omega_x \geq \omega_{x-1} + 180^\circ, && (5.17) \\
&\quad \omega_x = \omega_x + 360^\circ \textit{ while } \omega_x < \omega_{x-1} - 180^\circ, && (5.18) \\
&\quad M_x = M_x - 360^\circ \textit{ while } M_x \geq M_{x-1} + 180^\circ, && (5.19) \\
&\quad M_x = M_x + 360^\circ \textit{ while } M_x < M_{x-1} - 180^\circ, && (5.20) \\
&\}
\end{aligned}$$

where x is the fragment/pseudo-fragment number and N is the total number of fragments or pseudo-fragments. The values of Ω_0, ω_0 and M_0 (assigned to fragment/pseudo fragment zero) are used as the initial datum points in the above pre-mapping process. The fragment/pseudo-fragment used for the datum points changes from x to x+1 with each iteration of the process.

Figures 5.51 and 5.53 show the result of pre-mapping on the corresponding plots in Figures 5.50 and 5.52 for the debris cloud produced by a low-speed impact induced breakup in GEO as modelled by the IDES breakup model after being propagated conventionally over 100 years. The scatter plots have been transformed by the pre-mapping process into meaningful distributions and the rogue fragments effectively removed by simply mapping certain fragments' RAAN and argument of perigee values by 360°.

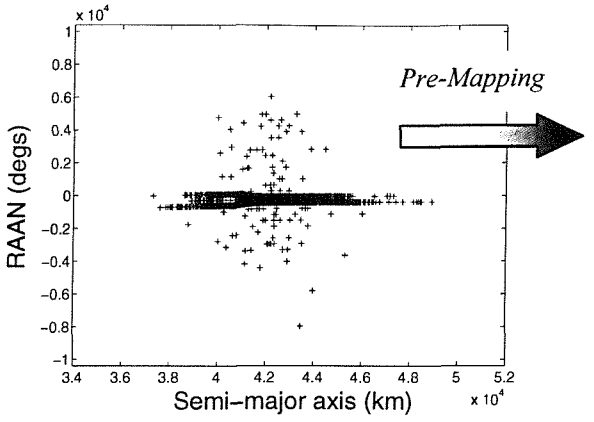

Figure 5.50 The a vs. Ω scatter plot after 100-year propagation following a low-speed collision

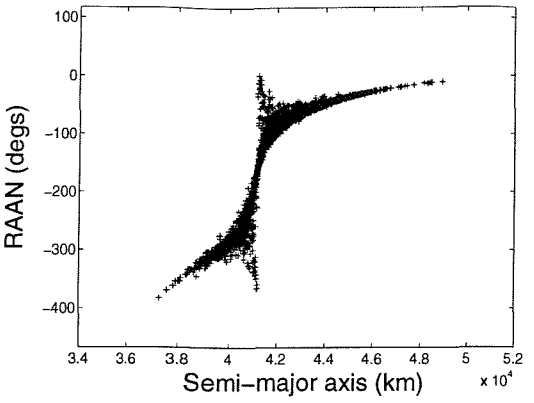

Figure 5.51 The pre-mapped a vs. Ω scatter plot after 100-year propagation following a low-speed collision

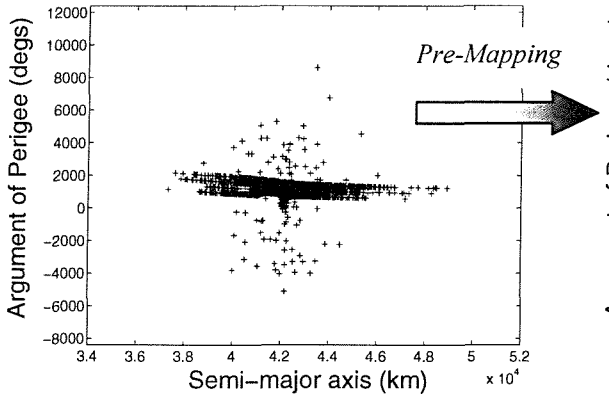

Figure 5.52 The a vs. ω scatter plot after 100-year propagation following a low-speed collision

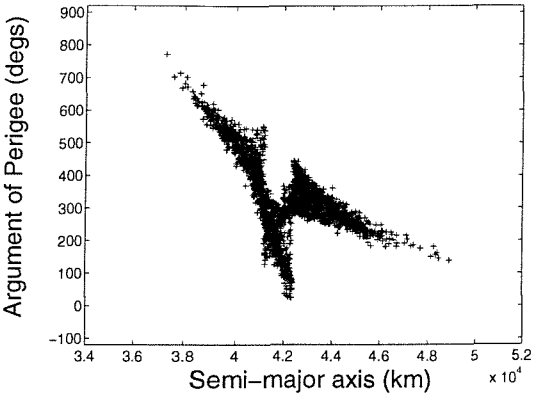

Figure 5.53 The pre-mapped a vs. ω scatter plot after 100-year propagation following a low-speed collision

The figure showing the pre-mapping effects on mean anomaly is omitted here because the range of values that mean anomaly takes after a 100-year propagation is so great that the effects of pre-mapping are not visible on the scatter plot when plotted to scale.

5.2.8 Mapping the Distribution Parameters (The 'Map Params' Routine)

The mapping of the fragments' orbital elements is also conducted in the 'Map Params' routine. Figure 5.49 shows the position of the 'Map Params' routine within the FCP.

This post-propagation mapping process maps the pseudo-fragments' elements from element-space to modified element-space, thus producing the continuous distributions required by the succeeding 'Unwrap' routine. The equations that define this mapping process are similar to those used in the pre-propagation mapping process used in the 'Map Frags' routine (see section 5.2.2). The main difference is that inclination is not mapped here, whereas it was mapped in the 'Map Frags' routine, and also the test used to decide whether mapping is necessary is different. The tests used in the pre-propagation mapping process depended on quadrant testing. However, these are only useful at the breakup epoch. Such tests would have no meaning following a lengthy propagation period. The equations that define the post-propagation mapping process are as follows:

$$\left.\begin{aligned} \Omega_{NEW} &= \Omega_{OLD} + 180^\circ \\ \omega_{NEW} &= \omega_{OLD} - 180^\circ \end{aligned}\right\} if\ a < a_{iMIN}, \tag{5.21}$$

$$\left.\begin{aligned} \omega_{NEW} &= \omega_{OLD} + 180^\circ \\ M_{\mathrm{NEW}} &= M_{OLD} - 180^\circ \end{aligned}\right\} if\ a < a_{eMIN}, \tag{5.22}$$

where the subscripts *NEW* and *OLD* refer to the new, mapped values of the elements and the old, unmapped values of the elements, respectively, and a_{iMIN} and a_{eMIN} represent the values of semi-major axis at the minimum values of inclination and eccentricity, respectively.

Equations 5.21 and 5.22 will only be executed if a V-plot exists in *a-i* space and *a-e* space, respectively. A V-plot will *usually* exist in *a-i* space if the inclination of the breakup orbit was such that $i \approx 0°$. Similarly, a V-plot will *usually* exist in a-e space if the eccentricity of the breakup orbit was such that $e \approx 0$. The a_{iMIN} and a_{eMIN} values essentially represent the lowest point in the V-plots that exist in *a-i* space and *a-e* space respectively. The test used to determine whether or not a V-plot exists in *a-e* space is simply

$$is\ e_{MIN} < 0.01$$

where e_{MIN} is the minimum value of eccentricity taken by any pseudo-fragment. A V-plot is assumed to exist in *a-e* space if the above expression is true. This expression is fast and has worked for every scenario run with the FCP.

A similar method to test the presence of a V-plot in *a-i* space proved ineffective, however, and a more robust, yet slower method had to be adopted. This method counts the number of times the orbit of each pseudo-fragment passes through the celestial equator, i.e. the $i = 0°$ plane, during the propagation phase. Each time this occurs, the orbit's RAAN changes by 180° in order to keep the inclination positive, as inclinations cannot take negative values (the argument of perigee also changes by 180°). This is performed by the DAMAGE propagator used in the FCP as part of the propagation process. If certain fragments' orbits have undergone changes of 180° in RAAN an even number of times and others have undergone changes of 180° in RAAN an odd number of times, bearing in mind the fragments' starting values of RAAN, then the propagated cloud lies across the celestial equator and a V-plot will exist in *a-i* space. The value of a_{iMIN} is then calculated and equation 5.21 is executed for each fragment, which effectively reverses the 180° changes in RAAN and argument of perigee undertaken during propagation to keep the inclinations of the fragments' orbits positive. This method requires a test to be undertaken during the propagation of each pseudo-fragment at each time-step and is thus very time consuming. The method to test for a V-plot in *a-e* space, although not as robust, is much faster, as it only requires one test at the end of the

propagation period. Thus, for example, in a 100-year simulation with an 8-day time-step, the V-plot test in *a-e* space is over 333,000 times faster than the V-plot test in *a-i* space.

The values of eccentricity and inclination have not been mapped since they already form continuous number distributions. Mapping RAAN, argument of perigee and mean anomaly without mapping eccentricity and inclination effectively changes the positions of the fragments. However, these changes will be fully reversed in the post-unwrapping 'Unmap Frags' routine.

The effect of pre-mapping and post-propagation mapping on the distribution parameters following 100-year propagation from a low speed impact in GEO is illustrated in Figures 5.54 – 5.57. Figures 5.54 and 5.55 show the effect of pre-mapping and mapping on the RAAN and Figures 5.56 and 5.57 show the effect of pre-mapping and mapping on argument of perigee. For reasons of clarity, these mappings are shown with respect to semi-major axis. Again, the effects of pre-mapping and mapping on the values of mean anomaly have been omitted because the data range in mean anomaly is so large after a 100-year propagation that the 360° mapping procedures would not be visible when plotted to scale.

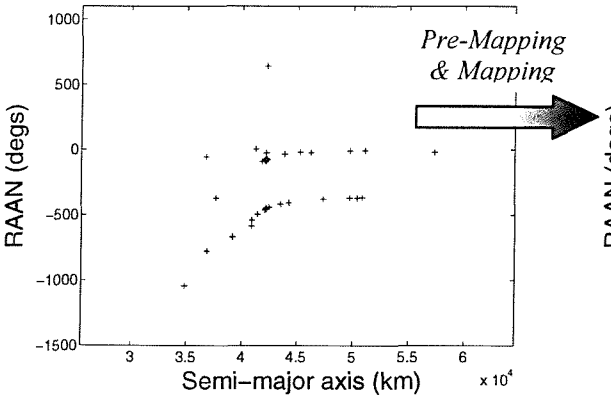

Figure 5.54 The distribution parameters in *a-Ω* space having been propagated over 100 years after a breakup in GEO

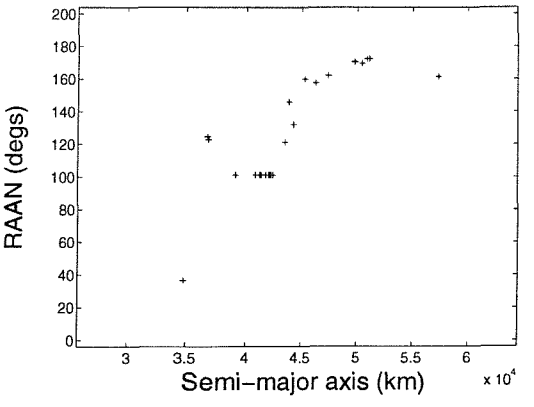

Figure 5.55 The mapped distribution parameters in *a-Ω* space having been propagated over 100 years after a breakup in GEO

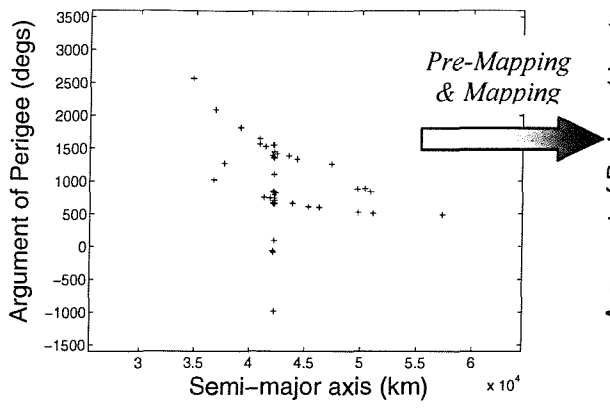

Figure 5.56 The distribution parameters in a-ω space having been propagated over 100 years after a breakup in GEO

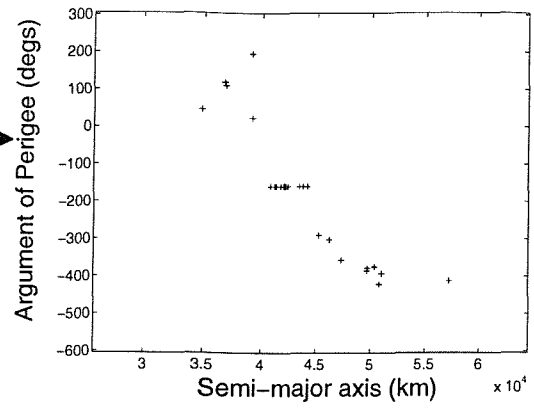

Figure 5.57 The mapped distribution parameters in a-ω space having been propagated over 100 years after a breakup in GEO

The original, unmapped distributions have a high variance, which makes the underlying trend difficult to distinguish. In the mapped distributions, however, the underlying trend can be distinguished clearly. These mapped distributions are used to re-construct the values of RAAN and argument of perigee.

5.2.9 Re-creating the Debris Cloud (The 'Unwrap' Routine)

The distributions are effectively 'unwrapped' and the fragments' orbital elements recovered in the 'Unwrap' routine. Figure 5.58 re-creates the FCP flowchart from Figure 5.36 and highlights the position of the 'Unwrap' routine within the FCP.

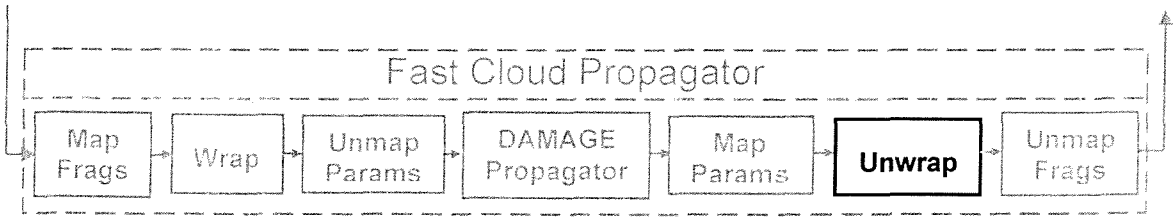

Figure 5.58 The position of the Unwrap module in the FCP

Once the distribution parameters have been propagated, the new position and shape of the hyperellipsoid in element-space can be reconstructed from the size parameters. Pseudo-fragment zero will denote the modes of each of the number distributions and pseudo-fragments 1 – 12 will denote the upper and lower limits of each of these distributions. Hence the new number distributions can be totally reconstructed from the propagated size parameters and a knowledge of the total number of fragments in the debris cloud, which of course remains constant. However, the real challenge is to re-create the element-relationships using the element-relationship scatter plots. Both the size parameters (pseudo-fragments 0 – 12) and spread parameters (pseudo-fragments 13 – 72) will be needed for this purpose.

Only five scatter plots need to be re-created by the Unwrap function directly, since only five scatter plots are required by the FCP to describe a six-dimensional distribution. The first element will be sampled from its number distribution and the remaining five elements will be sampled from the relevant scatter plots, thus recovering all the orbital elements for each fragment. The five scatter plots that are re-created directly by the FCP shall be called the *primary scatter plots*. The remaining ten scatter plots shall be called the *secondary scatter plots*. These will be re-created indirectly as a function of re-creating the five primary plots. The variance of the scatter plot (i.e. the variance of y for any given value of x in an x-y scatter plot) is crucial in deciding which should be the primary scatter plots. Scatter plots with the lowest variance are chosen, provided each one yields the value of a new orbital element, as this will reduce the error in the reconstructed debris cloud. Scatter plots with small variances yield a value of y that is randomised by a smaller amount for any given value of x in an x-y scatter plot. By using primary scatter plots with small variances (e.g. Figure 5.21), the secondary scatter plots with larger variances (e.g. Figure 5.26) will be reconstructed accurately. The opposite is not true, however. Primary plots with large variances will not necessarily result in accurate secondary scatter plots that have relatively small variances.

For non-geostationary orbits, empirical analysis has shown that the scatter plots with the lowest scatter are usually the a vs. e, a vs. i, a vs. Ω, a vs. ω, and a vs. M scatter plots.

However for geostationary orbits the plots with the minimum scatter are the a vs. e, a vs. i, e vs. Ω, e vs. ω, and a vs. M scatter plots. The original version of the 'Unwrap' function utilised a dynamic method of selecting the primary scatter plots on a case by case basis according to the criteria of smallest variance described above. This method proved very complex and time-consuming however and offered little improvement in accuracy. It was noted that the method almost always chose the aforementioned primary scatter plots. Whenever this dynamic method chose a primary scatter plot that was not in the above list, the difference in variance between the scatter plot chosen and the one it replaced in the aforementioned list was so small that it offered no noticeable improvement in accuracy. This dynamic method was thus eventually abandoned in favour of the static method described.

An example of the primary scatter plots showing the propagated pseudo-fragments' element relationships are depicted in Figures 5.59 – 5.63. These show the positions of the pseudo-fragments after 80 years following a low-speed impact induced breakup in an arbitrary non-geostationary orbit (a = 42165.0 km, e = 0.4, i = 40°, Ω = 70°, ω = 120°, and M = 0°). The scatter plots showing only the pseudo-fragments shall henceforth be referred to as the *skeletal scatter plots*, as they essentially provide the skeleton for the scatter plots that show all the fragments' elements.

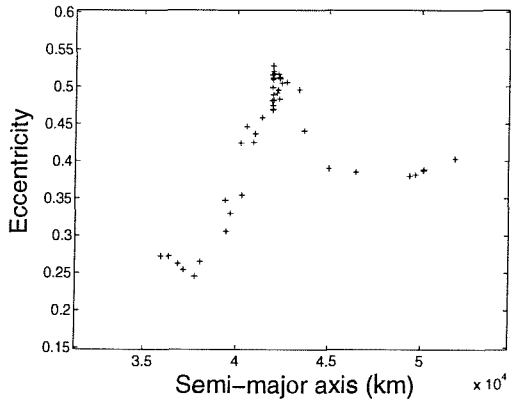

Figure 5.59 The skeletal semi-major axis vs. eccentricity scatter plot after 80 years

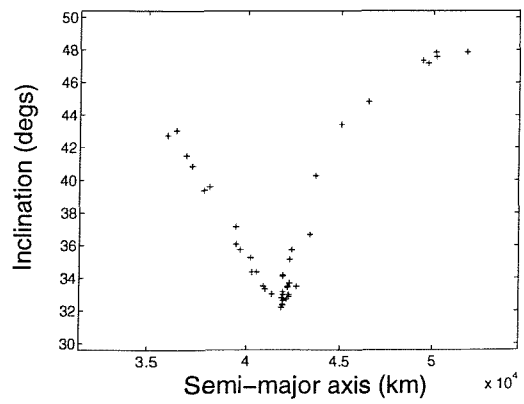

Figure 5.60 The skeletal semi-major axis vs. inclination scatter plot after 80 years

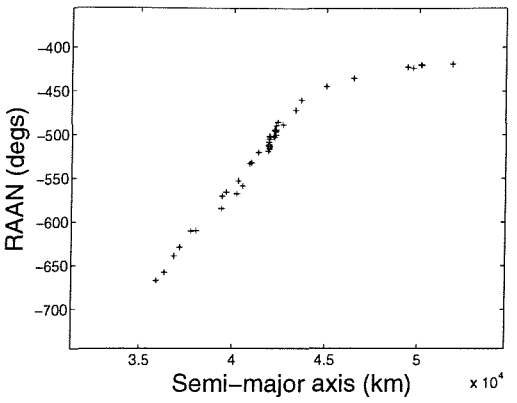

Figure 5.61 The skeletal semi-major axis vs. RAAN scatter plot after 80 years

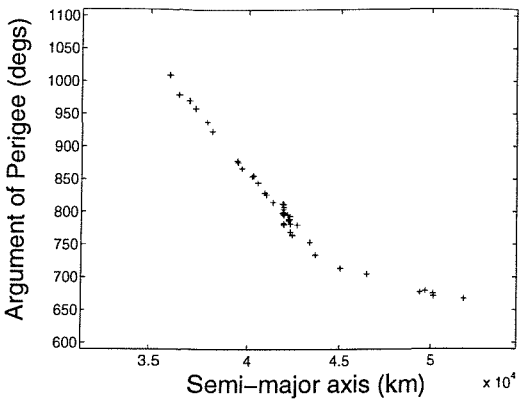

Figure 5.62 The skeletal semi-major axis vs. argument of perigee scatter plot after 80 years

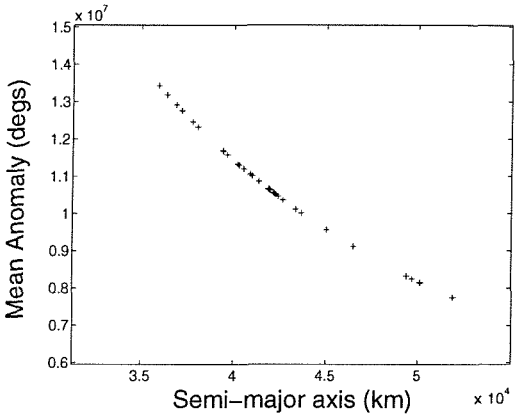

Figure 5.63 The skeletal semi-major axis vs. mean anomaly scatter plot after 80 years

5.2.9.1 The Isotropic Test

Before the fragments' orbital elements can be recovered, an isotropic test must be used to ascertain whether the scatter plot distribution is isotropic or not. This affects the way in which the FCP attempts to re-create the scatter plot. The isotropic test is performed by superimposing a 5 × 5 grid on to the scatter plot as illustrated in Figure 5.64. The 4 shaded grid boxes shown in the diagram are flag squares – if a pseudo-fragment is detected within one of these squares then a flag is raised, and if all 4 flags are raised then the distribution is assumed to be isotropic. The squares are centred on the modes of the number distributions for the *x*- and *y*-axis elements, as shown in the diagram. The sizes of

the squares have been optimised through empirical analysis to 20% of the data range of each element.

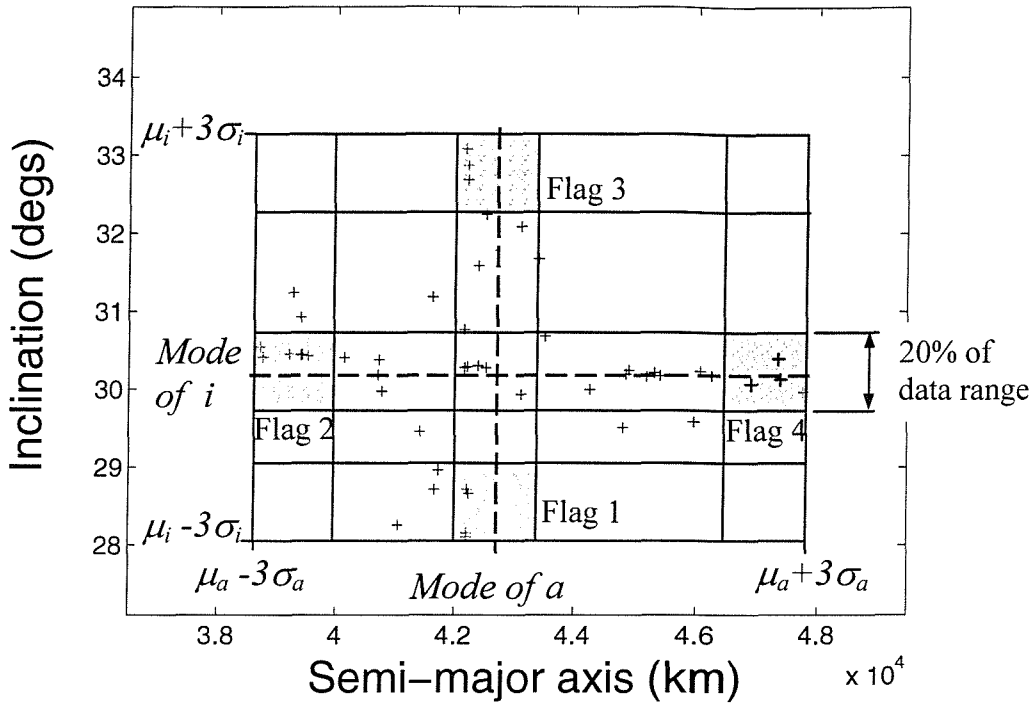

Figure 5.64 The isotropic test grid superimposed over a scatter plot with an isotropic distribution of pseudo-fragments

The number distributions are now classified as either normal or gamma distributions, where a shape parameter, γ, is calculated in order to define the exact shape of the gamma distribution. Unfortunately, the gamma distribution's probability density function (equation 5.2) cannot be re-arranged to yield the value of γ. Hence the value of γ which best matches the distribution shape must be determined iteratively. It should be noted at this point that the numerical method for generating normal distributions, the Polar method, is much faster than the Gamdev function used for generating gamma distributions. Thus if at all possible, the Polar method is used to generate the distributions. The distribution can be classified by comparing the value of the mode with that of the median. If the mode is within a certain tolerance of the median then the distribution can be classified as normal, otherwise it must be classified as a gamma distribution and the Gamdev numerical method must be used. This value of the tolerance has also been optimised through empirical analysis to 20% of the data range.

This value of 20% and the value of 20% used in the isotropic test grid were optimised through a process of trial-and-error by trying various values for different scenarios, breakup orbits and propagation periods and visually comparing the resulting element-relationship scatter plots and number distributions with those produced by the conventional propagation of the same debris clouds. Indeed, other values close to 20% may also have produced the desired result for many scenarios, but the value of 20% was eventually chosen and has been used successfully in several hundred simulations. The author has thus developed a high level of confidence in this value of 20% for both tests over time.

5.2.9.2 Re-creating the Debris Cloud for Orbits with $e \neq 0$ and $i \neq 0°$

The scatter plots can be reconstructed using the number distributions of the two elements represented by the x and y-axes of the scatter plots and some knowledge of the general shape of the scatter plot. If the scatter plot is non-isotropic then the general shape of the scatter plot is ascertained by fitting a curve to the data points in the skeletal scatter plots, which is done using the least-squares method. The least-squares method is an iterative method that attempts to fit a curve to a series of data points whilst minimising the sum of the squares of the distances between each of the data points and the curve. Thus a best-fit curve to a set of data points is produced. The FCP uses a numerical method called 'Leasqr' to perform the least-squares iterations [91]. This method was chosen because of its speed compared to other, more complex methods [85, 92-94]. It is able to fit a polynomial with up to 8 degrees of freedom to a set of data points.

Given enough degrees of freedom, the least-squares method can produce a fit which is perfect, i.e. a curve that passes through all the data points. However, this may not be the fit that best matches the overall trend. For example, the overall trend may require 2 degrees of freedom (as in Figure 5.63, for instance) but it is possible that the curve with the lowest RMS error that best fits the data in the corresponding skeleton scatter plot has

3 or 4 degrees of freedom. Whilst this best matches the data in the skeleton scatter plot, it is not the optimum solution. The degrees of freedom allowed for each of the primary scatter plots has thus been limited as a function of propagation time. This is because the scatter plots require more and more degrees of freedom with increasing time, particularly in the a vs. e and a vs. i scatter plots. The limitations on the degrees of freedom allowed for each of the primary scatter plots are presented in Table 5.3.

Propagation Time (yrs.)	Primary Scatter Plot				
	a vs. e	a vs. i	a vs. Ω	a vs. ω	a vs. M
< 2	1	1	1	1	≤ 2
< 15	≤ 3	≤ 2	≤ 2	≤ 2	≤ 2
≥ 15	≤ 8	≤ 5	≤ 3	≤ 3	≤ 3

Table 5.3 Limitations on the degrees of freedom permissible for the primary scatter plots as a function of propagation time.

The limitations on the degrees of freedom for the primary scatter plot curves expressed in Table 5.3 were again calculated by the author on a trial-and-error basis based on a number of test runs (see Chapter 6). The degrees of freedom for each scatter plot as a function of time were ascertained from the visual analysis of a number of conventionally propagated debris clouds. It was discovered that the a vs. e scatter plot in particular required a large number of degrees of freedom with increasing propagation time. However, after ~15 years the least-squares method was able to choose the optimum number of degrees of freedom with a greater rate of success for the a vs. e scatter plot, based on the lowest RMS value. This was largely due to the greater spread of pseudo-fragments in a-e space after this time. After 15 years the limitation on the degrees of freedom in the a vs. e scatter plot was thus increased to the maximum value of 8 permitted by the least-squares method used.

The least-squares curve is by definition the mean line through all the data points. An assumption must be made here that the mean line through the data points in the skeletal scatter plots is also the mean line through the data points in the scatter plots containing all the fragments' elements. However, the Unwrap function randomises the orbital elements

of the fragments about the mode lines, not the mean lines. The number distributions of fragments in the cross-sections of scatter plots are normal in the majority of cases, thus the mean lines and mode lines are the same. However, equating the mean lines and mode lines for cross-sections approximating to gamma number distributions, where the mode is offset from the mean, is an assumption. The accuracy of this assumption depends upon the skewness of the distribution. For example, if the gamma distribution is not at all skewed then it approximates to a normal distribution and the assumption holds true. The more skewed the distribution, however, the greater the offset between the mean and the mode. The best-fit curves fitted by the least-squares method shall thus be referred to as the *mode lines*, since they are assumed to give the coordinates of the modes of the number distributions. Figures 5.65 – 5.69 illustrate the skeletal scatter plots from Figures 5.59 – 5.63 with the least-squares mode lines fitted to them.

If at the required epoch, the fragments' orbits take values with $e \approx 0$ then the a vs. e primary scatter plot will be fitted with intersecting linear mode lines and the e vs. ω primary scatter plot (again with intersecting linear mode lines) will be used in place of the a vs. ω primary scatter plot. If the fragments' orbits take values with $i \approx 0°$ then the a vs. i scatter plot will also be fitted with intersecting linear mode lines and the e vs. Ω primary scatter plot (which will also be fitted with linear intersecting mode lines) will be used in place of the a vs. Ω primary scatter plot. Thus Table 5.3 is partly irrelevant to orbits with $e \approx 0$ or $i \approx 0°$, as these will not use polynomial curves fitted using the least-squares method. The method of fitting the linear intersecting mode lines to the primary scatter plots for orbits with $e \approx 0$ or $i \approx 0°$ is explained in the next section.

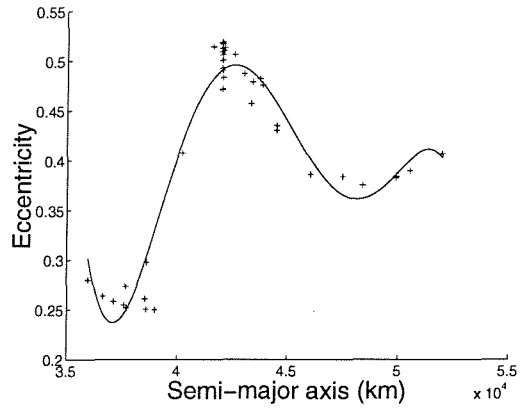

Figure 5.65 The semi-major axis vs. eccentricity skeletal scatter plot with least-squares curve

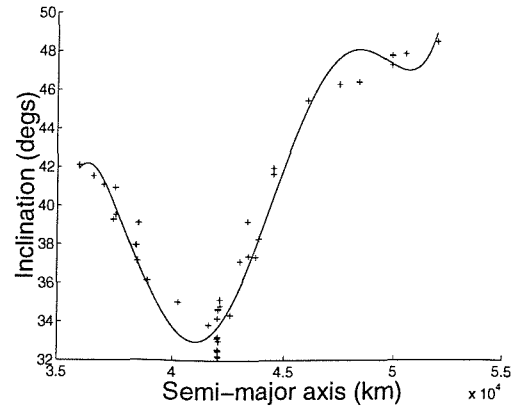

Figure 5.66 The semi-major axis vs. inclination skeletal scatter plot with least-squares curve

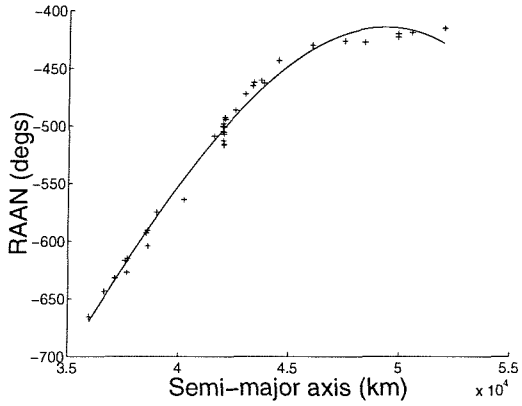

Figure 5.67 The semi-major axis vs. RAAN skeletal scatter plot with least-squares curve

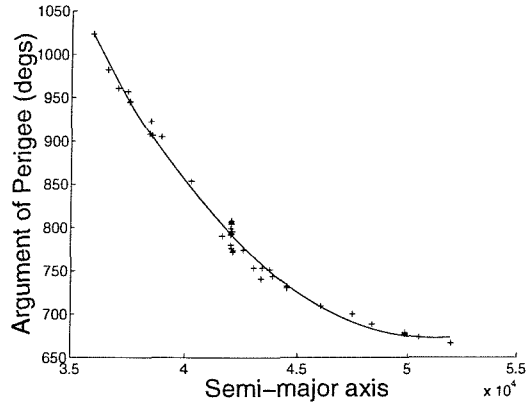

Figure 5.68 The semi-major axis vs. argument of perigee skeletal scatter plot with least-squares curve

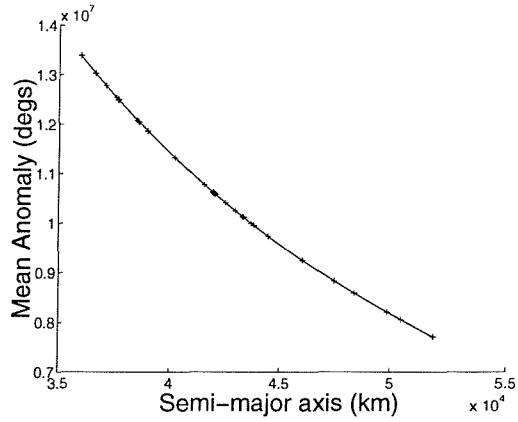

Figure 5.69 The semi-major axis vs. mean anomaly skeletal scatter plot with least-squares curve

For isotropic scatter plots, where there is no relationship between the scatter plot's x-axis and y-axis elements, there is no need to fit a curve using the least squares method. In this case, an equation of $y = y_{MODE}$ is used for the mode line, where y_{MODE} is the mode of the number distribution in y. This effectively allows the y-axis elements to be randomly assigned to the x-axis elements and saves time by not executing the iterative least-squares method.

Having obtained the mode lines for the 5 primary scatter plots, these scatter plots can now be fully re-created. The Unwrap function calculates the equations of the mode lines. For example, a mode line with 3 degrees of freedom in an x vs. y primary scatter plot will have an equation of the form

$$y = ax^3 + bx^2 + cx + d\,, \tag{5.23}$$

where a, b, c and d are constants that are calculated by the least-squares method. An input value of x is used to calculate a corresponding value of y. The y value can be randomised by assuming that it represents the mode of the number distribution in a cross-section through y at the value of x in the x vs. y scatter plot. Depending on whether the number distribution in y is a normal or gamma distribution, the Polar or Gamdev numerical methods can be used respectively to randomise the value of y. Consider the following example, which describes how the values of semi-major axis and eccentricity are recovered. First, a value of semi-major axis is sampled from the semi-major axis normal number distribution using the Polar method. This value of a is then used to find a corresponding value of e in the a vs. e scatter plot, according to the mode line equation which gives $e = f(a)$. This yields the most likely value of eccentricity for the input semi-major axis value, or e_{MODE}. Figure 5.70 re-creates the a vs. e scatter plot from Figure 5.21 and assumes an input semi-major axis value of 42500 km. The fragments taken from a 1000 km cross-section (about a = 42500 km) are plotted in the number distribution in eccentricity on right-hand side of the Figure. (The cross-section of 1000 km is chosen purely for illustration purposes in this example.)

The input value of a = 42500 km yields an e_{MODE} value of 0.29 from the equation of the mode line. This represents the mode of the number distribution in the cross-section shown on the right hand side of the Figure.

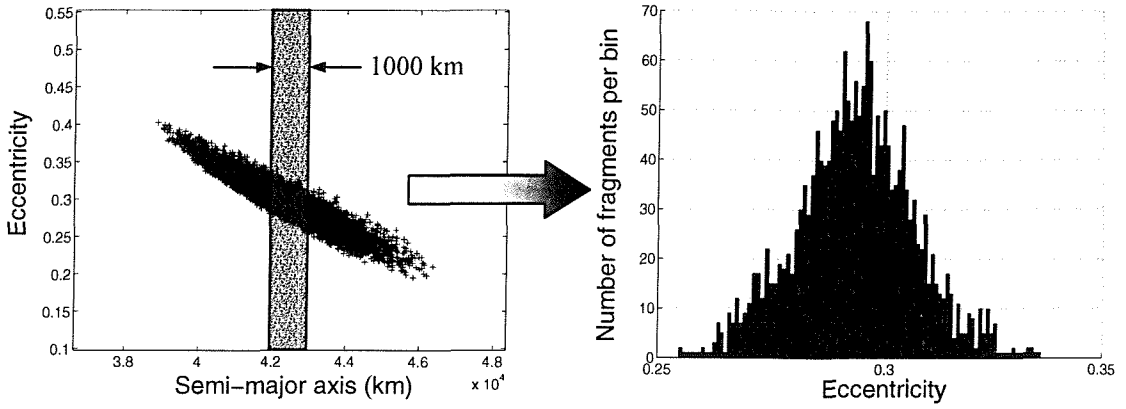

Figure 5.70 A 1000 km cross-section taken through the semi-major axis vs. eccentricity scatter plot (left) and the resulting number distribution in eccentricity in that cross-section (right)

A randomising spreading function is applied to the calculated mode value of eccentricity. For the example in Figure 5.70, this spreading function is a normal distribution, as shown in the number distribution on the right hand side of the Figure. However, the exact shape of this normal number distribution must first be defined. This is done using the mode value and the upper and lower limits of the distribution. The eccentricity mode value has already been calculated using the least-squares mode line equation, but the upper and lower limits of the distribution have yet to be recovered. The cross-section taken through the scatter plot will vary depending on the input semi-major axis value and the mode value will vary accordingly. However, the variance of the distribution will be assumed to remain the same, even though it clearly varies depending on where the cross-section is taken. The reason for this will become clear later in this section. The maximum variance will be used in every cross-section number distribution, regardless of where the cross-section is taken. The maximum variance is calculated by taking all the data points in the skeletal scatter plots and calculating their vertical distance away from the mode line, as illustrated in Figure 5.71. This is done separately for all data points above and below the mode line, thus generating a maximum positive distance and a maximum negative

distance from the mode line (given by the encircled fragments in Figure 5.71). These are then converted to the maximum upper limit and the maximum lower limit and are used in all distribution cross-sections.

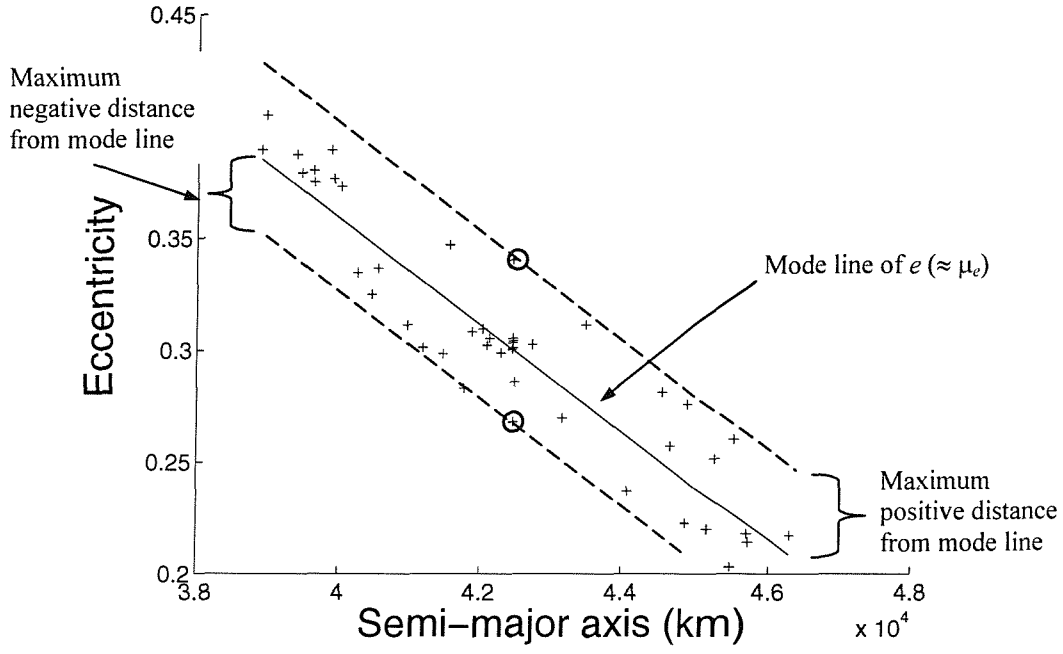

Figure 5.71 A skeletal scatter plot showing how the maximum upper and lower limits are calculated for the distribution cross-sections

With the knowledge of these three parameters, the number distribution cross-sections can now be classified as either normal distributions, or gamma distributions and the shape parameter calculated. This allows the eccentricity value to be randomised by sampling it from this distribution, which will correspond to the input semi-major axis value.

So how can one assume the maximum variance for all cross-sections through the scatter plot and why does this invalid assumption still work? Consider the case illustrated in Figure 5.70. The mode of the semi-major axis number distribution coincides with the location of the maximum variance in eccentricity in the a vs. e scatter plot, as must always be the case. As the value sampled from the semi-major axis number distribution deviates more and more from its mode value, the probability of sampling that value of semi-major axis decreases, by definition. As fewer values of semi-major axis are sampled, fewer corresponding values of eccentricity need to be sampled. With fewer

values of eccentricity being sampled at the edge of the semi-major axis number distribution, the probability of sampling a value of eccentricity with the maximum variance (from the number distribution cross-section in eccentricity) is considerably decreased. Thus even though the maximum variance is assumed for the eccentricity number distribution cross-section at every point, the sampled values of eccentricity at the edges of the semi-major axis number distribution will not have as great a variance as those cross-sections where the number of samples is greater. Therefore, the variance of the sampled eccentricity values changes as a function of the number distribution in semi-major axis. This provides a quick and simple method of accounting for the change in the variance observed throughout the scatter plot, and is furthermore compatible with the limited amount of information available from the propagated distribution parameters.

Once a corresponding value of eccentricity is chosen for the sampled semi-major axis value then the same procedure is used to sample corresponding values for inclination, RAAN, argument of perigee and mean anomaly. This process is repeated for each fragment until the elements have been assigned to all the fragments in the debris cloud. This process is illustrated in Figure 5.72, which shows how the scatter plots are reconstructed when the pseudo-fragments' orbits are such that $e \neq 0$.

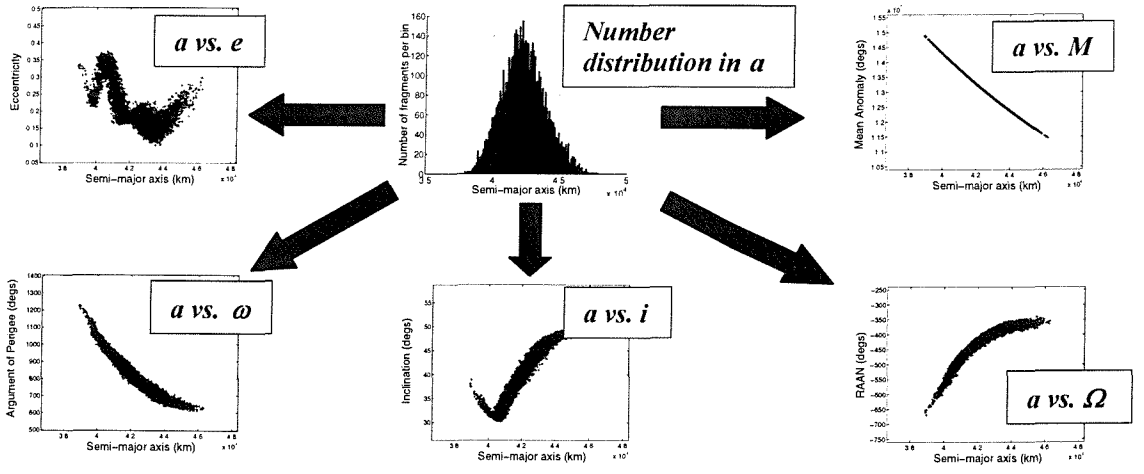

Figure 5.72 The order of cloud reconstruction when the pseudo-fragments' orbits are such that $e \neq 0$

5.2.9.3 Re-creating the Debris Cloud for Orbits with $e \approx 0$ and $i \approx 0°$

Figure 5.73 shows how the scatter plots are reconstructed if a V-plot exists in *a-e* space. A V-plot will usually exist in *a-e* space if any of the pseudo-fragments' orbits are such that $e \approx 0$. This situation tends to occur for breakup orbits with $e \approx 0$. When the pseudo-fragments' orbits are such that $i \approx 0°$, but $e \neq 0$, the scatter plots are re-constructed in the order shown in Figure 5.72. However, a V-plot will still need to be replicated in *a-i* space and the method for re-constructing V-plots is described in this section. An obvious example of an orbit with $i \approx 0°$ and $e \approx 0$ is GEO. The test for determining the existence of these V-plots was described in section 5.2.7.

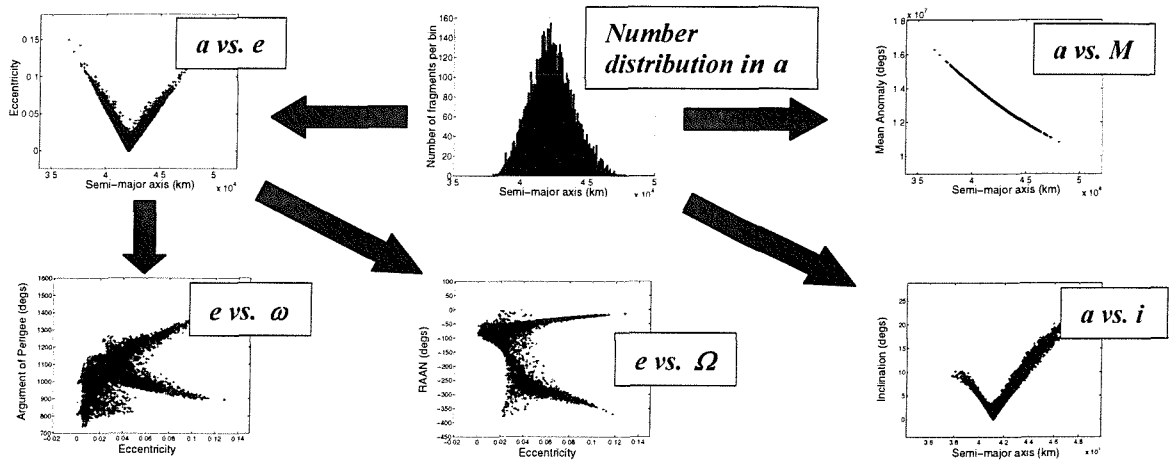

Figure 5.73 The order of cloud reconstruction when the pseudo-fragments' orbits are such that $e \approx 0$

Figure 5.72 represents the ideal scenario, where all the elements are created using the semi-major axis as an input. This reduces the errors in the re-created debris cloud to a minimum. In Figure 5.73, however, the values of RAAN and argument of perigee are re-created from eccentricity, which in turn is re-created using semi-major axis. This causes any errors in the semi-major axis and eccentricity distributions to be passed on to the RAAN and argument of perigee, whereas in Figure 5.72, the accuracy of the RAAN and argument of perigee are only dependent upon the accuracy of the semi-major axis distribution. The eccentricity distribution is used to re-create the RAAN and argument of perigee values for orbits with $e \approx 0$ because here the a vs. Ω and a vs. ω scatter plots

cannot be re-created easily using the FCP methodology. Figure 5.74 shows an a vs. ω scatter plot in modified element-space immediately following a LSI-induced breakup in GEO. It also shows the 2 dimensional binning of fragments in a-ω space – this is the equivalent of the a vs. ω scatter plot and the semi-major axis and argument of perigee number distributions all consolidated into one plot. The 3D plot clearly shows two distinct peaks, one at either extreme of the argument of perigee axis. This distribution could not have been re-created by distributing the fragments about a single mode line in a-ω space, as is current practice for orbits with $e \neq 0$, for instance. The only way to create the bi-modal distribution shown is with two distributions superimposed on top of one another. Two mode lines are required, with the fragments distributed about one of these using a gamma distribution and distributed about the other using a reversed gamma distribution. This can be done far more easily in modified e-ω space, where two mode lines intersect to form a V-shape (see the e vs. ω plot in Figure 5.73) and a gamma and reversed gamma distribution can be used to distribute the fragments about these mode lines, thus re-creating the bi-modal distribution illustrated in Figure 5.74. The same argument applies to re-creating the RAAN values in orbits where $e \approx 0$.

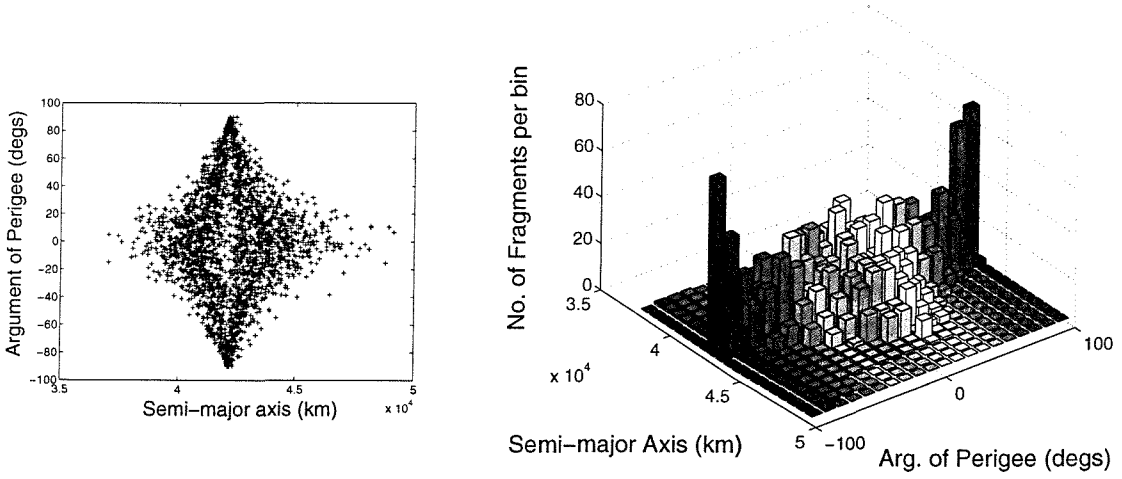

Figure 5.74 The a vs. ω distribution at the breakup epoch, as generated by a low-speed collision modelled by IDES. The 3-dimensional plot on the right shows the fragment density in the scatter plot on the left.

The V-shaped linear mode lines used to reconstruct the propagated values of eccentricity, inclination, RAAN and argument of perigee when a V-plot exists in *a-e* space and *a-i* space are shown in Figures 5.75 – 5.79 for a low-speed impact induced breakup in GEO as modelled by the IDES breakup model. The mean anomaly is reconstructed using a least-squares fitted polynomial as illustrated in Figure 5.79. The assumption of linear intersecting mode lines forming a V-shape for the a vs. e, a vs. i, e vs. Ω and e vs. ω scatter plots correlates well with the observed data (see Chapter 6) and its construction is much faster than that of a curved mode line, as it does not require the execution of the iterative least-squares routine.

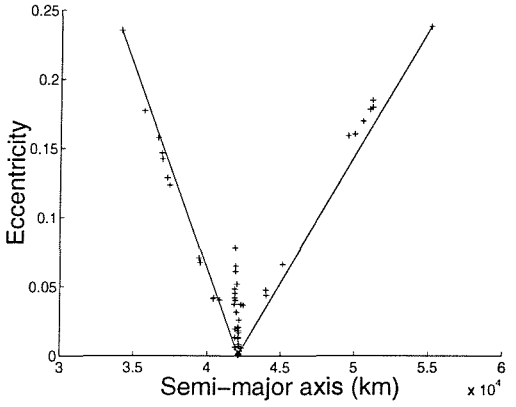

Figure 5.75 The skeletal scatter plot in *a-e* space with mode lines fitted after a 100-year propagation from a low-speed impact event in GEO.

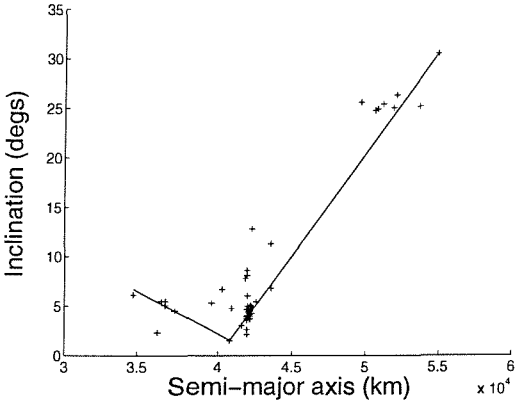

Figure 5.76 The skeletal scatter plot in *a-i* space with mode lines fitted after a 100-year propagation from a low-speed impact event in GEO.

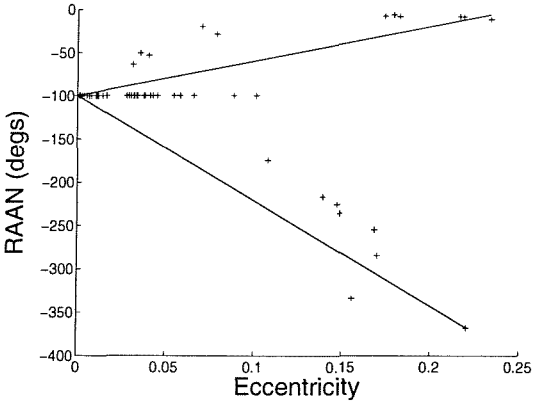

Figure 5.77 The skeletal scatter plot in modified *e-*Ω space with mode lines fitted after a 100-year propagation from a low-speed impact event in GEO.

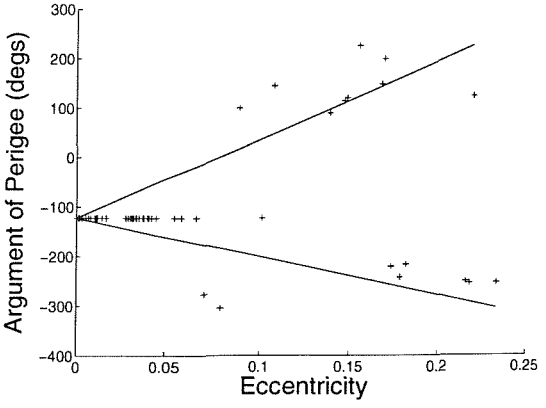

Figure 5.78 The skeletal scatter plot in modified *e-*ω space with mode lines fitted after a 100-year propagation from a low-speed impact event in GEO.

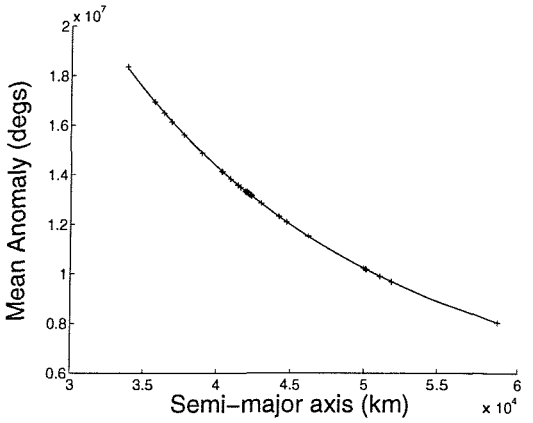

Figure 5.79 The skeletal scatter plot in modified *a-M* space with mode lines fitted after a 100-year propagation from a low-speed impact event in GEO.

It is not feasible to use the least-squares method to fit the linear mode lines required in the V-plots since the V-plots must intersect at $e = 0$ (for the V-plots in *a-e* space, *e-ω* space and *e-Ω* space) and must intersect at $i = 0°$ (for the V-plot in *a-i* space). This will not happen if the least-squares method is used to fit the lines. The slow, iterative least-squares method is also inefficient at plotting straight lines for the V-plots when other, faster methods are available, which are just as reliable. The equations for the intersecting linear mode lines required for the V-plots are of the form

$$y = mx + c, \tag{5.24}$$

where x and y are x-axis and y-axis elements, m is the gradient and c is the ordinate at $x = 0$. After sampling a value of a from the normal distribution in semi-major axis, the values of the remaining unrandomised elements may be recovered from the equations of the mode lines as follows:

$$e = -\left(\frac{e_{MAX(LHS)} - e_{MIN}}{a_{eMIN} - a_{MIN}}\right)a + \left[e_{MIN} + \left(\frac{e_{MAX(LHS)} - e_{MIN}}{a_{eMIN} - a_{MIN}}\right)a_{eMIN}\right] \text{ if } a \le a_{eMIN}, \tag{5.25}$$

$$e = \left(\frac{e_{MAX(RHS)} - e_{MIN}}{a_{MAX} - a_{eMIN}} \right) a + \left[e_{MIN} - \left(\frac{e_{MAX(RHS)} - e_{MIN}}{a_{MAX} - a_{eMIN}} \right) a_{eMIN} \right] \text{if } a > a_{eMIN}, \tag{5.26}$$

$$i = -\left(\frac{i_{MAX(LHS)} - i_{MIN}}{a_{iMIN} - a_{MIN}} \right) a + \left[i_{MIN} + \left(\frac{i_{MAX(LHS)} - i_{MIN}}{a_{iMIN} - a_{MIN}} \right) a_{iMIN} \right] \text{if } a \le a_{iMIN}, \tag{5.27}$$

$$i = \left(\frac{i_{MAX(RHS)} - i_{MIN}}{a_{MAX} - a_{iMIN}} \right) a + \left[i_{MIN} - \left(\frac{i_{MAX(RHS)} - i_{MIN}}{a_{MAX} - a_{iMIN}} \right) a_{iMIN} \right] \text{if } a > a_{iMIN}, \tag{5.28}$$

$$\omega = \left(\frac{\omega_{MAX} - \omega_{eMIN}}{e_{MAX(TOP)} - e_{MIN}} \right) e + \left[\omega_{eMIN} - \left(\frac{\omega_{MAX} - \omega_{eMIN}}{e_{MAX(TOP)} - e_{MIN}} \right) e_{MIN} \right] \text{if} \begin{cases} a > a_{eMIN} \ \& \ \omega_{aMAX} > \omega_{aMIN} \\ a \le a_{eMIN} \ \& \ \omega_{aMAX} \le \omega_{aMIN} \end{cases}, \tag{5.29}$$

$$\omega = -\left(\frac{\omega_{eMIN} - \omega_{MIN}}{e_{MAX(BOT)} - e_{MIN}} \right) e + \left[\omega_{eMIN} + \left(\frac{\omega_{eMIN} - \omega_{MIN}}{e_{MAX(BOT)} - e_{MIN}} \right) e_{MIN} \right] \text{if} \begin{cases} a > a_{eMIN} \ \& \ \omega_{aMAX} \le \omega_{aMIN} \\ a \le a_{eMIN} \ \& \ \omega_{aMAX} > \omega_{aMIN} \end{cases}, \tag{5.30}$$

$$\Omega = \left(\frac{\Omega_{MAX} - \Omega_{eMIN}}{e_{MAX(TOP)} - e_{MIN}} \right) e + \left[\Omega_{eMIN} - \left(\frac{\Omega_{MAX} - \Omega_{eMIN}}{e_{MAX(TOP)} - e_{MIN}} \right) e_{MIN} \right] \text{if} \begin{cases} a > a_{eMIN} \ \& \ \Omega_{aMAX} > \Omega_{aMIN} \\ a \le a_{eMIN} \ \& \ \Omega_{aMAX} \le \Omega_{aMIN} \end{cases}, \tag{5.31}$$

$$\Omega = -\left(\frac{\Omega_{eMIN} - \Omega_{MIN}}{e_{MAX(BOT)} - e_{MIN}} \right) e + \left[\Omega_{eMIN} + \left(\frac{\Omega_{eMIN} - \Omega_{MIN}}{e_{MAX(BOT)} - e_{MIN}} \right) e_{MIN} \right] \text{if} \begin{cases} a > a_{eMIN} \ \& \ \Omega_{aMAX} \le \Omega_{aMIN} \\ a \le a_{eMIN} \ \& \ \Omega_{aMAX} > \Omega_{aMIN} \end{cases}, \tag{5.32}$$

where the subscripts *MIN* and *MAX* are the minimum and maximum values of the elements, respectively. The notation y_{xMIN}, where x and y are orbital elements, means the value of y, for which x is a minimum. The subscripts *MAX(LHS)* and *MAX(RHS)* refer to the maximum values of the elements on the left-hand side and right-hand, respectively, of the a vs. e and a vs. i scatter plots. Similarly the subscripts *MAX(TOP)* and *MAX(BOT)* refer to the maximum values of the elements at the top portion and bottom portion, respectively, of the e vs. ω or e vs. Ω scatter plots. In each case, the division between the left and right hand sides of the scatter plot or the top and bottom of the scatter plots are

given by the relevant y_{xMIN} value. Thus, for example, the left-hand side of the a vs. e scatter plot is defined by all values of a for which $a \leq a_{eMIN}$. Similarly the right-hand side of the scatter plot is defined by all values of a for which $a > a_{eMIN}$.

The relationship between the left-hand side and right-hand side of the a vs. e scatter plot and the top and bottom portions of the e vs. ω and e vs. Ω scatter plots is dictated by the sign of the gradient of the a vs. ω and a vs. Ω scatter plots, respectively. This accounts for the expanded 'if' statements in the calculation of ω and Ω. The sign of the gradient of the a vs. ω and a vs. Ω scatter plots is determined by comparing the ω_{aMAX} and ω_{aMIN} values, in calculating the value of ω, and the Ω_{aMAX} and Ω_{aMIN} values, in calculating the value of Ω. For example, if $\Omega_{aMAX} > \Omega_{aMIN}$ then the gradient in the a vs. Ω scatter plot is positive, in which case the values of e calculated from the left-hand side of the a vs. e scatter plot correspond to the values of e in the bottom portion of the e vs. Ω scatter plot. These relationships are important, since, given the V-plots in e-Ω space and e-ω space (see Figures 5.77 and 5.78, respectively), an input value of e will yield two output values of ω and Ω. It is necessary to know which is the correct value, and this can be determined from the corresponding value of a, as described. The value of mean anomaly is calculated using the least-squares iterative process, as described in section 5.2.8.2.

The values of eccentricity, inclination, argument of perigee and RAAN are randomised using a gamma distribution (see equation 5.2) or reversed gamma distribution. The randomised values of the elements are sampled from a reverse gamma distribution in the same way as they are sampled from a gamma distribution, using the 'Gamdev' numerical method. The sampled element value is then modified according to the equation

$$x_{REV} = -x + 2x_{MODE}, \tag{5.33}$$

where x is the orbital element sampled using the 'Gamdev' function, x_{MODE} is the mode value of the distribution (i.e. the unrandomised value of x calculated from one of the equations 5.25 – 5.32), and x_{REV} is the x value from the reversed gamma distribution.

The values of eccentricity and inclination calculated from equations 5.25 – 5.28 are all randomised using a gamma distribution. The values of argument of perigee and RAAN calculated from equations 5.29 and 5.31 are randomised using a reversed gamma distribution and the values of argument of perigee and RAAN calculated from equations 5.30 and 5.32 are randomised using a gamma distribution. After unmapping, this yields the required distributions in element-space (see Chapter 6). The value of mean anomaly is randomised using a normal distribution, as specified in section 5.2.8.2. In each case, the upper and lower limits of the normal or gamma distributions are derived using the method illustrated in Figure 5.71.

5.2.10 Unmapping the Fragments' Elements (The 'Unmap Frags' Routine)

The final unmapping of the fragments' recovered orbital elements is conducted in the 'Unmap Frags' routine. Figure 5.80 re-creates the FCP flowchart from Figure 5.36 and highlights the position of the 'Unmap Frags' routine within the FCP.

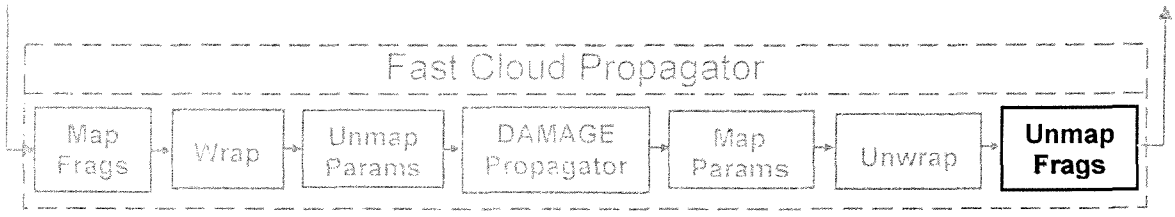

Figure 5.80 The position of the Unmap Frags module in the FCP

This post-propagation, post-unwrapping process is the reverse of the post-propagation mapping routine ('Map Params'), except that it does so on the orbital elements of the full complement of debris fragments that have since been recovered, rather than on the distribution parameters. This unmapping routine forms the last module in the FCP.

The defining equations used in this process are given by

$$\left.\begin{aligned} \Omega_{NEW} &= \Omega_{OLD} - 180^\circ \\ \omega_{NEW} &= \omega_{OLD} + 180^\circ \end{aligned}\right\} \text{if } a < a_{iMIN}, \tag{5.34}$$

$$\left.\begin{aligned} \omega_{NEW} &= \omega_{OLD} - 180^\circ \\ M_{\text{NEW}} &= M_{OLD} + 180^\circ \end{aligned}\right\} \text{if } a < a_{eMIN}, \tag{5.35}$$

where the subscripts *NEW* and *OLD* refer to the new, unmapped values and old, mapped values of the elements, respectively. The values of a_{iMIN} and a_{eMIN} were passed directly from the post-propagation mapping routine, 'Map Params'.

The effect of unmapping from modified element-space back to normal element-space on the RAAN and argument of perigee values is illustrated in Figures 5.81 – 5.84 for the condition when both a V-plot exists in the a vs. e scatter plot and in the a vs. i scatter plot (e.g. after a breakup in GEO). For reasons of clarity, this is demonstrated using the a vs. Ω and a vs. ω scatter plots. Figures 5.81 and 5.83 show the plots in modified element-space, whilst Figures 5.82 and 5.84 show the plots having been unmapped back to normal element-space. The figure showing the unmapping of mean anomaly has been omitted here because the large data range in mean anomaly and the scale of the plots makes this unmapping process impossible to see.

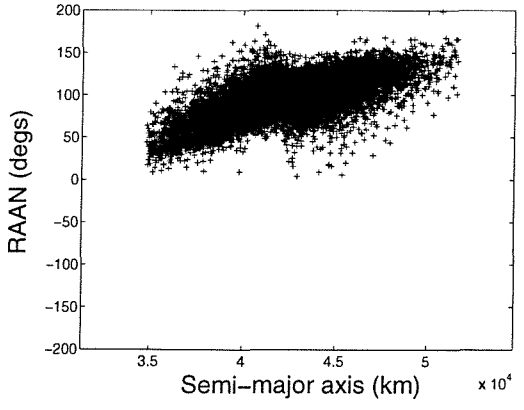

Figure 5.81 The semi-major axis vs. RAAN scatter plot in modified element-space after 100-year propagation from a breakup in GEO

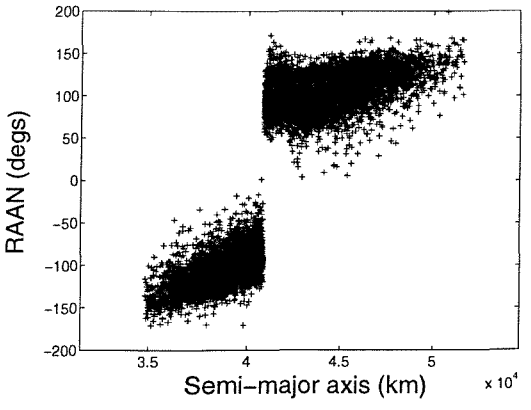

Figure 5.82 The semi-major axis vs. RAAN scatter plot in normal element-space after 100-year propagation from a breakup in GEO

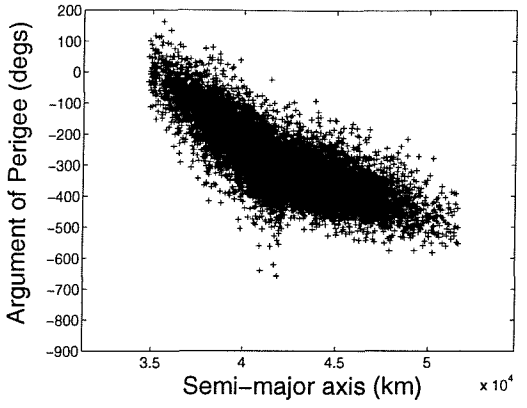

Figure 5.83 The semi-major axis vs. argument of perigee scatter plot in modified element-space after 100-year propagation from a breakup in GEO

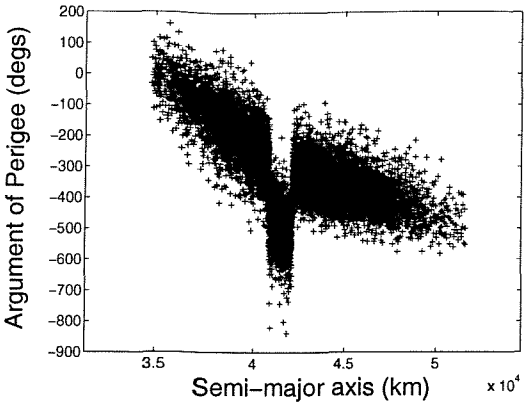

Figure 5.84 The semi-major axis vs. argument of perigee scatter plot in normal element-space after 100-year propagation from a breakup in GEO

The unmapping in RAAN occurs once because of the existence of a V-plot in *a-i* space, whereas argument of perigee is subject to two unmapping procedures, once due to the existence of a V-plot in *a-i* space and once due to the existence of a V-plot in *a-e* space.

5.3 The Effects of SRP

The FCP will not account for SRP perturbations due to the fact that SRP perturbative effects depend on the mass-to-area ratios of the fragments, as well as on the values of the orbital elements. The fragment mass-to-area ratios, together with the other physical characteristics of each fragment, are lost during the 'Wrap' routine of the current version of the FCP, and so there is no data from which to calculate the effects of SRP perturbations. Even if these physical characteristics were preserved, however, the FCP in its current state would be unable to account for the effects of SRP. The FCP is able to accurately model the changing properties of a debris cloud under the influence of gravitationally induced perturbations by virtue of the fact that it is the very positions of the fragments at one time-step (with respect to the gravitational field of the attracting body) that dictates the new positions of the fragments at the following time-step, as

explained in section 5.2.5. However, this is not the case for SRP and other non-gravitationally induced perturbations.

This section aims to justify the exclusion of SRP modelling in the FCP by showing that SRP effects are negligible compared to geopotential and luni-solar gravitational perturbations over a particular threshold fragment size. The scatter plots in Figures 5.85 – 5.94 compare the positions of fragments after a 100-year propagation under the influence of all perturbative effects (gravity-induced and SRP) with those that have been modelled under the influence of gravity-induced perturbations alone. The breakup scenario used to generate the debris cloud was a low-speed collision (produced by a 10 kg projectile impacting a 1500 kg target object with a speed of 800 m/s) in a GEO breakup orbit, as modelled by the IDES breakup model. For the sake of clarity, the scatter plots in Figures 5.85 – 5.94 show the distribution of the fragments for each of the elements vs. semi-major axis, since SRP had very little noticeable effect on semi-major axis. All fragments over 0.001 grams are considered in this study.

Actual Debris Cloud without SRP

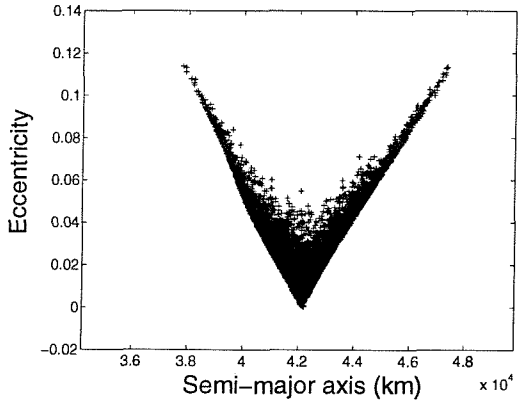

Figure 5.85 The *a* vs. *e* scatter plot after 100-year propagation under the influence of geopotential and luni-solar perturbation effects

Actual Debris Cloud with SRP

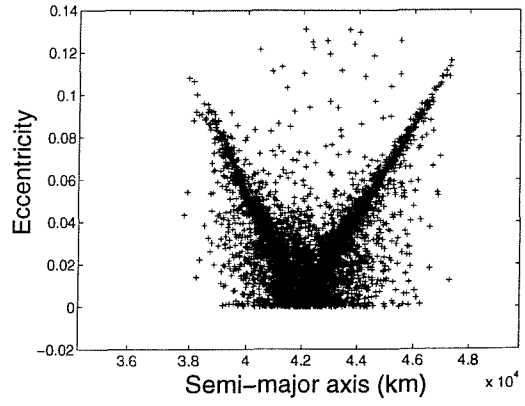

Figure 5.86 The *a* vs. *e* scatter plot after 100-year propagation under the influence of geopotential, luni-solar and SRP perturbation effects

Actual Debris Cloud without SRP

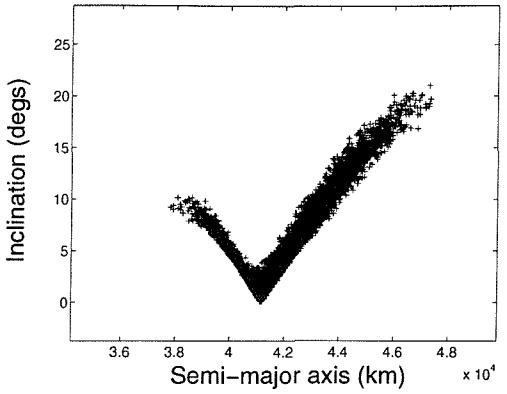

Figure 5.87 The a vs. i scatter plot after 100-year propagation under the influence of geopotential and luni-solar perturbation effects

Actual Debris Cloud with SRP

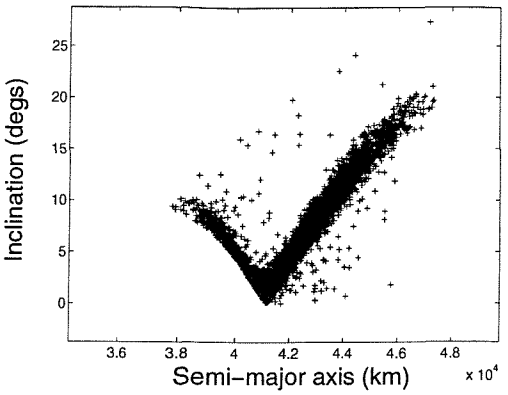

Figure 5.88 The a vs. i scatter plot after 100-year propagation under the influence of geopotential, luni-solar and SRP perturbation effects

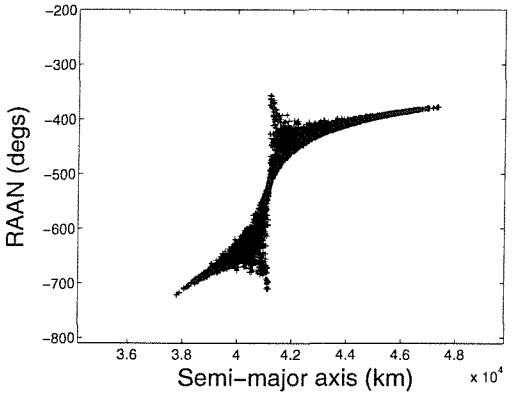

Figure 5.89 The a vs. Ω scatter plot after 100-year propagation under the influence of geopotential and luni-solar perturbation effects

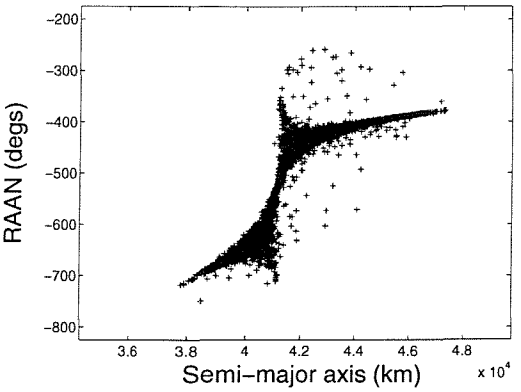

Figure 5.90 The a vs. Ω scatter plot after 100-year propagation under the influence of geopotential, luni-solar and SRP perturbation effects

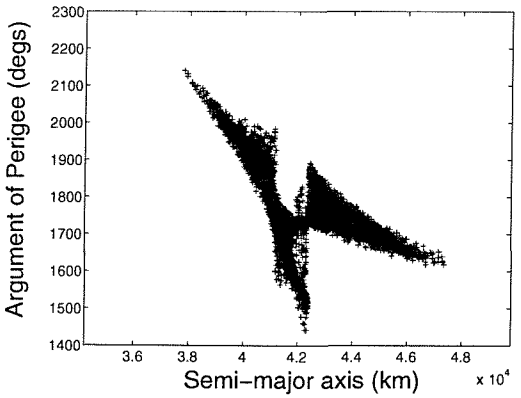

Figure 5.91 The a vs. ω scatter plot after 100-year propagation under the influence of geopotential and luni-solar perturbation effects

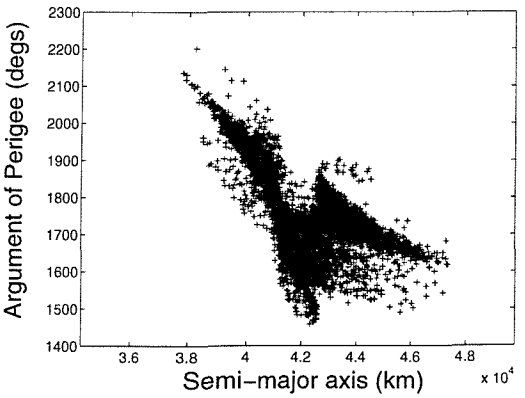

Figure 5.92 The a vs. ω scatter plot after 100-year propagation under the influence of geopotential, luni-solar and SRP perturbation effects

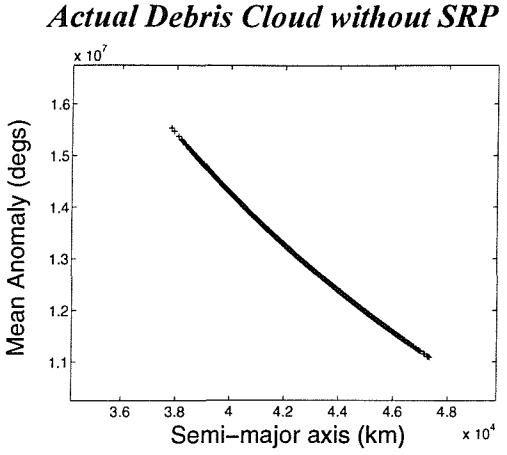

Figure 5.93 The a vs. M scatter plot after 100-year propagation under the influence of geopotential and luni-solar perturbation effects

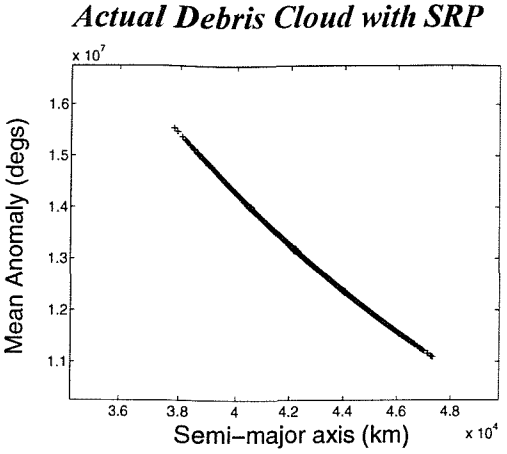

Figure 5.94 The a vs. M scatter plot after 100-year propagation under the influence of geopotential, luni-solar and SRP perturbation effects

The most notable effects of SRP are changes in the eccentricity and argument of perigee of certain fragments, as can be seen from the scatter plots in Figures 5.85 – 5.94. There is very little noticeable change in the values of semi-major axis, inclination, RAAN or mean anomaly, compared to the effects of the other perturbations for fragments over 0.001 grams. The fragments most greatly affected by SRP are those with low mass-to-area ratios and, as can be seen from the graphs in Figures 4.7 and 4.17 in Chapter 4, these correspond to fragments at the low mass end of the spectrum. Thus by using a higher mass threshold, above which debris fragments are generated, the effects of SRP on the cloud can be reduced to such an extent whereby the differences in the scatter plots become negligible. The effects of SRP are cumulative, hence a longer propagation time would require a larger mass threshold if the effects of SRP are to be reduced to the point whereby they become negligible. It is due to the cumulative effect of SRP that the scatter plots in Figure 5.85 – 5.94, which show the scatter plots following a 100-year propagation, show a worst-case scenario within the testing envelope for the FCP, which extends up to 100 years maximum. Similar runs over smaller propagation time periods show a considerably reduced effect of SRP perturbations. It should also be noted that the SRP effects shown in Figures 5.85 – 5.94 are very much orbit dependent. A different breakup orbit would have yielded different effects.

A study of the mass threshold required for SRP effects to become negligible at various propagation time periods was conducted and the results are presented in Figure 5.95. This study was conducted in GEO.

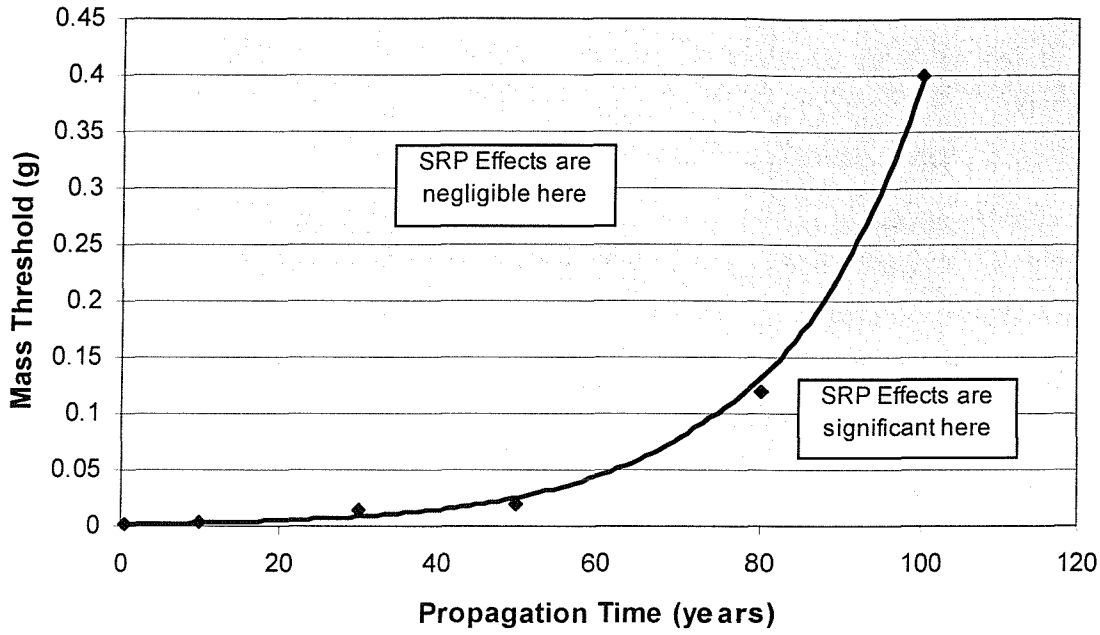

Figure 5.95 A graph to show the mass threshold required for SRP effects to be considered negligible as a function of propagation time

The curve of the graph in Figure 5.95 represents the region where SRP effects cause a standard deviation in eccentricity which differs by approximately 5% of the eccentricity data range compared to the standard deviation in the same data file propagated over the same time period under the influence of the same perturbations minus SRP effects. The figure of 5% was chosen rather arbitrarily and quite conservatively as a datum above which SRP effects would be considered significant. The method of generating this curve required the iterative process of deleting fragments with low masses and performing the error analysis until a difference in standard deviation of around 5% was reached. Thus the value of 5% is only an approximation.

The graph in Figure 5.95 shows an exponential increase of the SRP threshold mass with propagation time. The region above this line shows the envelope in which SRP effects

can be considered negligible compared to the other perturbation effects and is the envelope within which the FCP can be run with confidence. The region below this line is the region where SRP effects cannot be easily ignored and thus the FCP results in this region must be treated with caution, at least in terms of the fragment eccentricities and arguments of perigee produced. In reality, of course, there is no distinct threshold mass cut-off point where SRP effects suddenly become negligible. SRP affects all debris fragments, but this effect increases with decreasing mass (and thus decreasing mass-to-area ratios). The graph in Figure 5.95 thus merely serves as a guide. If it were not for the randomisation of fragment areas in all breakup models then there would be a direct relationship between fragment mass and mass-to-area ratio and the curve in Figure 5.95 could be lowered substantially. Due to this randomisation, however, a very high and conservative value of threshold mass must be maintained if all the fragments with a low enough mass-to-area ratio to cause significant changes in a fragment's position due to SRP are to be removed.

The graph in Figure 5.95 shows that even in the worst case, at 100 years, the threshold mass is still quite low at around 0.4 grams (approximately 0.8 mm in diameter). Running the FCP at masses above these threshold values can be justified, as, bearing in mind the relative speed of fragments in the GEO regime, fragments below this threshold mass will pose little threat to orbiting spacecraft. Nevertheless, it is desirable to improve on the performance of the FCP and to remove as many of its limitations as possible. To this end, future possible improvements to the FCP, which may allow the effects of SRP to be modelled, are proposed and discussed in Chapter 8.

It is important to note that the inclusion of SRP perturbations also reduces the speed of propagation quite considerably. A number of test runs have shown that the inclusion of SRP effects can increase propagation times by 500 – 1000%. Bearing in mind the relatively small effects of SRP compared to the effects of gravitationally induced perturbations in and around GEO, it may be argued that even if the FCP could account for SRP effects, they would be worth ignoring in order to take advantage of the further considerable time saving that their exclusion would provide.

Chapter 6

Fast Cloud Propagator Results

6.1 Introduction

This chapter is intended to provide the reader with a qualitative and quantitative assessment of the accuracy of the FCP compared to the conventional propagator. The speed increase of the FCP over the conventional propagator is also described herein. The applications of the method to the debris modelling community are fully described and the limitations of the method are summarised.

Section 2 presents the reader with the results of the FCP and provides a qualitative comparison between these results and the results from a conventional propagator for an example GEO and non-GEO breakup orbit. The element-relationship scatter plots and the number distribution histograms were used to facilitate this comparison. The main differences in the results are discussed at the end of the section.

Section 3 describes the error analysis that was performed on the FCP using 20 different case studies, the results of which were compared to similar results from a conventional propagator. For each case study, 10 Monte Carlo runs were conducted, producing a total of 200 data files from the FCP and 200 data files from the conventional propagator. The mean, minimum and maximum errors are tabularised in order to provide a quantitative comparison of the FCP results with the conventional propagator results. The error

analysis was performed on the means, standard deviations and correlations of the number distribution histograms, which were produced as a by-product of reproducing the element-relationship scatter plots.

Section 4 analyses the risks posed by these debris clouds to target objects in an effort to ascertain the impact of the FCP method on future collision prediction simulations. The results were compared with similar risk analyses performed on the debris clouds produced by identical runs of the conventional propagator. This provides an assessment of the acceptability of the errors produced by the FCP.

The following section examines the speed increase attained by the FCP over conventional propagation methods and presents this speed increase as a function of debris cloud size. The further speed increase of the method when a number of Monte Carlo iterations are required is also described and presented as a function of the number of fragments and the number of required iterations. Finally, section 6 describes the applications and limitations of the method.

6.2 Results

In order to provide a qualitative assessment of the accuracy of the FCP at propagating debris clouds, two debris clouds propagated by the FCP, which shall henceforth be referred to as *simulated debris clouds*, will be compared to the corresponding debris clouds that have been propagated conventionally using the DAMAGE propagator. These conventionally propagated clouds shall henceforth be referred to as the *actual debris clouds*. The simulated debris clouds can be compared to the actual debris clouds in terms of their element-relationship scatter plots, since an accurate re-construction of the scatter plots constitutes an accurate re-construction of the debris cloud. A comparison between the number distributions in each of the elements for the two clouds will also be made, which will give an indication of the variation in the spatial density of fragments within

the cloud. These number distributions are created as a by-product of re-creating the element-relationship scatter plots, apart from the number distribution in semi-major axis, which is used as the starting element in cloud re-construction, as described in Chapter 5.

The results of two case studies are presented here: that of a 100-year propagation of the debris cloud produced by a breakup in GEO (a = 42164.8 km, e = 0.001, i = 0.001°, Ω = 0°, ω = 0° and M = 0°) and that of a 100-year propagation of the debris cloud produced by a breakup in a non-geostationary high-Earth orbit (a = 42165.0 km, e = 0.4, i = 40°, Ω = 70°, ω = 120°, and M = 0°). The non-geostationary breakup orbit chosen for this case study is the same one used to illustrate the method in the previous chapter, and is one of the main orbits used to develop the FCP for non-GEO scenarios. Both case studies modelled a low-speed impact-induced breakup, with a projectile speed of 800 m/s and of mass 10 kg impacting a 1500 kg target object, as modelled by the IDES breakup model. The propagation time was 100 years, using an 8-day time-step, and the effects of the major Earth aspherical harmonics, comprising J_2, J_3, J_{22}, J_{31} and J_{33}, as well as the effect of luni-solar gravitational perturbations were modelled during the cloud propagation stage. All fragments with masses above 0.01 grams were included in both case studies. These two case studies were chosen because, between them, they provide some of the greatest variations in the scatter plot distributions and thus provide a rigorous test for the FCP.

The following results are for the GEO case study. Figures 6.1 – 6.30 provide a comparison of the actual and simulated clouds' scatter plots and Figures 6.31 – 6.42 provide a comparison of the number distributions produced in each element for the actual and simulated clouds.

Actual Debris Cloud

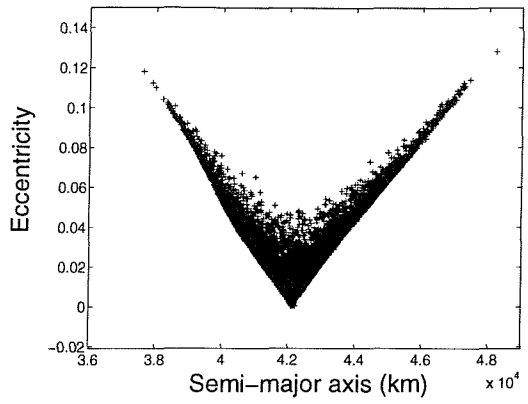

Figure 6.1 The semi-major axis vs. eccentricity scatter plot for the actual debris cloud

Simulated Debris Cloud

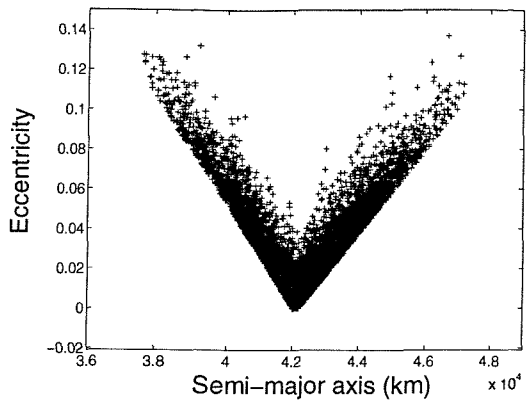

Figure 6.2 The semi-major axis vs. eccentricity scatter plot for the simulated debris cloud

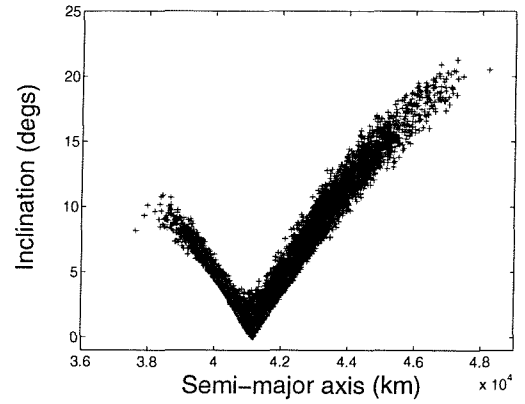

Figure 6.3 The semi-major axis vs. inclination scatter plot for the actual debris cloud

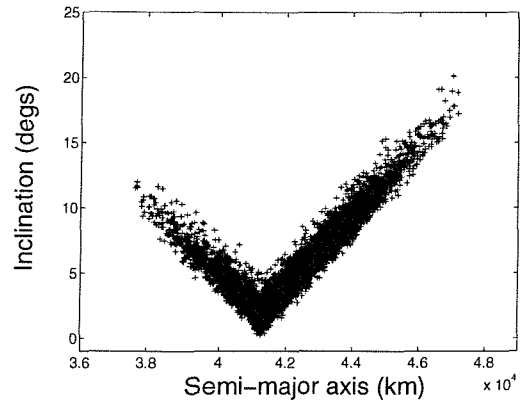

Figure 6.4 The semi-major axis vs. inclination scatter plot for the simulated debris cloud

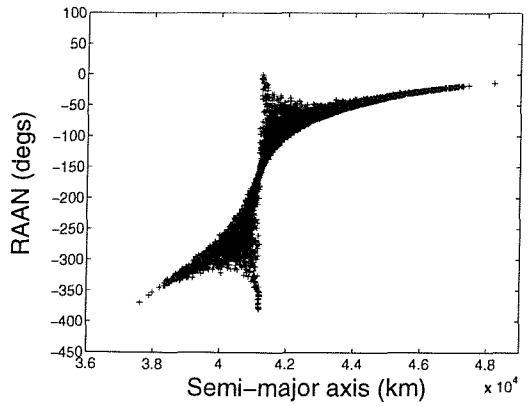

Figure 6.5 The semi-major axis vs. RAAN scatter plot for the actual debris cloud

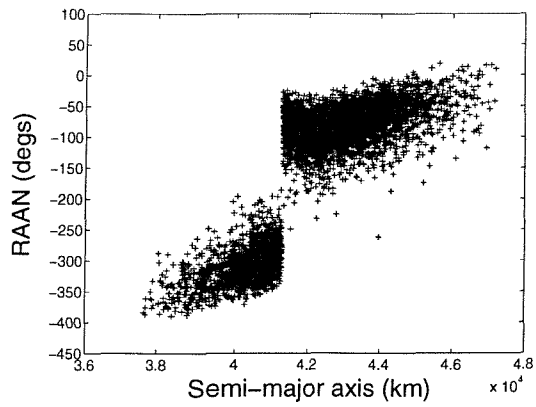

Figure 6.6 The semi-major axis vs. RAAN scatter plot for the simulated debris cloud

Actual Debris Cloud

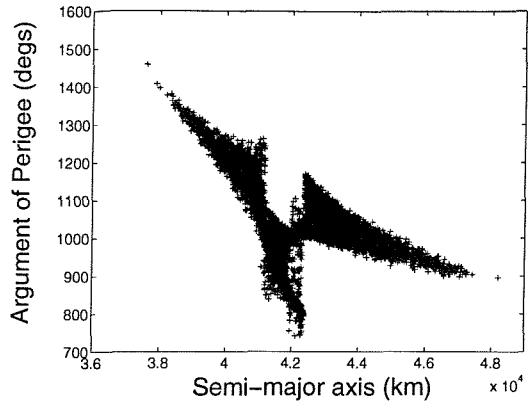

Figure 6.7 The semi-major axis vs. argument of perigee scatter plot for the actual debris cloud

Simulated Debris Cloud

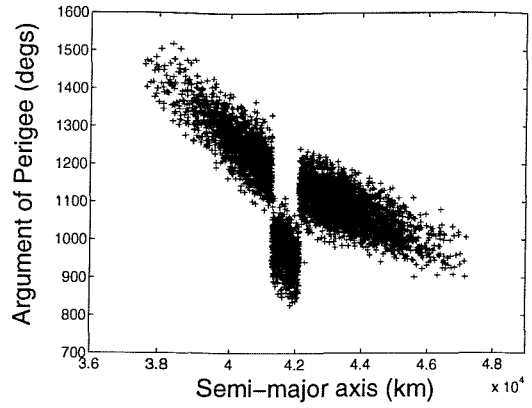

Figure 6.8 The semi-major axis vs. argument of perigee scatter plot for the simulated debris cloud

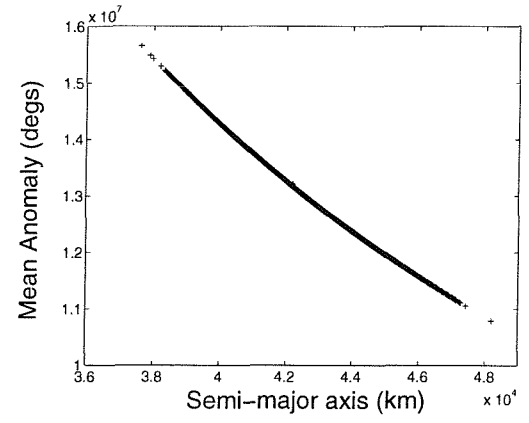

Figure 6.9 The semi-major axis vs. mean anomaly scatter plot for the actual debris cloud

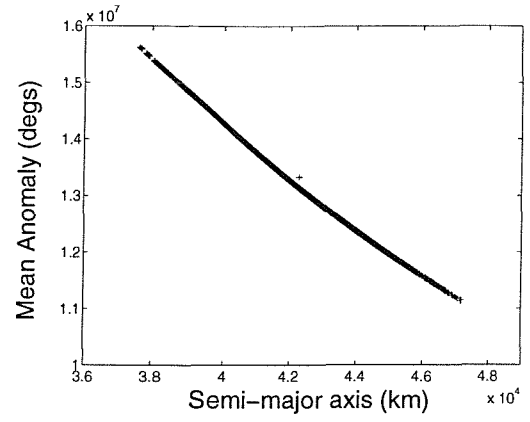

Figure 6.10 The semi-major axis vs. mean anomaly scatter plot for the simulated debris cloud

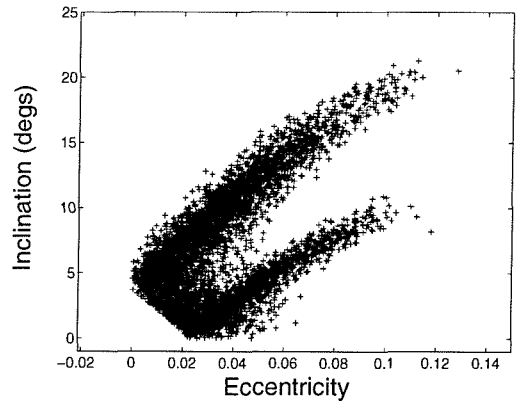

Figure 6.11 The eccentricity vs. inclination scatter plot for the actual debris cloud

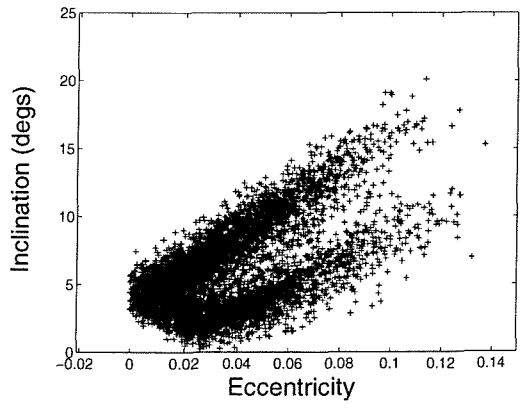

Figure 6.12 The eccentricity vs. inclination scatter plot for the simulated debris cloud

Actual Debris Cloud

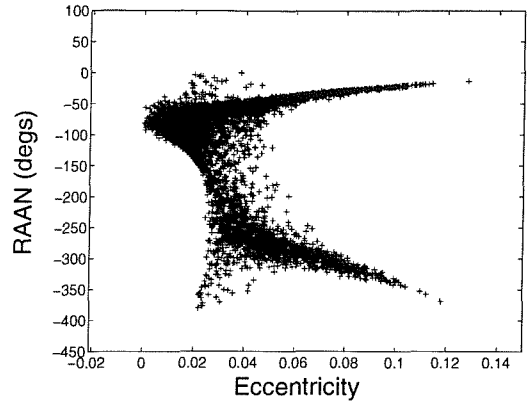

Figure 6.13 The eccentricity vs. RAAN scatter plot for the actual debris cloud

Simulated Debris Cloud

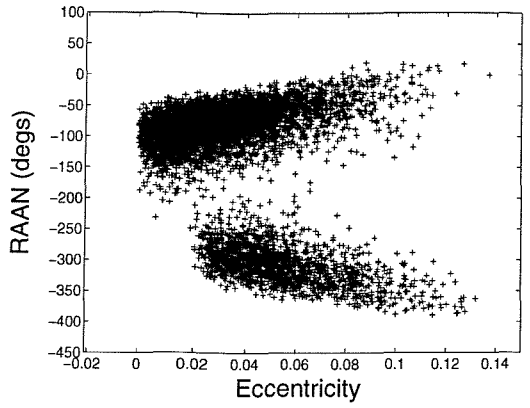

Figure 6.14 The eccentricity vs. inclination scatter plot for the simulated debris cloud

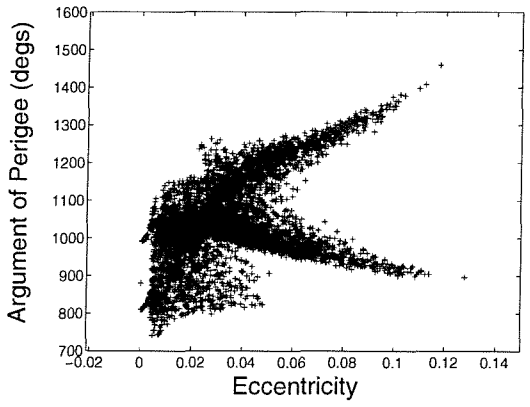

Figure 6.15 The eccentricity vs. argument of perigee scatter plot for the actual debris cloud

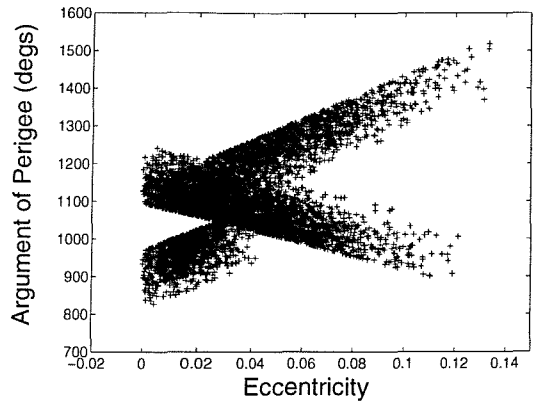

Figure 6.16 The eccentricity vs. argument of perigee scatter plot for the simulated debris cloud

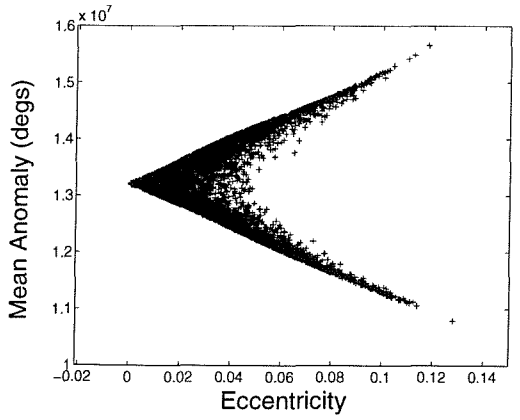

Figure 6.17 The eccentricity vs. mean anomaly scatter plot for the actual debris cloud

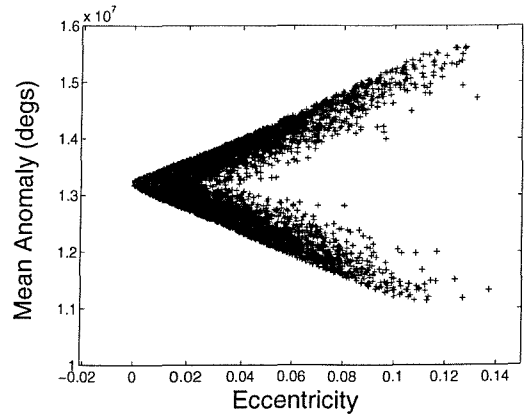

Figure 6.18 The eccentricity vs. mean anomaly scatter plot for the simulated debris cloud

Actual Debris Cloud

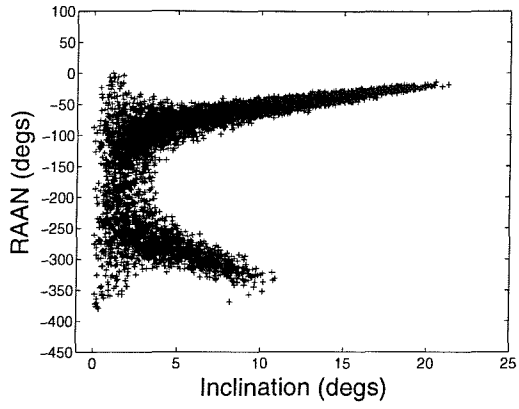

Figure 6.19 The inclination vs. RAAN scatter plot for the actual debris cloud

Simulated Debris Cloud

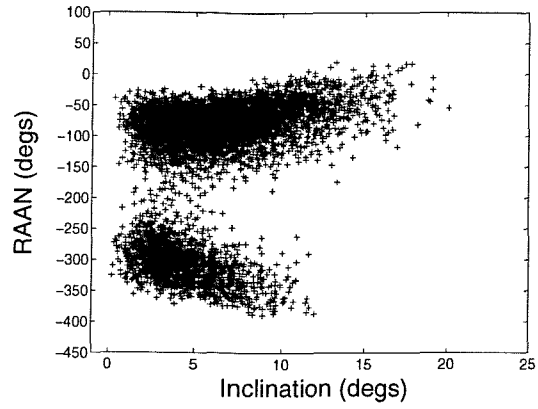

Figure 6.20 The inclination vs. RAAN scatter plot for the simulated debris cloud

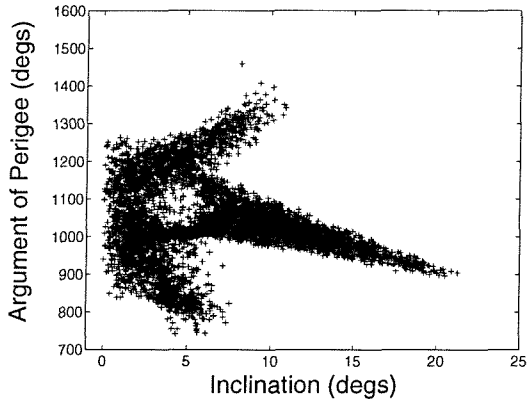

Figure 6.21 The inclination vs. argument of perigee scatter plot for the actual debris cloud

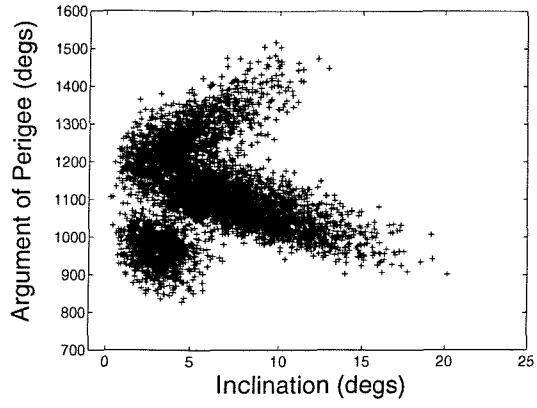

Figure 6.22 The inclination vs. argument of perigee scatter plot for the simulated debris cloud

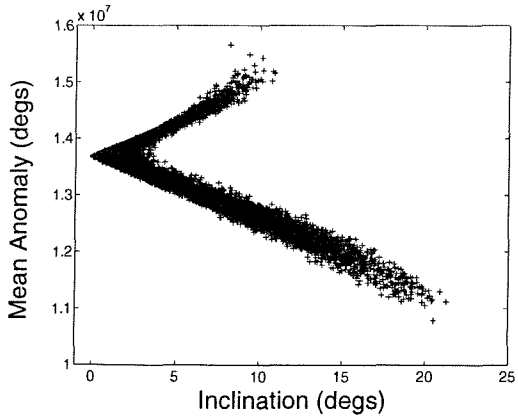

Figure 6.23 The inclination vs. mean anomaly scatter plot for the actual debris cloud

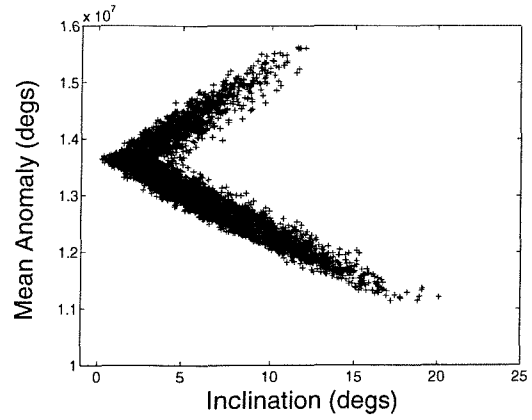

Figure 6.24 The inclination vs. mean anomaly scatter plot for the simulated debris cloud

Actual Debris Cloud

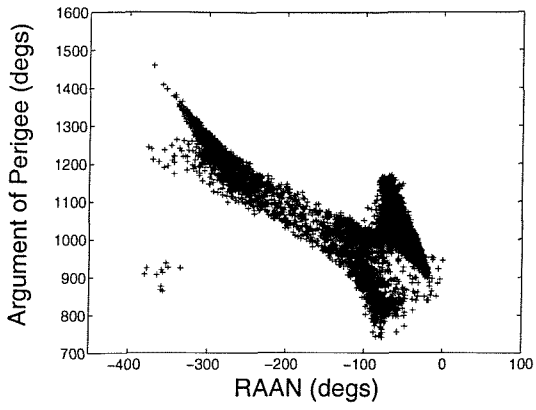

Figure 6.25 The RAAN vs. argument of perigee scatter plot for the actual debris cloud

Simulated Debris Cloud

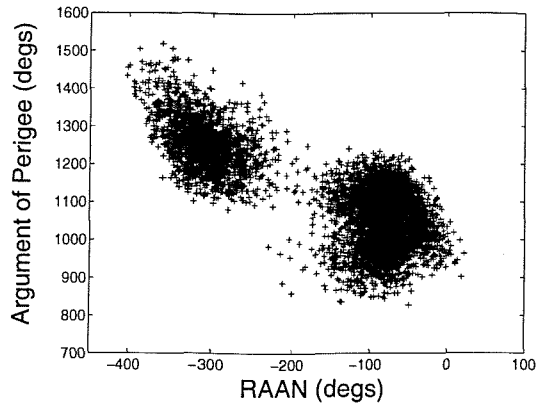

Figure 6.26 The RAAN vs. argument of perigee scatter plot for the simulated debris cloud

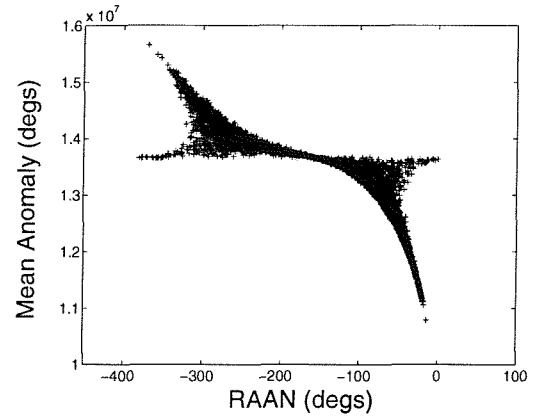

Figure 6.27 The RAAN vs. mean anomaly scatter plot for the actual debris cloud

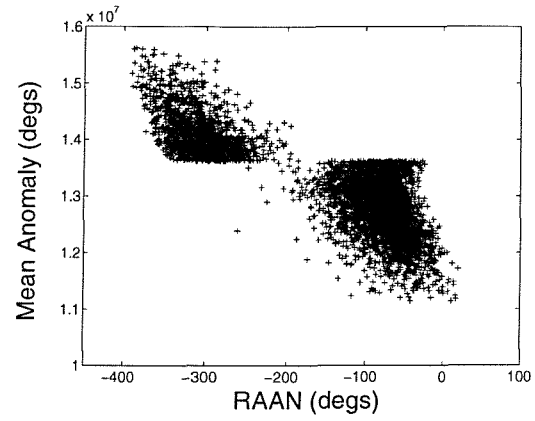

Figure 6.28 The RAAN vs. mean anomaly scatter plot for the simulated debris cloud

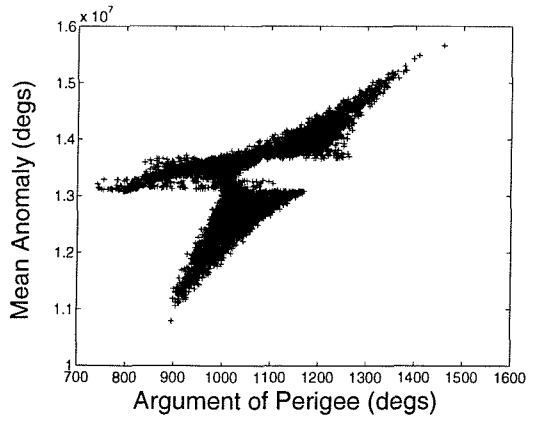

Figure 6.29 The argument of perigee vs. mean anomaly scatter plot for the actual debris cloud

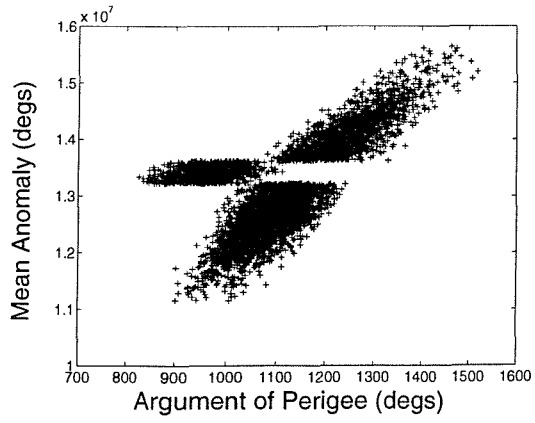

Figure 6.30 The argument of perigee vs. mean anomaly scatter plot for the simulated debris cloud

Actual Debris Cloud

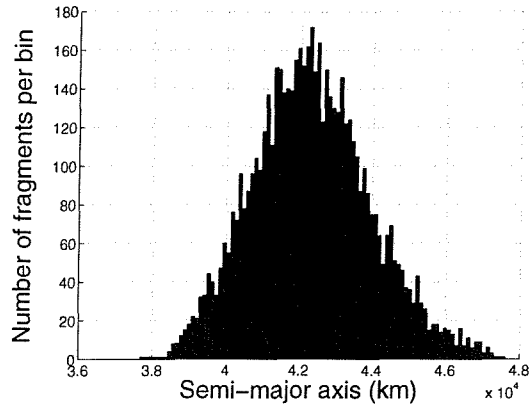

Figure 6.31 The number distribution in semi-major axis in the actual debris cloud

Simulated Debris Cloud

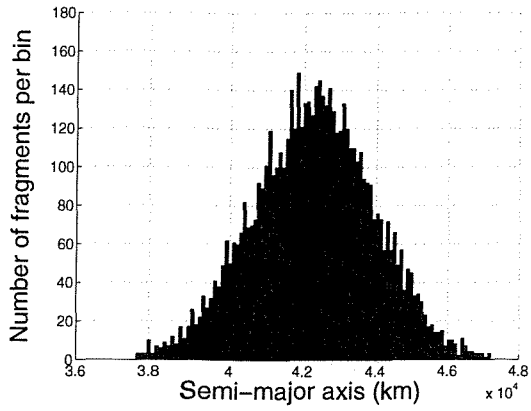

Figure 6.32 The number distribution in semi-major axis in the simulated debris cloud

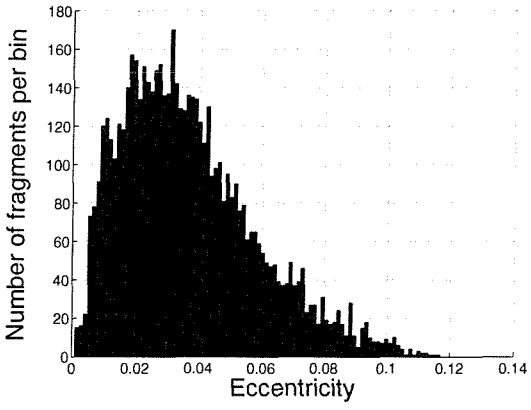

Figure 6.33 The number distribution in eccentricity in the actual debris cloud

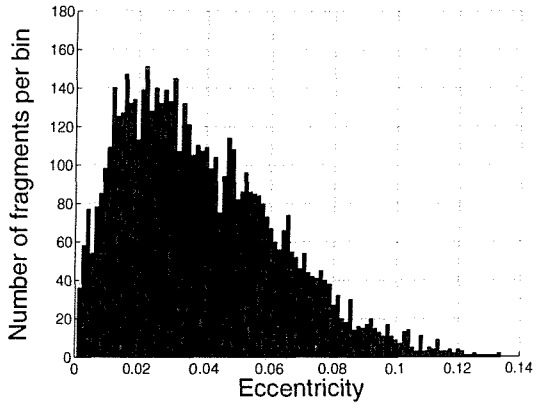

Figure 6.34 The number distribution in eccentricity in the simulated debris cloud

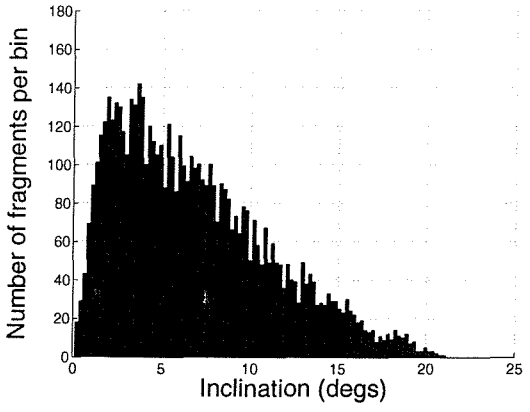

Figure 6.35 The number distribution in inclination in the actual debris cloud

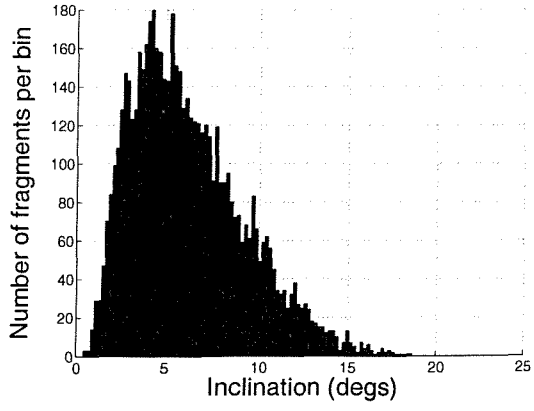

Figure 6.36 The number distribution in inclination in the simulated debris cloud

Actual Debris Cloud

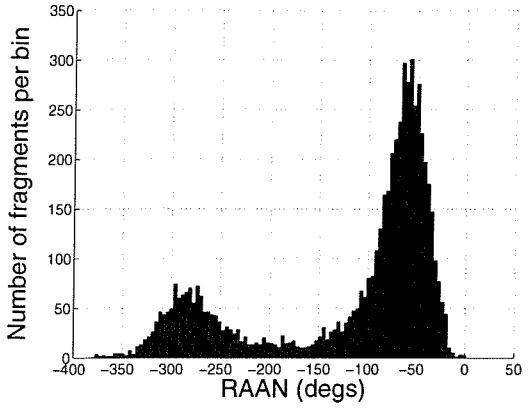

Figure 6.37 The number distribution in RAAN in the actual debris cloud

Simulated Debris Cloud

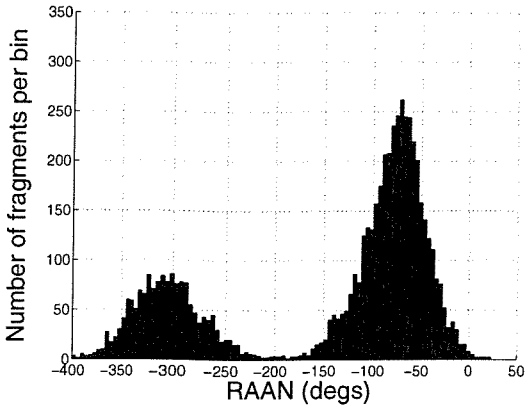

Figure 6.38 The number distribution in RAAN in the simulated debris cloud

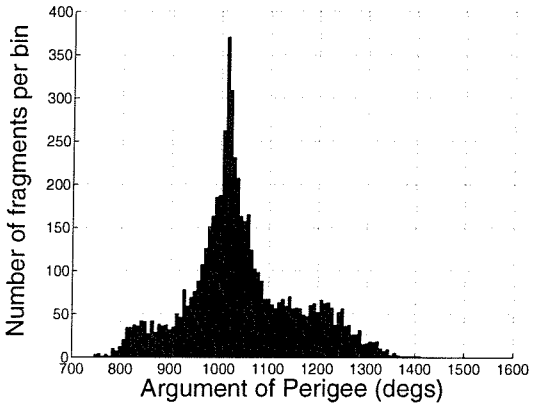

Figure 6.39 The number distribution in argument of perigee in the actual debris cloud

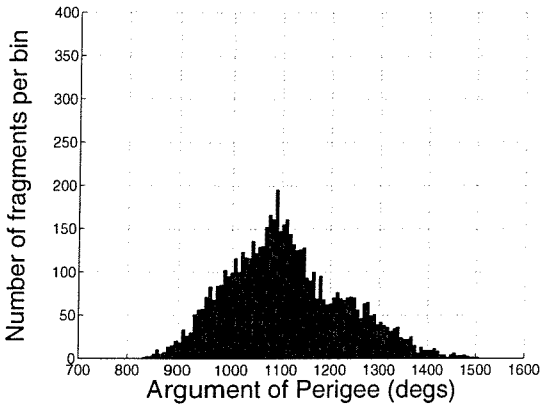

Figure 6.40 The number distribution in argument of perigee in the simulated debris cloud

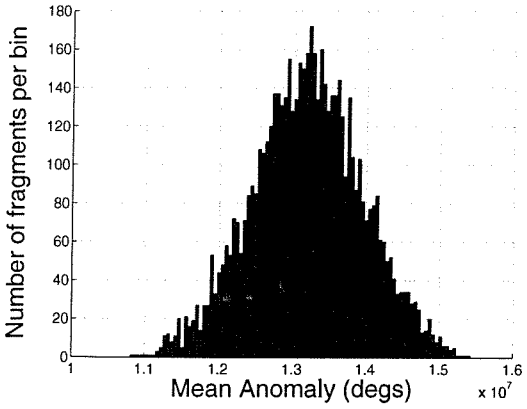

Figure 6.41 The number distribution in mean anomaly in the actual debris cloud

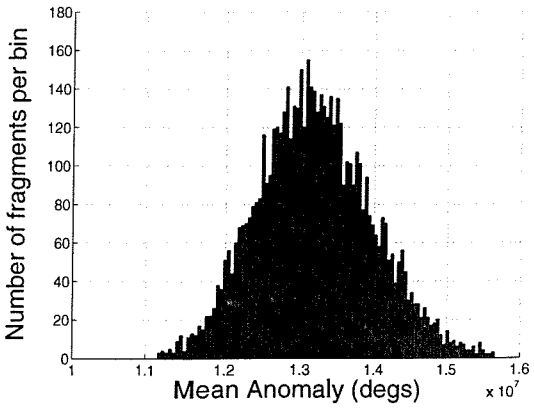

Figure 6.42 The number distribution in mean anomaly in the simulated debris cloud

The largest differences in the results for the GEO case study are to be found in the RAAN and argument of perigee values. The RAAN and argument of perigee values were constructed using eccentricity as a baseline from the e vs. Ω and e vs. ω simulated scatter plots (Figures 6.14 and 6.16 respectively), as described in Chapter 5. It was hoped that the two main 'arms' of the distribution in the e vs. Ω and e vs. ω scatter plots would become much narrower with increasing values of eccentricity (> 0.04), as depicted in the corresponding actual scatter plots (Figures 6.13 and 6.15). This should happen as a natural consequence of the shape of the gamma number distribution in eccentricity (Figures 6.33 and 6.34), i.e. the number of fragments in the eccentricity number distribution become fewer as eccentricity increases, thus the deviation of the fragments' argument of perigee and RAAN values from the mode lines should decrease with increasing eccentricity, producing a narrowing of the 'arms' at high eccentricity values. This effect can indeed be observed to some extent in the simulated scatter plots (Figures 6.14 and 6.16) – the arms become narrower as the eccentricity increases. However, the effect is not quite as pronounced as it is in the actual scatter plots (Figures 6.13 and 6.15). This difference can also be observed in the number distributions produced as a by-product of the scatter plots, and is particularly noticeable in argument of perigee, where a comparison between the actual and simulated plots (Figures 6.39 and 6.40) shows a noticeable difference in the shapes of the two curves.

On the whole, however, the FCP has managed to place the bulk of the fragments in the right place in element-space and has replicated the relationships between the majority of the elements correctly. This is further borne out by the similarity in the positions, variances and shapes of the simulated number distributions to the actual number distributions (Figures 6.31 – 6.42).

The following results are for the aforementioned non-GEO case study. Figures 6.43 – 6.72 illustrate the 15 element relationship scatter plots for both the actual and simulated debris clouds and Figures 6.73– 6.84 illustrate the resulting number distributions.

Actual Debris Cloud

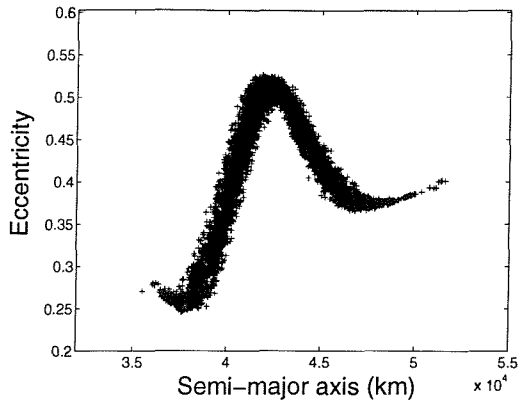

Figure 6.43 The semi-major axis vs. eccentricity scatter plot for the actual debris cloud

Simulated Debris Cloud

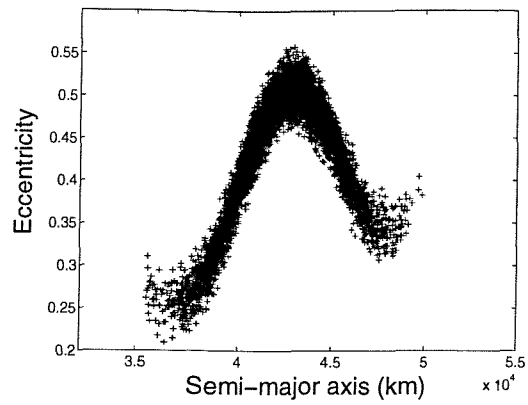

Figure 6.44 The semi-major axis vs. eccentricity scatter plot for the simulated debris cloud

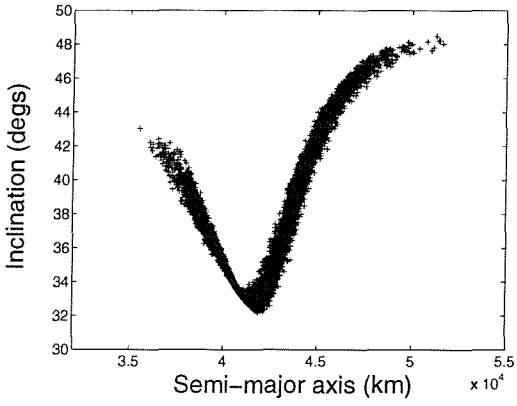

Figure 6.45 The semi-major axis vs. inclination scatter plot for the actual debris cloud

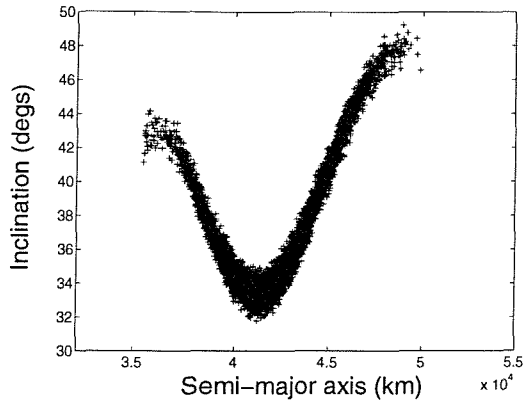

Figure 6.46 The semi-major axis vs. inclination scatter plot for the simulated debris cloud

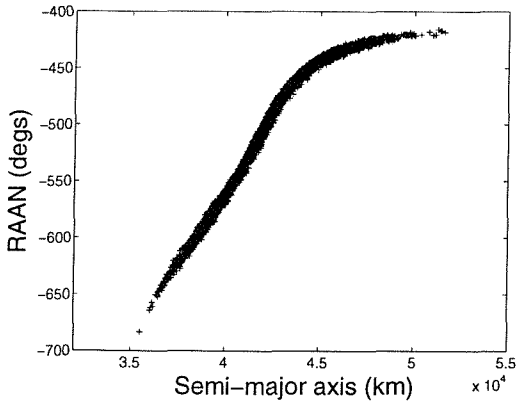

Figure 6.47 The semi-major axis vs. RAAN scatter plot for the actual debris cloud

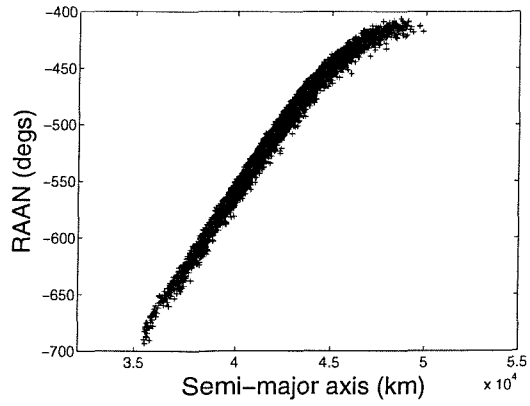

Figure 6.48 The semi-major axis vs. RAAN scatter plot for the simulated debris cloud

Actual Debris Cloud

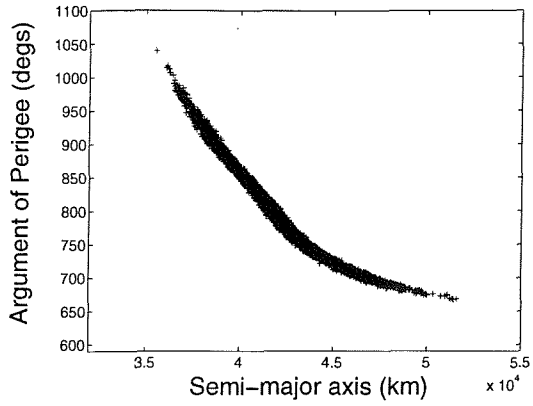

Figure 6.49 The semi-major axis vs. argument of perigee scatter plot for the actual debris cloud

Simulated Debris Cloud

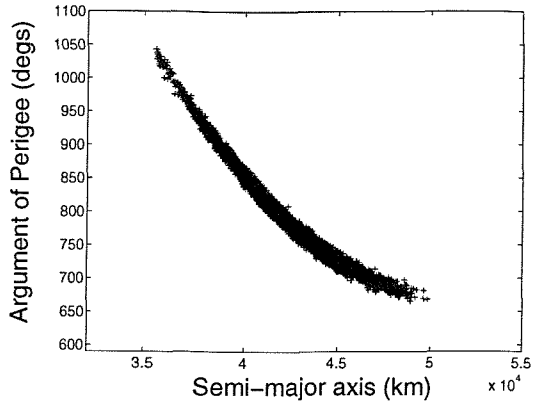

Figure 6.50 The semi-major axis vs. RAAN scatter plot for the simulated debris cloud

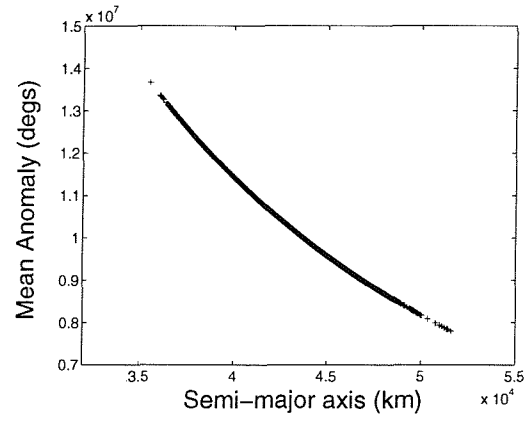

Figure 6.51 The semi-major axis vs. mean anomaly scatter plot for the actual debris cloud

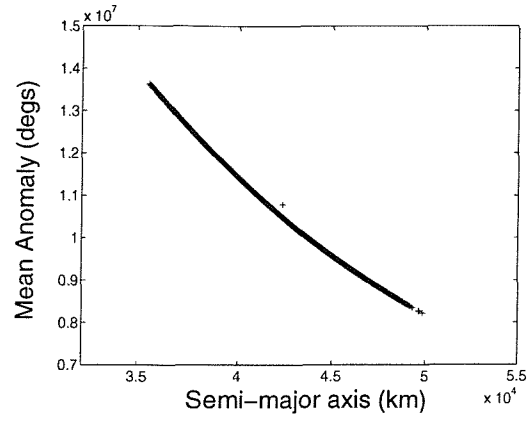

Figure 6.52 The semi-major axis vs. mean anomaly scatter plot for the simulated debris cloud

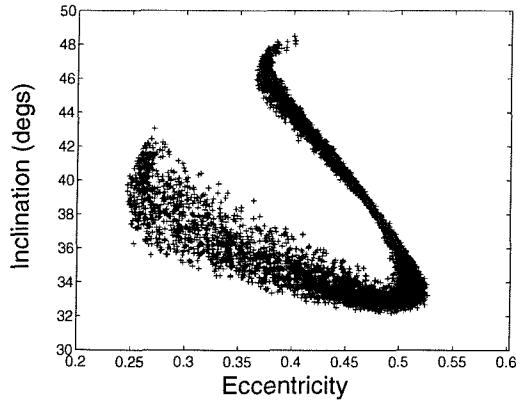

Figure 6.53 The eccentricity vs. inclination scatter plot for the actual debris cloud

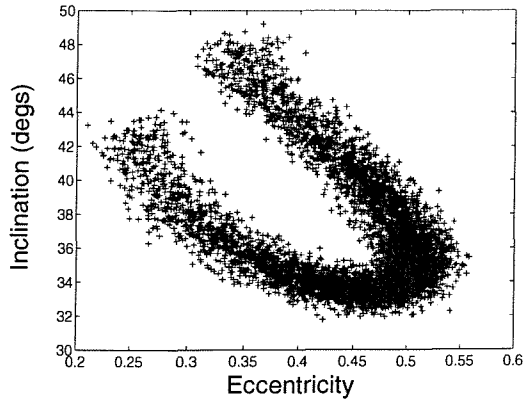

Figure 6.54 The eccentricity vs. inclination scatter plot for the simulated debris cloud

Actual Debris Cloud

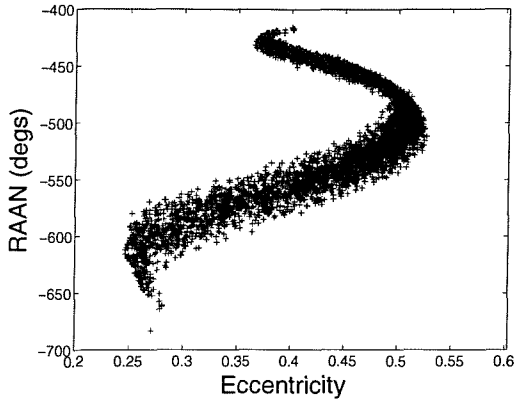

Figure 6.55 The eccentricity vs. RAAN scatter plot for the actual debris cloud

Simulated Debris Cloud

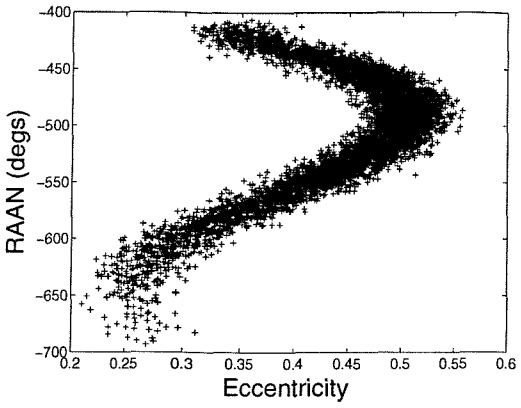

Figure 6.56 The eccentricity vs. RAAN scatter plot for the simulated debris cloud

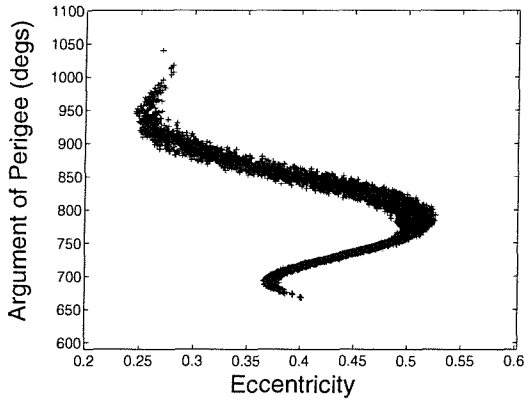

Figure 6.57 The eccentricity vs. argument of perigee scatter plot for the actual debris cloud

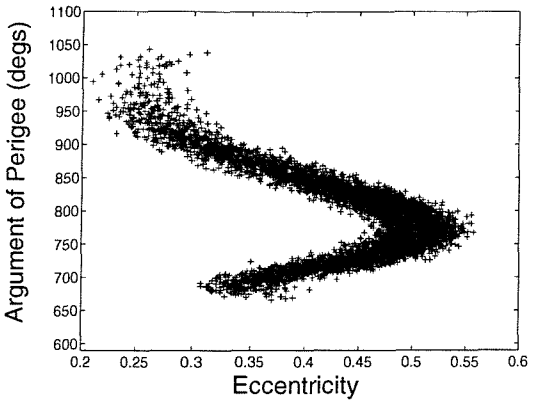

Figure 6.58 The eccentricity vs. argument of perigee scatter plot for the simulated debris cloud

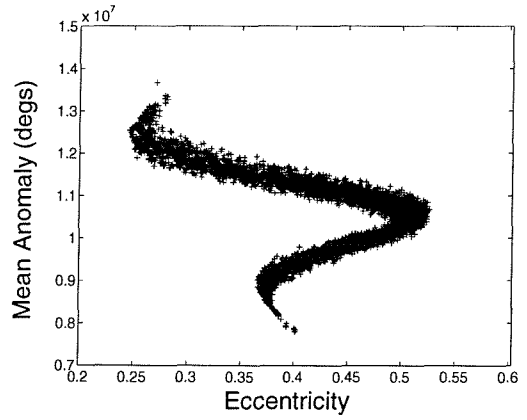

Figure 6.59 The eccentricity vs. mean anomaly scatter plot for the actual debris cloud

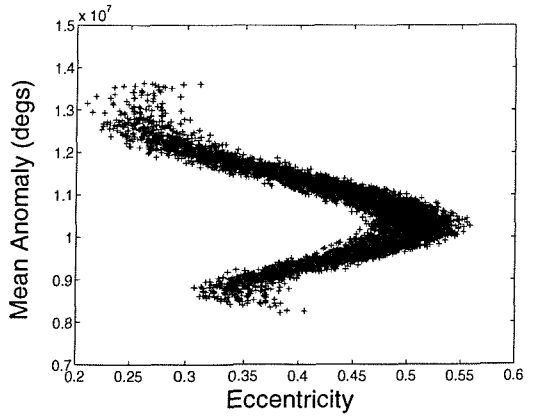

Figure 6.60 The eccentricity vs. mean anomaly scatter plot for the simulated debris cloud

Actual Debris Cloud

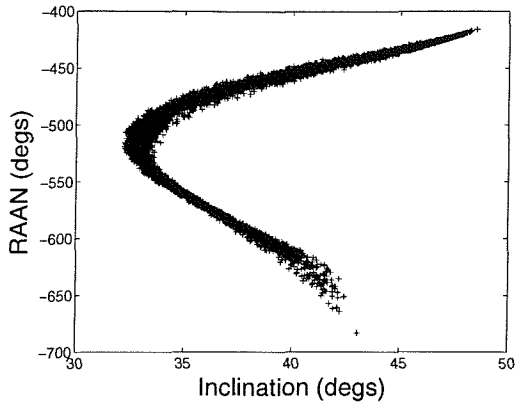

Figure 6.61 The inclination vs. RAAN scatter plot for the actual debris cloud

Simulated Debris Cloud

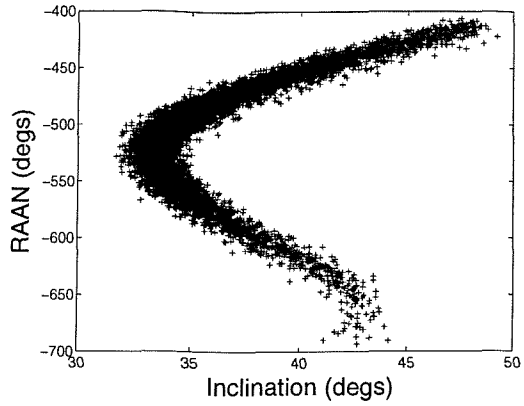

Figure 6.62 The inclination vs. RAAN scatter plot for the simulated debris cloud

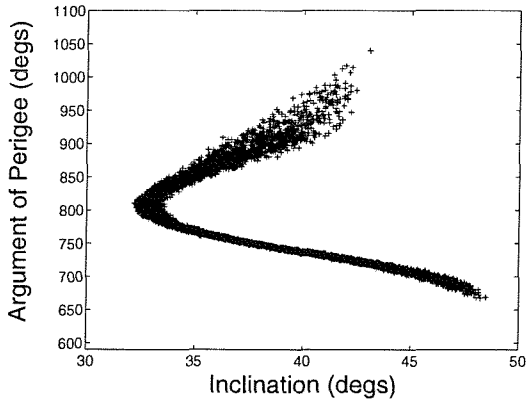

Figure 6.63 The inclination vs. argument of perigee scatter plot for the actual debris cloud

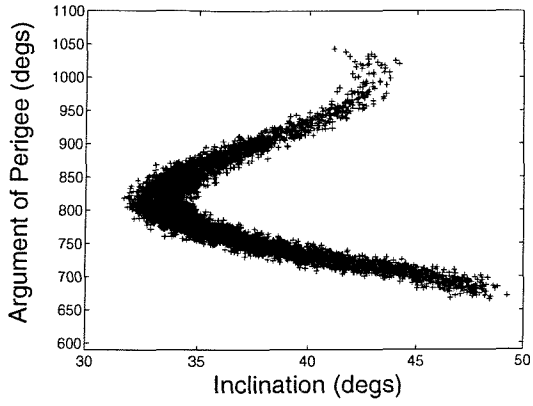

Figure 6.64 The inclination vs. argument of perigee scatter plot for the simulated debris cloud

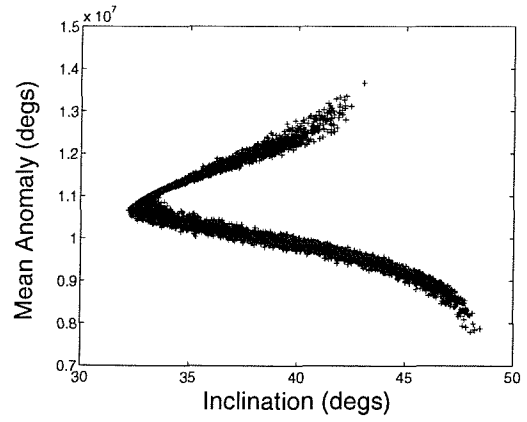

Figure 6.65 The inclination vs. mean anomaly scatter plot for the actual debris cloud

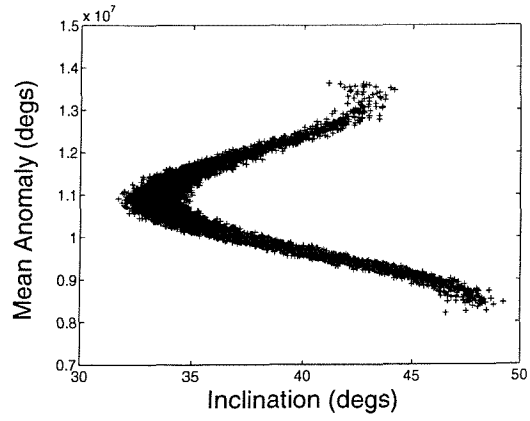

Figure 6.66 The inclination vs. mean anomaly scatter plot for the simulated debris cloud

Actual Debris Cloud

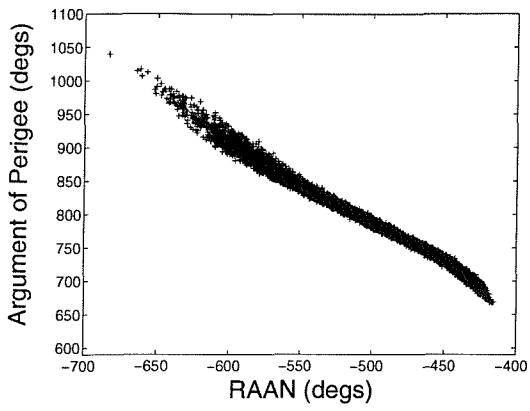

Figure 6.67 The RAAN vs. argument of perigee scatter plot for the actual debris cloud

Simulated Debris Cloud

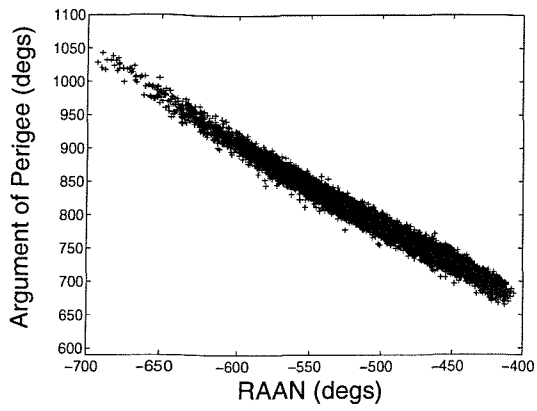

Figure 6.68 The RAAN vs. argument of perigee scatter plot for the simulated debris cloud

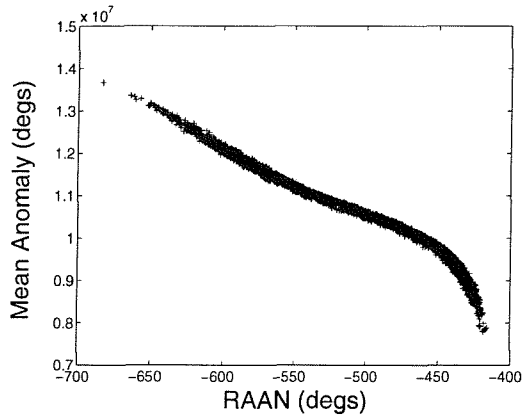

Figure 6.69 The RAAN vs. mean anomaly scatter plot for the actual debris cloud

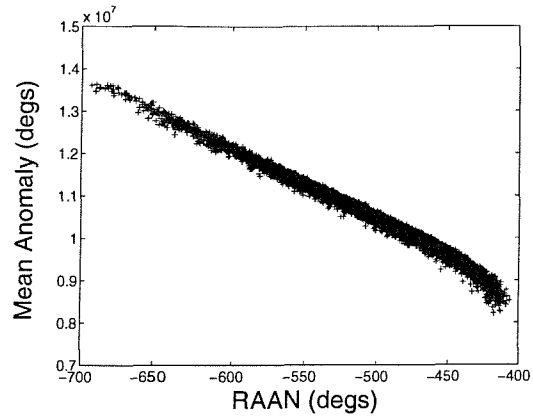

Figure 6.70 The RAAN vs. mean anomaly scatter plot for the simulated debris cloud

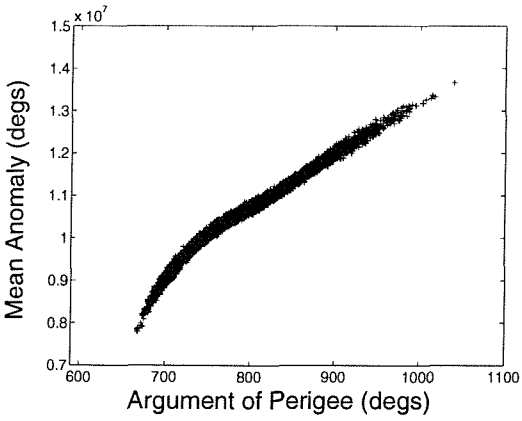

Figure 6.71 The argument of perigee vs. mean anomaly scatter plot for the actual debris cloud

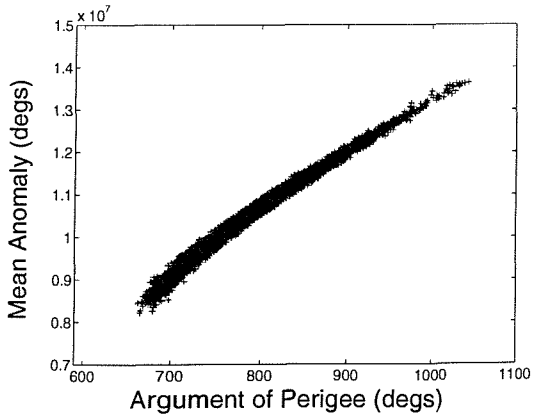

Figure 6.72 The argument of perigee vs. mean anomaly scatter plot for the simulated debris cloud

Actual Debris Cloud

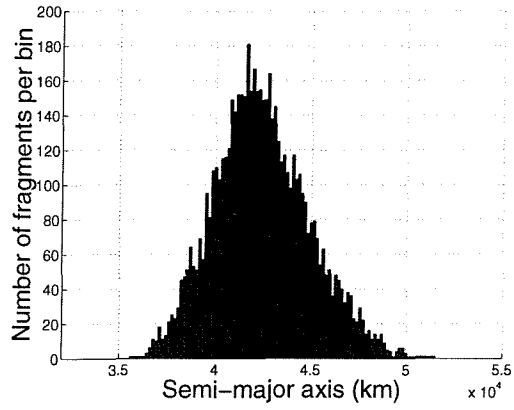

Figure 6.73 The number distribution in semi-major axis in the actual debris cloud

Simulated Debris Cloud

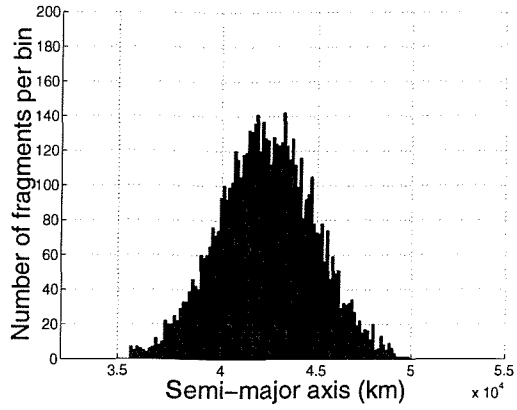

Figure 6.74 The number distribution in semi-major axis in the simulated debris cloud

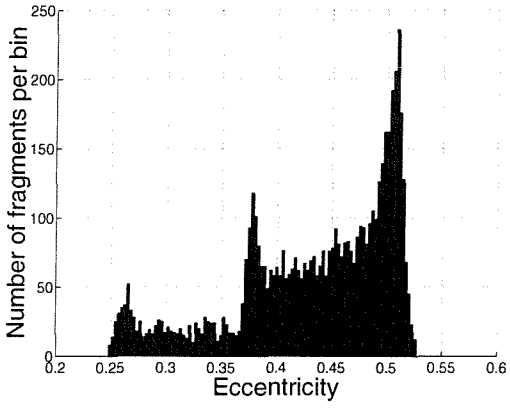

Figure 6.75 The number distribution in eccentricity in the actual debris cloud

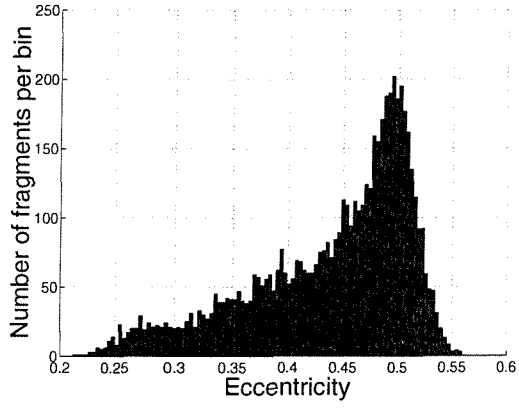

Figure 6.76 The number distribution in eccentricity in the simulated debris cloud

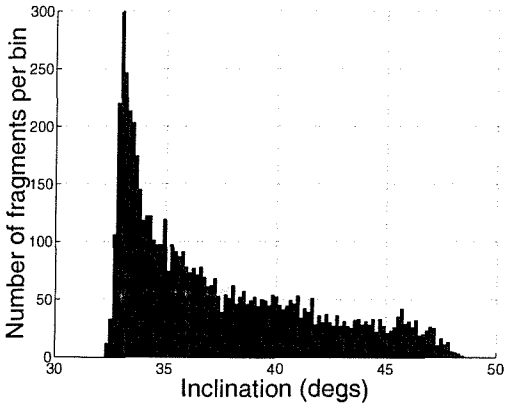

Figure 6.77 The number distribution in inclination in the actual debris cloud

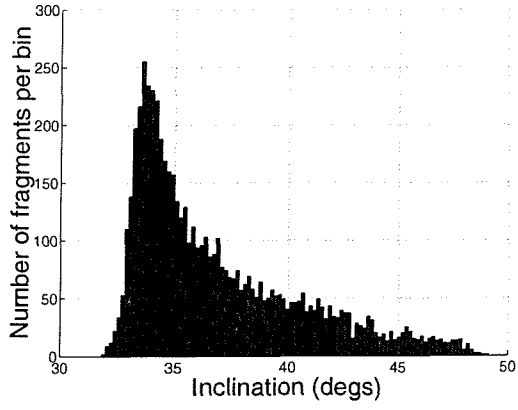

Figure 6.78 The number distribution in inclination in the simulated debris cloud

Actual Debris Cloud

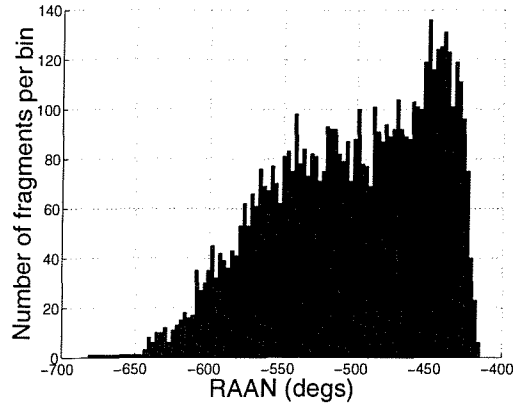

Figure 6.79 The number distribution in RAAN in the actual debris cloud

Simulated Debris Cloud

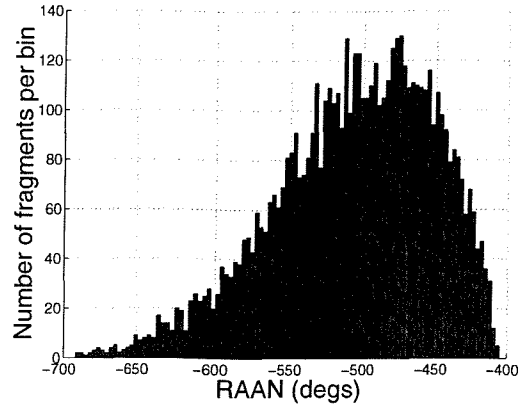

Figure 6.80 The number distribution in RAAN in the simulated debris cloud

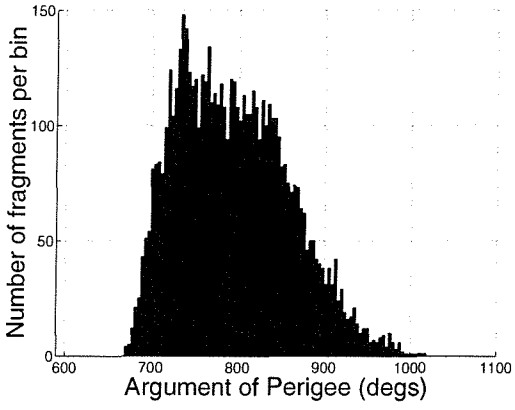

Figure 6.81 The number distribution in argument of perigee in the actual debris cloud

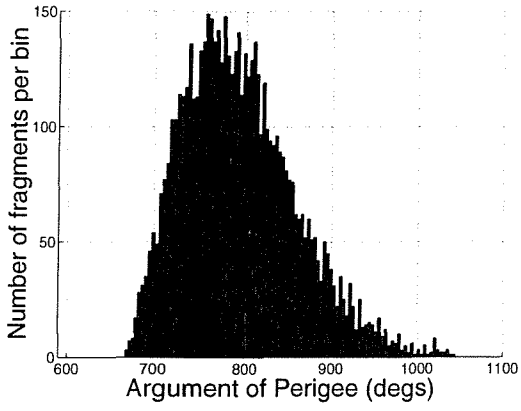

Figure 6.82 The number distribution in argument of perigee in the simulated debris cloud

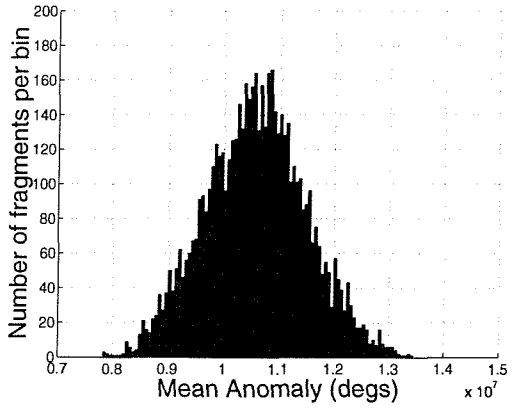

Figure 6.83 The number distribution in mean anomaly in the actual debris cloud

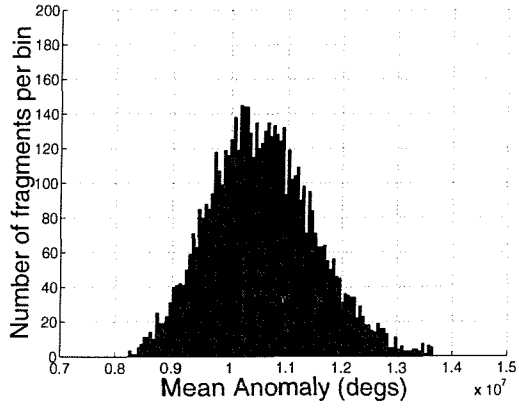

Figure 6.84 The number distribution in mean anomaly in the simulated debris cloud

A qualitative comparison of the actual and simulated debris clouds using the scatter plots in Figures 6.43 – 6.72 and the number distribution histograms in Figures 6.73 – 6.84 immediately reveals that, on the whole, the FCP has managed to place the bulk of the fragments in the right location in element-space and has replicated the relationships between the majority of the elements correctly.

There are occasional differences in the variances of the distributions at certain points on the scatter plots throughout, most notably in the a vs. e scatter plot at $e > 0.47$ and again at a $> 4.5 \times 10^4$ km (Figures 6.43 and 6.44) and in the a vs. i scatter plot at $i < 36°$ (Figures 6.45 and 6.46). These differences also manifest themselves in the other scatter plots containing eccentricity and inclinations, most notably in the e vs. i scatter plot (Figures 6.53 and 6.54).

The largest difference visible in the number distribution histograms is in the number of fragments vs. eccentricity, which shows a peak at e $\approx$ 0.375 in the actual number distribution (Figure 6.75), which is not present in the simulated number distribution (Figure 6.76). This is caused by a prominent tail in the a vs. e actual scatter plot above semi-major axis values of around 4.7×10^4 (Figure 6.43), which is not so prominent in the corresponding simulated scatter plot (Figure 6.44). A smaller maxima exists in the actual number distribution in eccentricity at e $\approx$ 0.27, which is absent from the corresponding simulated number distribution. This, again, is due to a slight error in the simulated a vs. e scatter plot, where the variance in e is over-estimated at $a < 3.8 \times 10^4$ km (Figure 6.44). These errors show that the number distribution histograms are highly sensitive to even the smallest errors in the element-relationship scatter plots.

Another error, visible only in the number distribution histograms, is the mismatch between the number of fragments at the mode values of the elements. The number of fragments at the modes were occasionally under-estimated by the FCP, as shown in the histograms produced from the simulated debris cloud. This is noticeable in the a, e, i and M number distributions (Figures 6.73 – 6.78, 6.83 and 6.84). These effects are highly localised, however.

All of these errors are artefacts of this particular case study and are not representative of the FCP's performance in all case studies. Possible sources of errors that may explain these differences include errors in the mode line fits, which subsequently cause errors in the maximum 3σ limits assigned to any particular scatter plot, and errors in the positions of the propagated spread parameters, which may not be perfectly indicative of the maximum spread required for the scatter plot.

6.3 Error Analysis

Error analysis was performed in order to assess the accuracy of the simulated debris clouds with respect to the actual debris clouds. The error analysis was used to assess the errors in the number distributions of fragments in element-space for the simulated clouds at various epochs up to 100 years. These number distributions are generated as a by-product of re-creating the element-relationship scatter plots. Thus any errors in these scatter plots will be reflected in the number distributions.

Twenty case studies were analysed, each with very different parameters. In each case study, ten Monte Carlo runs of the conventional propagator and the FCP were conducted. In each Monte Carlo simulation, the breakup model was run (with the same parameters each time) and the resulting fragments propagated by the conventional propagator and then by the FCP. This produced ten pairs of data sets for each case study, with the first of each pair representing the actual debris clouds and the second of each pair representing the simulated debris clouds.

The differences in the sample means and standard deviations for each of the element number distribution pairs were expressed as a percentage of the data range of each element in the actual debris cloud. In doing this, the errors are normalised and an appreciation is gained for the magnitude of the error with respect to the distribution. This also allows for the direct comparison of errors from different histograms, e.g. the number

distributions in semi-major axis and eccentricity. The average errors in the means and standard deviations were then calculated, as these approximate to the errors between the two parent distributions* and are largely independent of sampling variations. The minimum and maximum errors were also recorded, as this gives an indication of the variation in the error due to sampling. The correlation of the simulated data with the actual data for each orbital element in each of the ten Monte Carlo runs was calculated for each case study. The minimum, maximum and mean correlation coefficients were again calculated for each case study. In order to expedite the error analysis process, a series of macros were written in Visual Basic to automate the process of producing these descriptive statistics. The data analysis software that comes with Microsoft Excel was used in these macros in order to produce values for the means, standard deviations and correlation coefficients. This was considered the most prudent way of analysing the errors of such a large number of data files. (The 20 case studies containing 10 Monte Carlo runs for the actual and simulated clouds yielded 400 separate data files. Each data file contained 6 orbital elements, which had to be treated individually, thus requiring 2,400 error analysis iterations. Additional routines were required to normalise the errors and calculate the minimum, maximum and average errors.) The standard equations for calculating the means [95], standard deviations [96] and correlation coefficients [97] are as follows,

$$\bar{x} = \frac{\sum_{i=0}^{n-1} x_i}{n}, \tag{6.1}$$

$$s(x) = \sqrt{\frac{\sum_{i=0}^{n-1} \left(x_i - \bar{x}\right)^2}{n-1}}, \tag{6.2}$$

* The parent distribution is the distribution from which the samples were taken. For example, the semi-major axis parent distribution may be a normal distribution. However, the samples taken from this distribution may not form a perfect normal distribution. The correlation between the parent distribution and the distribution of the sampled values increases with the number of samples taken. Thus the average of ten distributions would provide a closer match to the parent distribution than would any one of the sampled distributions alone. Similarly, the average means, standard deviations and correlation coefficients of ten sampled distributions would provide a closer match to the means, standard deviations and correlation coefficients of the parent distribution.

and

$$r = \frac{n\sum_{i=0}^{n-1}\left[\left(x_i - \bar{x}\right)\left(y_i - \bar{y}\right)\right] - \sum_{i=0}^{n-1} x_i \sum_{i=0}^{n-1} y_i}{\sqrt{\left[n\sum_{i=0}^{n-1} x_i^{\,2} - \left(\sum_{i=0}^{n-1} x_i\right)^2\right]\left[n\sum_{i=0}^{n-1} y_i^{\,2} - \left(\sum_{i=0}^{n-1} y_i\right)^2\right]}}, \tag{6.3}$$

where x is the sample value, for example, a value of semi-major axis from the actual debris cloud, $\bar{x}$ is the mean of all the x samples, i is the sample number, n is the total number of samples, s is the standard deviation, r is the correlation coefficient and y is the sampled value of the element from which the x sample was taken, but in the alternate cloud, for example if x is a sample value of semi-major axis from the actual cloud then y is a sample value of semi-major axis from the simulated cloud.

The correlation coefficient is a measure of the linearity of the graph produced when the x data samples are plotted against the y data samples (in this case after both the x and y data samples had been sorted in ascending order, since there was no direct relationship between each x and y value). This provides a measure of the similarities in the shapes of the pairs of number distributions, and is independent of any differences in the means or standard deviations. The closer to unity the correlation coefficient, the more precisely the shape of the simulated distribution matches the shape of the actual distribution. Average correlations were calculated, which approximated to the correlations between the shapes of the parent number distributions. The minimum and maximum correlation coefficients were also recorded to give an indication of the variation in the correlation coefficients due to sampling.

As stated, the differences in the values of the means and standard deviations for the actual and simulated number distributions were expressed as a percentage of the data range in the actual number distributions. This was done according to the following equations,

$$\bar{x}_{\%DIFF} = \frac{\bar{x} - \bar{y}}{x_{MAX} - x_{MIN}} \times 100, \tag{6.4}$$

and

$$s_{\%DIFF} = \frac{s(x) - s(y)}{x_{MAX} - x_{MIN}} \times 100 , \tag{6.5}$$

where $\bar{x}$ is the mean of the samples from the actual debris cloud, $\bar{y}$ is the mean of the samples from the simulated debris cloud, $\bar{x}_{\%DIFF}$ is the percentage difference between the means, x_{MAX} is the maximum value of x, x_{MIN} is the minimum value of x, $s(x)$ is the standard deviation of the actual number distribution, $s(y)$ is the standard deviation of the simulated number distribution and $s_{\%DIFF}$ is the percentage difference between the standard deviations.

A comparison of the means compares the positions of the debris clouds in element-space, whereas a comparison of the standard deviations is a comparison between the sizes of the clouds. A comparison between the correlations, or shapes of the number distributions, provides a comparison between the spatial density distributions within the clouds. All three errors are independent of one another and any differences in the simulated and actual clouds will manifest themselves in at least one of these errors.

The case study parameters are presented in Table 6.1, where the breakup scenario designations LSI and LIX stand for Low-Speed Impact and Low Intensity Explosion, respectively. Studies including high-intensity explosion (HIX) induced breakups have been omitted in this exercise, as the current version of the FCP will not account for HIX scenarios. This limitation of the FCP will be discussed further in section 6.6. The orbit reference numbers correspond to one of 5 different orbits chosen for the case study – these orbits are presented in Table 6.2. Orbit 1 is a geostationary orbit, orbit 2 is a geostationary disposal orbit, or graveyard orbit, and orbits 3 – 5 are non-GEO, high-Earth orbits, which have been carefully chosen to test every path through the FCP decision-network, thus providing as rigorous a test as possible for the FCP. The variation of the propagation time and breakup parameters have also been chosen to provide a rigorous test for the FCP by generating as wide a range of distributions and scatter plot shapes as possible. The term "Thresh. Mass" in Table 6.1 stands for the threshold mass which was used in the simulation, which is chosen in such a way as to lie within the envelope where

SRP effects can be considered negligible – see section 5.3. "Prop Time" stands for the propagation time of the simulation. A variety of propagation times have been tested up to the maximum design threshold of 100 years. In each case the simulation is set to start at midnight on the 2nd August 1999, which corresponds to the epoch of the reference population used in the DAMAGE model, with which the FCP is designed to be compatible. The results of each case study are presented in Tables 6.3 – 6.23.

Case Study	Orbit Ref.	Breakup Scenario	Breakup Model	Thresh. Mass (g)	No. of Frags.	Target Mass (kg)	Proj. Mass (kg)	Impact Speed (m/s)	Prop. Time (yrs)
1	1	LSI	IDES	0.4	2743	1500	10.0	800	100
2	1	LSI	SDM	0.4	3441	1500	10.0	800	100
3	1	LSI	MASTER	0.05	3046	1000	0.5	2800	60
4	1	LSI	EVOLVE	0.4	1399	1500	5.0	100	100
5	1	LIX	IDES	0.4	853	2000	-	-	100
6	1	LIX	SDM	0.05	7220	1500	-	-	40
7	2	LSI	IDES	0.4	1424	500	5.0	500	100
8	2	LSI	SDM	0.4	314	1000	0.5	800	100
9	2	LIX	IDES	0.1	3451	1500	-	-	75
10	2	LIX	EVOLVE	0.4	2507	1000	-	-	25
11	3	LSI	MASTER	0.4	2111	500	15.0	800	20
12	3	LSI	SDM	0.4	3441	1500	10.0	800	80
13	3	LSI	EVOLVE	0.4	1071	1000	2.0	500	100
14	3	LIX	EVOLVE	0.1	3006	2000	-	-	40
15	4	LSI	IDES	0.4	2743	1500	10.0	800	100
16	4	LSI	SDM	0.4	3441	1500	10.0	500	100
17	4	LIX	IDES	0.25	5264	2000	-	-	50
18	5	LSI	MASTER	0.05	3956	500	1.0	2800	60
19	5	LIX	IDES	0.05	6216	500	-	-	60
20	5	LIX	SDM	0.4	214	250	-	-	20

Table 6.1 The case studies used in the FCP error analysis

Orbit Reference	a (km)	e	i (degs)	Ω (degs)	ω (degs)	M (degs)
1 (GEO)	42164.8	0.001	0.001	0.0	0.0	0.0
2 (Graveyard)	42500.0	0.001	0.001	0.0	0.0	0.0
3	42165.0	0.4	40	70	120	0
4	42165.0	0.3	30	170	90	200
5	30000.0	0.1	15	300	180	120

Table 6.2 The orbit references used in the error analysis case studies

	Means (%)			Standard Deviations (%)			Correlations		
	Min	Max	Average	Min	Max	Average	Min	Max	Average
a	0.1109	1.3692	**0.2468**	0.0558	1.9496	**0.0747**	0.9892	0.9947	**0.9927**
e	0.1528	6.5454	**2.4640**	0.0344	3.8539	**1.1035**	0.9933	0.9985	**0.9956**
i	3.7266	6.9202	**5.3472**	4.2735	7.1548	**5.3471**	0.9971	0.9995	**0.9986**
Ω	1.0348	10.1910	**7.0306**	0.2003	6.6304	**3.5908**	0.9158	0.9959	**0.9542**
ω	3.9543	22.6468	**9.0282**	0.0079	2.0401	**0.2678**	0.9431	0.9927	**0.9738**
M	0.0000	0.0039	**0.0008**	0.1965	2.0681	**0.3111**	0.9916	0.9962	**0.9943**

Table 6.3 Results of the error analysis for case #1

	Means (%)			Standard Deviations (%)			Correlations		
	Min	Max	Average	Min	Max	Average	Min	Max	Average
a	0.0382	3.6685	**0.1463**	0.2615	3.0491	**0.8974**	0.9972	0.9991	**0.9981**
e	0.3378	6.1825	**2.3443**	0.0232	6.7245	**2.9048**	0.9968	0.9988	**0.9981**
i	0.0320	5.0852	**1.4161**	0.2935	3.6156	**1.5260**	0.9914	0.9996	**0.9967**
Ω	0.5399	17.6228	**5.9937**	1.0852	11.5379	**4.7510**	0.8087	0.9948	**0.9351**
ω	0.4936	33.9344	**2.3097**	0.9857	17.2203	**6.0118**	0.9157	0.9787	**0.9509**
M	0.0003	0.0098	**0.0031**	0.2094	3.2240	**0.9213**	0.9973	0.9990	**0.9982**

Table 6.4 Results of the error analysis for case #2

	Means (%)			Standard Deviations (%)			Correlations		
	Min	Max	Average	Min	Max	Average	Min	Max	Average
a	0.2153	2.4494	**0.8385**	0.2628	6.2777	**1.5675**	0.9800	0.9946	**0.9890**
e	0.5489	9.2789	**4.4480**	0.3556	5.7453	**2.2758**	0.9782	0.9970	**0.9900**
i	0.0852	9.1527	**1.1561**	1.1626	8.3409	**4.2414**	0.9930	0.9995	**0.9971**
Ω	0.8131	8.3612	**4.6642**	0.1190	1.1411	**0.2468**	0.7457	0.9887	**0.9191**
ω	0.3518	18.8668	**0.3376**	0.0691	1.1710	**0.0999**	0.9128	0.9929	**0.9553**
M	0.0004	0.0060	**0.0003**	0.2080	1.8149	**0.9796**	0.9850	0.9951	**0.9905**

Table 6.5 Results of the error analysis for case #3

	Means (%)			Standard Deviations (%)			Correlations		
	Min	Max	Average	Min	Max	Average	Min	Max	Average
a	0.1569	14.4322	**2.8985**	0.3019	9.2625	**4.9814**	0.9895	0.9971	**0.9936**
e	1.0631	5.0166	**1.0803**	0.0440	3.7689	**1.3420**	0.9909	0.9977	**0.9958**
i	2.5216	6.5018	**3.5353**	0.0059	4.9830	**1.8176**	0.9874	0.9955	**0.9911**
Ω	1.1055	11.7401	**5.3475**	3.8855	8.4051	**6.1205**	0.9156	0.9687	**0.9484**
ω	5.4788	64.4036	**4.1108**	4.3878	36.7855	**22.0611**	0.5238	0.8109	**0.6865**
M	0.2932	1.0569	**0.3807**	0.9495	3.7671	**1.5248**	0.8187	0.8945	**0.8670**

Table 6.6 Results of the error analysis for case #4

	Means (%)			Standard Deviations (%)			Correlations		
	Min	Max	Average	Min	Max	Average	Min	Max	Average
a	0.3602	8.2249	**0.5061**	1.9239	9.1937	**5.4371**	0.7892	0.8860	**0.8447**
e	0.0155	13.6827	**0.0878**	0.8432	9.3973	**5.6555**	0.8742	0.9720	**0.9230**
i	0.8498	16.7321	**2.9462**	3.5925	15.1623	**9.3613**	0.8874	0.9924	**0.9554**
Ω	3.5352	15.4983	**0.6721**	2.4952	13.1958	**7.8182**	0.6701	0.9906	**0.8827**
ω	2.6284	15.8869	**2.3475**	0.0331	12.1604	**6.3483**	0.7466	0.9875	**0.9018**
M	0.0001	0.0011	**0.0001**	2.1735	10.1729	**5.4128**	0.8954	0.9477	**0.9245**

Table 6.7 Results of the error analysis for case #5

	Means (%)			Standard Deviations (%)			Correlations		
	Min	Max	Average	Min	Max	Average	Min	Max	Average
a	0.2303	3.5429	**0.8853**	4.6153	11.0328	**8.2111**	0.9130	0.9457	**0.9336**
e	4.2853	11.0446	**4.1471**	1.0537	11.2412	**5.8330**	0.9632	0.9919	**0.9784**
i	1.2827	10.9349	**3.1705**	7.8244	14.4395	**11.7984**	0.9756	0.9980	**0.9866**
Ω	2.8445	25.7783	**0.0665**	0.2648	12.3245	**4.4730**	0.7114	0.8870	**0.8198**
ω	2.4476	19.9106	**2.4824**	2.7195	12.8118	**6.3143**	0.7578	0.9952	**0.8890**
M	0.0001	0.0028	**0.0008**	3.6379	11.8736	**8.4892**	0.9598	0.9864	**0.9764**

Table 6.8 Results for the error analysis on case #6

	Means (%)			Standard Deviations (%)			Correlations		
	Min	Max	Average	Min	Max	Average	Min	Max	Average
a	0.1438	2.9387	**0.0017**	0.2900	2.5658	**1.0277**	0.9917	0.9958	**0.9934**
e	0.0654	4.6822	**0.8902**	0.3491	2.2148	**0.3057**	0.9874	0.9954	**0.9922**
i	1.3337	8.2001	**2.8433**	1.0679	3.9064	**3.0060**	0.9952	0.9990	**0.9974**
Ω	0.0775	3.1077	**0.0794**	0.0571	13.6653	**7.8285**	0.8182	0.9520	**0.8729**
ω	0.1241	29.9691	**2.5659**	0.0579	12.5436	**4.1217**	0.9117	0.9965	**0.9632**
M	0.0010	0.0090	**0.0006**	0.3171	2.6176	**0.9921**	0.9923	0.9961	**0.9938**

Table 6.9 Results for the error analysis on case #7

	Means (%)			Standard Deviations (%)			Correlations		
	Min	Max	Average	Min	Max	Average	Min	Max	Average
a	0.3333	4.7758	**1.7034**	0.5361	3.7246	**1.4848**	0.9765	0.9943	**0.9851**
e	0.9324	6.9453	**1.9057**	1.2212	3.3105	**0.3831**	0.9744	0.9915	**0.9821**
i	1.0413	6.0735	**0.7858**	0.5589	3.5763	**1.4411**	0.9784	0.9934	**0.9860**
Ω	0.4961	4.5936	**0.0228**	0.4709	20.7262	**3.1137**	0.9170	0.9907	**0.9703**
ω	5.4237	19.6577	**5.9406**	1.6217	26.1504	**0.7917**	0.9268	0.9766	**0.9626**
M	0.0002	0.0337	**0.0038**	0.5808	3.7953	**1.5032**	0.9767	0.9940	**0.9854**

Table 6.10 Results for the error analysis on case #8

	Means (%)			Standard Deviations (%)			Correlations		
	Min	Max	Average	Min	Max	Average	Min	Max	Average
a	0.0100	11.2867	**0.7394**	0.4107	7.5672	**3.8222**	0.8019	0.8485	**0.8189**
e	1.3057	7.8539	**0.9652**	0.0495	8.1269	**4.6925**	0.8900	0.9641	**0.9237**
i	1.1060	6.2304	**1.0829**	4.4437	8.8521	**7.1451**	0.8287	0.8926	**0.8646**
Ω	0.0548	9.1292	**2.4818**	0.4158	8.7471	**0.4502**	0.6380	0.9699	**0.8194**
ω	0.5098	13.6355	**1.2253**	0.3393	9.6147	**1.7230**	0.8106	0.9498	**0.8771**
M	0.0001	0.0020	**0.0000**	1.8320	7.9496	**2.5263**	0.8971	0.9233	**0.9145**

Table 6.11 Results for the error analysis on case #9

	Means (%)			Standard Deviations (%)			Correlations		
	Min	Max	Average	Min	Max	Average	Min	Max	Average
a	0.1658	2.1434	**0.1395**	1.4539	4.6344	**3.1303**	0.7596	0.8384	**0.8149**
e	0.1806	3.0223	**0.2586**	1.7377	5.7828	**3.7744**	0.8448	0.9332	**0.8990**
i	0.8639	10.2072	**1.6794**	1.7941	6.7174	**3.7376**	0.8679	0.9188	**0.9028**
Ω	0.6497	46.9647	**3.4439**	0.7406	59.3580	**14.7811**	0.3958	0.8624	**0.5925**
ω	3.1498	14.2282	**1.0607**	1.1932	7.3909	**1.3741**	0.8082	0.9897	**0.9021**
M	0.0001	0.0051	**0.0010**	2.0995	5.0660	**3.7762**	0.8476	0.9069	**0.8891**

Table 6.12 Results for the error analysis on case #10

	Means (%)			Standard Deviations (%)			Correlations		
	Min	Max	Average	Min	Max	Average	Min	Max	Average
a	0.0430	7.9115	**0.5817**	0.0674	3.8741	**0.2232**	0.9653	0.9797	**0.9737**
e	0.3756	6.4904	**0.8771**	0.0659	1.8290	**0.8326**	0.9383	0.9961	**0.9829**
i	0.1784	14.2130	**1.3465**	0.2399	7.9407	**0.4064**	0.9350	0.9875	**0.9758**
Ω	0.4965	7.0659	**0.4762**	1.0721	3.4197	**2.1696**	0.9611	0.9909	**0.9813**
ω	0.0746	7.4315	**0.1256**	0.8754	3.2404	**2.3030**	0.9780	0.9961	**0.9902**
M	0.0000	0.0087	**0.0007**	0.0537	3.4516	**1.2760**	0.9781	0.9904	**0.9857**

Table 6.13 Results of the error analysis for case #11

	Means (%)			Standard Deviations (%)			Correlations		
	Min	Max	Average	Min	Max	Average	Min	Max	Average
a	0.0125	3.6892	**1.1333**	1.3792	3.1647	**2.0059**	0.9964	0.9987	**0.9976**
e	0.0467	3.3246	**1.8954**	1.7603	4.8656	**3.0935**	0.9913	0.9986	**0.9962**
i	0.3699	4.4461	**1.3369**	0.8415	5.5938	**2.9991**	0.9938	0.9990	**0.9972**
Ω	0.0757	4.7778	**1.6379**	0.9338	3.9947	**2.4580**	0.9989	0.9997	**0.9994**
ω	0.1088	4.4145	**1.5260**	0.6954	3.5508	**2.0920**	0.9988	0.9997	**0.9994**
M	0.0004	0.0117	**0.0005**	1.4498	3.1742	**2.0251**	0.9974	0.9991	**0.9981**

Table 6.14 Results of the error analysis for case #12

	Means (%)			Standard Deviations (%)			Correlations		
	Min	Max	Average	Min	Max	Average	Min	Max	Average
a	0.6913	4.7696	**2.1771**	0.2175	1.8113	**1.2016**	0.9970	0.9984	**0.9978**
e	1.9764	5.8759	**3.9787**	0.6410	3.9510	**1.2408**	0.9956	0.9977	**0.9967**
i	0.4267	4.7380	**1.5438**	0.0901	3.6928	**1.2499**	0.9623	0.9811	**0.9731**
Ω	0.1549	6.1801	**2.5790**	1.0559	2.0636	**1.0359**	0.9952	0.9990	**0.9979**
ω	1.3201	5.9542	**4.0760**	0.2734	2.6858	**1.4449**	0.9961	0.9972	**0.9968**
M	0.0015	0.0427	**0.0084**	0.1781	1.9325	**1.2021**	0.9967	0.9982	**0.9976**

Table 6.15 Results of the error analysis for case #13

	Means (%)			Standard Deviations (%)			Correlations		
	Min	Max	Average	Min	Max	Average	Min	Max	Average
a	0.0523	2.0215	**0.0134**	0.6061	2.7948	**1.7571**	0.7659	0.8567	**0.8082**
e	0.1323	7.0898	**1.6542**	0.2071	5.3356	**2.1125**	0.7881	0.9624	**0.8568**
i	0.1128	3.9824	**0.6095**	0.3548	4.0070	**1.5606**	0.8026	0.9485	**0.9038**
Ω	0.2991	4.1438	**0.7085**	0.8492	2.0940	**0.8491**	0.8384	0.8992	**0.8714**
ω	0.3313	3.5431	**0.5358**	0.7461	2.2439	**1.1014**	0.7999	0.9032	**0.8613**
M	0.0003	0.0023	**0.0001**	0.9247	2.7085	**1.5210**	0.7964	0.8644	**0.8420**

Table 6.16 Results for the error analysis for case #14

	Means (%)			Standard Deviations (%)			Correlations		
	Min	Max	Average	Min	Max	Average	Min	Max	Average
a	0.0862	2.2319	**0.2811**	0.0258	1.7130	**0.4643**	0.9912	0.9957	**0.9934**
e	0.6379	4.6628	**0.4389**	0.0228	8.3517	**3.3002**	0.9260	0.9731	**0.9484**
i	0.1477	3.7080	**0.0016**	0.0937	2.9435	**0.4793**	0.9922	0.9973	**0.9949**
Ω	0.1701	2.6206	**1.3557**	0.0603	1.1569	**0.2572**	0.9872	0.9988	**0.9951**
ω	0.3468	1.9640	**0.1484**	0.2031	1.2431	**0.3806**	0.9927	0.9974	**0.9949**
M	0.0008	0.0079	**0.0004**	0.1100	1.5338	**0.3468**	0.9927	0.9964	**0.9946**

Table 6.17 Results of the error analysis for case #15

	Means (%)			Standard Deviations (%)			Correlations		
	Min	Max	Average	Min	Max	Average	Min	Max	Average
a	0.4170	3.9901	**0.3443**	0.0371	3.2534	**1.3966**	0.9960	0.9995	**0.9981**
e	0.1665	2.3836	**0.7957**	0.2760	4.0346	**0.8846**	0.9169	0.9626	**0.9387**
i	0.1641	4.4123	**0.2614**	0.8970	3.5012	**1.5549**	0.9952	0.9993	**0.9979**
Ω	0.0565	4.3976	**0.8579**	0.2149	3.2856	**1.3443**	0.9962	0.9987	**0.9977**
ω	0.3237	3.8554	**0.1329**	0.1658	3.3203	**1.2077**	0.9962	0.9988	**0.9976**
M	0.0000	0.0113	**0.0010**	0.0304	3.3004	**1.3693**	0.9963	0.9995	**0.9983**

Table 6.18 Results of the error analysis for case #16

	Means (%)			Standard Deviations (%)			Correlations		
	Min	Max	Average	Min	Max	Average	Min	Max	Average
a	1.0284	4.8688	**0.4112**	0.4826	5.5424	**2.9850**	0.8119	0.8887	**0.8635**
e	0.2720	9.1400	**3.8907**	2.0589	14.0856	**1.1472**	0.7146	0.9890	**0.9316**
i	0.0190	4.2221	**0.2818**	0.8124	7.9164	**2.5751**	0.0738	0.9777	**0.7841**
Ω	0.0806	15.5281	**1.0273**	0.6328	9.4016	**1.7347**	0.8721	0.9624	**0.9306**
ω	0.3291	16.1126	**0.9309**	0.3265	10.9769	**0.4678**	0.9272	0.9907	**0.9611**
M	0.0000	0.0050	**0.0002**	0.1395	4.4499	**2.1137**	0.9220	0.9390	**0.9324**

Table 6.19 Results of the error analysis for case #17

	Means (%)			Standard Deviations (%)			Correlations		
	Min	Max	Average	Min	Max	Average	Min	Max	Average
a	0.4894	5.7672	**0.0582**	0.1412	3.0063	**1.4646**	0.9799	0.9925	**0.9852**
e	1.1378	5.9849	**4.0144**	0.1138	5.4129	**1.8785**	0.9757	0.9982	**0.9924**
i	0.1769	4.9204	**1.2277**	0.0675	5.2881	**0.3812**	0.9848	0.9990	**0.9956**
Ω	0.7162	6.0911	**0.2679**	0.0746	1.9266	**0.3266**	0.9866	0.9969	**0.9914**
ω	0.0098	8.1804	**0.7371**	0.1352	4.0708	**1.5782**	0.9700	0.9937	**0.9875**
M	0.0002	0.0026	**0.0008**	0.1251	2.6004	**1.1981**	0.9891	0.9962	**0.9917**

Table 6.20 Results of the error analysis for case #18

	Means (%)			Standard Deviations (%)			Correlations		
	Min	Max	Average	Min	Max	Average	Min	Max	Average
a	0.2468	2.7705	**0.8557**	4.0777	6.3212	**5.5519**	0.7781	0.8618	**0.8131**
e	4.4887	8.2117	**5.7994**	3.8015	10.7603	**7.8919**	0.8587	0.9844	**0.9413**
i	0.0412	3.3565	**0.0973**	2.2568	6.7448	**3.8289**	0.9297	0.9664	**0.9503**
Ω	0.0082	5.6348	**0.2549**	1.0487	14.7069	**2.8213**	0.8055	0.9962	**0.9647**
ω	2.1215	19.9329	**2.5239**	0.7973	23.7047	**8.1581**	0.9130	0.9883	**0.9537**
M	0.0001	0.0010	**0.0002**	2.5573	6.4568	**4.7426**	0.9366	0.9599	**0.9457**

Table 6.21 Results of the error analysis for case #19

	Means (%)			Standard Deviations (%)			Correlations		
	Min	Max	Average	Min	Max	Average	Min	Max	Average
a	0.0486	4.1465	**0.2957**	5.3899	10.1317	**7.0960**	0.6729	0.9445	**0.8075**
e	4.4430	12.3672	**5.3088**	5.4879	14.9905	**4.8596**	0.8726	0.9767	**0.9256**
i	0.3895	3.8093	**0.3327**	0.8882	8.5341	**5.0982**	0.6997	0.9735	**0.8802**
Ω	3.7772	10.2689	**5.5078**	0.2985	17.4663	**10.5689**	0.8342	0.9926	**0.9133**
ω	0.4918	13.7003	**3.5150**	5.2296	15.3016	**5.6751**	0.7504	0.9764	**0.9009**
M	0.0002	0.0050	**0.0012**	3.8418	9.6316	**7.2798**	0.8984	0.9702	**0.9297**

Table 6.22 Results for the error analysis for case #20

The errors recorded in Tables 6.3 – 6.22 have been consolidated into Table 6.23. This table gives the average values of all the average errors in the means and standard deviations and also gives the average correlation coefficients for each of the orbital elements. Table 6.23 thus provides a measure of how the FCP behaved over all 20 of the case studies. These consolidated errors are very much case dependent however – it is important to realise that they may change significantly with a different set of case studies.

Orbital Element	Average Error in the Means (%)	Average Error in the Standard Deviations (%)	Average Correlations
a	0.8826	2.7343	0.9302
e	2.1472	2.7613	0.9593
i	1.7519	3.3472	0.9550
Ω	2.2238	3.8370	0.9215
ω	2.2830	3.6761	0.9371
M	0.0202	2.4756	0.9576

Table 6.23 Consolidated errors for each of the 20 error analysis case studies

Table 6.23 shows that the simulated number distributions exhibit average errors of less than 2.5% in the means, less than 4% in the standard deviations and correlations of over 0.9 for all the orbital elements, when compared to the actual number distributions.

On the whole, the FCP performs better at reconstructing debris clouds emanating from breakups in non-GEO target orbits (Tables 6.13 – 6.22) than it does at reconstructing debris clouds emanating from breakups in target orbits with zero eccentricities and zero inclinations, which include geostationary orbits, (Tables 6.3 – 6.12). This is because debris clouds in GEO are more complex to re-create than debris clouds in non-

geostationary orbits. In non-geostationary orbits, the FCP merely fits a least-squares mode line to the skeletal scatter plots and distributes the fragments about the mode line, usually according to a normal distribution. GEO debris clouds require mapping and unmapping routines to be employed and reconstruct the debris cloud by fitting least-squares polynomial mode lines to the skeletal scatter plots in some cases and fitting intersecting linear mode lines in other cases, i.e. for the V-shaped scatter plots. The debris fragments are also distributed about the mode lines using a combination of normal and gamma distributions, the latter of which may take a variety of shapes depending on the shape parameter, which must be calculated from the parameters in the skeletal scatter plots. Furthermore, the non-GEO debris clouds are re-created using only semi-major axis values as an input to calculate the other five elements, as depicted in Figure 5.72. GEO based debris clouds are recreated using semi-major axis values as a baseline input to calculate eccentricity, inclination and mean anomaly, and eccentricity values as an input to re-create the RAAN and argument of perigee values, as depicted in Figure 5.73. Thus for a GEO based cloud, the accuracy of the RAAN and argument of perigee distributions are subject to the accuracy of the eccentricity distribution, which in turn is subject to the accuracy of the semi-major axis distribution. For a non-GEO based cloud the accuracy of the RAAN and argument of perigee distributions are only subject to the accuracy of the semi-major axis distribution. This was described in section 5.2.8.3. Fortunately, however, the increased errors in the results for GEO breakups are mainly in the RAAN and argument of perigee distributions, which are of less importance than the semi-major axis, eccentricity and inclination distributions. This is because both the argument of perigee and RAAN are fundamentally more difficult to define in orbits for which $e \approx 0$ and $i \approx 0°$, respectively.

The FCP performs slightly better for IDES, SDM and MASTER than it does for EVOLVE. This is because the baseline model used in the design of the FCP was the IDES model, which has very similar characteristics to the SDM and MASTER breakup models, as explained in Chapter 4. The EVOLVE model, however, has very different characteristics, which results in number distributions in element-space that do not

approximate quite so well to normal distributions at the breakup epoch as the distributions produced by the other 3 models.

Generally, the FCP performs well at re-creating debris clouds that are the result of low-speed impact (LSI) induced breakups and low intensity explosions (LIX). The main difference between the effects of these scenarios on the results is in the standard deviations of the resulting distributions. The LIX scenario produces a great deal more rogue fragments than the LSI scenario. This is because of the differences in the number of small fragments generally produced by the LIX scenario compared to the LSI scenario (see Figures 4.3 and 4.15 in Chapter 4). The LIX scenario generally produces relatively few fragments with high velocities, which in turn form a large portion of the number of rogue fragments produced. The LSI scenario conversely produces a much larger number of high velocity, small fragments, which increase the spread of the distribution. The LSI scenario effectively produces so many small, high velocity fragments, that they can no longer be considered rogue fragments – instead they contribute to the core distribution and merely extend its range. The FCP can thus take these into account and include them in its reconstructed distribution. According to its design, the FCP does not usually take rogue fragments into account, as they normally lie outside of the 3σ limits of the initial distribution propagated by the FCP. However, the extremely high or low element values, taken by the relatively few number of rogue fragments in a LIX scenario, occasionally lie *within* the 3σ limits of the distribution and are thus propagated by the FCP. This is depicted in the examples illustrated in Figures 6.85 and 6.86, which show the propagated fragments in *a-i* space after 100 years for a LIX scenario and an LSI scenario, respectively. The 3σ limits of the semi-major axis and inclination number distributions have been superimposed onto the scatter plots in the form of dashed lines. It can be seen that some rogue fragments exist within these limits in the LIX scenario, whereas they are all successfully excluded in the LSI scenario. The number of fragments residing within the 3σ limits in a LIX scenario depends on the orbit and the propagation time. A sensitivity analysis of the limits required for a LIX scenario to successfully exclude all the rogue fragments is proposed in Chapter 8.

The rogue fragments sometimes propagated after a LIX breakup can have the effect of causing considerable errors in the standard deviations of the FCP results, which can sometimes lead to errors of up to 10% of the actual data range. It should be noted, however, that these errors are not noticeably reflected in the differences in the risks posed by actual and simulated clouds following a number of LIX breakups – see section 6.4. This is probably due to the poor resolution of the control volume commonly used to assess the risks posed by debris clouds to orbiting spacecraft.

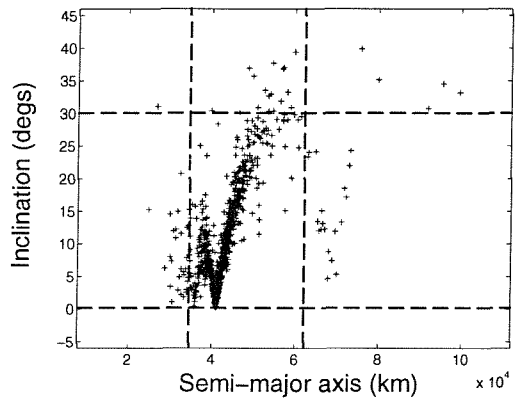

Figure 6.85 The a vs. i scatter plot for a LIX scenario in GEO (case #5) showing the 3σ limits of the distribution (dashed lines)

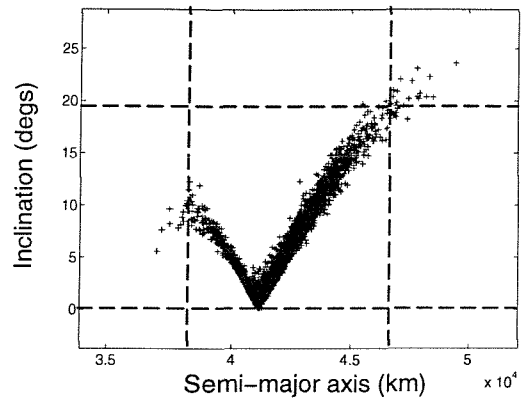

Figure 6.86 The a vs. i scatter plot for a LSI scenario in GEO (case #1) showing the 3σ limits of the distribution (dashed lines)

The effect of these FCP inaccuracies on the debris cloud is small. Even in the worst case, where all 3 sources of inaccuracy are compounded into one case study – e.g. case #10, which combines the EVOLVE model with a LIX scenario and a GEO-type ($e \approx 0$, $i \approx 0°$) target orbit, the errors are still small compared to the time saving attained. It should be noted that the largest errors in case #10 are again in RAAN, which is, as previously stated, hard to define in orbits for which $i \approx 0°$.

6.4 Risk Analysis Using FCP Data

Having quantified the errors in the FCP results from a wide range of case studies, it is now important to assess whether or not these errors are acceptable. This can be done by analysing the risk to an orbiting target object from the FCP reconstructed cloud and comparing the results to those obtained from a conventionally propagated debris cloud for each case study. If the risks are similar, then the errors in the FCP can be considered acceptable, and the FCP can be deemed accurate enough to be used in risk analysis studies and hence in future debris environment predictions.

The risk analysis undertaken on the propagated debris clouds was performed by comparing the debris flux encountered by a target object flown through the simulated debris cloud to the flux encountered by the same target object flown through the actual debris cloud for each case study. The flux environment was determined using a technique similar to the Klinkrad method [98]. To facilitate this, the orbital environment was transformed into a geocentric inertial control volume comprising a number of cells bounded by planes of declination and right ascension and by geocentric spheres of increasing radii extending outwards from the Earth. This control volume is illustrated in Figure 6.87, where Δr is the resolution of the cells in the radial direction, $\Delta\delta$ is the resolution of the cells in declination and $\Delta\alpha$ is the resolution of the cells in right ascension. The resolution of the control volume cells used in this study is based on that used by the IDES 3.0 model, an upgraded version of the IDES model, to calculate collision risks for objects in GEO and MEO. Table 6.24 gives the resolution of the bins used by IDES for GEO and MEO collision risk studies.

	Δr (km)	$\Delta\delta$ (degs)	$\Delta\alpha$ (degs)
GEO (41,378 – 43, 178 km)	50	5	10
MEO (8,378 – 41, 378 km)	1000	20	360

Table 6.24 Resolution of the control volumes used in IDES 3.0 [12]

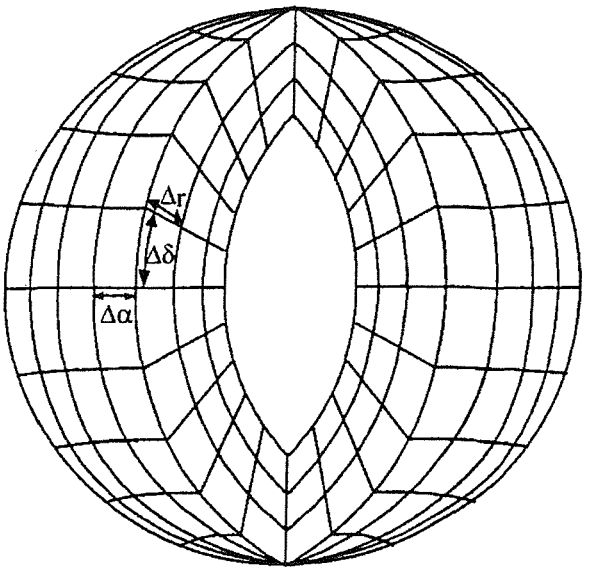

Figure 6.87 The geocentric inertial control volume used in the risk analysis [12]

For the purposes of this study, all cases with breakup orbits in the GEO regime (cases #1 – #10) were run with the IDES 3.0 GEO control volume resolution, and due to memory constraints all cases with breakup orbits outside the GEO regime (cases #11 – #22) were run with the IDES 3.0 MEO control volume resolution.

In calculating the collision risk to an orbiting target object, the debris cloud was frozen in time and the target object was flown through the control volume for one orbit, ensuring that the target orbital elements were chosen such that the target intersected the debris cloud during its flight. The probability of a collision between the target object and the debris fragments in any particular cell were then calculated for each cell of the control volume according to the equation,

$$P = \rho A v t, \tag{6.6}$$

where P is the probability of a collision, ρ is the spatial density of fragments in any particular cell, A is the projected surface area of the target object, v is the velocity of the target object at any particular time and t is the time-step used for the target object's

propagation. This equation is derived from the kinetic theory of gases and Poisson statistics and assumes that the debris behaves like a rarefied gas and that P is very small (i.e. that the probability of more than one collision is negligible) [13, 24, 99]. The sum of the collision probabilities for every cell is then calculated to yield the cumulative probability of a collision over a single orbit of the target object. This was done on a Monte Carlo basis for each of the 10 runs for both the actual and simulated debris clouds for each of the 20 case studies described in Table 6.1. The minimum, maximum and mean collision risks for each Monte Carlo run are presented in Table 6.25.

For the purposes of this study, a time-step of one minute was used for the target object and all perturbations were switched off, thus assuming Keplerian motion during the target's time of flight. In order to provide a robust test of the suitability of the FCP at generating debris clouds suitable for collision prediction studies, the target orbit was varied slightly for certain case studies, such that the target traversed the centre of the debris cloud in some cases, and traversed the cloud off-centre in other cases. The target orbits used for each case study are described in Table 6.26.

Case Number	Cloud Type	Minimum Risk ($\times 10^{-5}$)	Maximum Risk ($\times 10^{-5}$)	Mean Risk ($\times 10^{-5}$)
1	Actual	3.60	8.00	**5.53**
	Simulated	3.58	8.57	**5.99**
2	Actual	13.08	26.37	**20.05**
	Simulated	15.33	26.22	**19.08**
3	Actual	1.35	4.34	**2.76**
	Simulated	1.12	3.20	**2.21**
4	Actual	189.47	536.15	**367.39**
	Simulated	116.81	611.03	**298.08**
5	Actual	0.20	0.87	**0.46**
	Simulated	0.00	0.89	**0.46**
6	Actual	0.03	1.91	**0.47**
	Simulated	0.00	1.84	**0.52**
7	Actual	1.68	4.50	**2.41**
	Simulated	0.70	4.25	**2.73**
8	Actual	2.29	5.60	**4.04**
	Simulated	2.43	5.69	**3.41**

Case Number	Cloud Type	Minimum Risk ($\times 10^{-5}$)	Maximum Risk ($\times 10^{-5}$)	Mean Risk ($\times 10^{-5}$)
9	Actual	0.16	0.74	**0.34**
	Simulated	0.00	0.88	**0.35**
10	Actual	10.97	33.29	**19.54**
	Simulated	5.11	48.44	**18.10**
11	Actual	0.67	1.16	**0.90**
	Simulated	0.62	1.10	**0.87**
12	Actual	21.10	28.37	**23.67**
	Simulated	19.32	27.12	**22.39**
13	Actual	6.79	7.71	**7.21**
	Simulated	6.95	8.25	**7.60**
14	Actual	14.02	19.78	**16.94**
	Simulated	6.88	21.93	**12.41**
15	Actual	3.61	4.42	**3.89**
	Simulated	3.56	4.33	**3.90**
16	Actual	9.58	11.52	**10.37**
	Simulated	7.29	12.70	**11.54**
17	Actual	0.29	0.38	**0.32**
	Simulated	0.27	0.38	**0.32**
18	Actual	54.39	57.87	**56.25**
	Simulated	52.44	60.00	**55.07**
19	Actual	2.88	3.40	**3.16**
	Simulated	3.27	4.89	**3.88**
20	Actual	0.25	0.36	**0.30**
	Simulated	0.30	0.39	**0.36**

Table 6.25 Comparison of the risks posed by each cloud type for each of the 20 case studies presented in Table 6.1

Case Number	a (km)	e	i (degs)	Ω (degs)	ω (degs)
1	42164.8	0.001	0.001	0.0	0.0
2	42164.8	0.001	0.001	0.0	0.0
3	42164.8	0.001	0.001	0.0	0.0
4	42164.8	0.001	15.0	90.0	0.0
5	42164.8	0.001	0.001	0.0	0.0
6	42164.8	0.001	0.001	0.0	0.0
7	42164.8	0.02	5.0	290.0	250.0
8	42500.0	0.001	0.001	0.0	0.0
9	42500.0	0.01	12.0	0.0	0.0
10	42164.8	0.001	0.001	0.0	0.0
11	42165.0	0.4	40.0	70.0	120.0
12	42165.0	0.4	40.0	70.0	120.0

Case Number	a (km)	e	i (degs)	Ω (degs)	ω (degs)
13	42164.8	0.347	43.0	63.0	270.0
14	40000.0	0.48	35.0	120.0	120.0
15	40000.0	0.48	35.0	120.0	120.0
16	40000.0	0.48	35.0	120.0	120.0
17	42500.0	0.25	34.0	90.0	20.0
18	30000.0	0.2	15.0	100.0	0.0
19	30000.0	0.15	12.0	0.0	200.0
20	30000.0	0.1	15.0	90.0	0.0

Table 6.26 A table showing the target orbital elements used for each case study in the risk analysis

On the whole, the risks posed by the simulated debris clouds closely match those posed by the corresponding actual clouds. The large variation in the risks posed by different clouds in the same case study implies that the calculation of the risks is quite sensitive to the randomisation originally imparted to the cloud by the breakup model. Consequently, it could be concluded that 10 Monte Carlo runs may have been an insufficient basis upon which to conduct this study. However, 10 Monte Carlo runs of the conventional propagator and the FCP in 20 different case studies has generated 400 data files and as such the time required to perform the error and risk analyses was extensive. Thus the contemplation of additional Monte Carlo runs would have been impractical. The variation in the risks posed by the actual debris clouds for any particular case study was as much as 310% of the mean risk (recorded for case #6). Any discrepancies in the results must be thus treated with caution. It is likely that these discrepancies are, at least in part, caused by a lack of Monte Carlo simulations.

The sensitivity of the calculated risks to the randomisation imparted to the debris cloud by the breakup models' randomising functions is clearly an argument for conducting more Monte Carlo runs. However, the larger the number of Monte Carlo runs, the longer the simulation time becomes. This, in turn, is an argument for using the FCP, as the longer the simulation time becomes, the greater the need for a fast method of accurately propagating the debris fragments.

The greatest discrepancy between the mean risks posed by the actual and simulated debris clouds was recorded in case #14, where the mean risk posed by the simulated cloud was 26% less than the mean risk posed by the actual cloud (calculated as a percentage of the mean risk posed by the actual cloud). This may seem large, but, as stated, may well be due, in part, to a lack of Monte Carlo simulations. By comparison, the smallest discrepancy in the mean risks was approximately 0.3% and was recorded for case #15. The average mean risk error between the risks posed by the simulated clouds and the actual clouds over all 20 case studies was also 0.3%. This figure was calculated using

$$Average\ Mean\ Risk\ Error = \frac{\sum_{i=1}^{20}\left(\frac{AR\mu_i - SR\mu_i}{AR\mu_i}\right)}{20} \times 100, \tag{6.7}$$

where $AR\mu_i$ and $SR\mu_i$ denote the mean risks posed by the actual and simulated debris clouds respectively in the i^{th} case study. The fact that the average error of 0.3% is equal to the minimum error is purely coincidental. The average error can be as low as the minimum error because the average error takes negative percentages into account (see equation 6.7). The fact that this average error is so low shows that there was very little bias in the errors produced. In contrast, the average of the magnitudes of the errors over all 20 case studies (not taking negative percentages into account) is 10.0%.

It is important to put these figures into perspective. The differences in the mean risks posed by the actual and simulated debris clouds in this analysis range from 0.3% - 26% (as a percentage of the mean risk posed by the actual cloud). These numbers are very low when one considers that the differences in the risks posed by clouds produced by consecutive runs of the conventional propagator can be as high as 400% (calculated from case #6 as a percentage of the mean risk, i.e. (1.91 – 0.03)/0.47 × 100). Thus in conclusion, and based upon the 20 case studies analysed in this chapter, it can be said that the FCP produces debris clouds which pose similar risks to those posed by debris clouds propagated by conventional means, and that consequently, the FCP produces results that are accurate enough to be used in future debris environment predictions. Finally, it should

be noted that, as in the case of the error analysis, all the figures represented here are case dependent and will change with each new case. However, since the cases are many and varied and test each path through the FCP, it can also be said that these figures are representative of the FCP's performance overall.

6.5 The Speed Increase

The efficiency of the FCP over conventional propagation methods increases as the number of fragments in the debris cloud increases – regardless of the number of fragments in the debris cloud, the FCP will always propagate a constant 73 pseudo-fragments. Thus the speed increase of the FCP is best illustrated as a graph, showing its speed increase for propagating different numbers of fragments. This graph is presented in Figure 6.88. The speed of the FCP is presented as the speed increase over the conventional propagator when run on the same machine with the same time-step and all the same input parameters. This normalises out the speed and specifications of the machine and will allow other programmers to compare their propagation speeds against the FCP on any computer.

The speed increase in Figure 6.88 is defined as

$$Speed\ Increase = \frac{Time\ taken\ to\ run\ conventional\ propagator}{Time\ taken\ to\ run\ FCP}. \tag{6.8}$$

The graph shows that the efficiency of the FCP increases as a function of the log of the number of fragments, according to the following relationship:

$$FCP\ speed\ increase = 65\log(no.\ of fragments) - 180. \tag{6.9}$$

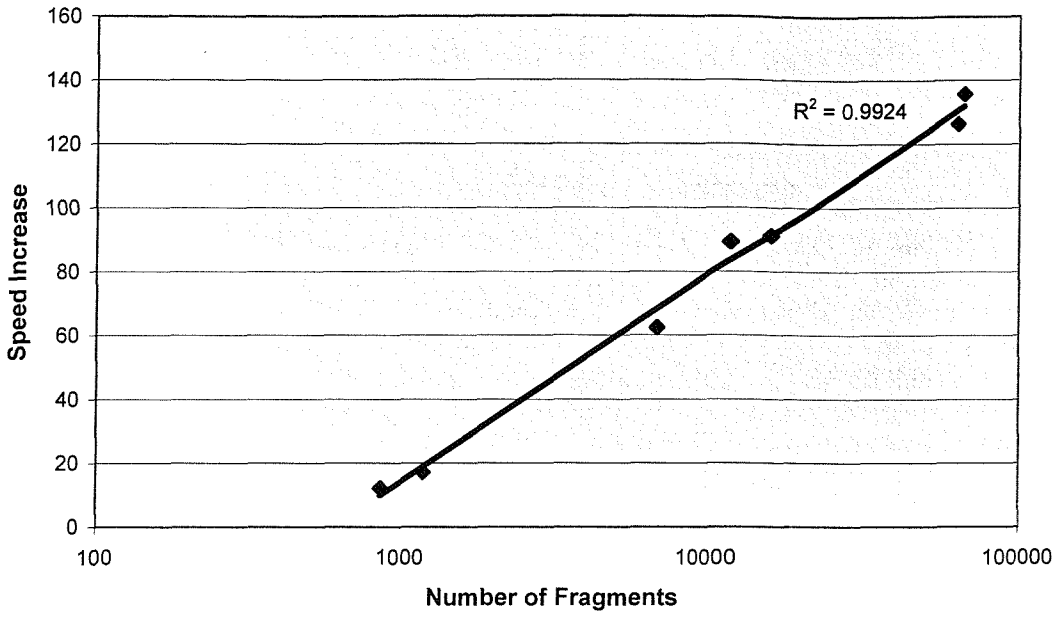

Figure 6.88 The speed increase of the FCP over the conventional propagator for different debris cloud sizes

It is difficult to compare the FCP efficiency against other orbital propagators, since their actual speeds in seconds, minutes or hours are usually quoted instead of their speed increases, and their speeds are highly dependent on the specifications of the machines upon which they were run.

The speed increase of the FCP over the conventional propagator is greater again if a number of Monte Carlo runs are required. The randomising functions that make Monte Carlo runs necessary are in the breakup model. The breakup model applies randomising functions to the positions of fragments, as well as their mass, delta-v's, and mass-to-area ratios, as described in Chapter 4. Thus when running a number of Monte Carlo runs with the conventional propagator, the breakup model and the propagator must be run sequentially over a number of iterations until the required number of data sets has been generated. This is extremely time consuming and leads debris modellers to only model a small number of Monte Carlo simulations, which fail to adequately smooth out all the peaks and troughs in the number distributions and fail to generate enough data files from which to be able to derive a meaningful averaged collision risk prediction. The FCP is

faster at running Monte Carlo simulations, not only because it can model a single propagation run much faster than a conventional propagator, but also because the important randomising functions in the FCP are at the end of the propagation phase, not at the beginning. The randomisation applied to the debris cloud by the breakup model makes little difference to the distributions that the FCP attempts to propagate, as the distributions of fragments in element-space vary very little from one breakup run to the next. The important randomisation in the FCP comes after the distribution parameters have been propagated and the distributions have been re-created. The important randomisation is in the re-creation of the fragments' elements due to the sampling of element values from the fragment number distributions in element-space at the required epoch. This is the way in which the FCP imparts randomness to the debris cloud, not through the breakup model. The importance of this is that the randomisation is applied *after* the propagation phase, not before. Thus in running Monte Carlo simulations, only the last part of the FCP model, namely the 'Unwrap' module and the subsequent 'Unmap Frags' module, need to be run iteratively (see Figure 5.36). The rest of the FCP, including the propagator, need only be run for the first Monte Carlo iteration. This concept is depicted graphically in Figure 6.89. This allows for a further significant time saving over the conventional propagator, which increases as the number of required Monte Carlo runs increases. The graph in Figure 6.90 shows the time saving attained by the FCP over the conventional propagator as a function of the number of fragments in the debris cloud for 1, 10, 100 and 1000 Monte Carlo runs.

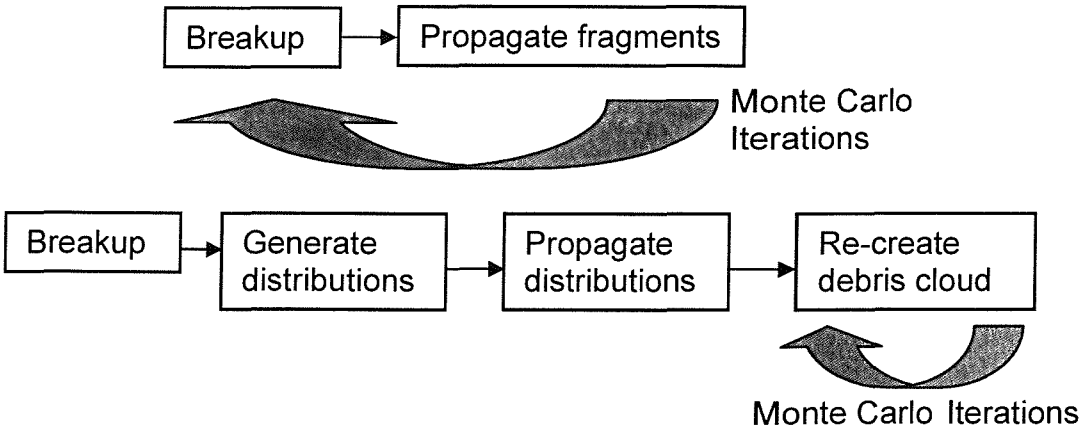

Figure 6.89 A graphic depicting Monte Carlo iterations using the conventional propagator (top) and the FCP (bottom)

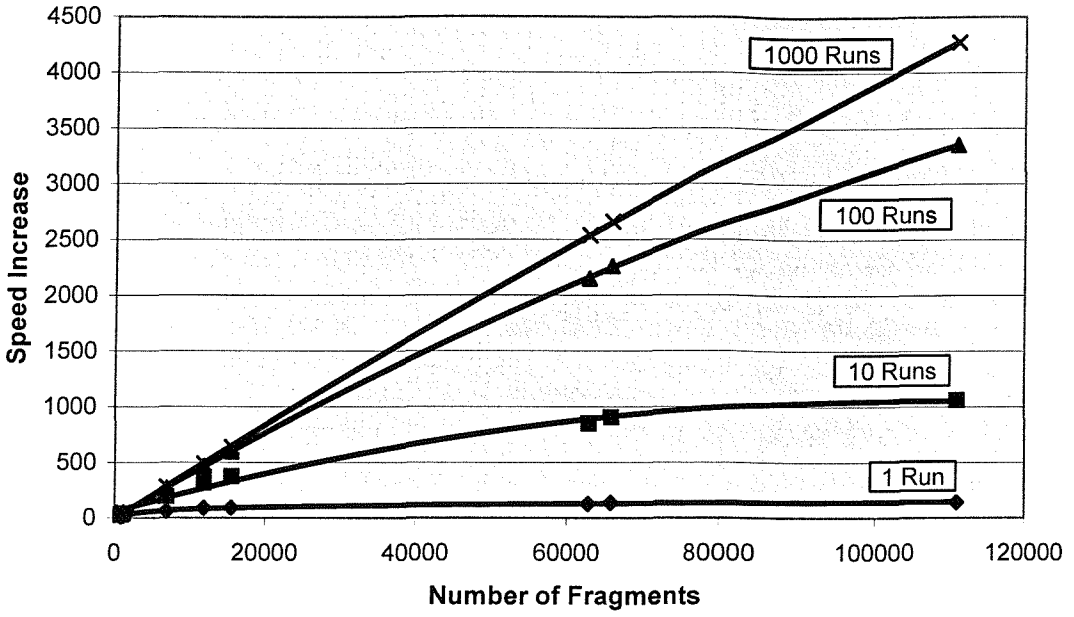

Figure 6.90 The speed increase of the FCP over the conventional propagator as a function of the number of fragments in the debris cloud for 1, 10, 100 and 1000 Monte Carlo runs

6.6 Applications and Limitations

The FCP method is very robust and has been shown to work well for propagating debris clouds through a range of non-geostationary medium and high-Earth orbits as well as in GEO and the GEO regime. It has proved itself portable for use with a number of leading breakup models, namely the breakup models used in IDES, SDM, MASTER (Battelle breakup model) and EVOLVE 4.0. The FCP is designed to work for all low-speed collisions (the only type of collision scenario experienced by objects in the GEO regime) as well as low-intensity explosions. The method has been successfully tested over a range of propagation periods and has been shown to work well up to 100 years of propagation time with no deterioration in the results.

Like any method, however, this one has its limitations. The model, in its current state, will not work for HIX, nor will it work for high inclination breakup orbits (typically

above 60 degrees). These scenarios both produce scatter plots in modified element-space where the mode line of the scatter plot cannot be represented by a polynomial with up to 8 degrees of freedom, which are the types of curves that can be fitted using the least-squares numerical method used by the FCP. The HIX scenario requires non-polynomial curves in the a vs. i scatter plots and the high inclination breakup orbit requires a polynomial with more than 8 degrees of freedom. This is a limitation in the least-squares method used however – not in the general FCP methodology. The least-squares numerical method was chosen because of its high speed, an obvious requirement for the FCP. However it lacks complexity, and whilst it is sufficient for most scenarios, it is unable to fit the mode lines required for certain HIX and high-inclination scatter plots. There are other least-squares numerical methods that can fit trigonometric functions, exponential curves and polynomials with more than 8 degrees of freedom [83, 85]. However these are very complex and slow compared to the relatively simple method chosen.

The method has other limitations, which are limitations of the method generally. The method will not work in LEO, where drag is a major perturbative force. The method will only account for gravitational perturbations – perturbations that depend upon the values of the orbital elements alone. For this reason, the current version of the model will also not account for SRP. However it has been shown that SRP has a negligible effect on an orbit compared to geopotential and luni-solar gravitational attractions, above certain fragment mass values. It should also be noted from Chapter 2 that smaller fragments tend to be more evenly distributed in space, thus reducing the importance of propagating these fragments.

The method will work for all low-speed impact induced and LIX breakup clouds, the definition of a cloud being all fragments emanating from a single breakup event. The method will not work for fragments that do not belong to a cloud. For example, the method cannot be used to propagate SRM slag, which is not the result of a breakup event. The method can however be used to propagate, and determine the increase in background debris, as long as that debris once emanated from a LIX or collision-induced breakup

event and thus forms part of a cloud, even if the cloud is so dispersed that it now forms part of the background debris environment.

The need for large numbers of Monte Carlo simulations was emphasised in the risk analysis section of this thesis, where it was shown that a large number of runs is needed if a meaningful average risk to a target object is to be derived from the cloud data. The FCP lends itself particularly well to generating large numbers of Monte Carlo simulations because of the even more dramatic speed increases that can be attained when performing large numbers of runs (see Figure 6.90). The generation of large numbers of Monte Carlo runs would otherwise often be impractical when using a conventional propagator.

It is envisaged that the FCP will be used in conjunction with conventional methods of evaluating risks to target objects, where the propagation of fragments is stopped at various time intervals for the risk analysis to be performed. For example, the IDES model freezes its debris population every six months and conducts the risk analysis on all target objects (using a method similar to that described in section 6.4) before propagating all its fragments or weighted particles for a further 6 months and conducting the risk analysis again and so on. In performing the risk analysis, it is envisaged that the distributions that are propagated by the FCP will need to be 'unwrapped' at each time interval and the fragments recovered. However, it will not be necessary to 'wrap up' the fragments again to reform the distributions before continuing the propagation, as the distributions at this epoch will already be stored in the FCP from their propagation over the previous time interval. This means that, whilst the 'Unwrap' function and its associated mapping and unmapping routines will need to be run every time the risk analysis is to be performed, the 'Wrap' function and its associated mapping and unmapping routines will only need to be run once, at the breakup epoch. If the risk analysis reveals that a breakup should be triggered at any particular epoch, it is envisaged that this breakup event will be flagged and ignored until the FCP has propagated the original debris cloud up to the required epoch. The flagged breakup will then be treated as a separate cloud, which the FCP will propagate up to the required epoch. This process of propagating one cloud at a time will be performed sequentially by the FCP. When all the fragments from each of the

propagated debris clouds have been recovered, the fragments from each cloud will be added to the predicted future debris environment.

The GEO debris environment comprises mainly operational and non-operational spacecraft, spent solid rocket motors, breakup induced debris, SRM slag and, on a much smaller scale, debris produced by the degradation of spacecraft surfaces and SRM ejecta. The degradation debris and SRM ejecta can be largely ignored, as they produce fragments which are sub-millimetre in size and thus pose little threat to larger objects. The spacecraft and SRM's are catalogued and thus their positions are known. The part of the future GEO environment comprising a number of breakup-induced debris clouds can be assessed using the FCP by superimposing several distributions on top of one another, where each distribution corresponds to a breakup event. Thus the future debris environment due to breakup debris can be assessed. This is depicted in the schematic in Figure 6.91, which shows the superposition of a number of fragment number distributions at the required epoch in Ω-space. Superimposing the catalogued spacecraft and SRM's onto this will yield the future debris environment, minus the SRM slag, which cannot be propagated by the FCP in its current state. By propagating several debris clouds indefinitely, the increase to the background environment can also be calculated accurately.

The FCP is designed to be compatible with all current models by outputting its data in terms of individual fragments, rather than merely as spatial density distributions in element-space. This means that it is portable and versatile and its modular design means it should be easy to integrate into any debris model.

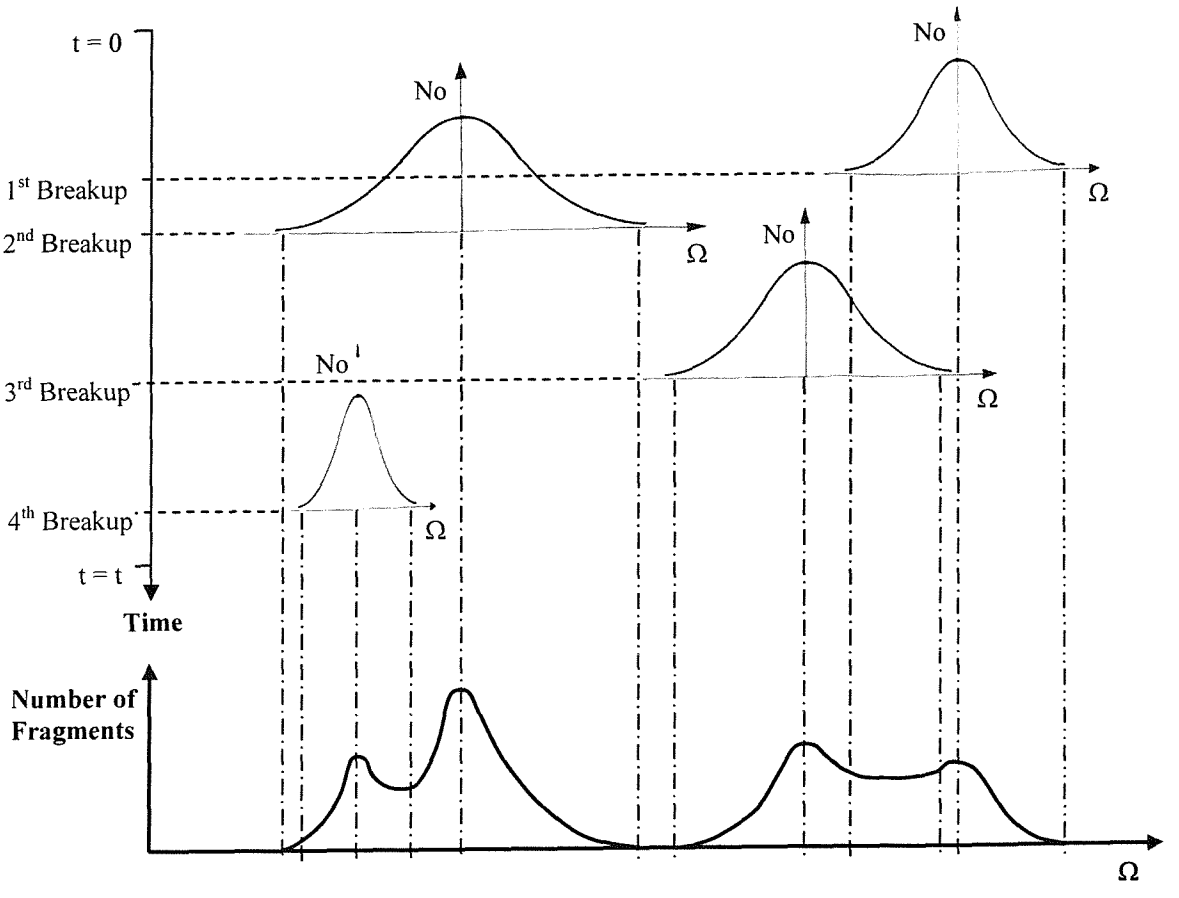

Figure 6.91 The superposition of propagated distributions in the right ascension of the ascending node

Chapter 7

Conclusions

7.1 Introduction

The work undertaken during the course of this PhD degree programme has focused primarily on two distinct aspects of debris modelling, namely the complex and non-trivial tasks of breakup modelling and debris cloud propagation, the latter forming the bulk of the novel work in the thesis. A great deal of background research was undertaken before the author was in a position to formulate his novel contribution, and this was followed by a detailed literature review of the start-of-the-art in the various techniques employed by debris modellers to attempt to reduce debris propagation times. This work breakdown has been clearly reflected in the organisation of this thesis, and the novel aspects of the work (contained predominantly in the whole of Chapter 5) have been clearly outlined.

This chapter is structured in such a way as to reflect the organisation of the thesis as a whole, and is sub-divided into sections that discuss the main findings from each chapter, which include the background debris environment, fast propagation methods, breakup modelling and the novel Fast Cloud Propagator, or FCP. Each section summarises the main points and draws any meaningful conclusions from each chapter of the thesis.

7.2 The GEO Background Debris Environment

It is clear from Chapter 2 that the proliferation of artificial debris in near-Earth orbit is of growing concern to spacecraft designers, manufacturers and operators. The growth of orbital debris in the GEO region, and in particular in GEO itself, is of particular concern, since the geostationary orbit is a unique and important resource, which furthermore has no natural sink to facilitate the removal of debris over time. The environmental consequences of a breakup in GEO are thus much greater than they are in LEO.

Chapter 2 discusses a broad range of issues that are pertinent to the LEO and GEO regimes. Some of the major points from Chapter 2 that are directly relevant to the GEO regime are summarised here.

- The accuracy of tracking equipment in tracking debris fragments in GEO is very poor. Consequently, relatively little is known about the debris population in the GEO regime. This makes the international community heavily reliant upon debris models to make predictions about the nature of the environment in this region.
- The ESA MASTER model 1999 estimates that there are approximately 10^{10} fragments in the GEO regime, of which over 20,000 are larger than 1 cm and are likely to have enough momentum to be able to cause serious damage to spacecraft in GEO. In contrast, USSPACECOM have catalogued just 762 objects in GEO.
- The rise in the GEO debris population is driven currently by explosions, with the risk of collision calculated at 1 in every 10,000 years or more. However, with explosion mitigation measures becoming commonplace and with the increasing likelihood of interaction between GEO debris and debris from GEO graveyard orbits as more and more non-operational spacecraft are re-orbited, this is a trend that is likely to be reversed in the future.
- Spacecraft and large debris fragments are clustered around particular longitudes in GEO, whereas in LEO they are fairly evenly spread. This is not the case for the smaller fragments, which tend to be evenly spread in terms of longitude in both regimes.

- In both the LEO and GEO regimes, large fragments (> 1 cm) are clustered around particular values of semi-major axis, eccentricity and inclination. Again, this is not so much the case for smaller fragments, which tend to be more evenly spread.
- The differences between LEO and GEO debris characteristics are such that it is not feasible to extend a LEO-dedicated debris model up to GEO altitudes, since many of the assumptions made in modelling debris in LEO are invalid in the GEO regime.
- Because of the difficulty of improving the space environment with existing technologies, the implementation of debris mitigation measures today is a prudent step towards preserving space for future generations. Some mitigation measures are already commonplace while others are still being introduced. However, a great deal more needs to be done in terms of mitigating the production of debris, especially in GEO, where the re-orbiting of spacecraft up to super-synchronous graveyard orbits can only serve as a short-term measure.

Finally, it should be emphasised that one of the factors that makes GEO modelling so important is the physical limitations of the measuring equipment. Large fragments of orbital debris are routinely tracked using radar, the resolution of which allows debris fragments with diameters as low as approximately 10 cm to be tracked effectively in LEO. However in GEO this resolution is reduced to around 1 m. Consequently, optical techniques are routinely used to track debris in the GEO region. However, optical techniques are highly variable and depend on many external factors, such as the reflectivity of the object, the position of the Sun relative to the object at the time of observation, the clarity of the sky, the orientation of the object, etc. This makes optical techniques unreliable compared to the radar techniques commonly employed in tracking LEO debris, especially when it comes to determining the orbital parameters of the objects. The consequence of this is that there is a gap in the knowledge base in terms of fragment size as far as GEO debris is concerned, which typically ranges from the sub-millimetre in diameter to diameters close to a metre. This sizeable gap in the observed GEO debris population makes the need for accurate GEO modelling techniques in this size range ever more important.

7.3 Orbital Debris Propagation

A review of the techniques used in various orbital propagators to improve their propagation speeds was undertaken in Chapter 3. One of the most popular solutions for improving the speeds of debris propagation included the use of weighted particles to represent a large number of fragments with similar characteristics, thus saving time by only propagating the weighted particles rather than the large numbers of individual fragments they represent. Another commonly used technique is the randomisation of RAAN, argument of perigee and mean anomaly at the end of the propagation process, thus saving time by not applying perturbative effects to these elements. Very often these two methods are combined with one another. These techniques are widely used in many debris models because they are easy to implement and they can provide a moderately large time saving over more conventional propagation methods whilst forfeiting moderately little in terms of the accuracy of the results produced.

The method of randomising the values of RAAN, argument of perigee and mean anomaly relies upon the assumption that the fragments are fairly evenly distributed in terms of these elements and that, as such, the effect of randomising them uniformly at the required epoch would produce much the same result as applying perturbative effects to them at each time-step and calculating their true final values. This assumption may be valid in LEO, but it does not hold true in the GEO regime, where spacecraft and hence debris fragments are clustered around the Earth according to their longitude. Thus, while this technique may provide a good approximation to the actual future spatial density of fragments in LEO, it cannot be used in GEO.

The method of using weighted particles to represent large groups of fragments is not without criticism either. Having propagated the weighted particles, which are usually initially located at the centre of mass of the groups of fragments that they represent, the model must now either re-distribute the fragments around the weighted particles or leave the propagated population in its weighted particle form. In the first instance, the model has lost all the information by which it can re-distribute the fragments, i.e. the model has

no way of knowing what kind of distribution to apply to these fragments, whether it be uniform, normal or otherwise, and has no way of knowing what the variance in this distribution should be. In the second instance, where the weighted particles are left as they are, the risk analysis method will have to be run using the weighted particles rather than the individual fragments. This effectively assumes that all the fragments that a weighted particle represents all occupy the same space at the same time, which is clearly an invalid assumption, and the outputs from the risk analysis routine will surely suffer as a result. However, in this instance the trade-off between accuracy and speed can be easily controlled by varying the weighting factor given to the weighted particles, i.e. the number of individual fragments that a weighted particle represents.

In retrospect, there are few models that could really be described as dedicated fast orbital propagators as such, i.e. models that use highly novel techniques to propagate a population of debris fragments. Most propagators are standard orbital propagators that utilise various add-on techniques to try and improve their speeds with as little reduction in accuracy as possible. Dedicated fast debris propagators do exist, e.g. STAT, PETRA, etc., although these are all dedicated to orbital propagation in the LEO regime because of one or more of the following:

- they mainly model the changes due to air drag (the largest perturbation effect in LEO – but which has no effect whatsoever in GEO);
- they only apply orbital perturbations to certain orbital elements, most commonly semi-major axis, eccentricity and inclination, whilst randomising the values of other elements, most commonly RAAN, argument of perigee and mean anomaly; and
- they neglect to model certain important geopotential harmonic terms, such as the second order sectoral harmonic coefficient, J_{22}, which has a cumulative resonant effect in GEO.

To summarise, the models described in Chapter 3 are not well suited for use in the GEO regime. To date, no fast debris propagator exists which has been tailored for use in GEO. As the GEO debris population continues to grow, such a propagator would be of great use

to the modelling community, especially when running a large number of Monte Carlo simulations or a number of future debris environment predictions with varying input parameters, such as changing mitigation options.

7.4 Breakup Modelling

The analytical modelling of the physics involved in fragmentation events is a virtually impossible task, requiring immense computing power and far too many input parameters, which in reality would simply not be available. Hence, the equations used in breakup models are all empirically derived from fragmentation ground tests and on-orbit explosions. The limitations of on-orbit measurement techniques preclude the possibility of measuring the number and properties of small fragments (less than around 10 cm in LEO and less than around 1 m in GEO) and this justifies the need for ground tests. The ground-based tests are conducted in test chambers and the number, velocities, masses and sizes of the fragments are measured. This is an extremely complex and error-prone procedure and the large numbers of fragments produced make the task of counting and measuring the fragments extremely time consuming. As a result, relatively few ground-based experiments have been undertaken and consequently there is relatively little data available upon which the empirically derived breakup equations can be based. Each fragmentation scenario must also be treated separately, as each produces different trends in the number, mass, size and velocities of fragments produced. These trends vary, not only according to the fragmentation scenario, but also according to many other factors, most notably collision speed, projectile mass, target mass and impact angle for collision induced fragmentations, and explosion energy and target mass for explosion induced fragmentations. This imposes limits on the usefulness of any equations which have been derived from any experimental data set, and yet these equations are routinely used beyond their intended limits in breakup modelling. The computational speed and ease with which present-day breakup models can be used however, makes this approach acceptable and outweighs any potential misgivings regarding the accuracy of the results

produced. Nevertheless, these results are undoubtedly inaccurate and any analyses based upon these results must therefore be treated with great caution.

Four leading breakup models were analysed in terms of the breakup characteristics they produced. These models, IDES, SDM, MASTER and EVOLVE 4.0, were later used to fully test the robustness of the FCP in propagating debris clouds. On the whole, the results of the IDES, MASTER and SDM models were in good agreement. This is unsurprising however, as the equations they employ are very similar and are largely based upon the same data sets. Thus these models are not truly independent of one another. The results from the EVOLVE 4.0 model, which is new and is marketed as the state-of-the-art in breakup modelling, are remarkably different for all scenarios. The EVOLVE 4.0 breakup model has benefited from a re-working of the breakup equations based on new data sets – hence the differences in the results. The degree of change to the equations and hence trends produced by the inclusion of new data to the underlying data set is worrying however. One cannot help but wonder, if in years to come, when yet more breakup data is available and the breakup equations are updated again, whether the trends produced by future models will change drastically once more.

Notwithstanding these issues, debris modellers have little choice but to rely on these breakup models, as, flawed though they may be, they represent the only realistic means by which to model breakup events. The future will undoubtedly yield many more fragmentation test results, which will be used to further update the equations used to describe on-orbit fragmentation events. Only when the pool of data upon which these equations are based is increased considerably, will the debris community truly begin to have real confidence in the results produced by debris models.

7.5 The Fast Cloud Propagator

The Fast Cloud Propagator, or FCP, differs fundamentally from every other propagator in the sense that it propagates distributions of fragments through time rather than

propagating individual fragments or weighted particles. This is far more meaningful than propagating individual fragments. The original positions of individual fragments are subject to randomising functions in the azimuths, elevations and delta-v's allocated to those fragments by the breakup model. Thus every time the breakup model is run – even with the same input parameters – it results in a different debris cloud each and every time. Clearly, it is the characteristics of the fragment distributions that count, and not the characteristics of the individual fragments themselves. The positions of the fragments exist only to describe a fragment density distribution at any given epoch. Thus it is far more meaningful to propagate these fragment distributions directly, and it is also much more efficient to do so, if only the minimum amount of information required to re-create each distribution is propagated during each simulation.

The FCP propagates the fragment distributions by carefully selecting a set of distribution parameters, which are chosen such that they fully characterise the distribution, and which are allocated to the minimum number of pseudo-fragments possible – numbering 73 in total. The FCP thus gains a large speed increase over conventional propagators by only propagating these 73 pseudo-fragments, regardless of the number of fragments that existed in the original debris cloud. Hence, the efficiency of the FCP increases as the size of the debris cloud increases. Empirical analysis has shown that the efficiency of the FCP increases as a function of the log of the number of fragments in the cloud. For example, when propagating a debris cloud with 10,000 fragments, the speed of the FCP is 80 times that of the conventional propagator, whereas when propagating a debris cloud with approximately 110,000 fragments, the speed of the FCP is 140 times that of the conventional propagator.

The FCP gains a further large speed increase over the conventional propagator if a number of Monte Carlo simulations are required, which are highly desirable in predicting the future debris environment. The randomising functions that make Monte Carlo runs necessary are in the breakup model. As stated, the breakup model imparts randomness to the azimuths, elevations and delta-v's of the fragments and also imparts randomness to their mass-to-area ratios. Thus, when running Monte Carlo simulations with the

conventional propagator, the breakup model and the propagator must be run sequentially over a number of iterations until the required number of runs has been completed. The objective here is to 'smooth out' any anomalous peaks or troughs in the future predicted spatial density distribution of fragments, which have been generated by unlikely events (e.g. explosions) in a minority of Monte Carlo runs. This can be extremely time-consuming and leads debris modellers to perform very few Monte Carlo simulations, thus generating an inadequate number of data files from which to draw a meaningful conclusion. The FCP allows a number of Monte Carlo runs to be generated quickly, not only by virtue of the fact that it propagates each debris cloud quickly, but also because the important randomisation imparted to the debris cloud in the FCP comes, not at the beginning of the simulation, but at the end. The randomness imparted by the breakup model to the original debris cloud makes relatively little difference when selecting the distribution parameters to be propagated by the FCP, as the overall distribution of fragments differs little from one run of the breakup model to the next. Randomisation is imparted to the debris fragments by the FCP in the sampling of fragment orbital elements from the propagated distributions. The fact that this process follows the propagation process means that the propagation process need not be run in each Monte Carlo simulation – it need only be run in the first iteration – only the last two modules of the FCP need be run iteratively to generate the Monte Carlo data files. This provides an enormous additional time saving for the FCP, which further increases as the number of required Monte Carlo runs increase. For example, the FCP is approximately 1100 times faster than the conventional propagator at performing 10 Monte Carlo runs of a debris cloud containing 110,000 fragments, whereas the FCP is approximately 4300 times faster than the conventional propagator at performing 1000 Monte Carlo runs of a debris cloud containing the same number of fragments .

Twenty case studies with varying parameters were used to test the accuracy of the results produced by the FCP. Each case study comprised 10 Monte Carlo simulations of the FCP and 10 Monte Carlo runs of the conventional propagator to facilitate meaningful comparisons of the FCP propagated and conventionally propagated debris clouds – also referred to as the simulated and actual debris clouds respectively. The clouds were

compared using the number distributions produced in element-space for each simulation, as these number distributions would completely reflect any variations between the clouds. For each pair of number distributions, the means, standard deviations and correlations were compared, as these values are independent of one another and together completely describe any differences in the distributions. The results showed that the debris clouds produced by the FCP closely matched those from the conventional propagator. On average, the differences between the means of the distributions for all 20 case studies was less than 2.5%, the differences between the standard deviations was less than 4% and the correlations were all greater than 0.9 for each element.

In order to assess the acceptability of these errors, a risk analysis exercise was performed on each of the 400 data files using a technique similar to the Klinkrad method, where the risks posed by the debris clouds to a variety of orbiting target objects were assessed. The discrepancies between the mean risks posed by the actual and simulated clouds for each case study ranged from 0.3% to 26%, with an average discrepancy over all case studies of 0.3% (the fact that this matches the lowest mean discrepancy is purely coincidental and can be so because negative errors were considered when calculating the overall average value). The average of the absolute errors (not taking negative errors into account) was 10%. These figures are low when compared to the variations in the risks posed by debris clouds generated by consecutive runs of the conventional propagator, which can be as high as 400% of the mean risk. Thus the FCP results can be deemed sufficiently accurate to be used in future collision event predictions, and hence in future debris environment predictions.

There are a number of errors due to invalid assumptions in the modelling of breakup events that detract from the accuracy of the original debris cloud, and thus from the accuracy of any evolved debris cloud. The assumption of an isotropic breakup in every case is one such assumption. These assumptions were discussed in detail in Chapter 4 of this thesis and imply an error in the characteristics of the conventionally propagated debris cloud, the extent of which is hard to determine. This is a further indication that the

level of error in the FCP is acceptable relative to the error in the conventionally propagated cloud.

The FCP is robust and has been shown to work well for propagating debris clouds through GEO and a variety of non-geostationary high-Earth orbits, both inside and outside the GEO regime. It is also portable with respect to many of the leading breakup models (e.g. IDES, SDM, MASTER and EVOLVE 4.0). It is designed to work for all low-speed collisions (the only type of collision scenario likely to be experienced by objects in the GEO regime) as well as low-intensity explosions. The method has been successfully tested over a wide range of propagation times, up to the maximum design threshold of 100 years, with no deterioration in the results.

The main limitations of the method are the loss of physical characteristics for the propagated fragments and the fact that, in its current state, the FCP will not accurately propagate debris clouds which are the product of high-intensity explosions. The fact that the FCP will not account for high-intensity explosion events is due to the limitations of the relatively simple least-squares numerical method used to generate the mode lines for the primary scatter plots produced by the FCP. This least-squares method was chosen because of its speed over more complex methods, an obvious requirement for the FCP. However it lacks the complexity to be able to model the non-polynomial curves required for mode lines of scatter plots that have been generated as a result of a high-intensity explosion. The loss of physical characteristics for the debris cloud fragments is an artefact of the FCP methodology – as soon as the individual fragments are reduced to a set of distribution parameters, the individual physical characteristics of each one is lost. However, Chapter 8 discusses an extension to the FCP methodology that will allow the recovery of these physical characteristics at the required epoch.

In short, the FCP in its current state represents the 'tip of the iceberg' in terms of the extent to which the general technique can be developed. The FCP, as it stands, is a novel, fast, accurate and useful tool for propagating debris clouds in the GEO regime and furthermore attains even greater speed increases if a number of Monte Carlo runs are required. It is envisaged that, at present, generating large numbers of Monte Carlo

simulations will be its most useful role. This role is essentially important however, as debris modellers are usually forced to curb the number of Monte Carlo runs they generate due to the practical limitations of time-constraints. This can have deleterious effects on the results produced. However, whilst the FCP is an important tool, in its current state it retains a number of limitations that prevent it from realising its full potential. It is envisaged that with these limitations removed and with further development, the FCP could become a powerful tool in modelling the future debris environment.

Chapter 8

Future Work

8.1 Introduction

The work presented herein describes the development and implementation of a new technique. However, a great deal more can be done in developing this to its full potential. Thus far, this thesis has described the development of the FCP to its current state. It stands as a self-contained piece of work, which in itself should be of great use in quickly propagating debris clouds in the GEO regime. However, the FCP in its current state merely represents the first version in what the author hopes will be a series of improvements to the methodology. This chapter will explain how the theory behind the FCP can be explored to its full potential and invites other researchers elsewhere to adopt and implement the ideas presented herein in order to fully exploit the method.

Future work on the FCP can be sub-divided into two categories: short-term and long-term. The short-term future work represents improvements to the existing FCP program in order to improve on the results and make the FCP more robust. However, it does so within the confines of the existing methodology. The long-term future work represents new ideas and an expansion of the current method, which will make the FCP a much more powerful tool in future space debris studies. These are described in the following sub-sections.

8.2 Short-Term Future Work

8.2.1 Compatibility with the HIX Scenario

The obvious first-step in the short-term improvements to the FCP would be to make it compatible with HIX (High-Intensity Explosion) scenarios. The FCP worked well for HIX scenarios before it was modified to account for the effects of luni-solar gravitational perturbations, i.e. when it only accounted for geopotential perturbations, as was the case when it was first introduced to the international community [2]. However, the inclusion of luni-solar perturbations causes long-term periodic changes in inclination and long-term periodic and/or secular changes in eccentricity, RAAN and in the argument of perigee [4]. The long-periodic changes in inclination were particularly problematic. The changes in inclination before the inclusion of luni-solar gravitational perturbations were quite small and thus the a vs. i primary scatter plot was one of the easiest to replicate. However, with the inclusion of luni-solar gravitational perturbations, the changes in inclination became very large. As a result, the a vs. i scatter plot became the hardest scatter plot to replicate. It is now a very variable distribution, which changes significantly depending on the breakup orbit and in particular on the propagation time. It is difficult to classify and hard to replicate and a great deal more code has been written to account for these changes. This has led to a reduction in the performance of the FCP overall, which has manifested itself in greater errors in the results when compared to a conventional propagator. This is particularly true of HIX scenarios, which produce high-energy fragmentations. The high energies involved in a HIX scenario means that the fragments are imparted with higher delta-v's and thus the initial debris cloud is larger, resulting in cloud fragments with a greater variation in the values of the orbital elements. The larger range in the values of inclination means that luni-solar effects are particularly pronounced on the particles with high inclinations and much less so on the particles with low inclinations, since the effect of luni-solar perturbations is highly inclination-dependent. This results in an a vs. i scatter plot distribution with non-polynomial mode lines. The least-squares method, which is used to fit the mode lines to the scatter plot distributions,

became ineffective at fitting these non-polynomial mode lines. The author attempted to implement a more robust and much more complex least-squares method [85], which could be used to fit polynomial as well as non-polynomial mode lines, however several errors were discovered in this numerical method and, with a lack of knowledge of the theory upon which this numerical method was based, it was impossible to correct these errors and make the method work properly. If a working, more robust least-squares method could be found, then this could be used to generate the mode lines for the a vs. i scatter plots in a HIX breakup event and then the FCP could be used for all breakup scenarios as modelled by all breakup models. It is recommended that the original least-squares method be maintained, however, as this was originally chosen for its speed and works well for all low-energy breakup events. It is proposed that the new least-squares numerical method be limited to fitting mode lines to the a vs. i scatter plot following a HIX event.

8.2.2 Improvements in Modelling LIX-Induced Clouds

Chapter 6 (section 6.3) highlighted a source of error in propagating debris clouds produced by low-intensity explosion (LIX) induced breakups. It was noted that the 3σ limits normally employed (in conjunction with the mode values) to describe the number distribution histograms at the breakup epoch are not always adequate to eradicate undesirable rogue fragments in LIX scenarios. Whilst these limits are always successful in excluding rogue fragments in LSI scenarios, they are sometimes too large for LIX scenarios, causing errors in the standard deviations of the number distributions. These errors seem to have little impact on the errors in the risks posed by the simulated debris clouds, however, probably because of the poor resolution of the control volume used to compute the spatial densities of fragments. However, in the interests of further improving the performance of the FCP, it is recommended that future work include a sensitivity analysis of the limits to be used in propagating clouds produced by low-intensity explosions. Smaller limits will undoubtedly be beneficial, although the optimum magnitudes for these limits may be orbit-dependent.

8.2.3 Using the Initial Semi-Major Axis Distribution as a Baseline for Reconstructing the Debris Cloud

There may be some room for improvement in the errors and correlations recorded for the simulated semi-major axis distributions in general. It has been noted that the values of semi-major axis do not change much on the whole for objects in high-Earth orbits. It is possible that a better approximation for the semi-major axis distribution at any time t may be obtained by simply using the semi-major axis distribution at the breakup epoch. Preliminary investigations reveal that this distribution more closely resembles the actual distribution at time t than the simulated distribution reconstructed using the FCP. For instance, the errors encountered in the mean and standard deviation (averaged over 10 Monte Carlo iterations) when using the actual initial distribution in semi-major axis for case #15, again, expressed as a percentage of the actual final mean and actual final standard deviation, are 0.0116% and 0.3225% respectively. The correlation between the initial and final distribution is 0.9989. In comparison, the Monte Carlo averaged errors in the mean and standard deviation of the simulated semi-major axis distribution were recorded as 0.2811% and 0.4643%, respectively, and the correlation between the actual and simulated semi-major axis distribution was recorded as 0.9934 (see Table 6.17). Thus a small but significant improvement would have been attained in this case by using the actual, initial distribution in semi-major axis rather than the simulated final semi-major axis distribution generated using the FCP. This improvement is significant because all other orbital elements are re-created using semi-major axis as a baseline. Thus improving the semi-major axis distribution should also improve the distributions of the other orbital elements. Furthermore, the use of the actual initial semi-major axis distribution should also provide a further small improvement to the speed of the FCP, as it will no longer have to re-calculate the values of semi-major axis at each time-step, nor will it have to reconstruct this distribution at the required epoch.

8.3 Long-Term Future Work

8.3.1 The Recovery of the Fragments' Physical Characteristics

The biggest disadvantage of using the FCP in its current state is the loss of the fragments' physical characteristics. The physical characteristics of each fragment, comprising its mass, diameter, area and mass-to-area ratio, are generated by the breakup model. The masses are assigned to each fragment according to the cumulative number of fragments vs. mass curve specific to the breakup model being run – see Chapter 4. The cumulative number of fragments are binned according to their mass and the fragment mass is randomly assigned to each fragment in that bin (within the confines of the mass range allocated to that bin). The fragment's cross-sectional area is calculated from the fragment's mass and then randomised according to a log-normal or normal distribution, depending on the breakup model in use. The fragment diameter is then easily calculated from the fragment area by assuming that the fragment is spherical. Unfortunately, as soon as the fragment distributions are generated, all the physical information pertaining to each fragment is lost – only the fragment number distributions remain. However, preliminary research in this area suggests that the physical characteristics of the fragments can be recovered easily by a simple extension of the current FCP methodology. The fragment masses conform to simple distributions in element-space, much like the fragment number distributions. Figures 8.1 – 8.6 illustrate the mass distribution in element space for each of the six orbital elements immediately following a low-speed collision induced breakup (produced by a 10 kg projectile impacting a 1500 kg target object with a speed of 800 m/s) in a non-geostationary orbit (a = 42165.0 km, e = 0.3, i = 30°, Ω = 170°, ω = 90°, M = 200°, i.e. orbit #4 from the error analysis case studies used in Chapter 5) as modelled by the IDES breakup model. The largest object, the spacecraft remnant, has been removed in order to make the remainder of the distribution visible on this scale.

The figures show approximately symmetrical distributions with large peaks in mass around the mean point of the distributions. These peaks in mass correspond to just a few dozen fragments that have a very high mass compared to the rest of the cloud. Figures 8.7

– 8.12 show the same distributions, this time with the most massive 5% of fragments removed.

After the removal of the most massive fragments, the large mass peaks present in the distributions in Figures 8.1 – 8.6 disappear and the remaining distributions (shown in Figures 8.7 – 8.12) approximate to normal distributions. The peaks and troughs in these distributions are due to sampling – these peaks and troughs can be smoothed out by binning the fragment masses of a number of different Monte Carlo simulations and plotting the average mass from each bin. The smoothed results from ten Monte Carlo runs for the same breakup scenario are presented in Figures 8.13 – 8.18. These Monte Carlo averaged mass distributions illustrate how closely the mass distributions resemble normal distributions at the breakup epoch.

In fact, the mass distributions themselves are not so important in reconstructing the mass values of each fragment. The FCP will need to use the mass-per-fragment distributions in element-space to recover the masses of each fragment. These are illustrated in Figures 8.19 – 8.24, again with the most massive 5% of fragments removed.

The peaks and troughs are more noticeable in Figures 8.19 – 8.24 due to the fact that the y-axis has a much greater scale – thus any variations due to sampling or binning are more noticeable. There are large peaks near the edges of several of the distributions because there are very few fragments per bin in these regions, thus any fragments that have unusually large masses here will dominate, as their effects will not be smoothed out as much by the remaining fragments. Nevertheless, the underlying distributions are still very clear and may be approximated using a series of normal distributions, although further study may be necessary to determine the optimum distribution to represent these samples. The fragment mass values can be generated by sampling from any one of these distributions, in the same way that the element values were recovered by sampling from the number distributions.

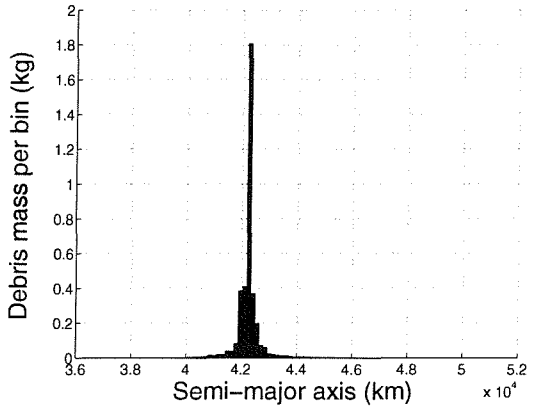

Figure 8.1 The distribution of mass in semi-major axis following a low-speed collision in orbit #4

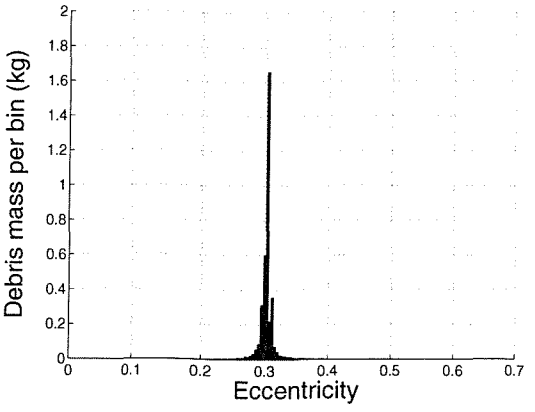

Figure 8.2 The distribution of mass in eccentricity following a low-speed collision in orbit #4

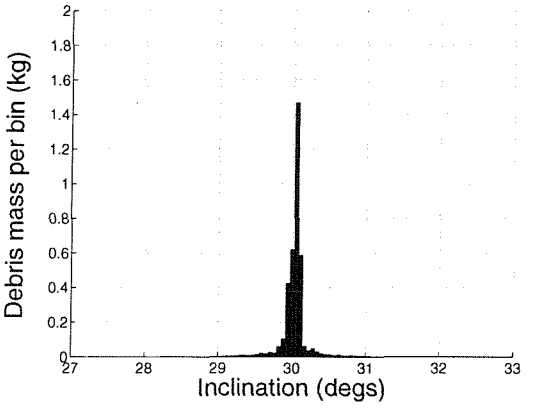

Figure 8.3 The distribution of mass in inclination following a low-speed collision in orbit #4

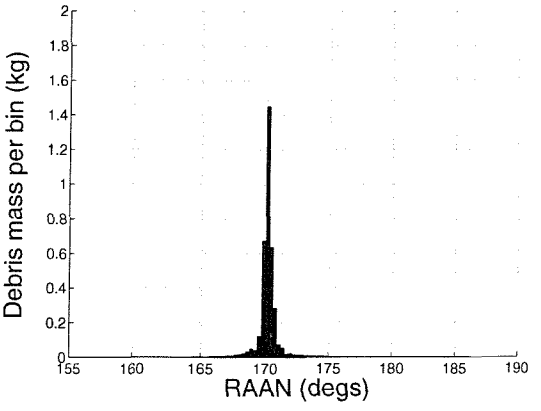

Figure 8.4 The distribution of mass in RAAN following a low-speed collision in orbit #4

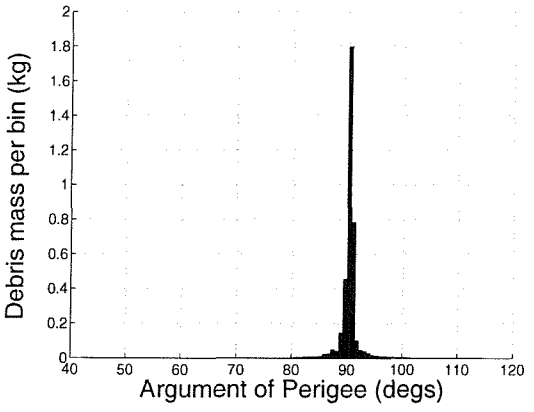

Figure 8.5 The distribution of mass in argument of perigee following a low-speed collision in orbit #4

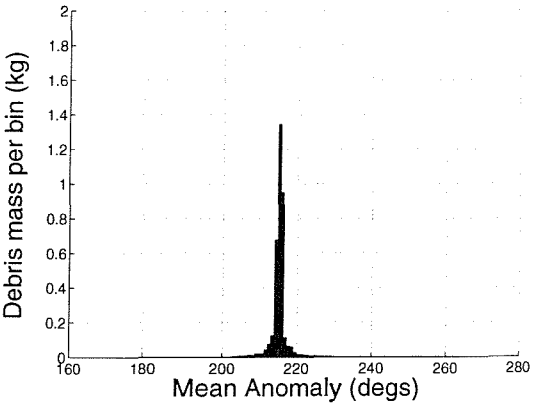

Figure 8.6 The distribution of mass in mean anomaly following a low-speed collision in orbit #4

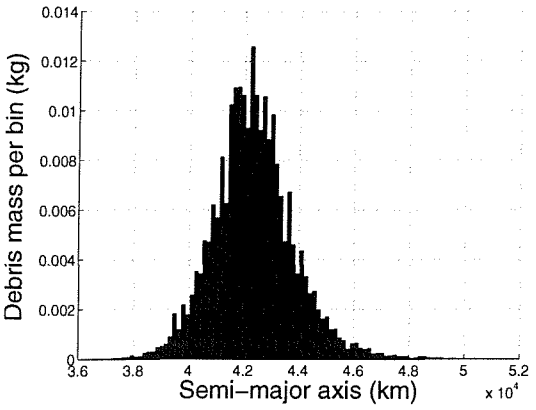

Figure 8.7 The distribution of mass in semi-major axis following a low-speed collision in orbit #4 (most massive 5% of fragments removed)

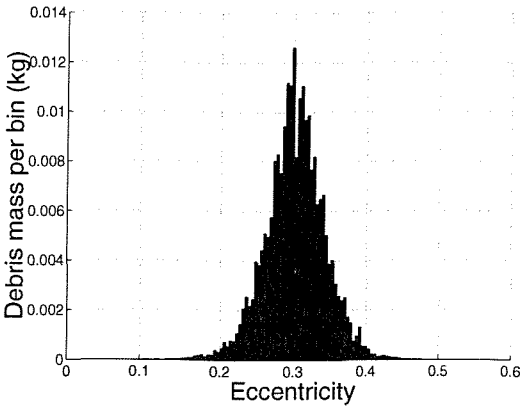

Figure 8.8 The distribution of mass in eccentricity following a low-speed collision in orbit #4 (most massive 5% of fragments removed)

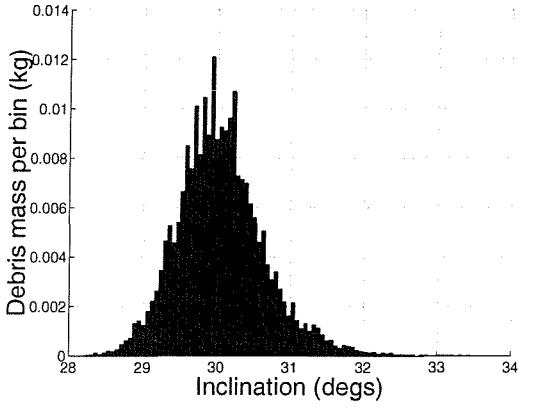

Figure 8.9 The distribution of mass in inclination following a low-speed collision in orbit #4 (most massive 5% of fragments removed)

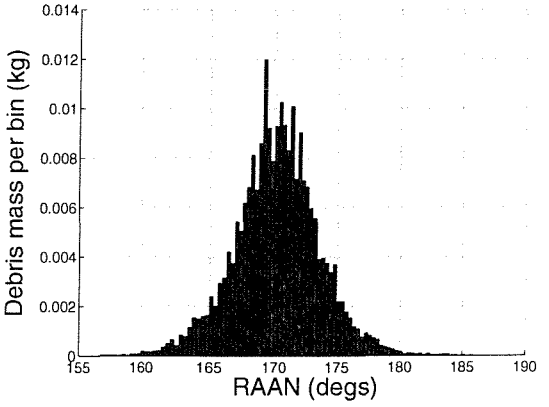

Figure 8.10 The distribution of mass in RAAN following a low-speed collision in orbit #4 (most massive 5% of fragments removed)

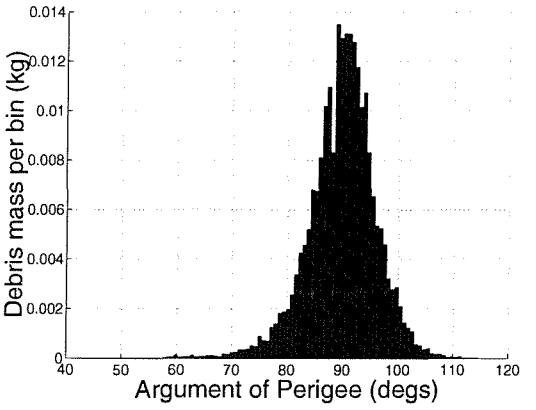

Figure 8.11 The distribution of mass in argument of perigee following a low-speed collision in orbit #4 (most massive 5% of fragments removed)

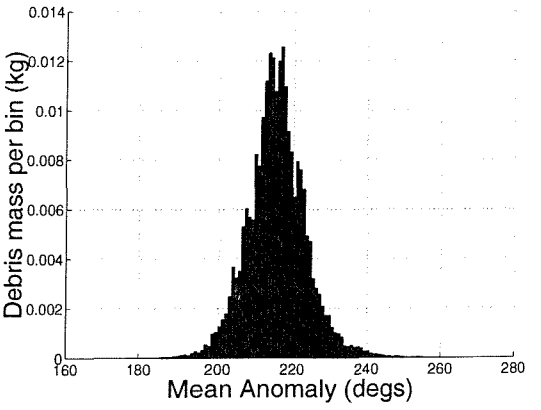

Figure 8.12 The distribution of mass in mean anomaly following a low-speed collision in orbit #4 (most massive 5% of fragments removed)

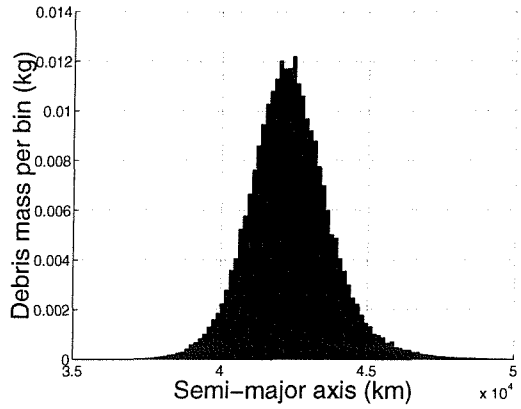

Figure 8.13 The Monte Carlo averaged distribution of mass in semi-major axis following a low-speed collision in orbit #4

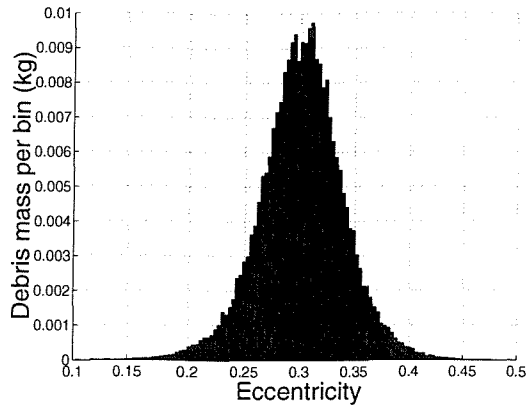

Figure 8.14 The Monte Carlo averaged distribution of mass in eccentricity following a low-speed collision in orbit #4

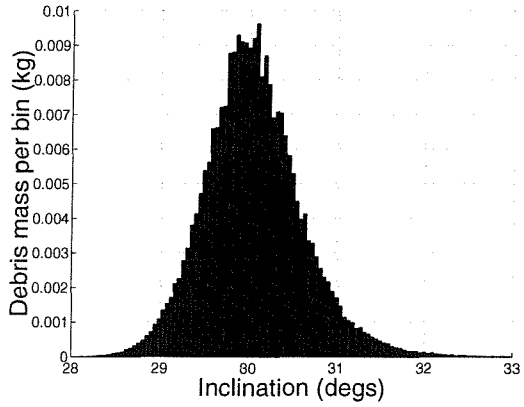

Figure 8.15 The Monte Carlo averaged distribution of mass in inclination following a low-speed collision in orbit #4

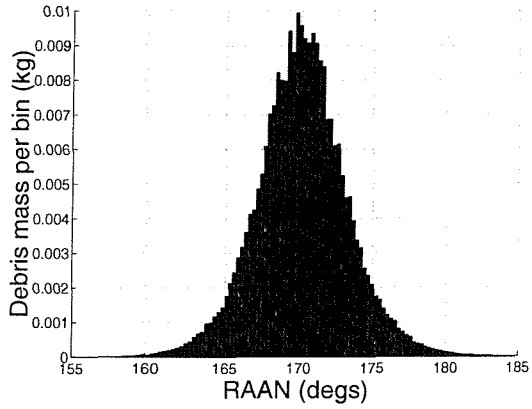

Figure 8.16 The Monte Carlo averaged distribution of mass in RAAN following a low-speed collision in orbit #4

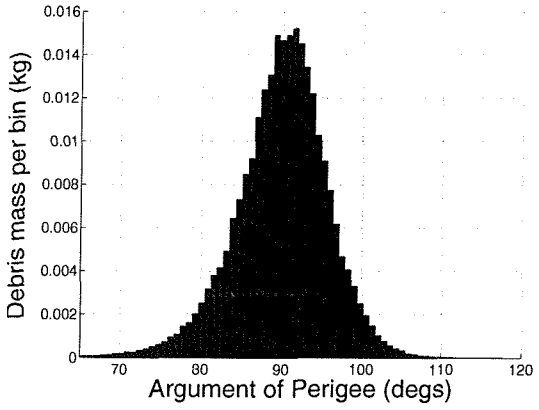

Figure 8.17 The Monte Carlo averaged distribution of mass in argument of perigee following a low-speed collision in orbit #4

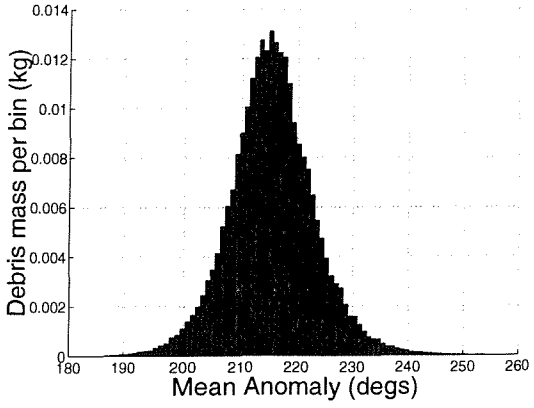

Figure 8.18 The Monte Carlo averaged distribution of mass in mean anomaly following a low-speed collision in orbit #4

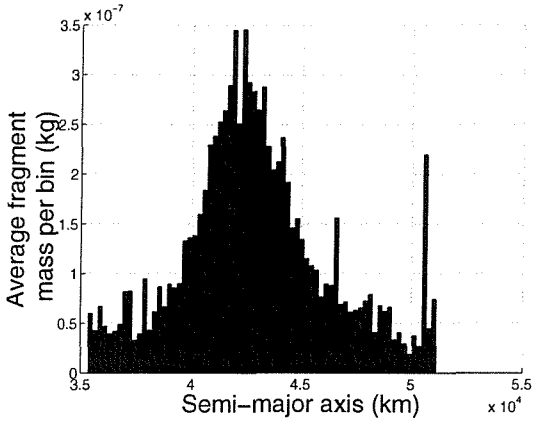

Figure 8.19 The Monte Carlo averaged distribution of mass in semi-major axis (most massive 5% of fragments removed)

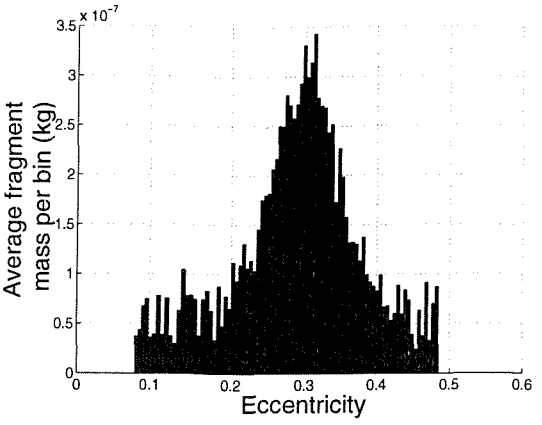

Figure 8.20 The Monte Carlo averaged distribution of mass in eccentricity (most massive 5% of fragments removed)

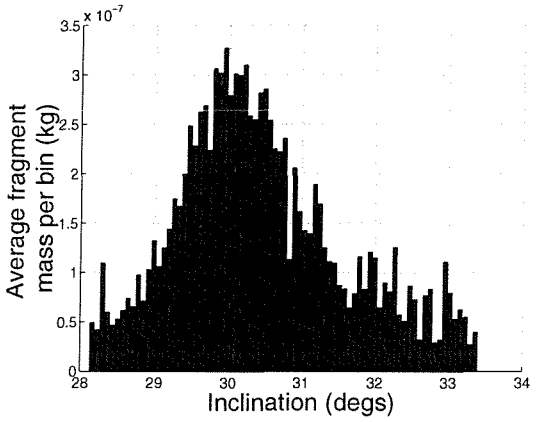

Figure 8.21 The Monte Carlo averaged distribution of mass in inclination (most massive 5% of fragments removed)

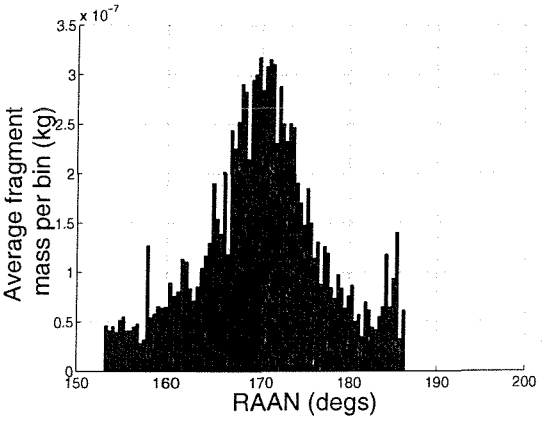

Figure 8.22 The Monte Carlo averaged distribution of mass in RAAN (most massive 5% of fragments removed)

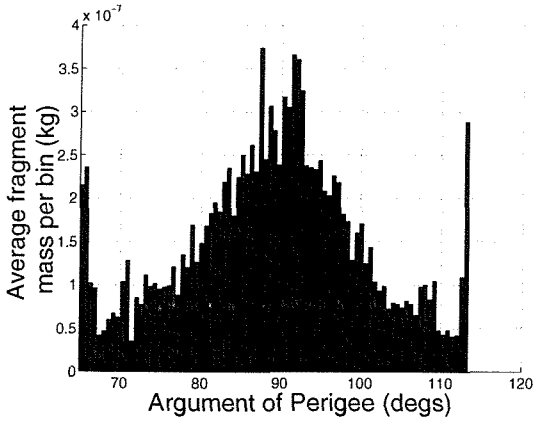

Figure 8.23 The Monte Carlo averaged distribution of mass in argument of perigee (most massive 5% of fragments removed)

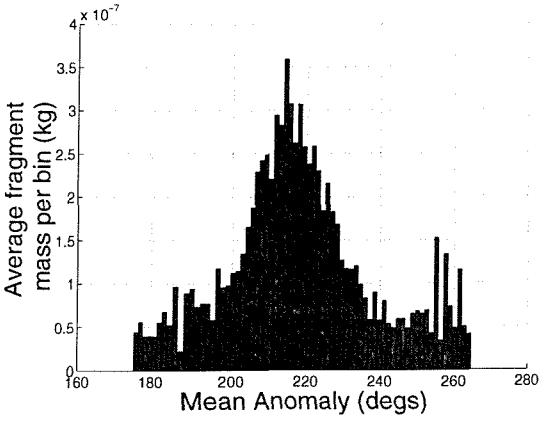

Figure 8.24 The Monte Carlo averaged distribution of mass in mean anomaly (most massive 5% of fragments removed)

It is anticipated that the most massive 5% of fragments would be propagated individually, thus maintaining their physical characteristics, whilst the remaining 95% will be propagated using the FCP and their physical characteristics calculated from their recovered mass values. The fact that the original mass values will not be recovered is not important, as these values were subject to random variables in the breakup model, and thus a second run of the breakup model would generate different mass values for each fragment anyhow. Furthermore, the relationship between the fragment mass and position need not be exact, since the positions of the fragments are randomised with each run of the breakup model. This is another example of a situation where the exact values are unimportant – it is the resulting distributions which are important, and not the values used to generate them. The fragment number distributions in element-space change with time. However the number distribution in semi-major axis remains normal at all times. The same applies to the mass and mass per fragment distributions in semi-major axis. The FCP will only require one distribution from which to recover the fragment masses – it is anticipated that the distribution it will use will hence be the mass per fragment distribution in semi-major axis.

The mode values and 3σ limits of these distributions correspond to those of the number distributions. Hence there will be no need to propagate any additional information in order to reconstruct these distributions and recover the fragments' mass values. The only reduction in speed, therefore, will be due to the time it takes to sample from the mass per fragment vs. element distribution in semi-major axis, which will be negligible compared to the speed of the FCP overall. Once the fragments' masses have been recovered, the fragments' cross-sectional areas can be calculated according to the equations used in the appropriate breakup model. These values can then be randomised, if desired, according to the spreading function used in the chosen breakup model. The mass-to-area ratios of the fragments can be easily calculated, and by assuming spherical fragments, so can the diameters. Thus the physical characteristics of the cloud can be completely re-created according to the breakup model used.

8.3.2 Modelling SRP Effects

The FCP in its current state will model a cloud's evolution under the influence of all gravitational perturbations. It has already been shown that the effects of SRP are largely negligible compared to the effects of gravitational perturbations and it is widely known that drag has no effect in the GEO regime. Thus the current model is ideally suited for GEO. However, it is only its inability to model the effects of drag that preclude it from also being used in LEO. What if the FCP methodology could be developed to include the modelling of drag effects? There is some evidence to suggest that the FCP could be modified to do just that. Drag, as well as SRP, have the greatest effect on fragments with low mass-to-area ratios, and have the least effect on fragments with high mass-to-area ratios. In accurately modelling drag or SRP effects using the FCP, it is therefore important to propagate distribution parameters in element-space that correspond to the extremes of the mass-to-area ratio distribution. In the sampling of fragments for FCP propagation, samples are taken from the edges of the debris cloud in six-dimensional element-space, and also from the centre of the cloud. Figures 8.25 – 8.30 illustrate the Monte Carlo averaged area-to-mass ratio per fragment distribution plotted against each of the six orbital elements following the same low-speed collision induced breakup scenario used in the examples in section 8.3.1, again, as modelled by the IDES breakup model. Area-to-mass ratios rather than mass-to-area ratios are used in these figures, since their distributions in element-space can be more clearly defined if area-to-mass ratios are used.

The distributions in Figures 8.25 – 8.30 show that the fragments near the centre of the cloud have higher area-to-mass ratios on average than those at the edge of the cloud. These distributions may approximate to quadratics, although further analysis will be necessary to determine the distribution shape that best describes this data. Again, the large peaks near the edges of the distributions can be attributed to the small number of fragments in these bins, thus reducing the smoothing effect of the Monte Carlo averaging techniques and allowing any fragments with unusually large area-to-mass ratios to dominate.

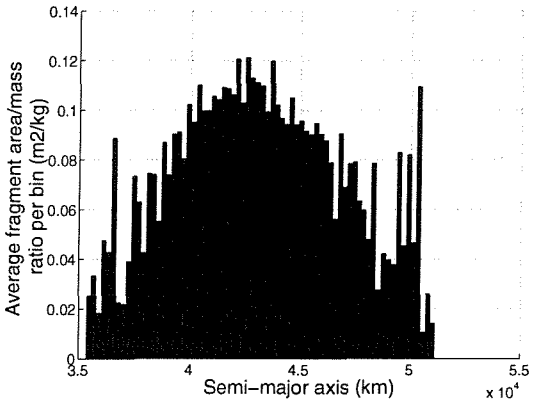

Figure 8.25 The Monte Carlo averaged distribution of fragment area-to-mass ratio in semi-major axis following a low-speed collision in orbit #4

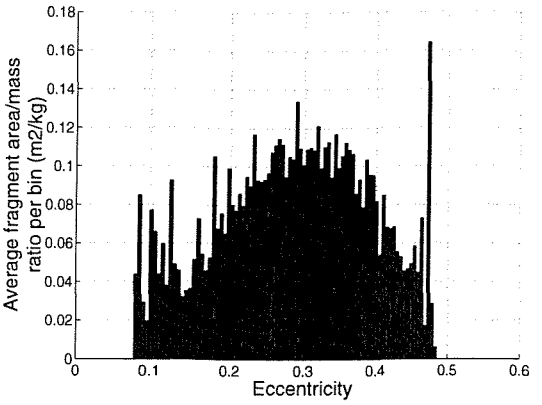

Figure 8.26 The Monte Carlo averaged distribution of fragment area-to-mass ratio in eccentricity following a low-speed collision in orbit #4

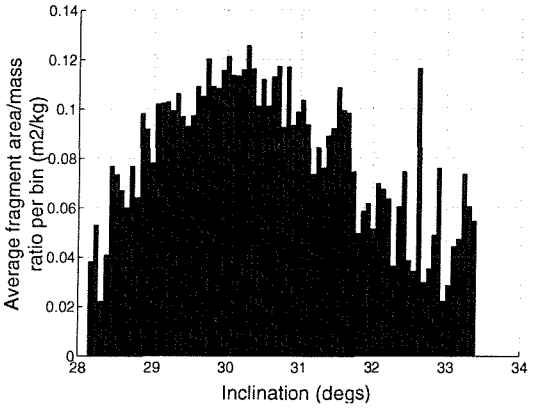

Figure 8.27 The Monte Carlo averaged distribution of fragment area-to-mass ratio in inclination following a low-speed collision in orbit #4

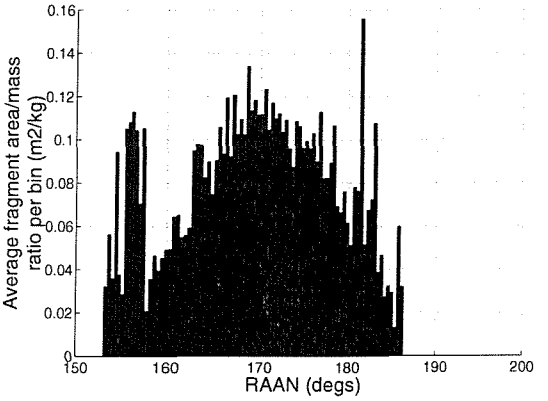

Figure 8.28 The Monte Carlo averaged distribution of fragment area-to-mass ratio in RAAN following a low-speed collision in orbit #4

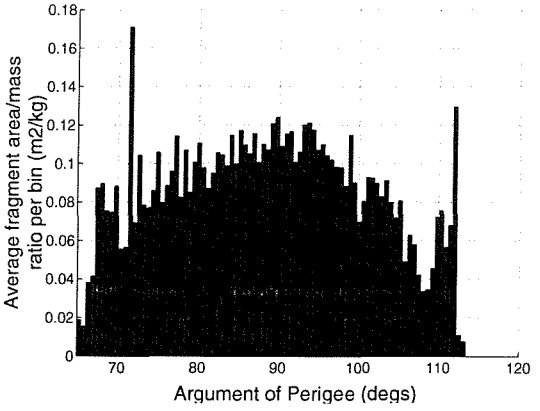

Figure 8.29 The Monte Carlo averaged distribution of fragment area-to-mass ratio in argument of perigee following a low-speed collision in orbit #4

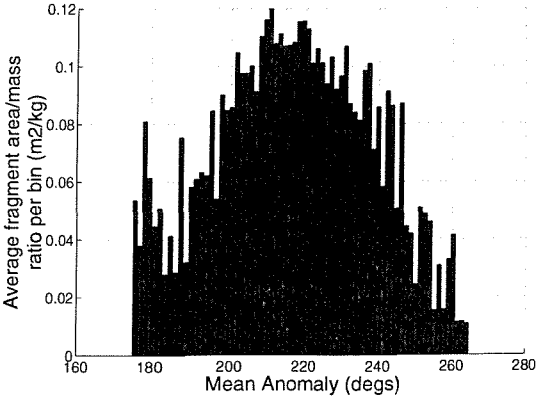

Figure 8.30 The Monte Carlo averaged distribution of fragment area-to-mass ratio in mean anomaly following a low-speed collision in orbit #4

The extremities and mode values of these distributions correspond to the 3σ limits and mode values of the number distributions, which are sampled and propagated by the FCP in its current state. By sampling fragments with the maximum and minimum area-to-mass ratios, the FCP has sampled those fragments that are most susceptible to drag (and SRP) effects, as well as those that are least susceptible. Thus the FCP should be able to model the largest and smallest changes in the cloud due to drag and SRP perturbations and should be able to pin-point the new position and size of the cloud following its propagation under the influence of these perturbations. Whilst the FCP may be able to replicate the new position and size of the cloud in element-space, an accurate reconstruction of the shapes of the scatter plots will be necessary if the FCP is to accurately model the evolution of the cloud under the influence of drag effects. This may be possible using sophisticated mapping techniques and/or the superpositions of different distributions in the primary scatter plots. However, this would require further investigation into the properties of these scatter plots for various breakup scenarios (including high-energy collisions) and for various propagation periods, and would require extensive modifications to the current FCP program. The question that then arises is: will 73 pseudo-fragments contain enough information about the evolved debris cloud in order to reconstruct these complex scatter plots? If not, more pseudo-fragments may need to be propagated, which will reduce the efficiency of the FCP.

8.3.3 Propagating Clouds Produced by Non-Isotropic Breakups

The distributions propagated by the FCP are the result of modelling isotropic breakups, where it is assumed that the fragments are randomly, uniformly distributed about a unit-sphere. This is highly unlikely in reality, as the fragments in a debris cloud produced by any breakup event will almost certainly not be uniformly distributed. In the absence of enough input parameters however, such as the structure and size of the spacecraft, impact angle, projectile composition, etc., the assumption of an isotropic breakup is necessary. There are, however, breakup models that allow for non-isotropic breakups to be modelled, e.g. SDS [13], although these require inputs that would not be available in

reality. A further possible enhancement to the FCP would be to examine the viability of propagating debris clouds produced by non-isotropic breakups. In these cases it is unlikely that the distributions produced would be mostly normal and much more likely that they would mostly be skewed, possibly approximating to gamma distributions. Gamma distributions of many different shapes can be modelled by the FCP in its current state. However, it remains to be seen whether the element-relationship scatter plots produced by such an event can be easily replicated.

Another facet of this modification would be the investigation of the distributions produced by SRM slag in GEO. The slag produced by an apogee-kick motor at the end of motor firing is a major cause of GEO debris. The production of this slag is totally different to an isotropic breakup and thus it can be expected that the number distributions produced in element-space would be quite different to those produced by a breakup event. However, if these distributions can be classified and replicated then there is every reason to believe that the FCP could be modified, albeit extensively, to model the evolution of SRM slag clouds.

8.3.4 A Unified Model

Perhaps the most ambitious way in which the theory could be extended would be to produce a unified breakup – propagation – risk analysis model, which explicitly used fragment distributions – where the need for individual fragments could be eliminated completely. The randomising spreading functions in the breakup model could be removed and the breakup model's delta-v and azimuth and elevation distributions could be converted directly into fragment number distributions in element-space, without having to sample from these distributions and assign delta-v's, azimuths and elevations to individual fragments in the interim. However, the process of transforming the distributions produced by the breakup model directly into fragment number distributions in element-space remains unclear. The fragment number distributions could be input directly into the FCP, which would negate the need for much of the code that currently

makes up the FCP's 'Wrap' module. After propagation, the distributions could be converted directly into collision probabilities, again, without having to re-create the properties of the individual fragments, although the method by which this could be done also remains unclear. This would negate much of the code that currently makes up the FCP's 'Unwrap' module.

The probability of a collision induced breakup of a particular target object is generated from the flux encountered by the target object as it traverses the debris field. There are many ways of calculating the collision probability of a target object – one of the most widely used methods is the incremental flux method, or Klinkrad method as it is also known [98], which was briefly described in Chapter 6. In this method, the debris flux encountered by a target object over one orbital period is calculated at regular intervals (in IDES, for instance, the flux is calculated every 6 months). If the flux is above a critical value then a collision induced breakup is triggered by the model, where the breakup occurs at the point of greatest flux.

In order to calculate the flux encountered by an object, the spatial density of orbital debris must first be quantified in the regions through which the target object will pass. In the Klinkrad method, this is done by calculating the spatial density of fragments in various cells of an inertial, geocentric control volume. The number distribution histograms in element-space, which show the number of fragments per bin, are equivalent to spatial density distributions, where the control volume cells are not defined in 3-dimensional, geocentric, Cartesian space, but are instead defined in 6-dimensional element-space and where the resolution of the control volume is dictated by the bin size. If these number distributions in element-space, together with the scatter plots that define the relationships between them, could somehow be used to create the spatial density distribution in 3-dimensional, geocentric, Cartesian space, then the risk to any target object could be calculated without the reconstruction of individual fragments or their properties, and without the need for a geocentric control volume with a fixed resolution. This would vastly reduce the time required to run a future space debris environment simulation and furthermore would be a more meaningful method, as it will totally negate the need for

individual fragments, the properties of which are not of prime interest. The method may also yield more accurate risk predictions, as the bin sizes used to calculate the spatial density distribution could be much smaller. Smaller bin sizes would be accommodated by the method since the calculation of the number of fragments in each bin would be instantaneous, rather than requiring the time-consuming calculation of individual fragment positions and the summation of the number of fragments in each bin, as is current practice.

This method may seem ambitious, and even dubious. However it would produce the optimum solution to debris modelling in terms of speed, accuracy and memory requirements. The method thus merits consideration. However, a great deal of further thought and investigation would be required to determine whether or not it is possible, and if so, feasible.

If the unified model described above could be brought to fruition, then it may also negate the need for Monte Carlo runs. Monte Carlo simulations are run to smooth out the peaks and troughs in spatial density distributions caused by randomising spreading functions in the breakup model. Whilst the randomness imparted to the properties of debris fragments can be reduced, for example by removing the randomising spreading functions used to randomise the fragment delta-v's and mass-to-area ratios about their mean values, they cannot be removed entirely. Randomness is necessary, for instance, in allocating the azimuths and elevations to fragments – how else should they be distributed if not randomly? Therefore, the use of individual fragments requires the implementation of randomness to the fragments' properties, which in turn requires the need for Monte Carlo averaging techniques to determine the most likely future spatial density distribution and hence the most likely risk of impact to an orbiting body. However, remove the individual fragments completely, and the need for randomness in the breakup model is also removed and so is the need for Monte Carlo simulations. If this ambitious method is feasible then it would provide further vast time savings to current debris models by producing the most likely impact risk on the first iteration.

This concept is rather abstract at present and may even be unfeasible. Two of the crucial steps in this process remain undefined. However, it has been presented here nonetheless in the hope that other researches may solve these problems and develop a truly unified space debris model.

8.3.5 A Hybrid Model

Fast debris propagators can essentially be divided into two distinct categories. The first category includes those propagators that gain a speed increase by only propagating a limited set of pseudo-fragments. Examples of propagators in this category include the FCP and the weighted particle approach. These propagators are faster than conventional propagators at propagating clouds of particles, but they use a conventional propagator to propagate each individual pseudo-fragment. Thus, by definition, they are no faster at propagating each individual pseudo-fragment than a conventional propagator. The second category includes those propagators that gain a speed increase by replacing the conventional propagator with sophisticated techniques to evolve each individual fragment. An example of a propagator in this category includes PETRA, which propagates all the fragments of a debris cloud, but does so using look-up reference tables and thus avoids the lengthy iterative process of calculating the changes in the fragments' orbital elements over each time-step. Thus PETRA is faster than a conventional propagator at evolving each fragment, unlike fast propagators in the first category. The fastest conceivable propagator would be a hybrid between these two methods, where a debris cloud could be sampled to reduce it to a limited set of pseudo-fragments and then these pseudo-fragments could be propagated quickly using a non-iterative approach, before the cloud was reconstructed at the required epoch. An example of a possible hybrid model would be a PETRA/FCP hybrid. Although these would not be compatible in their present states, since PETRA is designed for LEO and the FCP is designed for GEO.

In summary, this chapter has outlined some possible improvements to the FCP and has suggested some enhancements to the methodology behind it. Some of these improvements have been explained in detail, whereas others are merely ideas, which require greater thought to bring them to fruition. A great deal more work can be done in fragment distribution manipulation and propagation, both in short-term improvements to the FCP and in ambitious long-term enhancements to the methodology, which could potentially produce a unified model capable of operating at all altitudes with all breakup scenarios, which might also be capable of quickly and accurately assessing the risks to target objects without having to create or manipulate individual fragments.

Bibliography

1. Williams, N., Swinerd, G.G., Lewis, H.G., Gittins, G., *A Sensitivity Analysis of Breakup Models.* Space Debris 2001, Science and Technology Series, AAS, Univelt, San Diego, 2002., 1 - 5 October 2001. **115**: p. 97 - 115.
2. Williams, D.N., Swinerd, G.G., Lewis, H.G., Gittins, G.L. *A New Fast Cloud Propagator for Use in the GEO Regime.* in *34th COSPAR/World Space Congress 2002.* 10 - 19 October 2002. Houston, Texas, USA.
3. Committee on Space Debris, *Orbital Debris - A Technical Assessment*, ed. N.R. Council. 1995, Washington D.C.: National Academy Press.
4. Chobotov, V.A., ed. *Orbital Mechanics.* 2nd ed. Education Series. 1986, AIAA.
5. *Interagency Report on Space Debris.* November 1995, Office of Science and Technology Policy.
6. Belk, A.A., Robinson, J.H., Alexander, M.B., Cooke, W.J., Pavelitz, S.D., *Meteoroids and Orbital Debris: Effect on Spacecraft.* NASA Reference Publication 1408, 1997.
7. Walker, R., et al., *Update ofthe ESA Mitigation Handbook - Executive Summary.* ESA Contract 14471/00/D/HK, Ref. QINETIQ/KI/SPACE/CR021539, July 2002.
8. Various Authors, *ESA Space Debris Mitigation Handbook.* European Space Agency, February 1999(Release 1.0).
9. *Second Quarter 2002 Launch Report.* 2002.

10. Schildknecht, T., Ploner, M., Hugentobler, U., *The Search for Debris in GEO.* 33rd COSPAR Scientific Assembly, July 16 - 23 2000.

11. Wegener, P., Bendisch, J., Krag, H., Oswald, M., Stabroth, S., *Population Evolution in the GEO Vicinity.* 19 October 2002.

12. Walker, R., *The Long-Term Interations of Satellite Constellations with the Orbital Debris Environment*, in *Aeronautics and Astronautics*. February 2002, University of Southampton.

13. Barrows, S., *Evolution of Artificial Space Debris Clouds*, in *Aeronautics and Astronautics*. 1996, University of Southampton.

14. Author, U., *Orbiting Debris: A Space Environmental Problem.*

15. Jehn, R., *Dispersion of Debris Clouds from In-Orbit Fragmentation Events.* Esa Journal 1991, 1991. **15**.

16. Chobotov, V.A., *Dynamics of Orbiting Debris Clouds and the REsulting Collision Hazard to Spacecraft.* Journal of the British Interplanetary Society, 1990. **43**: p. 187-195.

17. Bendisch, J., Krag, H., Wegener, P., *The Future Debris Environment from LEO to GEO.* 52nd International Astronautical Congress, Toulouse, France (IAA-00-IAA.6.6.03), 1-5 October 2001.

18. Unknown Authors, *Technical Report on Space Debris.* Text of the Report adopted by the Scientific and Technical Subcommittee of the United Nations Committee on the Peaceful Uses of Outer Space, United Nations Publication (ISBN 92-1-100813-1), 1999.

19. Schildknecht, T., *Optical Observations of Space Debris in GEO and in Highly Eccentric Orbits.* PEDAS1-B1.4-0007-02, World Space Congress, Houston, Texas, USA, 2002.

20. Chobotov, V.A., Johnson, C.G., *The Effects of Satellite Bunching on the Probability of Collision in Geosynchronous Orbit.* Proceedings of the First

European Conference on Space Debris, Darmsatdt, Germany (ESA-SD-01), 5-7 April 1993: p. 651-655.

21. Yasaka, T., Oda, S., *Breakup, Collision and Population Growth in Geostationary Orbit.* Proceedings of the First European Conference on Space Debris, Darmsatdt, Germany (ESA-SD-01), 5 - 7 April 1993.

22. Hanada, T., Yasaka, K., *Debris Cloud Evolution and Probability of Secondary Impact after Collision in Geosynchronous Region.* 21st International Symposium on Space Technology and Science, Sonic City, Omiya, Japan, May 24-31, 1998.

23. Luu, K., Sabol, C., *Effects of Perturbations on Space Debris in Supersynchronous Orbits.* Final Report, Air Force Research Laboratory, Space Vehicles Directorate, 3550 Aberdeen Ave, Air Force Materiel Command, Kirtland Air Force Base, NM 87117-5776, (AFRL-VS-PS-TR-1998-1093), October 1998.

24. Johnson, N.L., McKnight, D.S., *Artificial Space Debris*. A Foundation Series. 1987: Orbit Book Co. Ltd.

25. Watson, C., *NASA Human Spaceflight.* (http://spaceflight.nasa.gov/realdata/sightings/SSapplications/Post/JavaSSOP/orbit/ISS/SVPOST.html), 2003.

26. Flury, W., Massart, A., Schildknecht, T., Hugentobler, H., Kuusela, J., Sodnik, Z., *Searching for Small Debris in the Geostationary Ring - Discoveries with the Zeiss 1 metre Telescope.* ESA Bulletin 104, 2000.

27. Hanada, T., Krisko, P., Anz-Meador, P., Johnson, N. *Consequences of Continued Growth in the GEO and GEO Disposal Regimes*. in *51st International Astronautical Congress*. 2 - 6 October 2000. Rio de Janeiro, Brazil.

28. Hanada, T., Yasaka, T., *GEO Space Debris Environment Evolution Model Update.* 50th International Astronautical Congress, 4-9 October 1999.

29. Walker, R., Martin, C.E., *Cost-Effective and Robust Mitigation of Space Debris in Low Earth Orbit.* 2002.

30. *NASA Safety Standard 1740.14 - Guidelines and Assessment Procedures for Limiting Orbital Debris.* (http://www.orbitaldebris.jsc.nasa.gov/mitigate/nss1740/nss1740.html), 2001.

31. Forward, R.L., Hoyt, R.P., *Scientific American: Space Tethers.* (http://www.sciam.com/article.cfm?articleID=000A8124-EC87-1CB8-B4A8809EC588EEDF), February 1999.

32. *Fundamental Tether Concepts:.* (http://www-ccar.colorado.edu/asen5050/projects/projects_2001/eby/introduction.html).

33. Estes, R.D., Lorenzini, E.C., Sanmartin, J., Pelaez, J., Martinez-Sanchez, M., Johnson, C.L., Vas, I.E., *Bare Tethers for Electrodynamic Spacecraft Propulsion.* Journal of Spacecraft and Rockets, April 2000. **37**(2): p. 205-211.

34. Kessler, D.J., Reynolds, R.C., Anz-Meador, P.D., *Orbital Debris Environment for Spacecraft Designed to Operate in Low Earth Orbit.* NASA-TM-100471, 1988.

35. Zhang, J., Kessler, D.J., Matney, M.J., Eichler, P., Reynolds, R.C., Anz-Meador, P.D., Stansbery, E.G., *The NASA Engineering Model: A New Approach.* Advances in Space Research, 1997. **19**(2): p. 281 - 290.

36. Eichler, P., Rex, D. *Debris Chain Reactions*. in *Orbital Debris Conference: Technical Issues & Future Directions, AIAA-90-1365,*. April 1992. Baltimore, USA: AIAA/NASA/DoD.

37. Nazarenko, A.I. *The Development of the Statistical Theory of a Satellite Ensemble Motion and its Application to Space Debris Modelling.* in *2nd European Conference on Space Debris, ESA SP-393*. May 1997. Darmstadt, Germany.

38. Reynolds, R., *Documentation of Program EVOLVE: A Numerical Model to Compute Projections of the Man-Made Debris Environment.* System Planning Corporation Report OD91-002-U-CSP, 1991.

39. Reynolds, R.C., Bade, A., Eichler, P., Jackson, A.A., Krisko, P.H., Matney, M., Kesler, D.J., Anz-Meador, P.D. *NASA Breakup Model Distribution Functions (from NASA Standard Breakup Model 1998 Revision).* in *LMSMSS-32532*. September 1998.

40. Johnson, N.L., Krisko, P.H., Liou, J.-C., Amz-Meador, P.D. *NASA's New Breakup Model of EVOLVE 4.0.* in *33rd Scientific Assembly of COSPAR.* 16 - 23 July 2000. Warsaw, Poland.

41. Unknown Authors, *Orbital Debris Quarterly News.* NASA Orbital Debris Programm Office, April 1998. **3**(2).

42. Unknown Authors, *Orbital Debris Quarterly News.* NASA Orbital Debris Programm Office, October 1998. **3**(4).

43. Anselmo, L., Cordelli, A., Farinella, A., Pardini, C., Rossi, A., *Study on Long-Term Evolution of Earth Orbiting Debris.* Final Report of ESOC Contract 10034/92/D/IM(SC), February 1996.

44. Cordelli, A., Farinella, P., Rossi, A., *The Influence of the Fragmentation Threshold on the Long-Term Evolution of the Orbital Debris Environment.* 16 December 1997, CNUCE: Pisa, Italy.

45. Rossi, A., Anselmo, L, Cordelli, A., Farinella, P., Pardini, C., *Modelling the Evolution of the Space Debris Population.*

46. Pardini, C., Anselmo, L., Rossi, A., Cordelli, A., Farinella, P. *The 1997 CNUCE Orbital Debris Reference Model.* in *8th AAS/AIAA Space Flight Mechanics Meeting, AAS 98-173.* 1997.

47. Rossi, A., Cordelli, A., Pardini, C., Anselmo, L., Farinella, P. *Modelling the Space Debris Evolution: Two New Computer Codes.* in *AAS/AIAA Spaceflight Mechanics Meeting.* February 13 - 16, 1995. Alberquerque, New Mexico.

48. Sdunnus, H., *ESA MASTER Model Final Report.* ESOC Contract 10453/90/D/CS, July 1995.

49. Klinkrad, H., Sdunus, H., Bendisch, J. *Developmrent of the ESA Space Debris Reference Model.* in *COSPAR Meeting No. B-12 (Space Debris).* 11 - 22 July 1994. Hamburg, Germany.

50. Klinkrad, H., Bendisch, J., Wegener, P., Wiedemann, C., Krag, H., Rex, D., Sdunnus, H., Bunte, K., Brandt, T., Walker, R., *ESA MASTER Model User's Manual.* ESA SD-CD03 Release 1.09, May 2000.

51. Klinkrad, H., Bendisch, J., Bunte, K.D., Krag, H., Sdunnus, H., Wegener, P., Walker, R., Wiedemann, C., Rex, D., *ESA MASTER POEM Software Algorithms Document.* 23 June 2000.

52. Klinkrad, H., Bendisch, J., Bunte, K.D., Krag, H., Sdunnus, H., Wegener, P., Walker, R., Wiedemann, C., Rex, D., *Upgrade of ESA's MASTER Model - Final Report.* ESA Contract No. 12318/97/D/IM, 23 June 2000.

53. Martin, C., Lewis, H.G., Walker, R. *Studying the MEO and GEO Space Environments with the Integrated DEbris Evolution Suite (IDES) Model.* in *3rd European Conference on Space Debris.* 19 - 21 March 2001. ESOC, Darmsdatd, Germany.

54. Lewis, H.G., Swinerd, G., Williams, N., Gittins, G. *DAMAGE: A Dedicated GEO Debris Model Framework.* in *3rd European Conference on Space Debris.* 19 - 21 March 2001. ESOC, Darmstadt, Germany.

55. Lewis, H.G., Swinerd, G., Williams, N., Gittins, G., *Investigating the Long-Term Evolution of the Debris Environment in High Earth Orbit Using the DAMAGE Model.* Space Debris 2001, Science and Technology Series, AAS, Univelt, San Diego, 2002., 2002. **105**: p. 167 - 180.

56. Divine, N. *Five Populations of Interplanetary Meteoroids.* in *Second LDEF Post-Retrieval Symposium.* June 1992.

57. Matney, M. *Updated Divine Meteoroid Engineering Model (METEM).* in *NASA Presentation Slides (Unknown Conference).*

58. Sdunnus, H., et al. *Upgrade ofStatistical Meteoroid/ Debris Models for GEO.* in *Progress Meeting #4 at eta_max space GmbH (presentation slides).* 15 - 16 June 2000. Braunschweig, Germany.

59. Sdunnus, H. *The Implementation of Flux Contributions from the Meteoroid Population in ESA's MASTER Model.* in *17th IADC Meeting.* 11 -13 October 1999. ESOC, Darmstadt, Germany.

60. Roy, A.E., *Orbital Motion.* 3rd ed. 1998: Adam Hilger.

61. King-Hele, D., *Observing Earth Satellites.* 1983: Macmillan London.

62. Kozai, Y., *The Motion of a Close Earth Satellite.* The Astronautica Journal, 30 October 1959: p. 367 - 377.

63. Merson, R.H., *Satellite Orbit and Attitude Theory and its Use with Skynet 2.* Technical Report 77083, Royal Aircraft Establishment, Controller, HMSO, London, June 1977.

64. Housden, J., Rajasenan, C., *Eumetsat Polar System: EPS Mission Conventions Document.* Eumetsat/ESA, Doc. No. EPS/SYS/SPE/990002, August 1999.

65. Lewis, H.G., *DAMAGE: Debris Analysis and Monitoring Architecture for the Geostationary Environment.* 2003: University of Southampton.

66. Cooke, G.E., *Luni-Solar Perturbations of the Orbit of an Earth Satellite.* The Geophysical Journal of the Royal Astronomical Society, April 1962. **6**(3): p. 271 - 291.

67. Klinkrad, H., et al., *FOCUS: Fast Orbit Computation Utility.* 2001, ESOC, Darmstadt, Germany.

68. Aksnes, K., *Short-period and Long-period Perturbations of a Spherical Satellite due to Direct Solar Radiation.* Center for Astrophysica, Havard College Obervatory and Smithsonian Astrophysical Observatory, Cambridge, Massachusetts, 02138, Preprint Series No. 230,, December 1974.

69. Jehn, R., *Modelling Debris Clouds*, in *Mission Analysis Section.* 1996, ESOC: Darmstadt, Germany.

70. King-Hele, D., *Satellite Orbits in an Atmosphere.* 1987: Blackie and Son, Ltd., Glasgow/London.

71. Hanada, T., Yasaka, K., Goto, K., *Fragments Creation via Impact at Low Speed.* AAS-97-486, Advances in Astronautical Science, 1997. **96**.

72. Yasaka, T., Hanada, T., Hirayama, H., *Low-Velocity Projectile Impact on Spacecraft.* Acta Astronautica, 2000. **47**(10): p. 763 - 770.

73. Yasaka, T., Hanada, T., *GEO Debris Accumulation Model Viewed from Low Speed Impact Tests.* Space Forum, 1996. **1**: p. 151-160.

74. McKnight, D.S., *Determination of Breakup Initial Conditions.* Journal of Spacecraft and Rockets, 1990. **28**(4): p. 470-477.

75. Bess, T.D., *Mass Distribution of Orbiting Man-Made Space Debris.* NASA Document No. TN D-8108, December 1975.

76. Bess, T.D., *Size Distribution of Fragment Debris Produced by Simulated Meteoroid Impact on Spacecraft Wall.* NASA Document No. SP-379, 1975.

77. McKnight, D., Nagl, L., *Key Aspects of Satellite Breakup Modelling.* Proceedings of the First European Conference on Space Debris, Darmsatdt, Germany, 5-7 April 1993.

78. Reynolds, R., *The NASA Orbital Debris Guidelines: An Historical Perspective on Orbital Debris Modelling Supporting the Development of Policy on the Use of Space.* IAA-00-IAA.6.6.08, 51st International Astronautical Congress, 2 - 6 October 2000, Rio de Janeiro, Brazil.

79. Martin, C., Walker, R., Klinkrad, H., *The Sensitivity of the ESA Delta Model.* 34th COSPAR/World Space Congress 2002, Houston, Texas, USA, October 2002.

80. Rossi, A., Cordelli, A., Farinella, P., Anselmo, L., Pardini, C., *Long Term Evolution of the Space Debris Population.*

81. Anz-Meador, P.D., Matney, M.J., *An Assesment of the NASA Explosion Fragmentation Model to 1mm Characteristic Sizes.* 34th COSPAR/World Space Congress 2002, Houston, Texas, USA, October 2002.

82. LEAD Technologies, I., *SPSS for Windows.* Release 11.5.0, 6 Sept 2002.

83. The Mathworks, I., *MATLAB: The Language of Technical Computing.* Version 6.0.0.88, Release 12, 2000.

84. Brown, S., *Inferences About Correlation.* http://www.acad.sunytccc.edu/instruct/sbrown/stat/correl.htm, 2003.

85. Press, W.H., Flannery, B.P., Teukolsky, S.A., Vetterling, W.T., *Numerical Recipes in C : The Art of Scientific Computing.* January 1993.

86. Timpone, R., *The Polar Method - Random Draws from a Normal Distribution.* http://psweb.sbs.ohio-state.edu/faculty/rtimpone/computer_resources/polar.htm.

87. Holmes, S.P., *The Polar Method for Generating Normal Random Variables.* Stanford University Introductory Probability Course, Statistics 116, http://www-stat.staford.edu/~susan/courses/s116/node121.htm.

88. *Polar Method.* http://137.208.57.90/lv/9993/einheit6/node31.html.

89. Law, A.M., Kelton, W.D., *Simulation Modelling and Analysis (2nd edition).* McGraw-Hill (ISBN: 0-07-100803-9), 1991.

90. Bishop, C.M., *Neural Networks for Pattern Recognition.* 1995: Oxford University Press.

91. Gerald, C.F., Wheatley, P.O., *Applied Numerical Analysis.* 5th ed. 1994: Addison-Wesley Publishing Company.

92. Fassbender, H., *On Numerical Methods for Discrete Least-Squares Approximation by Trigonometric Polynomials.* Mathematics of Computation, April 1997. **66**(8): p. 719 - 741.

93. Bjorck, A., *Numerical Methods for Least-Squares Problems.* April 1996: Society for Industrial and Applied Mathematics, (ISBN: 0898713609).

94. Dennis, J.E., Schnabel, R.B., *Numerical Methods for Unconstrained Optimization and Nonlinear Equations (Classics in Applied Mathematics).* February 1996: Society for Industrial & Applied Mathematics (ISBN: 0898713641).

95. *MathsNet: A-Level Statistics.* (http://www.mathsnet.net/asa2/modules/s12calcmean.html).

96. *Descriptive Measures: Excel and Equations.* (http://www.cba.nau.edu/pinto-j/Commands/MeasuresExEq.html).

97. Kaplan, I., *Basic Statistics.* (http://www.bearcave.com/misl/misl_tech/wavelets/stat/), May 2003.

98. Klinkrad, H., *Collision Risk Analysis for Low Earth Orbits.* Advances in Space Research, 1993. **13**(8): p. 177 - 186.

99. Barrows, S.P., Swinerd, G.G., Crowther, R., *Review of Debris Cloud Modelling Techniques.* Journal of Spacecraft and Rockets, July - August 1996. **33**(4): p. 550-555.